The Aspect of Versatility in the Design of a Lightweight Robot for Surgical Applications

Der Aspekt der Vielseitigkeit in der Entwicklung eines Leichtbauroboters für chirurgische Applikationen

Von der Fakultät für Maschinenbau
der Gottfried Wilhelm Leibniz Universität Hannover
zur Erlangung des akademischen Grades

Doktor-Ingenieur

genehmigte Dissertation
von

Dipl.-Ing. Ulrich Hagn

geboren am 21. Februar 1971 in München-Pasing

2011

1. Referent:	Prof. Dr.-Ing. Tobias Ortmaier
2. Referent:	Prof. Dr.-Ing. Gerhard Poll
3. Referent:	Prof. Dr.-Ing. Gerd Hirzinger
Tag der mündlichen Prüfung:	15.12.2010

Acknowledgements

This thesis summarises my research in the field of surgical robotics, conducted at the *German Aerospace Center (DLR), Institute of Robotics and Mechatronics*.

I would like to thank all colleagues at the institute for their help, advice and, opinions. In particular, I want to thank Prof. Dr.-Ing. Gerd Hirzinger for his confidence in my work and for giving me the opportunity to join the medical robotics research activities at the very beginning. The distinguished expertise and teamwork culture at his institute always stimulated my work.

I thank Prof. Dr.-Ing. Tobias Ortmaier (*Leibniz Universität Hannover*) for his advice and guidance during the composition of this thesis and for the inspiring joint research years. For joining the examination committee, I thank Prof. Dr.-Ing. Ludger Overmeyer and Prof. Dr.-Ing. Gerhard Poll.

I also want to thank all fellow researchers and students of the *DLR*'s medical robotics research group, for their commitment to the surgical robotics projects. In particular, I thank Georg Passig, Robert Haslinger, Thomas Bahls, Alexander Nothhelfer, Florian Fröhlich, Bernhard, Kübler, Ulrich Seibold, Sophie Thielmann, Julian Klodmann, Andreas Tobergte, Oliver Eiberger, Michael Suppa and Tilo Wüsthoff for the exceptional teamwork and collegiality.

Especially, I want to thank my colleagues Mathias Nickl, Stefan Jörg, Rainer Konietschke, Alin Albu-Schäffer, Luc Le-Tien, Bertram Willberg, Franz Hacker, and Markus Grebenstein for their dedication to the idea of building a medical robot from the beginning until now.

A warm thank you to my parents, for their wisdom and love, reminding me to always think first and then follow my own path.

I dedicate this thesis to my beloved wife Nathalie and son Christopher, who always show me the real meaning of life.

Ulrich Hagn

Abstract

This work presents the design and the prototypical implementation of a versatile lightweight robot for surgical applications the *MIRO*.

With respect to the design of a surgical robot arm, two antipodal approaches define the range of design strategies. One is to focus on a single application with a specialised system. The second approach focuses on a versatile system for a range of applications. This work follows the second approach in order to enable rapid prototyping of new surgical techniques, to cover more than one step during an operation by the robotic system, and to broaden the foundation for the use of robotic technologies in different surgical applications. Therefore, the goal of this thesis is to prove the feasibility of designing a surgical robot with extended versatility.

Based on a survey of the current state of surgical robotics, this work identifies central design aspects for medical robots. The applied development method avoids the limitation of the desired versatility in early development phases: First, a generic design of the robot arm is developed, based on design aspects which are supposed to generally enhance the use of the system in operating rooms. Second, concrete performance requirements from a range of surgical applications are derived for the *MIRO* and the generic design is scaled and optimised accordingly.

The *MIRO* robot weighs 9.8 kg with a maximum payload of 3 kg. The seven DoF serial kinematics intentionally resembles those of the human arm in order to increase the familiarity of non-technical users with the robot arm. Furthermore, the joint redundancy allows for collision avoidance by null-space motion. The low weight of the *MIRO* targets different setup options, like mounting of one or multiple arms at an operating table or a ceiling boom. Setups with multiple arms demand for compact dimensions of the robot, which are achieved by coupling joints. Wrist and end effector design enable the use of endoscopic and conventional instruments. Integrated joint torque sensors are applied to measure external interaction forces, to enable hands-on robot approaches, compensate for elasticities, or to detect collisions.

The *MIRO* robot is applied and evaluated in prototypical surgical applications at the *DLR*. In a navigated robot-assisted biopsy application, a precursor of the

robot was combined with a surgical navigation system and combines hands-on with autonomous procedural steps. In the *ASTMA* project, the *MIRO* robot guides an ultrasound transducer in order to explore the left internal thoracic artery. In tests for osteotomy tasks in orthopaedic surgery, the *MIRO* robot proves robustness against the vibrations of an oscillating saw. The position accuracy and repeatability of the *MIRO* for laser-osteotomy tasks was identified with 0.5 mm and 0.2 mm, respectively. In the *MiroSurge* system, three *MIRO* arms are integrated as telemanipulators in a telerobotic minimally invasive surgery setup.

In conclusion, this thesis proves the feasibility of designing a robot with extended versatility, optimised for the use in operating rooms, and applicable in a comprehensive, but not unlimited, range of surgical applications.

Keywords: Robotics, Versatility, Surgery

Kurzfassung (German Abstract)

Die vorliegende Arbeit präsentiert die Entwicklung und prototypische Implementierung des *MIRO*, einem vielseitigen Leichtbauroboter für chirurgische Anwendungen.

Bezüglich der Entwicklungstrategie für einen Chirurgieroboter existieren zwei orthogonale Ansätze: Der erste Ansatz strebt nach einem spezialisierten System für eine einzelne Anwendung. Im Gegensatz dazu zielt der zweite Ansatz auf ein vielseitiges System für einen breiten Anwendungsbereich ab. Für den *MIRO* wurde der zweite Ansatz gewählt, um die Entwicklung neuer Applikationen zu beschleunigen und um mehr als einen einzelnen Operationsschritt mit dem Robotersystem durchführen zu können. Des Weiteren soll dadurch die Nutzungsbreite der Technologien erhöht werden. Ziel der vorliegenden Arbeit ist, die Machbarkeit der Entwicklung eines vielseitigen Chirurgieroboters nachzuweisen.

Ausgehend vom Stand der Technik identifiziert die vorliegende Arbeit zentrale Designaspekte für Roboter. Das im Weiteren gewählte Vorgehen verhindert eine Abschwächung des Vielseitigkeitsanspruches in frühen Entwicklungsstadien: Hierfür wird im ersten Schritt ein generisches Design des Roboters basierend auf Eigenschaften entwickelt, welche allgemein als vorteilhaft für chirurgische Applikationen eingeschätzt werden. Anschließend werden konkrete Leistungsspezifikationen aus einer Reihe chirurgischer Applikationen für den *MIRO* abgeleitet und das generische Design skaliert und optimiert.

Der *MIRO* hat eine Traglast von 3 kg bei 9,8 kg Eigengewicht. Die serielle 7-Achs-Kinematik ähnelt dem menschlichen Arm, wodurch eine natürliche Interaktion von Anwendern mit dem System erreicht werden soll. Darüber hinaus begünstigt die Gelenkredundanz Ansätze zur Kollisionsvermeidung durch Nullraum-Bewegungen. Das geringe Gewicht zielt auf verschiedene Aufstellarten ab, wie die Befestigung eines oder mehrerer Arme an einem Operationstisch oder an Deckenstativen. Vor allem in Mehrarm-Anwendungen sind kompakte Abmessungen wichtig, was durch neuartige

Koppelgelenke erreicht wird. Die Konstruktion der Handachsen erschließt den Einsatz sowohl endoskopischer wie auch konventioneller Instrumente. Ansätze wie Kraftregelung, handgeführte Anwendungen oder Kollisionsdetektion werden durch Gelenkdrehmomentsensorik ermöglicht.

Der *MIRO* wird am *DLR* in prototypischen Applikationen eingesetzt und untersucht. In einer Anwendung für navigierte, roboter-assistierte Biopsien wurde eine Vorstufe des *MIRO* mit einem chirurgischen Navigationssystem betrieben und handgeführte mit autonomen Betriebsmodi kombiniert. Im Projekt *ASTMA* führt der *MIRO* einen Ultraschallkopf, um den Verlauf der linken Brustwandarterie zu explorieren. In Tests für die orthopädische Chirurgie zeigt sich der *MIRO* robust gegenüber den Schwingungen von oszillierenden Sägen. Hinsichtlich des Führens von Lasersystemen zur Trennung von Knochengewebe wurde die Genauigkeit des *MIRO* untersucht, welche mit einer Positionsgenauigkeit von ca. 0,5 mm und einer Wiederholgenauigkeit von 0,2 mm angegeben werden kann. Im Robotersystem *MiroSurge* sind drei *MIRO* Arme als Telemanipulatoren für telerobotische minimal invasive Anwendungen integriert.

Die vorliegende Arbeit weist die Machbarkeit der Entwicklung eines vielseitigen Roboters nach, der für den Einsatz im Operationssaal optimiert wurde und in einer großen, jedoch nicht unbegrenzten, Zahl von chirurgischen Applikationen eingesetzt werden kann.

Schlüsselbegriffe: Robotik, Vielseitigkeit, Chirurgie

Contents

Notations

Notation in this thesis:	Scalars are notated as lower case italic letters and vectors by lower case italic, bold letters.
$+, 0, -$	rating symbols for += good, 0= average, −= poor
50NiCr13	chrome nickel steel
AC	abbreviation for alternating current
AD	abbreviation for anaesthetics devices
AH	abbreviation for anaesthetist helper
a_i	parameter according to the Denavit-Hartenberg notation
α_{i-1}	parameter according to the Denavit-Hartenberg notation
α_{elec}	electronic motor angle
α_{mec}	mechanical motor angle
AlZnMgCu1.5	a standard aluminium alloy for mechanical parts
AN	abbreviation for anaesthetist
aRD	abbreviation for agile robot development
AS	abbreviation for assistant surgeon
A	cross-section area
BA	abbreviation for textile barrier
β_{max}	maximum torsion of a beam
bg	abbreviation for bevel gear
b_i	digit i of a standard binary code
g_i	digit i of a graycode binary code
BLDC	abbreviation for brushless digital current
br	abbreviation for brake
b_{tooth}	tooth face width
b	number of rigid bodies in a kinematic chain
CABG	abbreviation for coronary artery bypass grafting
CA	abbreviation for C-arm (X-ray)
CA	abbreviation for cardiac technician
CAD	abbreviation for computer-aided design

CI	abbreviation for circulating nurse
CM	abbreviation for C-arm monitor
COTS	abbreviation for commercial off-the-shelf
CS	abbreviation for cell saver
CT	abbreviation for computer tomography
CU	abbreviation for ceiling supply units
C	eccentricity in cycloidal drives
DC	abbreviation for direct current
DFG	German abbreviation for *German Science Foundation*
DI	abbreviation for displays
DIN	German abbreviation for *German Institute for Standardization*
D_i	diameter of object/ component/ portion i
d_i	parameter according to the Denavit-Hartenberg notation
DLR	German abbreviation for *German Aerospace Center*
d_{cs}	number of degrees of freedom in the kinematic chain of a robot
DoF	abbreviation for degrees of freedom
DVD	abbreviation for digital versatile disc
EC	abbreviation for endoscopy cart
EEPROM	abbreviation for electrically erasable programmable read-only memory
elec	abbreviation for electronics
EMC	abbreviation for electro-magnetic compatibility
ϵ_i	strain of state i
Er:YAG	abbreviation for erbium-doped yttrium aluminium garnet
ESWL	abbreviation for extracorporeal shock-wave lithotripsy
E	Young's modulus
$\boldsymbol{f}_{contact}$	vector comprising all forces and torques caused by the contact of the instrument with its environment
FEM	abbreviation for finite elements method
$\boldsymbol{f}_{i,external}$	vector comprising all forces and torques applied to link i of the robot
$F_{friction}$	friction force
$\boldsymbol{f}_{i,gravity}$	vector comprising the gravitational forces of link i of a robot
Φ_i	magnetic flow of portion i
F_{mot_i}	force on a tendon evoked by motor i
F_m	tangential force generated by a winding of a motor

F_O ..... orthogonal force on a tooth face

$\boldsymbol{f}_{payload}$ ..... vector comprising the forces and torques caused by the payload

fps ..... abbreviation for frames per second

F_{spring} ..... spring force

F_{tan} ..... tangential force on a tooth face

F_x, F_y, F_z ..... force in direction x, y, or z

GmbH & Co. KG ..... German abbreviation for limited partnership with a limited liability company as general partner

GmbH ..... German abbreviation for limited liability company law

G_s ..... grid spacing of a Bragg grating

G ..... modulus of rigidity

HLM ..... abbreviation for heart-lung machine

i-DoF constraint ..... a constraint which blocks i DoF

ILM ..... German abbreviation for inrunner motor

ISO ..... abbreviation for *International Organization for Standardization*

i_{st} ..... number of constrained DoF during a surgical task

I_{Tc} ..... torsion constant of a closed cross-section

IT ..... abbreviation for instrument table

I_{Ts} ..... torsion constant of a slit cross-section

I_T ..... torsion constant of a cross-section

$I_{x,y}$ ..... geometrical moments of inertia

i ..... general index

φ_d ..... nonius signal

φ_i ..... position angle of the MR-sensor in relation to a magnetic pole pair of track i of the pole ring

j_i ..... joint i, counted from the base to the tip, starting with i=1

jps ..... abbreviation for joint-sided position sensor

j_{stat} ..... not-actuated, lockable joint

jts ..... abbreviation for joint-sided torque sensor

K_M ..... motor constant

K_T ..... motor torque constant

λ_i ..... wavelength of state i

LED ..... abbreviation for light-emitting diode

LGA ..... abbreviation for land grid array

$link_i$ ..... link connecting joint j_i with joint j_{i+1}

LITA ..... abbreviation for left internal thoracic artery

$loops_i$	number of possible revolutions (turns) of a component
LWR	abbreviation for *DLR*'s lightweight robots
l	length
MIMO	abbreviation for multiple input multiple output
$miro_i$	joint module integrating joint(s) j_i
μ	friction coefficient
M	maximum moment of a bearing
mot	abbreviation for the motor module, consisting of motor, motor position sensor and brake
m_p	DoF motion of a robot during the positioning of an instrument
MRI	abbreviation for magnetic resonance imaging
m_{st}	DoF motion of a robot during the surgical task
m	number of DoF the robot end effector can be controlled independently known as the mobility
n_{active}	number of actuated DoF in a kinematic chain
n/a	abbreviation for not available
n_c	number of friction pairs in a brake
$n_{passive}$	number of passive DoF in a kinematic chain
$n_{pole\,pairs,mot}$	number of pole pairs of a motor
$n_{redundancy}$	number of redundant joints in a kinematic chain
n_{trocar}	number of DoF of a trocar joint (=4)
n_{wind}	number of windings of a motor
n	number of joints in a kinematic chain
OL	abbreviation for operating light
OR	abbreviation for operating room
OT	abbreviation for operating table
PCB	abbreviation for printed circuit board
PC	abbreviation for personal computer
pin	abbreviation for pinion
PKM	abbreviation for parallel-kinematics machine
P	abbreviation for patient
PWM	abbreviation for pulse-width modulation
$\boldsymbol{q}$	vector comprising all joint positions
$\dot{q}_{mot_i}$	velocity of motor i
$\dot{q}_i$	velocity of joint i
$\boldsymbol{q}_d$	vector comprising the desired joint positions of a robot
q_i	rotary position of joint i

$ratio_{rg_i}$	ratio of a reduction gear i (joint revolutions per motor revolutions)
RCM	abbreviation for remote center of motion
rev_{elec}	one electrical revolution of a motor
rev_{mec}	one mechanical revolution of a motor
rg	abbreviation for reduction gear
ρ_{rad}	combined radii of a gearing
ρ	electrical resistivity
ri_{av}	average refraction index
ri_i	refraction index of portion i
R_m	middle line radius of the wall of a tubular cross-section
R	electrical resistance
R_{TT}	motor terminal resistance
σ_b	tooth root stress
$\sigma_{h,max}$	maximum Hertzian stress
SPA	abbreviation for single port access
S	abbreviation for surgeon
sg	abbreviation for strain gauge
ST	abbreviation for scrub technician
T_{AT}	average torque of a reduction gear
$\boldsymbol{\tau}_d$	a vector comprising the desired joint torques of a robot
τ_i	torque of joint i
τ_{mot_i}	torque of motor i
τ_{rg_i}	(high) torque of reduction gear i
T_{brake}	holding torque of a brake
TB	abbreviation for trash bin
TCP/IP	abbreviation for transmission control protocol/internet protocol
TCP	abbreviation for tool center point
T_{CT}	collision torque of a reduction gear
tg	abbreviation for transmission gear
Θ_i	coordinate system of joint j_i
t_i	thickness of portion / object i
T_{RPT}	repeated peak torque of a reduction gear
T	torque
ujs	abbreviation for universal joint shaft
U	electrical voltage
VDI	German abbreviation for *Association of German Engineers*

vf	abbreviation for virtual fixtures
V	spatial volume
w	weight
$\boldsymbol{x}$	pose vector of the end effector
$\boldsymbol{x}_{desired}$	the desired position and orientation of the end effector notated as a vector
$\Delta\boldsymbol{x}_{elasticity,joints}$	attributable pose error of the TCP due to the elasticity of joints
$\Delta\boldsymbol{x}_{elasticity,links}$	attributable pose error of the TCP due to the elasticity of the links
$\Delta\boldsymbol{x}_{elasticity,TCP}$	pose error of the TCP, due to elasticity and loads
$\boldsymbol{x}_{trocar}$	the position of the trocar in endoscopic surgery written as a vector
Y_{Fa}	shape correction factor
Δy_{max}	maximum deflection of a beam in y-direction
z_i	number of teeth of a gear i

"Today is the good old time of tomorrow." - Karl Valentin (1882-1948)

Chapter 1

Introduction

The application of robotic systems in surgery is one of the most sensitive areas of robotics research. There are many challenges faced by the technology when the health of a patient depends on a machine that is at least somewhat intimidating. The essential question regarding the application of a robot in the operating room relates to the benefit for the patient and the surgeon. Robots can be designed to manipulate objects with high pose accuracy, to handle high payloads, to reach hard-to-access areas, or to operate in non-human-friendly environments. In surgery these conditions can be optimised to benefit both the patient and the surgeon. Most of the surgical robotic systems are thereby based on the approach of guiding an instrument with a robot. Only a few systems choose another approach, where the robot moves the patient in relation to a more or less stationary instrument like a radiation device.

The precision of robots is mainly utilised when preplanned data have to be physically transferred into the operating room, by closing the "digital gap" between planning and therapy. These systems are built, for example, to cut bone tissue precisely or to perform biopsies according to preoperative planning.

In telerobotic approaches the dexterity of the surgeon is enhanced with the precision of the robotic system by means of motion scaling and filtering. Furthermore, the capability of reaching hard-to-access areas is utilised in these applications. With robotic systems, the location of the surgeon in relation to the robot is more or less arbitrary. This can be used in teleconsultation to bridge distances, enabling an expert to interact during an operation without being physically present. In minimally invasive surgery the surgical treatment is performed inside the patient's body. The barrier being crossed is therefore the body wall of the patient, and not distance. Here, robotic approaches can enable design possibilities for complex miniaturised instruments, which e.g. enhance the dexterity inside the patient's body, but can no longer be hand-

Humans	*Robots*
Strengths	*Strengths*
Strong hand-eye coordination	Good geometric accuracy
Dexterous (at human scale)	Stable and untiring
Flexible and adaptable	Can be designed for a wide range of scales
Can integrate extensive and diverse information	May be sterilized
Able to use qualitative information	Resistant to radiation and infection
Good judgement	Can use diverse sensors (chemical, force, acoustic, etc.) in control
Easy to instruct and debrief	
Limitations	*Limitations*
Limited dexterity outside natural scale	Poor judgement
Prone to tremor and fatigue	Limited dexterity and hand-eye coordination
Limited geometric accuracy	Limited to relatively simple procedures
Limited ability to use quantitative information	Expensive
Large operating room space requirement	Technology in flux
Limited sterility	Difficult to construct and debug
Susceptible to radiation and infection	

Table 1.1: Strengths and limitations of a surgical robotic system in relation to the human surgeon [Howe and Matsuoka, 1999]

led manually. Closely related to these approaches the robot can be used to protect the surgeon from non-human-friendly environments for example in MRI[1]- or X-Ray guided surgery.

In other applications the ability to handle higher loads are applied to relieve the surgeon. This approach unlocks potentials in the design of more complex and thus heavier instruments, including radiation devices.

Howe and Matsuoka summarise strengths and limitations of a robotic system related to the surgeon as shown in table 1.1 [Howe and Matsuoka, 1999]. Therefore, the advantages of a robotic system for the patient and the surgeon can be manifold. Thus, a central question in the design of a surgical robotic system is whether to focus on one of the shown benefits in order to build a dedicated system or to aim for a versatile system covering multiple benefits.

Looking at the original meaning and definitions of the term *robot*, the title of this thesis seems to be a pleonasm, because a robot should be versatile *per se*. The author Karel Čapek brought up the term robot for factory-produced "artificial people"

[1]Magnetic Resonance Imaging

which serve humans [Čapek, 1920]. The *International Organization for Standardization* defines a robot as follows:

> *"... an automatically controlled, reprogrammable, multipurpose, manipulator programmable in three or more axes, which may be either fixed in place or mobile for use in industrial automation applications." [ISO 8373, 1996]*

Both references comprehend the aspect of versatility, but do not consider its extent. Based on these definitions, a versatile robot ranges from a system that can perform only two different tasks, to an "all-in-one device suitable for every purpose". Neither extent is satisfying or feasible. Therefore, in the author's opinion, the extent of versatility remains unclear in the definition of a robot.

Research initiatives approaching the development of robotic systems for surgery are often triggered by clinicians and, thereby, focus on a specific surgical task or the treatment of a single disease. These developments tend to neglect the versatile aspect of the system in return for performance in a single application. Furthermore, with ongoing research in medical treatment, specialised robotic systems could lose their niche. A descriptive example regarding the impact of new methods is the development of the Extracorporeal Shock-Wave Lithotripsy (ESWL) of kidney and ureteric stones by *Dornier Medizintechnik GmbH* in the 1980s. This non-invasive method for the destruction of stones replaced the surgical dissection of stones as gold standard [Segura et al., 1997]. Therefore, it is essential to reduce the development time and redesign of a medical device system in order to react rapidly to new emerging medical treatments and techniques.

In contrast, a versatile robotic system is targeted towards different applications in sub-domains of surgery. The aspect of versatility can be a key to enable rapid prototyping of new surgical techniques, to cover more than one step during an operation by the system, and to broaden the basis for the use of new emerging technologies in different surgical applications. With surgical robotics being an interdisciplinary research field involving technicians and surgeons, the rapid prototyping idea can enhance the collaboration between the two groups, by providing prototypical systems for evaluation with feasible effort. In the current state-of-the-art product development, products with a high amount of hardware have longer iteration cycles in design and manufacturing than systems with a smaller amount of hardware, despite the achieved possibilities through rapid prototyping processes. One possibility when considering this fact is the strategy of building a versatile system, which is basically applicable within a wide range of applications and to establish its configuration for a dedicated application through software.

1.1 Motivation and Goal of this Work

The term *versatile* is commonly interpreted as a desirable attribute for a device. However, the intention of designing a versatile system often faces connotations like "all-in-one device suitable for every purpose", causing doubts in the feasibility or its performance in a specific application. One reason for this rating is the infinite range of requirements for the design of an *ideally* versatile system and the assumed inevitable trade-offs. In this regard, a specialised system is assumed to be based on solid requirements from the start, enabling a straightforward design. However, versatile, not *ideally* versatile, systems exist, like the personal computer or the Swiss army knife. The goal of this thesis is therefore to prove the feasibility of designing a robot with extended versatility, optimised for use in operating rooms, and applicable in a comprehensive, but not infinite, range of surgical applications: *MIRO*.

1.2 Organisation of this Thesis

The following sections of chapter 1 clarify terms used for the description of robotic systems and applications in this thesis.

In chapter 2 the aspect of versatility is analysed on the basis of industrial products. Hereby, different approaches of system design are considered, which are targeted at providing a versatile product.

Chapter 3 reviews the current state of surgical robotics. Various taxonomies of surgical robotic systems in the literature are analysed. Taxonomies outline systems regarding their application, technical approach, or performance. As an ideally versatile system would elude any kind of limitations, the applied taxonomies show aspects for the robot design which can enhance its versatility. Finally, the current state of surgical robotic systems is analysed.

Chapter 4 comprehensively describes the development of the robot's design concept. First design parameters are identified, which the author assumes will enhance the versatility of a robotic system for the surgical domain. After the selection and adaptation of a design strategy and methodology, a set of design rules is formulated to enable the development of a generic design concept of the robot arm. Then, the development of the kinematic concept is described, followed by a comprehensive description of the mechatronic concept of the robot. Relevant performance parameters are defined for the design of a prototypical robot arm based on the developed design concept. This chapter is concluded by a detailed description of the resulting *MIRO* robot.

In chapter 5, preliminary test results with the *MIRO* in prototypical applications are shown in order to validate the design approach.

Chapter 6 summarises the findings of the thesis at hand and points out possible future research topics, as well as the proposed further development of the *MIRO* robot.

1.3 Surgical and Robotic Terminology

In contrast to the use of robots in industrial applications, surgical robotics is an interdisciplinary field, using diverging technical and medical terminologies for procedures and components. It is essential as a first step to select a basic terminology for this thesis both for the components and the use of a surgical robotic system.

1.3.1 Terminology in Surgery

This thesis focuses on surgery as the field of application for the robotic system. Surgery can be defined as a "*... medical treatment to remove or repair body tissue during an operation*" [Cancer Research UK, 2002]. The main purpose of surgical robotic systems is therefore physical intervention on the tissue of a patient.

For this thesis, a *surgical task* (e.g. cutting tissue, feeding a needle, etc.) is defined as the smallest incremental step in surgery, which corresponds with the definition in robotics. The way *surgical tasks* are performed and which technologies are applied is defined as the *surgical method* or *technique*. For example, in orthopaedic surgery an osteotomy (cutting bone tissue) is a task, which can be pursued with different instruments (saws, drills, laser, ultrasound, etc.). Additionally, this task can be performed in open or minimally invasive surgery. The technique can vary from patient to patient for the same task. Laser osteotomy in maxillofacial surgery is therefore a *surgical technique*, with cutting bone tissue as the *task*. The terminology in this thesis is therefore defined in the following way:

- *surgical task*: the smallest step in physical intervention on tissue
- *surgical technique*: the technologies and methods applied to perform a surgical task
- *surgical procedure*: a sequence of single surgical tasks
- *surgical application*: the sum of techniques and procedures

As an example for the use of these definitions a hip arthroplasty (hip replacement) is a *surgical application*, with a surgical procedure being the removal of the proximal end of the *femur*. This *procedure* comprises various *tasks*, with cutting the femur tissue being one of them. A *surgical technique* for this *task* is, for example, the placing of

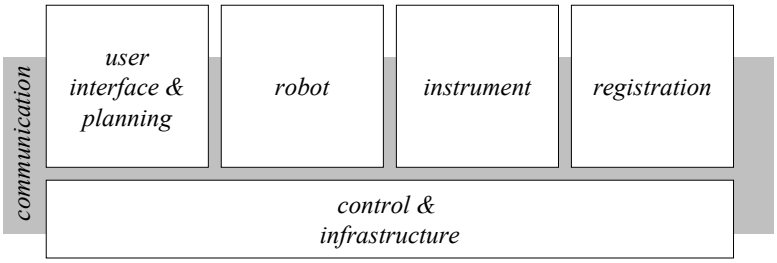

Figure 1.1: Abstract system architecture of a surgical robotic system

intersecting planar cuts by utilising an oscillating bone saw [Moctezuma and Schuster, 1995].

1.3.2 Functional Architecture of a Surgical Robotic System

For the scope of this thesis the functionality of a surgical robotic system can be abstracted by five different blocks as shown in figure 1.1, whereby a block can be integrated in one or multiple instances. In contrast, communication can be present within every single block or between blocks. It must be noted here that these definitions are imprecise regarding robotic systems, which do not integrate an extracorporeal portion of the robot. Therefore, capsule-like robots and implantable robots are left unconsidered in this thesis.

1.3.2.1 User Interface and Planning

This block serves as the front-end for the user. The functionality of the two constituent parts is tightly interwoven, with the planning part focusing on the offline and the user interface on the online interaction with the system. The balance between these two areas depends mainly on the level of autonomy of the robotic application. In telerobotic setups for example, the user interacts mainly online with a control interface comprising haptic interfaces, triggers for switching to different modes as well as vision or haptic feedback components. In autonomous robot applications, e.g. osteotomy with the *CASPAR* robotic system, the user defines most of the system's actions offline by means of pre- or intra-operative planning, the control interface during the surgical task is reduced to supervisory control by the user [Cenk Cavusoglu, 2006].

1.3.2.2 Control and Infrastructure

The control of the system comprises all software processes that calculate desired values for the robotic system based on predefined or actual values. In contrast to the

widespread understanding of a robot control being a separate boxed hardware unit, the definition of the term *control* in this thesis is independent from the place it is implemented. In this sense this part interconnects all other components and can be distributed among more or less all units of the system.

1.3.2.3 Robot

The central component for this thesis is the robot consisting of the actuated kinematics, which is commonly named the robot arm, and optional remote units comprising components for operating the robot arm. For the scope of this thesis, the function of the robot arm is the extracorporeal manipulation of instruments. According to the definition of control in section 1.3.2.2 it is possible that the control is partly implemented in the robot arms hardware, the remote units, or the instruments.

1.3.2.4 Instrument

The instrument is a detachable tool with a clear focus on a *surgical task* in a specific *surgical technique*. The instrument adapts the abstract action of the robot arm to a dedicated surgical treatment. It may comprise robotic functionality such as additional degrees of freedom (DoF) or implement control processes. In this sense and in analogy to the control interface/ planning, the instrument bears the interdisciplinary transition between robotics and surgery.

1.3.2.5 Registration

In general, a robotic system is capable of manipulating the position and orientation of a tool in robot-centred coordinate systems. All processes and methods used to find a transformation between the robot coordinate systems and the actual environment are named registration. The effort for the registration depends mainly on the nature of the environment and the desired precision and dynamics. In static, predictable environments a singular registration of the system before the operation can be sufficient. In contrast, dynamic scenes with changing conditions and limited predictability require an incremental or perpetual registration process.

1.3.3 Workflow in Surgical Robotics

This section describes briefly the workflow of surgical robotic applications. It is important at this point to define clearly the terms used to describe the number of degrees of freedom (DoF) of robots in the following section:

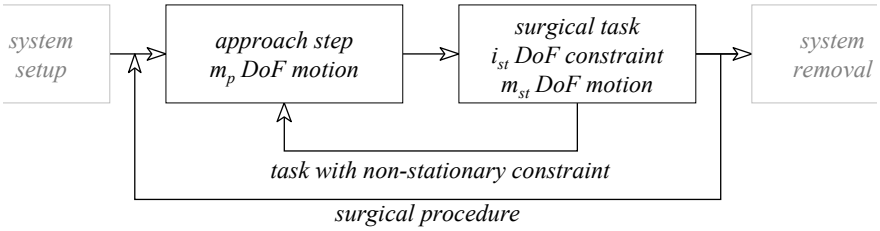

Figure 1.2: Basic workflow for the application of a surgical robotic system

- DoF in configuration space (d_{cs}): The number of DoF in the kinematic chain of the robot.
- DoF in task or Cartesian space (m): The number of DoF in which the robot end effector can be controlled independently, known as its mobility with $d_{cs} \geq m$ and $m \leq 6$.

In general the workflow during a surgical robotic application can be abstracted into the steps shown in figure 1.2. After the initial setup of the robotic system in the operating room, all surgical robotic systems comprise an approach step in which the pose of the robot is configured according to the intended surgical task. Basically this step aims to reach the correct pose of the robot to comply with the kinematic constraint of the surgical task. This step can be implemented in a passive sensor-applied way or by actuated joints. A purely passive positioning without sensory feedback indicating proper positioning is regarded as part of the setup phase. After the desired posture of the robot is reached, the surgical task is conducted with the limitations of an i_{st}-DoF additional constraint[2] (e.g. aligning a needle on a planed path) and a desired motion m_{st} of the instrument. Iterations of this last step or both of these steps compose a surgical procedure, whereby i_{st} and m_{st} are determined by the surgical technique. At this point the following assumptions can be formulated. The approach step involves a certain kinematic motion capability m_p to reach a pose, which is required by the constraint of the surgical task, with:

$$m_p \geq i_{st} \, . \tag{1.1}$$

The minimum DoF of a robot in configuration space $d_{cs,min}$ can be derived by:

$$d_{cs,min} \geq m_{st} + i_{st} \, . \tag{1.2}$$

[2] An i DoF constraint limits the motion in i DoF, whereas an i DoF joint offers i DoF motion.

Chapter 2

Versatility

The focus of this thesis is on the design of a versatile robot for surgical applications. This chapter analyses the term *versatility* regarding methodologies, benefits, and feasibility. In the first sections different technical products are analysed regarding the methodology of how versatility is provided by these products and who is addressed by it. The findings are summarised and transferred to robotic systems in section 2.2.

2.1 Versatility in Commercial Products

Versatility is a commonly used term (e.g. *DVD*, the digital versatile disc) for multipurpose systems or products ranging from a positive interpretation like "Swiss army knife" to a meaning like "all-in-one device suitable for every purpose", calling its feasibility into doubt. Although versatility is a goal to aspire to, a crucial parameter for versatility is therefore the likeliness of achieving the desired versatility and the usability/ performance of the resulting device. In the following sections, products regarded as versatile are considered in order to identify how versatility is achieved and to whom it is addressed.

2.1.1 The Swiss Army Knife

This product is literally used as a synonym for multipurpose products. The handheld device contains fold-out tools like knifes, scissors, rasps, etc., mostly for outdoor use. The advantage of the Swiss army knife lies in the fact that a complementary and compact set of tools is at hand. Regarding the definitions in section 1.3.1 this device can be used in various applications and procedures (crafting, repair, assembling, etc.), but the proposed techniques and tasks are limited according to the design of the

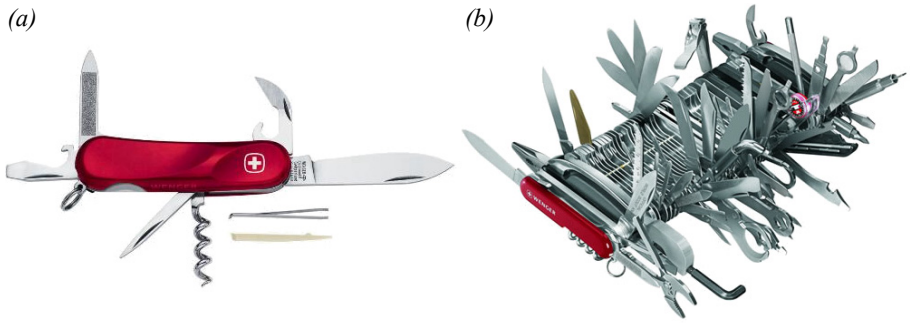

Figure 2.1: Swiss army knives (pictures copyright *Wenger SA* - Manufacturer of the Genuine Swiss army knife): *Wenger Evolution 10 (a)*, *Wenger Giant 2007 (b)*

single tools. The extent of versatility is therefore defined by the amount and shape of tools integrated into the device. The two Swiss army knife configurations depicted in figure 2.1 show very well the impact of feasibility on the aspect of versatility. The *Evolution 10* appears to be a sensible device, whereas the ergonomics and usability of the *Giant 2007* with its 87 tools, targeted at collectors, are at the very least questionable.

The versatility of a Swiss army knife is achieved by the amount of tools integrated by the manufacturer. The user is not able to reconfigure this device according to his needs. Additionally, a specific task-technique combination can be performed better with a specialised tool compared to the corresponding tool of a Swiss army knife. All tools integrated in a Swiss army knife are hardware and must be physically present in the device at all times, which reduces usability with every additional tool. Therefore, the question is: What is the limit for the integration of functions in a versatile device with still feasible effort, adequate quality (performance) of the tools, and usability? The two aspects quality and usability must be balanced carefully according to the requirements of the selected application.

2.1.2 Automotive Design

The aspect of versatility has always been a strong design issue for cars, because of the relatively high purchase cost of a car in comparison to other end-user products. Versatility can be seen on the industry side (platform concepts) and on the user side (versatile cars). A simple example to distinguish these two different approaches is the seat configuration of a passenger car. In order to adapt the seat configuration to the needs of the customer according to the ratio between space for passengers and for loads, three different approaches are currently in use:

(1) Configuration during production: Based on a modular concept the customer is able to define a specific, static seat configuration by order.

(2) Configuration by the user before travel: The customer can rearrange the modular seat components. Components which are not needed cannot be stored in the car.

(3) Configuration by the user while travelling: The customer can reconfigure the seat arrangement, whereby all components can remain in the car.

These approaches differ on the point in time when the need for a certain configuration can be defined. It is obvious that the amount of conceivable configurations decreases from (1) to (3), due to boundary conditions and the fact that components must be integrated (reduction of weight, space saving design, etc.). Approach (3) is therefore the equivalent to the Swiss army knife. In contrast, concept (1) can be seen as a versatility aspect for the manufacturer, which enables selling different products based on the same platform. This strategy has been utilised in the automotive industry in many areas. The most important are group platforms, the strategy of building different cars on the basis of the same components [Balu, 2004]. As an example, the *Volkswagen* PQ35 platform has been applied to produce a range of seven models[1] in various body styles. Besides savings during design and production, the platform concept also makes new technologies accessible to a broader range of products. A common disadvantage of this strategy is the risk of look-alike models and common errors in all models.

2.1.3 The Personal Computer

Beginning with systems like the *Apple II* by *Apple Computer Inc.* in 1977 and the *IBM PC* (*IBM – International Business Machines*) in 1981, computers have been targeted at a broad range of end-users. The targeted range of users demanded a variety of applications, in contrast to the specialised (expert) computer systems that came before. Therefore, the computers integrated functionality, which had been performed manually or with specialised devices such as calculators or type writers. Additionally, the personal computers had to be operable and adaptable by a user without extensive experience in computer technology. As already described in section 2.1.1, the crucial question is the balance between the extent of versatility and the feasibility of configuring the device for a certain application. In contrast to the preceding examples that imply only hardware components, the personal computer integrates hardware

[1] *VW Golf*, *VW Jetta*, *Audi A3*, *Skoda Octavia*, *Seat Leon*, *Seat Toledo*, and *Seat Altea*. [Roventa and Weber, 2006]

and software components, like a robotic system. The *IBM PC* compatible personal computers are a good example for the context of this thesis and are analysed regarding versatility aspects.

From the beginning the *PC* comprised an extendable hardware platform based on a modular design with different operating systems and expansion slots to integrate additional hardware. By this, the system could be adapted to a certain task by adding or exchanging hardware and software components, which was feasible for the end user. The user therefore configures the platform according to his application. Over the years new functionalities have first been introduced in the form of software (synthesisers, 3D graphics, video players), then integrated into hardware expansions (sound cards, graphic cards, video decoder) and finally integrated into the platform (on-board sound, graphics, video decoding). This is due to the faster iteration cycles in software design and the advantages of modular design. Regarding the different approaches in section 2.1.2, the configuration of a personal computer shows three analogous possibilities:

(1) Configuration during production: based on a modular concept the customer is able to define a specific hardware and software configuration.

(2) Configuration through the user by integration or exchange of hardware components before or during use.

(3) Configuration through the user during operation of the computer by installation of software components.

In comparison to the preceding examples, it should be pointed out that with increasing amount of software; the configurability of a system is shifted towards the period of use (in-field configurability).

2.1.4 Industrial Standard Manipulator Design

The main applications of robots are still in manufacturing processes, such as in the automotive industry, the handling of workpieces and tools. Through the development of the last several decades, a standard design of industrial robots for medium to high payloads has evolved. This standard design comprises a vertically mounted, serial kinematics with six joints (roll, pitch, pitch, roll, pitch, roll). As an example, figure 2.2 shows three robots of different manufacturers (*ABB*, *KUKA*, *REIS*) with a maximum payload of 16-20 kg and a maximum reach of 1500-1610 mm. The robots show almost identical kinematic designs (compare figure 2.2 *(d)*) and dimensioning. In order to adapt this standard design to specific applications, manufacturers offer a whole class of robots based on this standard design varying mainly by maximum payload and

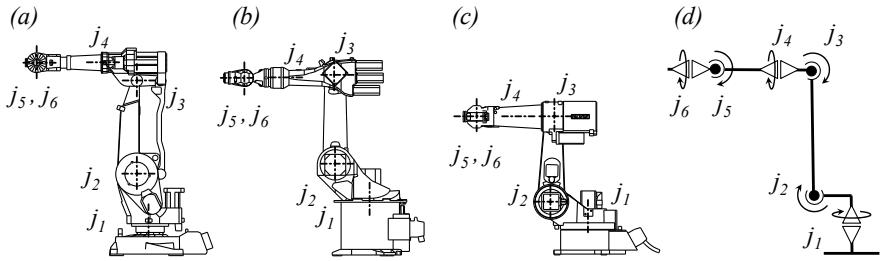

Figure 2.2: Industrial robots: *ABB IRB 2400/16 (a)*, *KUKA KR 16 (b)*, *REIS RV20-16 (c)*, standard kinematic chain of industrial robots *(d)*

maximum reach. Robots with higher payloads usually offer a larger maximum reach than robots with smaller payloads. This is due to the fact that heavier workpieces usually have larger dimensions than lighter workpieces.

Thus the aspect of versatility in industrial robots is achieved by two main design processes. The first process comprises the design of a generic robot, which is basically capable of solving many tasks due to its kinematic design, programming capabilities, and additional features (e.g. multi-turn joints). In the second process, domain specific (e.g. automotive manufacturing) scaling parameters are identified in order to build a class of robots based on the generic design. It has to be pointed out that this process does not automatically result in a standard manipulator design. It is probable that more than one design solution exists for the generic robot. A standard design is a result of the performance and success of the design. This fact is apparent in pick-and-place applications of small objects where serial scara-like robots (e.g. *KUKA KR 5 scara R350*) compete with robots based on parallel kinematics (e.g. *ABB IRB 360 FlexPicker™*).

2.1.5 Modular Robotics

One way to shift the hardware configurability of robots towards the phase of usage is the approach of modular robotics. Unlike the industrial standard manipulator which is based on a more or less fixed generic design, modular robotics aims at providing an array of components with compatible interfaces that can be configured after production to form systems for dedicated applications.

An example for commercial modular robotics is the automation components of *Schunk GmbH & Co. KG*, Germany. The range of available components include rotary joints, linear joints, grippers, sensors, etc. [Schunk, 2007b]. The components apply different physical principles (e.g. pneumatics, electro-magnetic drives) and are available in a significant range of performance parameters (e.g. torque range).

Regarding state-of-the-art robotic arms (compare chapter 3), it can be seen that almost all kinematic chains are composed only of rotary joints (pitch, yaw), linear joints, and structural parts. In fact, the light weight robot *LWA 3* [Schunk, 2007a] is composed almost completely of these *Schunk* automation components. However, regarding non-technical fields of application (e.g. surgery) this configurability is not aimed at the end user (e.g. clinician) during in-field use, but at a customisation step before, conducted by specialists.

In this sense, for the non-technical user, the modular robotics approach is an equivalent to the Swiss army knife (see section 2.1.1), the seat configuration methods (1) and (2) in cars (see section 2.1.2), and the PC configuration methods (1) and (2) (see section 2.1.3). However, the introduction of the *LWA 3* by *Schunk GmbH & Co. KG* indicates that there is a significant range of applications which can be covered by a single configuration. Additionally, industrial robots and other technical systems (e.g. automotive platform concept) are also designed and manufactured in a modular way. Thus, the modular robotics approach aims at making the configurability accessible to specialists.

2.2 Conclusions on the Aspect of Versatility

The examples of products which have been presented introduce different ways of providing versatility for a field of applications. It has been shown so far that the solutions differ mainly in the person or the institution which is required to configure the system. Figure 2.3 displays an abstract comparison of three methodologies to provide solutions for different applications. Exemplarily, a number of three different applications (*I-III*) is chosen. Although the different steps in development (hardware design, software design, and evaluation) are in reality conducted more or less in parallel, the sequential depiction was chosen to simplify the figure.

Ideally dedicated systems This approach comprises systems that are built from the scratch for a single application, without synergistic effects between different systems. To provide solutions for three different applications, the development cycle including hardware design, software design, and evaluation has to be conducted for each system (depicted by the loops in figure 2.3).
The complexity and therefore the effort of solutions for three different applications (indicated by the vertical dimension of the loops in figure 2.3) is made up of three complete iteration cycles.

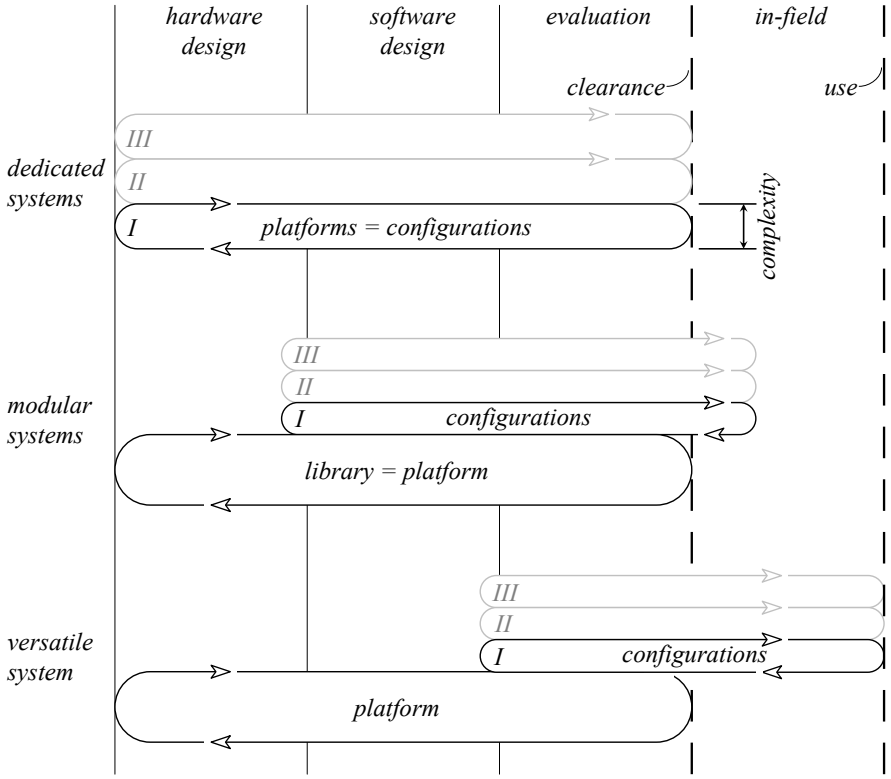

Figure 2.3: Abstract iteration cycles for the design/configuration of systems for three different applications (*I-III*)

Modular systems In the sense of modular robotics, these systems are based on a library of hardware and software components, which is composed to be configured for a certain application. An ideal modular system provides different functions through the composition of components, not by their parametrisation. The library of components can be named the platform of the system. In this sense, for an ideally dedicated system, platform and configuration are equivalent. With the modular approach, the development cycles of the platform (library) must be conducted only once, including testing and clearance of the components. However, the complexity of the platform is higher than the analogous step in the design of a single dedicated system. This is due to the number of necessary components (e.g. set of joints with a scale of torques) and additional design criteria, like the compatibility of components (e.g. interface design). The configuration cycles are conducted three times starting with a small amount of hardware design (e.g. adapters), whereby the complexity of the configuration cycles is smaller, because of synergistic effects between different configurations. Additionally,

the configurability of a modular approach reaches into the in-field phase. In analogy to the preceding description of the *PC* (see section 2.1.3), this in-field configurability focuses on exchanging hardware components (e.g. expansion cards). Regarding the seat arrangement in a passenger car (section 2.1.2), the modular approach comprises a set of different components (e.g. single seats, back seat), which can be mounted in the car by the customer. However, this version of configurability in the context of modular robotics is not feasible during use of the system.

Ideally versatile systems These systems are based on an already integrated platform, which comprehends all features and performance magnitudes of the component library in the modular approach. As with the modular system, the development cycle of the versatile platform must be conducted only once. In contrast though, the configuration of a versatile system is performed by selection and parametrisation of integrated features of the platform, instead of exchanging components. This approach shifts the configurability towards the use of the system and avoids the steps of hardware design. In analogy to the *PC* (see section 2.1.3), this approach relates to the option of saving data on the integrated hard disk or to a *DVD*. In the context of seat arrangement in passenger cars (section 2.1.2) the versatile approach would relate to seats, which can be configured into different setups, without exchanging them. Therefore, the concept of an ideally versatile system also targets non-technical users or customers to configure the system.

It has been shown that versatility is a goal to aspire to in the design of a system, provided that the configurability is accessible and does not interfere with the performance and the usability. Versatility can enhance the implementation of new applications, enable faster adaptation to specific needs, and reduce costs. On the other hand and in contrast to a dedicated system, this approach bears risks including reduced performance and applicability, as well as exaggerated complexity. In the opinion of the author, the quality *versatile* comprises not only the capability of performing different tasks, but also a certain convenience in usage and configuration. The following conclusions can therefore be made:

- The versatility of a system must be balanced with its usability and performance.
- A versatile platform integrates different functions, features, and performance magnitudes, which are selected and configured for an application.
- The possibility of configuring the system in-field can help the user to adapt the system to changing conditions and needs.

- Versatility can help to reduce the time period necessary for the design of new applications once the platform is established.
- Versatility can be accessible by the manufacturer and the user.
- An ideally versatile system with an open range of applications is not feasible.

Regarding the last statement, it is essential to analyse the range of applications and to define a broad, but not infinite, subset of applications which can be covered by a single versatile robot design.

Chapter 3

The Current State of Surgical Robotics

This survey on the current state of surgical robotics pursues two main goals. The first goal is to obtain a comprehensive overview of current applications, solutions, and technologies. The second is to clarify the meaning of the term *versatility* by identifying the limitations of the presented systems.

In section 3.1 taxonomies in literature are summarised and analysed with a focus on the demarcation between the categories, as an ideally versatile system would defy these limitations. In the second step selected surgical robotic systems in research and industry are analysed in section 3.2. This chapter is concluded by a summary on the current state of surgical robotics in section 3.3.

3.1 Taxonomy of Surgical Robotic Systems

To simplify the comparison of systems, various categorisations of robotic systems have been proposed in literature. These taxonomies are either derived from the current state of surgical robotics, leaving possible future applications unconsidered, or arise from a more comprehensive technological view.

3.1.1 Medical Subdomain

One common method for the first approach is categorisation according to the medical subdomain of the robotic system. Smith-Guerin et al. utilise this categorisation for robotic systems [Smith-Guerin et al., 2008] by distinguishing various medical subdomains:

- neurosurgery
- orthopaedics
- echography
- minimally invasive surgery
- punctures, radiotherapy
- coloscopy
- others

The definition of clearly demarcated off subdomains is difficult. For example, minimally invasive spine surgery is a surgical application, which falls under orthopaedics, neurosurgery, and minimally invasive surgery. Additionally, this taxonomy is derived directly from a survey about the current state of medical robotics and leaves new fields of application assigned to the category "others". This categorisation is not appropriate for this thesis, which focuses on versatile aspects and the possibility of new applications.

Other categorisations offer a more robotic view, as opposed to a medical view, on the systems and attempt to group the systems according to their architecture (e.g. type of interaction in section 3.1.2) or capabilities (e.g. level of autonomy in section 3.1.3). In reverse, the criteria applied for these approaches bear the limitations of the systems. An ideally versatile system would defy these kinds of categorisations. Therefore, it is important at this point to analyse these taxonomies, with a focus on the applied demarcations for the different groups.

3.1.2 The Type of Interaction

The type of interaction with a robotic system was introduced by Troccaz et al. [Troccaz et al., 2002], distinguishing systems according to their degree of passivity. This categorisation groups systems in the following way:

- passive
- active
- semi-active

Passive systems simply display information in relation to pre-planned data, and active systems perform at least parts of the procedure autonomously. Although a totally passive system may comprise a robot, it is at least questionable whether such a system

type of interaction	type of access: traditional	type of access: minimally invasive	type of access: endocavitary / endoluminal
autonomous	ROBODOC, CASPAR	Stereotaxis Inc.	MUSYC/EMIL
interactive	Eye scalpel, RinC	AESOP, MIAS	Active Catheters
teleoperated	Mammotome, PAKY	da Vinci, Zeus	MiNOSC
passive	PinPoint	HALS (not robotic)	Given Imaging (not robotic)

Figure 3.1: Classification of medical robotic systems by DARIO et al., based on type of interaction and access [Dario et al., 2004]

can be titled a robotic system as defined on page 3. Furthermore, the assignment of telerobotic systems, where the user controls the robot motions from a remote interface, remains unclear with this taxonomy.

A similar taxonomy for medical robotics is given by DARIO et al. combining the type of interaction with the type of access in a matrix style [Dario et al., 2004] (compare figure 3.1). The type of interaction forms the rows of the matrix and comprises autonomous, interactive, teleoperated, and passive systems. The columns of the matrix are formed by the type of access to the surgical site (traditional, minimally invasive, or endocavitary/endoluminal access). As an example, the *da Vinci® Surgical System* [Ballantyne and Moll, 2003] (compare section 3.2.1) is classified as a telerobotic system, utilising minimally invasive access to the surgical site.

The *Marconi PinPoint* arm is specified as a passive system. This arm comprises a passive kinematic structure with integrated brakes [Cleary et al., 2001], which therefore misses the definition of a robot [ISO 8373, 1996]. Other approaches utilise an actuated robot arm for a first positioning of instruments. During the surgical procedure the robot's pose is locked and it acts like a stand. The instrument can then be moved manually due to additional passive joints between instrument and robot

[Götte, 2002]. Therefore, these systems have passive as well as active capabilities. It can be summarised that if a system refers to the definition of a robot it cannot be a completely passive system. The quality *passive* therefore can only be assigned to a procedural step or a portion of the robot.

3.1.3 The Level of Autonomy

Cenk Cavusoglu applies a more comprehensive taxonomy utilising the autonomy of a robotic system [Cenk Cavusoglu, 2006], based on the level of autonomy of the system which comprise the levels *autonomous*, *shared-control* and *teleoperated*.

Industrial robots are used in manufacturing processes to perform repetitive tasks without user interaction in a mostly predictable environment. With the integration of sensors capturing the environment, such systems can be programmed to perform different tasks according to changing situations. This ability to select an appropriate, preconfigured task for the actual situation is called *autonomy* in the sense defined by Hexmoor and Kortenkamp [Hexmoor and Kortenkamp, 2000]. Although a system which only performs a single automated task violates this definition, it is categorised as *autonomous* in this thesis, because the task is completed autonomously. This particular use of robots is called *automation*.

If a robot is used in a hard-to-predict environment, it may not perform its actions autonomously and user interaction must be considered. This is achieved by applying other control principles such as telerobotics and shared control, depending on the amount of user interaction.

Telerobotics is a sub-domain of telemanipulation where the remote manipulator is a robot. In contrast, other telemanipulation systems are based on purely mechanical, hydraulic, or pneumatic coupling between the operator and the remote manipulator. In the case of telerobotics, a robot is mainly controlled by the user remotely. It is imaginable that the user input is replaced by automated input (e.g. pre-planned trajectories) to implement automated tasks. However, most of the telerobotic systems are designed to close the position control loop via the surgeon and, therefore, have inferior absolute position accuracy, compared to robots designed for autonomous applications.

In the shared control approach the conduction of tasks is shared between the user and the robotic system. For example, the robot can limit motions according to pre-planned data (e.g. prohibited areas), whereas the surgeon conducts motions specific for the procedure. Thereby the control strategies vary according to the level of autonomy of the robotic system. Figure 3.2 sets the different control strategies in relation to the degree of autonomy and user interaction.

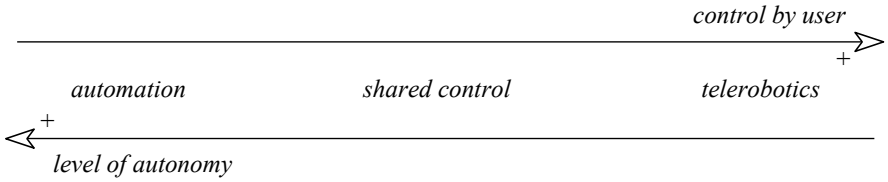

Figure 3.2: The level of autonomy in robotic system

The essential criteria for the choice of a certain control principle can therefore be summarised by two questions:

- Which tasks can be performed by the robotic system autonomously?
- How much user interaction is desired?

It is important to raise both questions with the first one directed at the designers of robotic systems and the second one directed to the user. Especially in non-technical fields of application, like surgery, the level of acceptance for new technologies is crucial for their success. Completely autonomous robotic actions are regarded sceptically. However, the answers to these questions may vary from application to application and from surgeon to surgeon. This suggests an approach to implement the level of autonomy of a new system in a configurable and, therefore, adaptable way.

The level of autonomy has been proposed for the categorisation for medical robots by various publications due to the fact that all robotic applications can be distinguished by this criterion.

3.1.4 The Level of Remoteness of the Surgeon

The necessary or possible extent of interaction between the user and the system is defined by the level of autonomy shown in section 3.1.3. These control strategies have impact on the way the surgeon interacts with the robotic system. One factor can be described by the physical remoteness of the surgeon during the surgical procedure. In classical manual surgery, the surgeon is close to the operation site and can monitor the operation with all his sensory skills. Therefore, the level of physical remoteness is very low. In a telerobotic application, the surgeon sits remotely at a user interface, which has to imitate the perception of a manual surgical procedure in order to provide the appropriate level of immersion for the surgeon. Technical functions to provide increased immersion in telerobotics are, for example, stereo vision to give the surgeon a best possible visual immersion or force feedback to display the applied forces and torques from the remote scene.

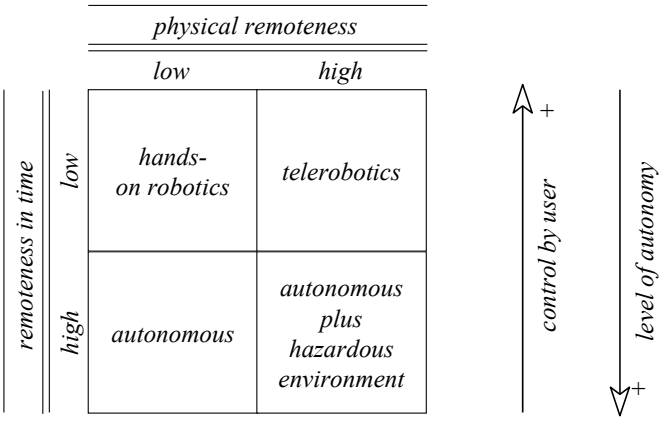

Figure 3.3: The level of remoteness of the surgeon

Autonomous systems incorporate two different factors of remoteness. The system operates autonomously on pre-planned tasks with only limited interaction during the operation. Thus, this includes a certain remoteness regarding time. Additionally autonomous systems are operated hands-off for safety reasons, keeping the surgeon away from the surgical site. The interaction is more or less limited to emergency stop commands.

In contrast, shared-control approaches can allow closer contact between the surgical site and the surgeon. One shared-control example is *hands-on* robotics [Davies, 2002], where the instrument is guided by the surgeon and the robot in conjunction. The instrument is fixed to the tip of the robot and the surgeon guides the instrument by hand. This is achieved by sensing the forces applied through the surgeon and controlling the robots motions accordingly. By programming, the free motion of the instrument can be limited in various forms, such as virtual walls, linear motions or complete blocking. This enables the haptic display of planned data, e.g. guiding the surgeon to an area of interest.

The level of remoteness is one factor describing the psycho-physical interaction of the surgeon with the robotic system. In contrast to the level of autonomy, remoteness is a judgemental parameter. A low remoteness is desirable to give the surgeon a good level of immersion. Remoteness may be necessary due to safety reasons (e.g. autonomous robot) or accessibility reasons (e.g. robot operating inside a MRI tomograph). It can be noticed that an increased level of remoteness requires additional system functions to restore the immersion of the surgeon to the site. This results in a taxonomy based on the remoteness of the surgeon as shown in figure 3.3, which characterises the relationship between the surgeon and the surgical site.

Regarding the usability of a robot covering all four approaches, its design must consider the following aspects:

- ergonomics of the robot for enabling natural interaction in hands-on applications
- multi-modal (e.g. forces, torques) feedback from the remote site in telerobotic applications
- collision avoidance and detection, as well as reduction of collision severity in autonomous applications
- sensory surveillance of the remote, autonomous operation

3.1.5 The Fulcrum Point

One of the most obvious kinematic constraints in surgery is the *fulcrum point* in minimally invasive surgery. The way the robotic system complies with this particular kinematic constraint can be used to distinguish between robotic systems [Pott et al., 2005], [Gangloff, 2004]. According to a survey on medical robotics, 30% of all medical robots are designed for minimally invasive surgery [Smith-Guerin et al., 2008]. Thus, the taxonomy of the fulcrum point is applicable to a significant range of robots. It is analysed in the next paragraphs after a short introduction to endoscopic surgery.

An endoscope is an optical device, which enables the surgeon to look inside the patient's body through a small incision or a natural orifice. In the case of incisions, mostly rigid instruments are used and the incisions are called ports or trocars[1]. The diagnostic procedure was introduced already in the beginning of the last century [Kelling, 1923]. It has been expanded to surgical procedures by introducing endoscopic instruments, which allow for tissue manipulation. Although the surgical procedure inside the patient's body is the same as in open surgery, these techniques are summarised with the term *minimally invasive surgery*, whereas *minor access surgery* would be more precise [Siewert, 1993]. As shown in figure 3.4, an endoscopic instrument comprises an extracorporeal[2] handle, an elongated shaft, and a functional tip. New instrument designs integrate multiple forceps (e.g. two forceps and an endoscope) into a single instrument [Larkin et al., 2007]. This technique is called single port access (SPA) surgery. With this approach the number of incisions into the body can be reduced whereas the size of the single incision increases. Nevertheless, the constraint introduced by the fulcrum point, as described in the following paragraph, persists.

[1] In laparoendoscopic surgery the abdomen of the patient is insuflated with gas (*aeroperitoneum*) to provide an adequate workspace for the instrument and visibility. To prevent gas leakage a trocar is inserted into the incision. A trocar is a hollow cylinder with a gas sealant, which bears the instrument.

[2] Outside the patient's body.

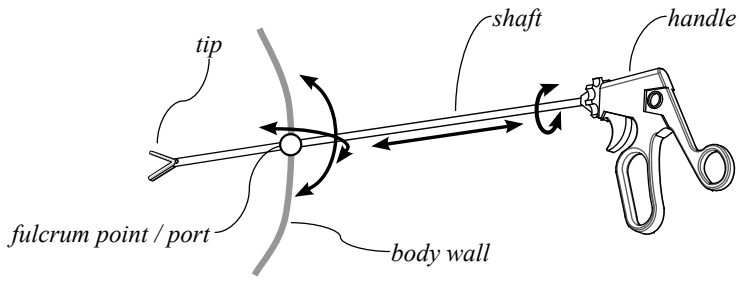

Figure 3.4: The fulcrum point in endoscopic surgery

The instrument is inserted into the patient's body through a port. Although the body wall has a certain thickness (e.g. abdominal wall) and the tissue has anisotropic elasticity properties (skin, muscle tissue, costal arch), the resulting kinematic constraint can be assumed as a combination of a prismatic and a spherical joint. Therefore, the instrument can then be moved only in four DoF anymore (three rotary DoF and one linear DoF). Both linear motions normal to the shaft axis are blocked by the fulcrum point. Exerting forces in these directions must be avoided, because they can cause harm to the tissue near the incision.

The point where the rotary and linear axes intersect is known as the *fulcrum point* in the literature [Tie et al., 2007] and the kinematic constraint is referred as *trocar kinematics* [Mayer et al., 2007]. Thus, a robotic system has to avoid exerting forces in the fulcrum point orthogonal to the shaft axis. The way a robotic system is principally capable of complying with the fulcrum point can be applied as taxonomy for surgical robotics. The following possibilities have been adapted from definitions by Dombre et al. [Dombre et al., 2004] and Gangloff [Gangloff, 2004]:

- Remote centre of motion (RCM)
- Passive joints
- Patient mounted robots
- Active control

The different approaches are shown in figure 3.5. The kinematic joints are abstracted utilising graphical symbols defined in the *VDI 2861* standard [VDI 2861, 1988].

The RCM approach integrates a mechanism, which pivots the instrument about a virtual point. This can be achieved, for example, by a parallel mechanism as shown in figure 3.5 *(a),* belt drives (as shown later in section 3.2.1) or differential gears like with the *CoBRASurge* developed at the *University of Nebraska-Lincoln* [Zhang et al., 2009]. These mechanisms are usually combined with dedicated joints (compare

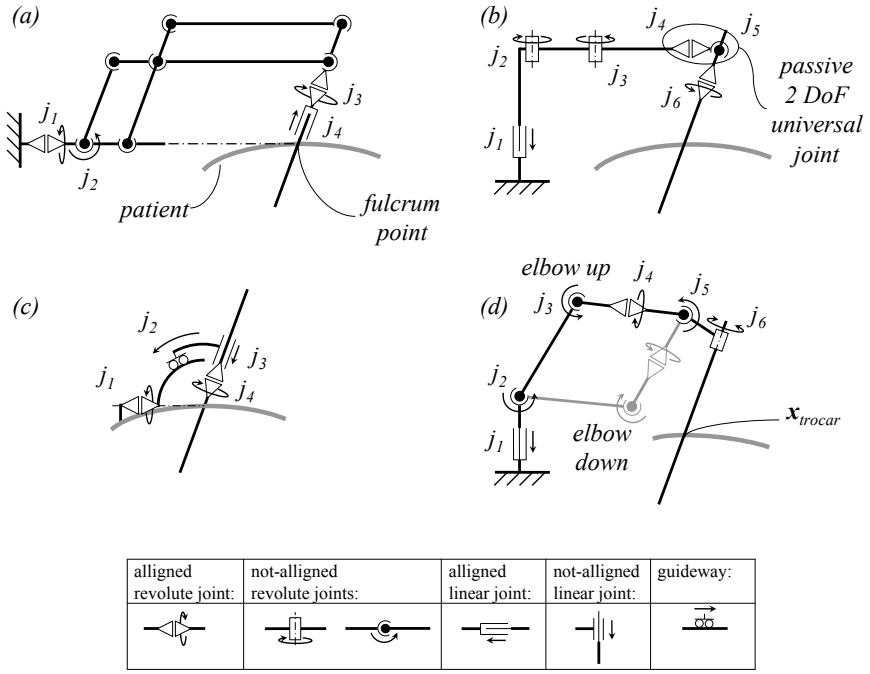

Figure 3.5: Schematic overview of the principles of remote centre of motion *(a)*, passive joints *(b)*, patient-mounted robots *(c)*, active controlled kinematics *(d)*. Graphical abstraction according to *VDI 2861* [VDI 2861, 1988].

j_1, j_3, and j_4) to form a hybrid kinematics. In figure 3.5 *(a)* the active joint j_2 drives a parallel mechanism, which pivots the end effector (e.g. instrument) about a virtual point, which has a fixed relation to the robot's base. The axis of the dedicated rotary joint j_1 intersects with this point. The rotation about the shaft axis and the linear motion along the instrument axis are supplemented by a serial kinematics (j_3, j_4). Therefore, four actuated DoF are provided by the robot. To comply with the constraint introduced by the fulcrum point, the robot must be placed in such a way that the fixed point of the parallel kinematics is congruent with the fulcrum point. The position of the fulcrum point in relation to the robot's base must be assumed as constant during an operation. Additionally, this approach limits the possible setup positions of the robot in the operating room.

A second possibility to comply with the constraint of the fulcrum point is the integration of additional passive joints (j_4, j_5) as shown in figure 3.5 *(b)*, forming a passive two DoF universal joint, supplemented by at least four active joints (j_1, j_2, j_3, and j_6). This approach has been shown by the *Zeus*® [Reichenspurner et al., 1999] telerobotic system. By this, no other torques are applicable by the robot on

the instrument except a torque about the shaft axis. As a result the robot moves the instrument in only four DoF, whereas the instrument is supported by the trocar (passive joint) itself. This approach can be shown mathematically by applying the GRUEBLER equation:

$$m = 6 \times (b - n - 1) + d_{cs} \ . \tag{3.1}$$

This equation gives the mobility m of a spatial kinematic assembly based on the number of rigid bodies b, the number of joints n, and the DoF in configuration space d_{cs} . In the case of the configuration shown in 3.5 *(b)* the number of joints is $n_{active} + n_{passive} + n_{trocar} = 7$. Assuming the patient's body as fixed, the number of rigid links is $b = 7$. All joints have one degree of freedom except the trocar joint, which has four DoF. The motion capability of the instrument tip is therefore calculated as follows:

$$m_{instrument} = 6 \times (b - n_{active} + n_{passive} + n_{trocar} - 1) + (6 + 4) = 4 \tag{3.2}$$

A major advantage of this approach is that the fulcrum point can be located more or less arbitrarily in relation to the robot, which enhances the robot setup in the operating room (OR) and takes the motions of the patient into consideration (e.g. through aspiration). On the other hand, those forces at the instrument's tip, which are orthogonal to the shaft axis are strut at the trocar. Another disadvantage of this concept is the fact that the robot cannot be operated without a trocar present. This strictly limits the usage of such robots to minimally invasive surgery.

A third approach overcomes the problem of positioning an RCM controlled robotic system in relation to the trocar by mounting the robot directly onto the patient's body. This concept has been implemented for example with the *LER* robot [Berkelman et al., 2003]. These robots integrate either an RCM approach as denoted with axis j_2 in figure 3.5 *(c)* or use the body's curvature to align a dedicated joint axis with the trocar (j_1). Such robots are directly placed on the patient as a kind of active trocar. When the position of the port is decided by the surgeon the placement of this robot is simple, with only one DoF in orientation to be decided. All forces and torques are shored by the body wall of the patient and the size of these robots is crucial, especially when multiple instances are needed.

A fourth method is shown in figure 3.5 *(d)*. In order to avoid specialised kinematics, the fulcrum point can be set by applying appropriate control strategies to a robot which has six or more actuated joints.

The calculation of the necessary joint angles $\boldsymbol{q}$ of a robot for a desired position

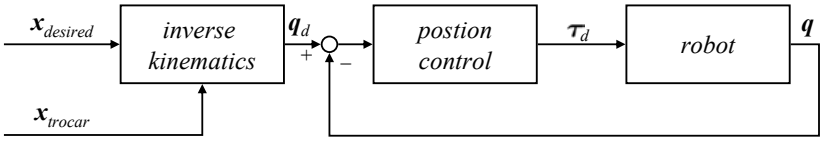

Figure 3.6: Control scheme for a six DoF robot with endoscopic constraint utilising position control

and orientation $\boldsymbol{x}$ of the end effector is known as the inverse kinematic problem:

$$\boldsymbol{q} = \boldsymbol{f}(\boldsymbol{x}) \tag{3.3}$$

For a robot with six joints, this equation gives multiple, but not an infinite number of solutions for a demanded six DoF pose of the end effector. One example is thereby that a certain pose of the end effector can be reached with "elbow up" and "elbow down" as indicated in figure 3.5 *(d)*. If the position of the trocar $\boldsymbol{x}_{trocar}$ in relation to the robot is known, it is feasible to control the active joints in a way that the instrument always intersects with the fulcrum point. As shown by Ortmaier and Hirzinger for an *AESOP* medical robot, the desired position of the instrument $\boldsymbol{x}_{desired}$ is then calculated in combination with $\boldsymbol{x}_{trocar}$ by the inverse kinematics to adequate desired joint positions $\boldsymbol{x}_d$ [Ortmaier and Hirzinger, 2000]. In a closed loop control, a position control algorithm then generates desired torques $\boldsymbol{\tau}_d$ based on the actual joint positions $\boldsymbol{q}$ as shown in figure 3.6. If the position of the trocar is only measured once during the initial step, it has to be assumed fixed during the use of the robot, which imitates the RCM approach. In contrast, a continuous measurement of the trocar position allows adjustment to the motions of the patient.

In the case of a redundant robot with seven or more joints, the dimension of the configuration space d_{cs} exceeds the dimension of the taskspace m and the equation 3.3 calculates infinite solutions. Therefore, a redundant robot can reach a desired end effector pose with an infinite range of different postures. This fact can be utilised, for example, to apply additional criteria (e.g. position of the elbow for collision avoidance), the so-called nullspace criteria, forcing a single solution of the equation. The feasibility of complying with the constraint of the fulcrum point by applying a redundant robot and appropriate control has been shown in the *MARGE* project [Dombre et al., 2004].

Apart from position control, robots can also be operated in force/ torque control modes, which requires additional force/ torque measurement. Thus, lateral forces in the fulcrum point must be avoided as this appears to be an apposite approach. One basic method is shown in [Albu-Schäffer et al., 2007b], applying a robot as depicted

in 3.5 *(b)* whereby the passive wrist joints are replaced by active torque-controllable joints. If the output torques of these two joints are set at zero ($\boldsymbol{\tau} \equiv \mathbf{0}$), this imitates the passive joints solution. This approach shows the same disadvantages of shoring the loads at the tip of the instrument in the fulcrum point.

However, the presented taxonomy of the fulcrum point limits the survey to minimally invasive robotic systems.

3.1.6 Kinematic Constraints

The taxonomy of the fulcrum point has shown that the systems can be divided according to the technological solution applied to comply with a certain kinematic constraint. However, this taxonomy is limited to minimally invasive surgery.

In contrast, the *taxonomy of the kinematic constraints* described in this section distinguishes systems according to the different kinematic constraints which are apparent during their main surgical task. Besides the demanded DoF of motion of the instrument, the kinematic constraints introduced by the surgical procedure are central design aspects, which can be utilised as taxonomy for surgical robotic systems. It is evident that a desired motion capability of a robot end effector in n independent DoF, demands at least n independently controllable DoF in the robot arm. Although robots exist with seven or more DoF [Pott et al., 2005], the maximum DoF in Cartesian space are always limited to six DoF (three linear and three rotary DoF). Additional joints in the kinematic chain of the robot are utilised to close kinematic loops within the robot arm (parallel kinematics) or to enhance the motion capability during an application by compensating for additional constraints, such as workspace limitations. It is common sense that a robot with six DoF in task space is more versatile than a robot with fewer DoF regarding its motion capabilities, because it can reach desired positions in more or less arbitrary orientations. According to the definitions in section 1.3.1, the kinematic parts of a surgical robotic system can be separated into the robot arm and the instrument. Both components can integrate motion capabilities, but according to the definition in this thesis (see section 1.3.2) the robot arm is responsible for the extracorporeal manipulation of the instrument and for the compensation of external kinematic constraints. Additional DoF of instruments can be utilised to comply with kinematic constraints which cannot be compensated by the kinematics of the robot arm alone[3]. For the reduction of moved masses, it is preferred to integrate the necessary DoF into the robot arm.

The kinematic constraint apparent during the surgical task can be utilised to categorise surgical robotic systems. The following paragraphs explain examples of surgical applications and their kinematic constraints:

[3]For example to reach full six DoF of motion capability inside the patient in endoscopic surgery.

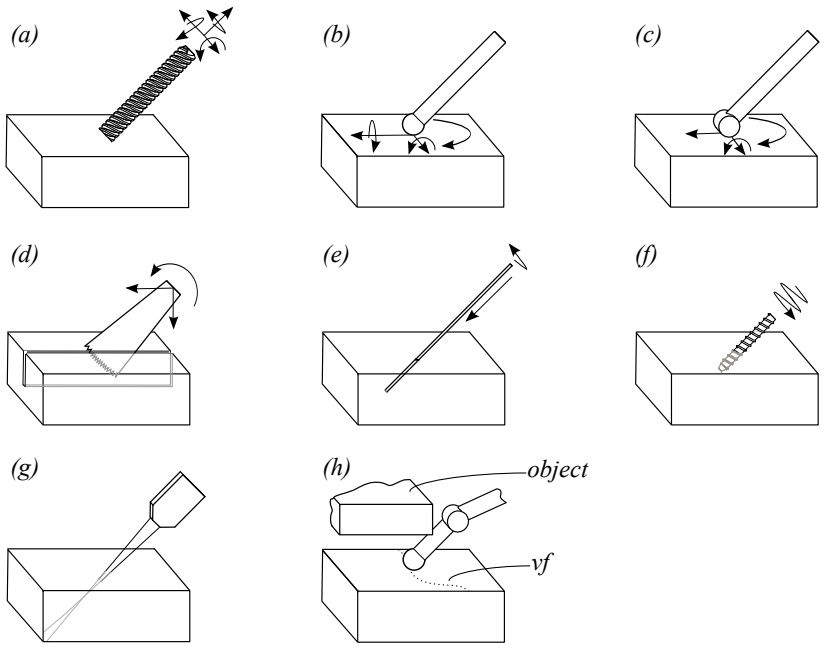

Figure 3.7: Kinematic constraints in surgical tasks: milling *(a)*, palpation *(b)*, linear ultrasound transducer *(c)*, osteotomy saw *(d)*, biopsy needle *(e)*, osteosynthesis screws *(f)*, radiation treatment *(g)*, and multiple sets of constraints *(h)*

"0-DoF" Constraints Systems assigned to this category demand a motion of the instrument in six DoF, whereby no additional constraints are present. One exemplary surgical task is the guidance of a milling machine to cut a 3D geometry into bone tissue as depicted in figure 3.7 *(a)*. A milling cutter carves in all directions and therefore the motions are not limited. Although the desired final geometry of the bone can be seen as a constraint, the trajectory for the milling process is assigned to the motion capability m_p in this taxonomy.

"1-DoF" Constraints In order to identify variations of soft tissue (e.g. skin) or to identify non-visible anatomic structures (e.g. blood vessels) surgeons palpate the tissue with their finger tips. There, the finger is pressed with a more or less constant force onto the tissue and moved around a certain area. Due to the almost spherical shape of the finger tip, the motion is only limited in the direction of the perpendicular to the contact point. If a robotic system guides a tactile sensor [Provancher, 2003] with a spherical shape, the motions are therefore constrained in one DoF and five DoF are left for manipulation, as shown in figure 3.7 *(b)*.

"2-DoF" Constraints As an example of this category the fulcrum point has already been discussed in section 3.4. Another medical task in this category is the guidance of a linear ultrasound transducer [Pierrot et al., 1999]. These medical imaging sensors have an almost cylindrical surface, which is pressed onto the tissue (e.g. skin), to obtain ultrasound images in the form of planar slices of the tissue. The motion of a cylinder contacting a plane with its cylindrical surface is limited in two DoF as depicted in figure 3.7 *(c)*.

"3-DoF" Constraints One example of a 3-DoF constraint in robotic surgery is the guidance of an oscillating saw for osteotomy. The medical indication *hip dysplasia* describes a deformity of the hip joint [Pschyrembel, 1993]. This can be corrected by cutting the proximal end of the thighbone (femur), then repositioning and fixing it in a corrected position. For the cutting of the bone (osteotomy), the use of oscillating bone saws is standard. As shown in figure 3.7 *(d)* these saws comprise blades in the shape of a segment of a circle. During cutting tissue the blade is shored in the resulting kerf of the bone tissue, which limits the motion of the saw to two linear and one rotary DoF. The robotic guidance of an oscillating osteotomy saw has been shown by GOETTE [Götte, 2002]. Based on pre-operative planning data, the robot correctly positions the oscillating saw.

"4-DoF" Constraints A biopsy is a medical procedure for the removal of body tissue samples (e.g. tumour tissue) which have to be analysed. A popular method is the needle aspiration biopsy, where an elongated needle with a cavity at the tip is used to retrieve the tissue sample. The needle is inserted into the patient's body or an organ and fed until the cavity reaches the area of interest. Some needles have a mechanism that cuts out the tissue sample and bears it in the cavity. As soon as the needle, which is assumed to be a rigid body[4], penetrates the body or organ, the direction of the biopsy towards the area of interest can no longer be changed. It is therefore essential to orient the needle precisely before penetrating the tissue. This first step depends on the kind of biopsy being performed and includes the positioning of the needle in up to five DoF (m_p), whereby the rotation of the needle about its longitudinal axis can be left unconsidered. During the next step, where the needle is inserted into the patient's body, only the linear DoF along the needle axis and the rotation about its axis are applicable, as depicted in figure 3.7 *(e)*. In general, a robotic system for biopsy must have a kinematic chain that is capable of positioning the needle and maintaining the linear motion of the needle during biopsy.

[4]If the needle is treated as a flexible body, changes in the direction after insertion are possible [Simaan et al., 1998].

"5-DoF" Constraints A possible constraint in this category would be a special case of biopsy, where the needle must not be rotated during the surgical task. Besides this variation of the biopsy constraint, more complex 5-DoF constraints can be deduced from the list of *lower pair joints*[5] [Tsai, 2000] in mechanics. Joints with only one degree of freedom comprise prismatic, revolute, and screw pairs [Volmer. et al., 1995]. Although screwing comprises two different motions (one linear and one rotary) these two motions are related by the pitch of the thread. Therefore, this constraint blocks five DoF.

Applying screws in orthopaedic surgery is a common method for connecting bone tissue (osteosynthesis). This surgical procedure comprises mainly two tasks. In the first step, a hole is drilled into the bone tissue and then, in the second step, the screw is turned in. For example, in the clinical case of osteotomy in spine surgery, the screws are implanted into the pedicle of a vertebra. The correct position and orientation of the screw is critical regarding the resulting geometry of the synthesised bone fragments and because of the danger of harming other anatomic structures nearby (e.g. the aorta and the spinal cord). The task of drilling the hole precisely was identified as a possible application for a robotic system [Döbele, 2008], [Sukovich et al., 2006]. Therefore, it is desirable that a robotic system also performs the second step of placing the screw as shown in figure 3.7 *(f)*. This screwing action, combining linear and rotary motion, can be performed by a dedicated screw joint with a fixed pitch based on the pitch of the screw. However, it cannot be assumed that all available pedicle screws have the same pitch. Three different pitches have already been mentioned in a small survey [Goel et al., 2003]. A more feasible possibility to solve this constraint is the coordinated motion of multiple joints of the robot.

"6-DoF" Constraints Some tasks in surgery demand the fixed pose of an instrument for a certain period of time. Especially with instruments that apply energy to body tissue e.g. by radiation [Shiomi et al., 2000], the instrument must be aimed at the target tissue as indicated in figure 3.7 *(g)*. A defined focal point and a non-circular shape of the radiation beam also require that the distance and orientation must be considered. Holding an instrument in a fixed position and orientation is trivial and possible with almost every kinematics, besides kinematics integrating passive joints. However, it has to be considered that reaching a desired posture in six DoF requires at least an equal number of DoF in the positioning step (see equation 1.1). Additionally, if the target area cannot be assumed stationary during the exposition time, the robot has to keep constant pose relative to a moving target (compare figure 1.2).

[5] Only six different joint types between to bodies exist based on surface contact. These joint types are known as the *lower joint pairs* in literature and comprise: revolute pairs, prismatic pairs, screw pairs, cylindrical pairs, spherical pairs, and planar pairs.

Besides capturing the pose of the target, this can only be accomplished by adequate control of multiple joints whereby the kinematics must grant the desired posture of the end effector $\boldsymbol{x}_{desired}$ derived from the target motions. In contrast to the category of unconstrained systems, the required dynamics of these systems derive from the positioning and not from the surgical task.

The categories presented focus on the constraint of the end effector of the robot or the instrument attached to it. If additional constraints are affecting other portions of the robot, the robot must integrate additional joints in order to comply with these constraints. Regarding the actual surgical task, the robot then has a redundancy of joints. It can comply with the constraint with an infinite range of different poses, which is called the nullspace [Khatib et al., 2004]. One example for a nullspace criterion is to choose a pose which avoids the collision of a robot link with other objects (compare with figure 3.7 *(h)*). Another possibility for nullspace criteria is to implement virtual constraints, for example, to demarcate forbidden areas surrounding vital anatomic structures or spatial pathways along anatomic structures. This approach, known as virtual fixtures (*vf*) [Rosenberg, 1993], overlays abstract information in the form of kinematic constraints. A robot which is capable of obtaining the desired pose of its end effector in six DoF with an infinite number of joint angles is henceforth referred to as a *redundant robot*. Then, the number of joints ($d_{cs,min}$) is calculated as follows, with m_{st} being the demand motion capability of the end effector, i_{st} the DoF of the constraint, and $n_{redundancy}$ the number of additional DoF:

$$d_{cs,min} \geq m_{st} + i_{st} + n_{redundancy} \ . \tag{3.4}$$

At this point it can be assumed that a robotic system which is capable of complying with multiple different sets of constraints is more versatile than a system which is dedicated to a single specific constraint.

3.2 Robots for Surgery in Research and Industry

In the past two decades many research and commercial systems for robotic surgery have evolved. Taylor and Stoianovici describe 36 medical robotic systems, categorised as *surgical CAD/CAM* or *surgical assistant systems* [Taylor and Stoianovici, 2003]. The *MERODA* database [Pott et al., 2005] developed by the *University Clinic Mannheim, Germany* listed 456 medical robotic projects online as of August 2010 [Pott, 2010] and Smith-Guerin et al. document in [Smith-Guerin et al., 2008] statistics on 70 robotic systems for medical applications. A condensed list of these surveys, focused on surgical robotic systems supplemented with the author's own findings is shown in appendix B, categorised according to the taxonomies identified in section 3.1. Figure 3.8 partitions the 55 systems of this list according to the taxonomy of the surgical constraint. These are considered according to their main application published in the literature. Therefore, this statistic is not precise regarding systems with various applications. However, this chart shows that a majority of the systems (≈81.5%) are designed for "0-DoF" constraints (mainly orthopaedics), "2-DoF" constraints (mainly minimally invasive surgery) and "4-DoF" constraints (mainly biopsy).

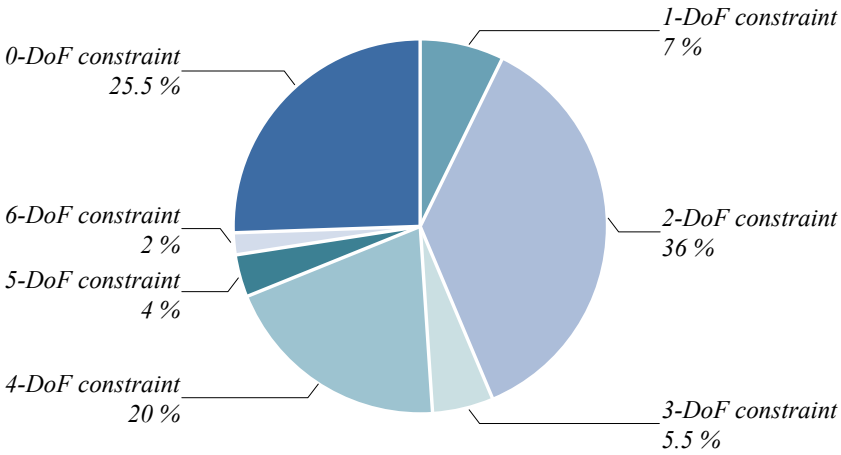

Figure 3.8: Categorisation of surveyed surgical robotic systems according to the taxonomy of the surgical constraint

A more detailed view of a selection of surgical robotic systems is given in the next sections. In accordance with the focus of this thesis, this survey focuses on extracorporeal manipulators. Therefore, capsule-like robots, active implants, and robotic patient positioners are not considered. The systems introduced here have been selected either because of their importance for the current state of surgical robotics, their representation of a group of similar systems or their peculiarity regarding versatility. Within

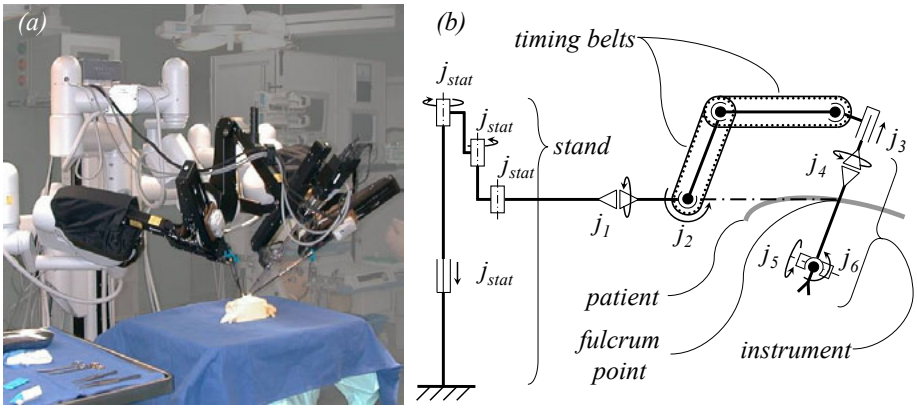

Figure 3.9: The *da Vinci® Surgical System* (*Intuitive Surgical® Inc.*): Three arm robotic setup *(a)*, kinematic chain of a single telemanipulator *(b)*

the context of this thesis, the survey focuses on the robotic components of the system and only briefly describes other system components like vision components or user interfaces.

3.2.1 da Vinci® Surgical System

Today's most successful commercial surgical robotic system is the *da Vinci® Surgical System* [Ballantyne and Moll, 2003] by *Intuitive Surgical® Inc.*, USA. The concept of this robotic system, which utilises a specialised kinematics based on the RCM approach (comparable to figure 3.5 *(a)*), applies to an entire group of cognate systems including *Artemis* [Rininsland, 1993], *Black Falcon* [Madhani et al., 1998] or *RobIn Heart* [Podsedkowski, 2005]. According to table B.3 in appendix B, the system can be classified as an active, telerobotic system for minimally invasive surgery, complying with the 2-DoF constraint of the fulcrum point by means of an RCM approach. The system is used for procedures in cardiac, general, paediatric, gynaecological, urological, and thoracic surgery. The surgeon controls the robotic system from a remote console with bimanual haptic interfaces under stereo vision. The patient-side components of the robotic system comprise three to four robotic arms guiding the left- and right-hand instruments (e.g. forceps, scissors), an endoscopic camera, and optionally supplemental instruments (e.g. for holding tasks) in position control mode. Considering only one arm, the kinematic chain is portioned into two components as depicted in figure 3.9 *(b)*:

- A remote centre of motion (RCM) manipulator with two rotary (j_1, j_2) and one linear DoF (j_3). This portion comprises the components with black housings

depicted in figure 3.9 *(a)*. In contrast to the parallel mechanism driven by joint j_2 in figure 3.5 *(a)*, the *da Vinci® Surgical System* utilises timing belts to implement this portion of the kinematics.

- An endoscopic instrument with three DoF comprising the rotation about the shaft axis (j_4) and two wrist joints (j_5, j_6) near the tip of the instrument. Additionally, the instrument integrates a functional DoF e.g. gripper. None of the actuators (motors) for the instrument joints are integrated into the instrument, but are placed in the RCM manipulator.

The four DoF outside the patient's body are supplemented beyond the fulcrum point with two additional DoF (wrist) in order to achieve motion capability in six DoF inside the body of the patient. In order to achieve a proper alignment of the RCM manipulator's fulcrum point with the actual position of the trocar, the manipulators are mounted on a massive stand integrating passive joints (see grey components in figure 3.9 *(a)* and joints j_{stat} in figure 3.9 *(b)*). In accordance with the defined workflow shown in figure 1.2, the alignment of the system with the fulcrum point belongs to the setup phase ($m_p = 0$). The close integration of the three robot arms apparent in figure 3.9 *(a)* shows the necessity of collision avoidance between the different robot arms.

3.2.2 Zeus®

The discontinued *Zeus®* [Reichenspurner et al., 1999] telerobotic system for minimally invasive surgery was developed by *Computer Motion Inc.*, now part of *Intuitive Surgical®*.

Targeted at cardiac and general surgery, the system comprises three separate robot manipulators based on the *AESOP* robot, mounted to the operation table. This mounting solution at the operating table makes an additional stand unnecessary and avoids problems which occur when an actuated operating table changes its position compared to a floor-, cart- or ceiling-mounted robotic system. Like the *da Vinci® Surgical System*, the *Zeus®* robots are controlled by the surgeon sitting at a remote control console. In contrast to the RCM approach, the *Zeus®* robots comply with the constraint of the fulcrum point by two additional passive joints j_4, j_5 (see figure 3.10 *(b)*) in analogy to figure 3.5 *(b)*.

The four active joints j_1, j_2, j_3, and j_6 of the robots form a scara-like kinematics, capable of manipulating instruments in four DoF, including the rotation of the instruments about their shaft axis. Thus, the *Zeus®* arms comply perfectly with the definition in section 1.3.2.3 of an extracorporeal robot, because it covers all the DoF that can be implemented outside the patient, including the rotation of the instrument

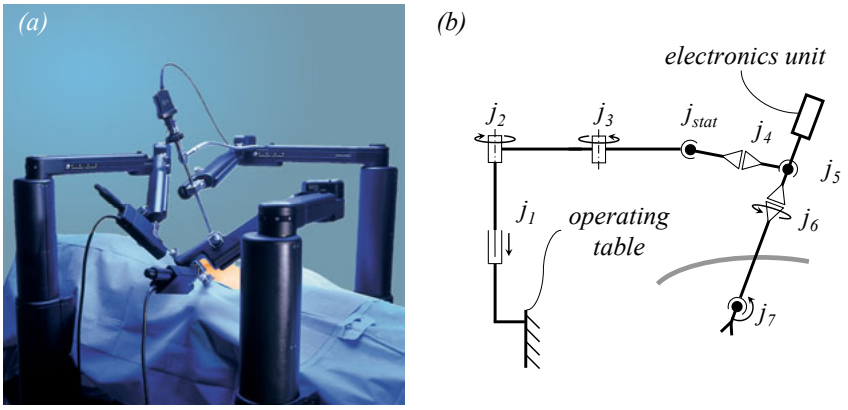

Figure 3.10: The *Zeus*® telerobotic system: Three arm configuration at the operation table, picture courtesy of *Intuitive Surgical*® *Inc. (a)*, kinematic chain of a single telemanipulator *(b)*

about its shaft axis (j_6). Instruments are mounted to the *Zeus*® arm in a way that even if the robots are blocked, the instruments can be removed from the patient linearly along their shaft axis in order to avoid injuries. This is achieved by the hollow shaft design of j_6. The instrument is mounted to the robot by feeding the instrument with its tip ahead through this hollow shaft, leaving the bigger supply unit of the instrument (motors, electronics) on the far side of the robot in relation to the patient. Additionally, this design enables the use of unmodified endoscopic instruments like standard endoscopic cameras.

Compared to the *da Vinci*® *Surgical System*, the *Zeus*® system provides instruments with only one additional wrist joint (j_7) to enhance the dexterity inside the patient's body.

A preconfigurable static joint j_{stat} is integrated in order to allow adaptation of the robot's workspace. Additionally, the robot arms can be placed at different locations along the side of the operating table. This results in two static DoF for the positioning during the setup procedure.

Due to the approach of utilising passive joints and the additional, preconfigurable static joint, the *Zeus*® robots are able to comply with fulcrum point locations within a significant portion of their workspace. A drawback to this approach is that the manipulation forces at the tip of the instruments and their gravitational forces are supported by the trocar.

Thus, the application of the *Zeus*® arms is only feasible in minimally invasive surgery. They are not operable, for example, in open surgery where no trocar is present.

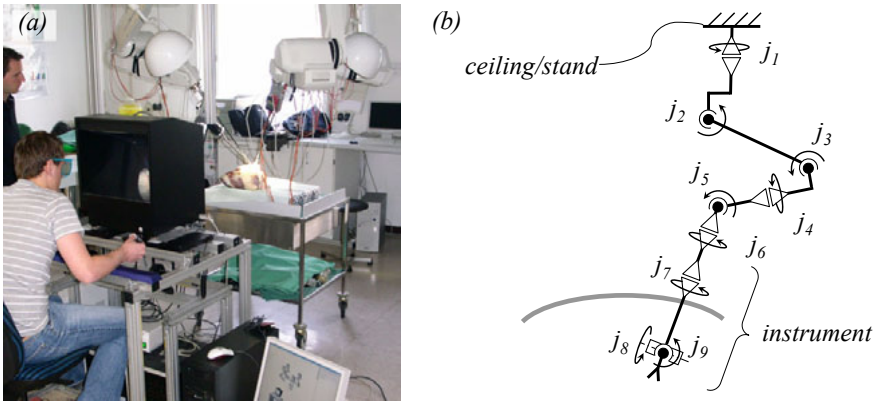

Figure 3.11: *Aramis*: Prototypical setup, picture courtesy of *TUM (a)*, kinematic chain of a single telemanipulator *(b)*

3.2.3 Aramis

The *Aramis* [Mayer, 2008] telerobotic system (depicted in figure 3.11 *(a)*) was developed by the *Technische Universität München TUM, Department of Robotics and Embedded Systems*. Like the preceding systems, *Aramis* is designed for endoscopic telerobotic surgery. It represents an entire group of robotic systems which comply with the constraint of the fulcrum point in minimally invasive surgery by active control. Another system in this group is the *ALF-X* system [Morales, 2009], developed by the *Institute for the Protection and Security of the Citizen*, Italy[6].

The surgeon controls the system from a remote master station integrating haptic interfaces and stereo vision. The *Aramis* system can therefore be classified as an active, telerobotic system for minimally invasive surgery, considering the 2-DoF constraint of the fulcrum point with active control. The system is used to perform research on semi-autonomous actions like suturing during telepresence operations. Hence, its level of autonomy can be described as medium or semi-autonomous.

Four ceiling mounted *Mitsubishi MELFA RV-6 SL* robots guide the endoscopic instruments comprising an endoscopic stereo camera and modified instruments of the *da Vinci® Surgical System*. The commercial *Mitsubishi* robots integrate six joints ($j_1 - j_6$) as depicted in figure 3.11 *(b)*, providing motion capability of the robot end effector of $m = 6$ DoF. The instrument provides three joints ($j_7 - j_9$) and an additional actuated gripper. Since the robot arms do not provide additional actuators for the instruments like the manipulators of the *da Vinci® Surgical System*, an additional unit with servo drives for the instruments has been integrated.

[6] Announced for commercialisation by *SOFAR S.P.A.*, Italy.

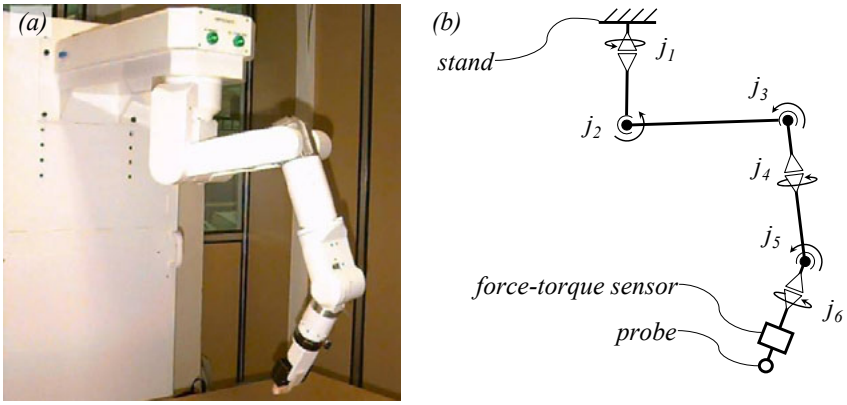

Figure 3.12: The *Hippocrate* robot: The robot arm mounted on a cantilever support, picture courtesy of *LIRMM (a)*, kinematic chain of the manipulator *(b)*

The number of redundant DoF calculates with equation 3.4 to:

$$n_{redundancy} = d_{cs} - m_{st} - i_{st} = 9 - 6 - 2 = 1 \ . \tag{3.5}$$

As described in section 3.1.6 additional DoF can be utilised to avoid collisions. Due to the coaxial alignment of joints j_6 and j_7, forming a kinematic singularity, the options for the definition of nullspace criteria are limited. To avoid collisions, only the link between j_6 and j_7 can be controlled independently. Therefore, in order to avoid collisions between the robot arms (elbows), the robots' bases have to be setup in such a way that the robots' workspaces do not overlap or the robots' workspaces must be restricted.

3.2.4 Hippocrate

The *Hippocrate* [Pierrot et al., 1999] robot was introduced in 1999 by the *Laboratoire d'Informatique, de Robotique et de Microélectronique de Montpellier* (*LIRMM*) as depicted in figure 3.12 *(a)*. In contrast to the preceding examples, the *Hippocrate* robot is targeted at single arm setups and applications where probes like ultrasound transducers or instruments like dermatomes are guided on the patients skin (in analogy to figure 3.7 *(b), (c), (h)*). The *Hippocrate* integrates six actuated joints ($j_1 - j_6$) in a kinematic configuration (compare figure 3.12 *(b)*) similar to the *Mitsubishi MELFA 6 SL* robot. The robot is mounted to a gibbet stand in order to establish a vertical configuration as depicted in 3.12 *(a)*.

The robot integrates a dedicated force-torque sensor at the flange, which serves two purposes. It can be used to guide the robot by hand through exerting forces

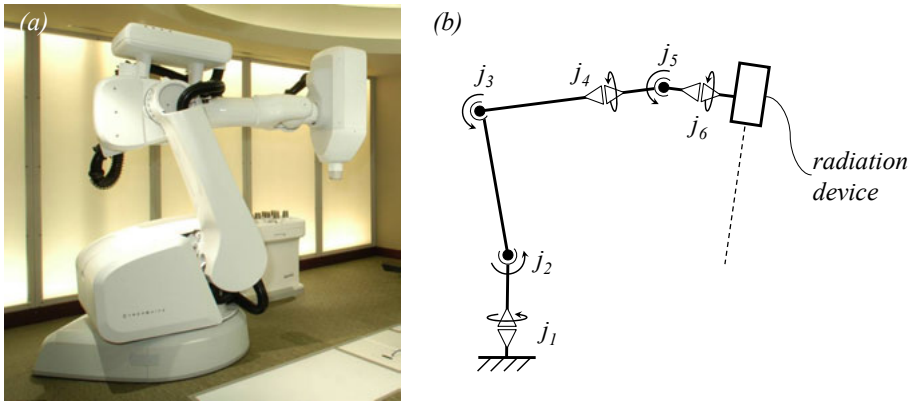

Figure 3.13: The *CyberKnife System®*: The robot with mounted linear particle accelerator, image used with permission from *Accuray® Inc. (a)*, kinematic chain of a *KUKA KR-240-2 (b)*

to the probe and to establish force sensitive contact of the probe with the skin of the patient. The robot can adhere to different kinematic constraints acting on the end effector through programming. However, the kinematic chain is not redundant regarding, for example, the 2-DoF constraint in minimally invasive surgery:

$$n_{redundancy} = d_{cs} - m_{st} - i_{st} = 6 - 4 - 2 = 0 \ . \tag{3.6}$$

Therefore, the robot can reach a certain pose of the end effector under the constraint of the fulcrum point only with a limited number of joint configurations.

3.2.5 CyberKnife System®

The *CyberKnife System®* (*Accuray® Inc.*) provides a non-invasive method for the treatment of benign and malignant lesions within the human body. By applying X-band radiation to the tumour tissue, the DNA of these cells is damaged causing them to die or to reproduce more slowly [Hoffelt, 2006]. Thus, the application of radiation has to be limited to tumour tissue in order to avoid harm to healthy tissue.

Conventional therapies apply a stationary radiation source and move the patient in order to centre the radiation beam on the identified position of the tumour. In contrast, the *CyberKnife System®* moves the X-band linear particle accelerator by means of a robot arm. With this approach it is possible to apply radiation to the tumour from various directions in order to reduce the exposure time on healthy tissue. Additionally, the robot is capable of compensating for the movements of the patient (e.g. through respiration), which helps to avoid invasive fixation like stereo-

tactic frames in cranial oncology. The *CyberKnife System®* integrates a floor mounted modified industrial robot (*KUKA KR-240*) with six joints ($j_1 - j_6$) as depicted in figure 3.13 *(a, b)*. This robotic system has a large workspace, which removes the need for an additional stand or cart for positioning during the setup steps. On the other side, the size of the robot dominates the treatment room, making multipurpose usage of the room difficult. Although this very large system certainly marks the edge of the current state of surgical robotics regarding workspace (≈ 55 m^3) and payload ($\leq$ 240 kg), it can be seen as a prime example for the group of industrial versatile robots in medical applications.

Other examples include *CASPAR* and *RobaCKa* (based on *Stäubli* robots) and *ROBODOC* [Kawalla, 2007]. The selection of an industrial robot for a medical application is mostly based on the availability of a comprehensive range of models scaled by the maximum payload and the demand for high position accuracy.

3.2.6 Evolution 1

The discontinued *Evolution 1* (compare figure 3.14 *(a)*) was introduced by *URS Universal Robot System* and is based on the *M-850* robot now distributed by *Physik Instrumente GmbH & Co. KG*. Like *CyberKnife®* or *ROBODOC* this system is mainly operated in an autonomous way and the interaction with the surgeon is reduced to simple control commands. Hence, it belongs to the systems with a relatively high level of remoteness from the surgeon. The system is targeted on precise positioning of probe-like instruments (e.g. needles) or bone cutting instruments (e.g. milling) in cranial and orthopaedic surgery.

In contrast to all preceding examples, but similar to the *OTTO 1* [Hein et al., 2001], this robot is based on a parallel kinematics. The six DoF parallel robot ($j_1 - j_6$) is combined with a supplemental linear joint (j_7) for feeding the instruments as depicted in figure 3.14 *(b)*. The *M-850* integrates a *Stewart-platform* kinematics with six actuated linear joints and displays remarkable position accuracy (repeatability better than 2 μm) and stiffness (k_x, $k_y = 3$ N/μm, $k_z = 100$ N/μm) [Physik Instrumente, 2009]. The joints are connected to the base and the moving top by 2-DoF-passive joints and are arranged in an octahedral assembly. In order to position the robot such that its workspace covers the desired workspace of the application, the robot is mounted onto an actuated, mobile C-arm, well-known from X-ray systems. By integrating seven actuated joints ($j_1 - j_7$), the tip of the parallel kinematics portion can perform a nullspace motion along the axis of the instrument. Due to the maximum travel of 0.1 m of the *M850* in this direction, the benefit for collision avoidance is limited.

Disregarding the discussion in the literature about the general comparison between serial and parallel kinematics, it must be pointed out that the *M-850* robot offers a

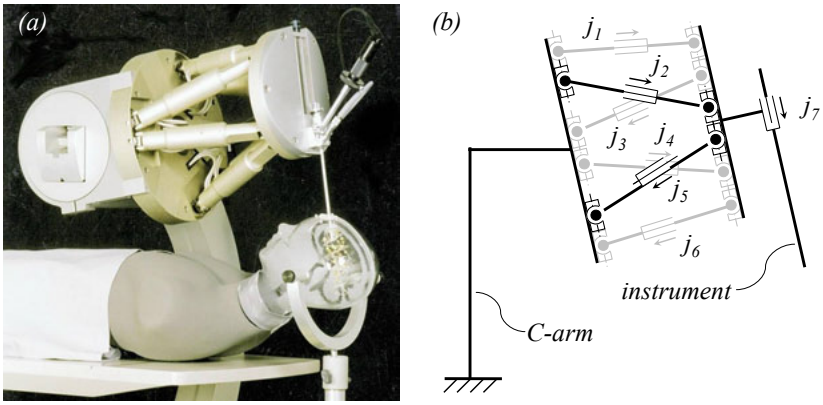

Figure 3.14: *Evolution 1*: Setup for an application in neurosurgery, picture courtesy of *Physik Instrumente GmbH & Co. KG (a)*, kinematic chain *(b)*

significantly smaller rotary travelling range of the tip ($q_z = \pm 30°$, $q_{x,y} = \pm 15°$) compared to a standard serial manipulator like the *KUKA KR 240-2* (range of joint 5 = $\pm 125°$, range of joint 6 = $\pm 350°$) [KUKA, 2002]. This issue is independent from scaling according to payload, size, and velocity, as it relates directly to the parallel kinematic design. This characteristic reduces the applicability in minimally invasive surgery, because in order to reach the entire abdomen of a patient the motion ranges are not sufficient. The desired rotary ranges for pivoting the endoscopic instrument about the fulcrum point have been identified as 60° and 90°, respectively [Lum et al., 2004], and rotations about the shaft axis up to 360° [Hayashibe et al., 2005].

3.2.7 neuroArm

The *neuroArm* was developed during a collaboration of the *University of Calgary* and *MacDonald Dettwiller Associates*, Canada [Sutherland et al., 2008a] (compare figure 3.15 *(a)*). It represents an entire group of surgical robots (e.g. *Robitom* [Fischer et al., 2004], *INNOMOTION* [Melzer et al., 2008]), which are designed to be compatible with MRI scanners[7]. These scanners introduce three main design limitations for a robotic system. First, the space inside the gantry is very limited and the robot must therefore be very compact. Second, the magnetic fields of the scanner must not be interfered by the robot, in order to guarantee high imaging quality. The third and most important issue however is that the robot hardware must be compatible with

[7] An MRI scanner is an imaging system using magnetic fields. These scanners integrate a tubular space for the patient, which is called the gantry. The scanning principle is based on the synchronous electromagnetic excitation of the protons in the body tissue and the following measurement of signals that are sent out when the protons go back to their unexcited condition.

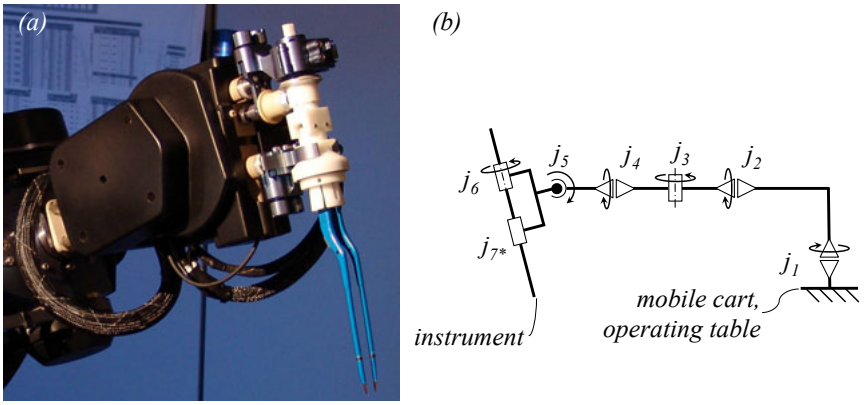

Figure 3.15: The *neuroArm:* end effector with tweezers, picture courtesy of *University of Calgary (a)*, kinematic chain *(b)*

magnetic fields of up to 3 Tesla[8]. This demands the absence of ferromagnetic material in the robot. By this, it eliminates the use of classic mechatronic technologies like electromagnetic motors and standard gears as well as many electronic components.

The *neuroArm,* shown in figure 3.15 *(a)*, is used in microsurgery and biopsy-stereotaxis applications and consists of one or two manipulators, which are either mounted on a mobile cart or to the operating table. The arms are teleoperated from a remote console and integrate force measurement at the TCP to provide force feedback. To adapt to the magnetic fields of an MRI scanner, the design of the robot arms avoids any ferromagnetic materials and, therefore, for example, uses piezo-stepper motors instead of conventional electro-magnetic motors. A single *neuroArm* manipulator, as depicted in figure 3.15 *(b)*, integrates six actuated joints ($j_1 - j_6$) for the manipulation of instruments and an additional DoF (j_{7*}) for the actuation of instruments (e.g. to open/close a gripper). In principle, this enables additional hands-on robotics approaches as described with the *Hippocrate* robot (see section 3.2.4).

Like the preceding six DoF robots, the *neuroArm* cannot reach a certain end effector pose with infinite postures in order to avoid collisions. Additionally, the payload of 750 g [Sutherland et al., 2008b] limits the range of applications beyond micro-surgery and biopsy.

[8]For example *Philips Achieva 3.0T TX MRI [Philips Electronics, 2009]*

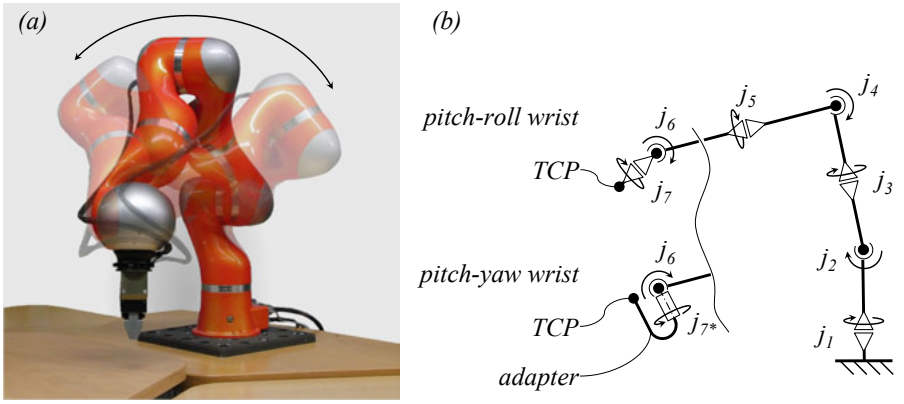

Figure 3.16: The *DLR LWR III* (preliminary *KUKA* design) with pitch-roll wrist and overlayed nullspace motion *(a)*, kinematic chain of the *LWR III (b)*

3.2.8 Redundant Lightweight Robots

In order to reach a certain pose with the robot end effector in six DoF with infinite joint configurations (compare figure 3.16 *(a)*), various robot arms with seven joints have been introduced in the last years. The range of applications for these robot arms includes assistant systems in manufacturing processes [Stemmer et al., 2007] and integrated humanoid robotic systems [Ott et al., 2006]. The aspect of lightweight addresses two topics: First, humanoid robotic systems are mobile and low weight is therefore advantageous to reduce power consumption. Second, lightweight design can reduce the reflected inertia of the moving robot, which is one way to reduce the severity of collisions with the human being [Haddadin et al., 2008].

Besides robots which are directly designed for the use in humanoid robotic systems, like the arms of *ASIMO* by *Honda* [Sugiura et al., 2006], *ARMAR* by *Forschungszentrum Karlsruhe* [Brudniok, 2007], or *ROBONAUT* by *NASA* [Diftler and Ambrose, 2001], redundant lightweight robot arms have been introduced for an extended range of applications. These robots include the *LWR III* [Hirzinger et al., 2002] developed by the *German Aerospace Center, DLR* (Fig. 3.16 *(a)* depicts a *LWR III* from a pilot series by *KUKA*), the *PA10-7C* by *Mitsubishi Heavy Industries* [Higuchi et al., 2003], the *LWA 3* by *Schunk GmbH & Co. KG [Schunk, 2007a],* and the *WAM™ Arm* by *Barret Technology® Inc [Rooks, 2006].* All four robots integrate seven active joints, forming a similar kinematic chain (roll-pitch-roll-pitch-roll-pitch-roll) as shown in figure 3.16 *(b)*. With the *LWR III*, the last joint can be converted easily to a yaw joint j_{7*} by rotating the initial position of j_6 by 90° and attaching an L-shaped adapter to joint j_7 as depicted in figure 3.16 *(b)*. However, the mounting of an endoscopic

instrument as it is shown by the *Zeus*® robot in section 3.2.2 is not feasible. The important rotary motion of the instrument about its shaft axis demands an aligned joint of the robot in order to avoid extensive motions of the arm, which eliminates the pitch-yaw configuration. On the other hand, mounting an endoscopic instrument with its supply unit to the pitch-roll configuration, like the gripper in figure 3.16 *(a)*, excludes the possibility of removing the instrument from the patient if the robot is blocked.

Though all robots can be equipped with a force-torque sensor at the TCP in order to guide them by hand or to sense interaction forces, only the *DLR LWR III* integrates dedicated joint torque sensors. Not only are the interaction forces and torques at the TCP captured in this way, but forces and torques applied to the robot links are also partly captured. This function is implemented in the *WAM*™ *Arm* by backdrivable joints and control of the motor currents. Regarding the issue of collision avoidance/ detection, this technology is interesting for the application of one or more arms in a setup with small footprint.

Although these robot arms are not designed for medical applications regarding workspace, payload, and size, the *Mitsubishi PA10* has been used in several research projects for surgical applications [Pierrot et al., 1999], [Trejos et al., 2008], [Desai et al., 2007] as well as in the *OTTO 2* system at the *Charité* in Berlin, Germany [Lueth, 2006]. The *WAM*™ *Arm* has been adopted for surgical applications by *MAKO Surgical Corporation*™ in the field of orthopaedic surgery with the *RIO*™ system (Robotic Arm Interactive Orthopaedic) [MAKO, 2009]. Both *OTTO 2* and *RIO*™ apply the hands-on robotics approach with their systems, where the surgeon and robot guide the surgical instrument in conjunction and the robot limits the free motion of the instrument according to preoperatively planned paths.

3.3 Conclusions on the Current State of Surgical Robotics

The robotic systems presented, display many diverging aspects regarding complexity, design, application, and control methods. Tables 3.1, 3.2, and 3.3 summarise the key parameters and the categorisation within the taxonomies of robotic systems described in section 3.2. The comparison can be summarised as follows:

- *da Vinci*® *Surgical System*: The mechanical RCM approach is not sensible for application in open surgery, where no fulcrum point is present. Without the instrument, the robot arms provide only three DoF motion of their end effectors, which limits possible applications. Additionally, the robots do not integrate

redundant joints. Therefore, collision avoidance can only be achieved either by configuring the setup in such a way that the workspaces of the robots do not overlap or by limiting the workspace of each robot according to the actual postures of the other arms. Collisions with other objects (e.g. ceiling supply units) or persons (e.g. nurse) are not detected, due to the absence of adequate sensors like the torque sensors in the *DLR LWR III* (compare section 3.2.8). Additionally, the robots do integrate only three active joints. Therefore, to achieve a manipulability of six DoF, the instruments must integrate at least three additional joints. Therefore, the RCM manipulators alone cannot be seen as versatile.

- *Zeus®*: The modular approach of three single arms makes configurations with a different number of arms feasible. The wrist and end effector design with its hollow shaft in joint j_6 is optimised for the use of unmodified, standard endoscopic instruments. However, the passive joints of the robots make applications where no fulcrum point is present impossible. Due to the absence of redundant joints and additional sensors, collision avoidance is limited to the methods described above for the *da Vinci® Surgical System.*

- *Aramis*: The *Mitsubishi MELFA 6 SL* robots integrate six joints. Due to the weight of the robots, an operating-table-mounted version is not feasible[9]. Although the combination of instrument and robot provides kinematic redundancy, the *Aramis* system has only limited ability to avoid collisions of the robot arms beyond the methods described above with the *da Vinci® Surgical System.*

- *Hippocrate*: This robotic arm shows a promising space-saving and low weight design. Setups integrating multiple arms mounted on an operating table appear feasible. Additionally, the robot integrates a force-torque sensor and can therefore be operated in additional control modes like hands-on approaches. However, like the examples above, the arm does not integrate joint redundancy in order to avoid collisions or adequate sensors for detecting collisions with its environment. Additionally, the wrist and end effector design is not targeted to the use of endoscopic instruments, as it is with the *Zeus®* robots.

- *CyberKnife System®:* Like the *Aramis,* the *CyberKnife System* is based on a standard industrial robot with six actuated joints. Thus, the annotations given

[9] An operating table for increased patient weight like the *ALPHAMAQUET 1150.02* [Maquet, 2009] by *MAQUET* has a maximum payload of 245 kg (arbitrary patient position). Leaving additional accessories, the payload of the robots and the weight of the patient unconsidered, the total mass of four *Mitsubishi MELFA 6 SL* already adds up to 240 kg.

above for the *Aramis* system can be applied likewise. Regarding the size of the *CyberKnife System®* or the *ALF-X*[10], it is obvious that large systems dominate the setup of the operating room more than systems with a smaller footprint.

- *Evolution 1*: The *M850* parallel robot shows exceptional performance data regarding accuracy, stiffness, and payload in relation to its low weight of 17 kg ($j_1 - j_6$). The combination of the joint j_7 and the *M850* robot provides joint redundancy. However, the benefit for collision avoidance is small, because nullspace movements are limited to motions of the M850 along the axis of j_7. Furthermore, the small rotary travelling range of the *M850*'s rules out applications involving minimally invasive surgery. Additionally, regarding figure 3.14, it is apparent that the size of the *M850* is not appropriate for telepresence setups with three or four robots like with the *da Vinci® Surgical System*.

- *neuroArm*: The *neuroArm* robots can be seen as the cutting edge in MRI compatible robots today. The robots integrate force-torque measurement at the TCP and a specialised end effector design for the convenient use of standard (manual) instruments like tweezers. The relatively low payload of 500 g [Sutherland et al., 2008a] or 750 g, respectively, [Sutherland et al., 2008b] (at a speed of 200 mm/s) limits the application of the robots beyond microsurgery and biopsy. It is unclear whether this payload was designed intentionally or derives as a trade-off from the MRI compatible technologies (e.g. piezo actuators). Integrating six joints for positioning and orienting the instruments, the annotations given for the *Aramis* regarding collision avoidance also apply.

- Redundant lightweight robots: The robots described in section 3.2.8 cover a large range of different features. They can be operated in telepresence, autonomous, and hands-on applications. They integrate seven joints, enabling enhanced collision avoidance compared to standard kinematics with six joints. Due to the application in humanoid robotics, their payload-to-weight ratio is far better than those of standard industrial robots (e.g. comparison of the *Aramis* with the *DLR LWR III* in tables 3.1 and 3.2). Furthermore, the measurement of the joint torques introduced with the *DLR LWR III* and the *WAM™ Arm* enables the detection of collisions with other objects and personnel. However, these robots do not integrate a wrist and end effector design that enables both the optimal use of conventional instruments (drills, milling machines) and endoscopic instruments like the *Zeus®* system.

[10] Both systems integrate floor-mounted robot arms, which have approximately the total height of a human.

To conclude the current state of surgical robotics, it can be summarised that the group of redundant lightweight robots shows a promising potential regarding versatility in surgical applications. However, these robots are not optimised for surgery. The workspace of these robots exceeds the necessary workspace in most surgical applications, which can be roughly equated with the size of the patient's torso. Wrist and end effector design is not optimised for the instruments in surgery, especially not for endoscopic instruments. Furthermore, these robots are designed for a preferably steady, high dexterity within their entire workspace. Again, the site of an operation is much smaller. Therefore, it can be assumed that an optimisation of kinematics, payload, and dynamics according to the field of surgical applications enables designs with further reduced size and weight for redundant robots.

Therefore, the central purpose of this dissertation is the design of a compact, lightweight robot with seven or more torque-controllable joints, wrist and end effector-design for conventional, as well as endoscopic instruments, dedicated for the surgical field.

	da Vinci®	*Zeus®*	*Aramis*	*Hippocrate*
arms per system	3 or 4	3	4	1
actuated joints per arm	3	4	6	6
actuated joints per instrument	3 +gripper	1 +gripper	3 +gripper	-
mounting	cart	table	ceiling stand	stand
static DoF (setup)	4+	1+1	n/a	n/a
kinematics (arm)	serial+RCM	serial	serial	serial
maximum reach (arm)	n/a	≈ 0.7 m	0.9 m	0.84 m
payload (arm)	n/a	2 kg	6 kg	2 kg
weight (arm)	n/a	n/a	60 kg	9 kg+base
dedicated constraint	fulcrum point	fulcrum point	fulcrum point	no
constraint solved by	RCM	passive joints	programming	programming
position control	yes	yes	yes	yes
torque control on joint level	no	no	no	no
surgical field	endoscopic surgery	endoscopic surgery	endoscopic surgery	echography
type of interaction	active, telerobotic	active, telerobotic	active, telerobotic	active
level of autonomy	low	low	medium	medium
level of remoteness	physical: high time: low	physical: high time: low	physical: high time: low	physical: low time: low

Table 3.1: Comparison of the selected robotic systems - part 1

	CyberKnife®	*Evolution 1*	*neuroArm*	*LWR III*
arms per system	1	1	1 or 2	1
actuated joints per arm	6	7	6	7
actuated joints per instrument	-	-	1	-
mounting	floor	C-arm	table / cart	n/a
static DoF (setup)	-	2+	4	-
kinematics (arm)	serial	parallel+serial	serial	serial
maximum reach (arm)	2.7 m	$\approx$ 0.1 m ($j_1 - j_6$)	n/a	0.9 m
payload (arm)	240 kg	50 kg ($j_1 - j_6$)	0.75 kg (at 200 mm/s)	14 kg
weight (arm)	1267 kg	17 kg ($j_1 - j_6$)	n/a	14 kg
dedicated constraint	no	no	no	no
constraint solved by	programming	programming	programming	programming
position control	yes	yes	yes	yes
torque control on joint level	no	no	no	yes
surgical field	radiotherapy	orthopaedic, neurosurgery	neurosurgery	n/a
type of interaction	active	active,	active, telerobotic	active, telerobotic
level of autonomy	high	high	programmable	programmable
level of remoteness	physical: high time: high	physical: high time: high	physical: high time: low	n/a

Table 3.2: Comparison of the selected robotic systems - part 2

	PA10-7C	*LWA 3*	*WAM™ Arm*
arms per system	1	1	1
actuated joints per arm	7	7	7
actuated joints per instrument	-	-	-
mounting	n/a	n/a	n/a
static DoF (setup)	-	-	-
kinematics (arm)	serial	serial	serial
maximum reach (arm)	1 m	0.78 m	1 m
payload (arm)	10 kg	5 kg	4 kg
weight (arm)	35 kg	18.7 kg	25 kg
dedicated constraint	no	no	no
constraint solved by	programming	programming	programming
position control	yes	yes	yes
torque control on joint level	no	no	yes
surgical field	various	n/a	orthopaedic surgery
type of interaction	active, telerobotic	active, telerobotic	active, telerobotic
level of autonomy	programmable	programmable	programmable
level of remoteness	n/a	n/a	n/a

Table 3.3: Comparison of the selected robotic systems - part 3

Chapter 4

Design of the DLR MIRO

The preceding chapters have analysed the aspect of versatility in technical products and presented a survey of state-of-the-art surgical robotics. Finally, the central objective of this work was formulated: The design of a compact, lightweight robot with seven or more torque-controllable joints, wrist and end effector-design for conventional, as well as endoscopic instruments, dedicated for the surgical field: *MIRO*. Among the targeted applications are telerobotic minimally invasive surgery (e.g. coronary bypass graft operation), orthopaedic surgery (e.g. laser osteotomy), and neurosurgical applications (e.g. brain biopsy).

This chapter describes the design of the *MIRO* robot, focusing on the overall concept, kinematics, and mechanical design. Although the robot was developed according to the iterative design methodology described in section 4.2, for the convenience of the reader the structure of this chapter is organised in a causal, sequential manner in order to descriptively show the path of design decisions for the *MIRO*. Electronic and control design are described briefly as they do not belong to the author's research work. In the first step, design goals for the *MIRO* robot are developed, by defining the outlines of the technical system and by identifying design aspects which benefit the versatility of the robot (see section 4.1). Then, a methodology for the design of the robot is selected and described briefly in section 4.2. After this, the central design paradigms for the robot are formulated (section 4.3), followed by the design of the kinematic chain in section 4.4. Based on these findings, a generic, mechatronic concept for the robot is developed (compare section 4.5). Section 4.6 defines the scope of applications for the *MIRO* and derives the performance parameters for the robot. This chapter is concluded by a description of the final design of the *MIRO* and overviews of electronics, communication infrastructure, and control.

4.1 Design Goals

Chapter 2 described general benefits and methodologies of the versatility aspect in technical products. In this section, these findings are transferred to the design of a versatile surgical robot and a surgical robotic system.

Though a robot is a system as well, these two terms need to be defined:

- The robot integrates the robot arm and all supplemental components which are needed to operate it.
- The surgical robotics system integrates all components which are needed to perform the operation, including user interfaces, registration components or instruments.

4.1.1 Modularisation of the Robotic System

The current state of surgical robotics as described in chapter 3 has shown that surgical robotic systems can comprise different numbers of robots and various other components, such as instruments or user interfaces. It is common sense that the large scale of different configurations and the heterogeneity of components cannot be represented by a single versatile robotic system. On the other hand, building different surgical robotic systems using a dedicated approach contradicts the main intention of this thesis and limits the adaptability of the systems to changing requirements. Thus, the design strategy for the development of the surgical robotic systems at the *DLR* is based on a modular approach. Additionally, the analysis has shown that a single ideally versatile robot covering all possible applications is not feasible. Thus, it is important to define the range of applications for the versatile robot and to identify possible ways to extend this range. The design strategy for the surgical robotic system, developed at the *DLR*, and the versatile robot (*MIRO*) are defined as follows:

- The surgical robotic system is developed according to a modular approach
- The robotic arm is one instance of the modular platform and is designed as a versatile component

The scope of this thesis is the design of the robot component. Therefore, it is important to identify the interfaces of this component within the surgical robotic system. The basic functional partitioning of a surgical robotic system was introduced in section 1.3.2. In the first step of system design, this functional partitioning must be transferred to a partitioning of building blocks or components, in order to assign system features to the components. Figure 4.1 depicts the functional partitioning

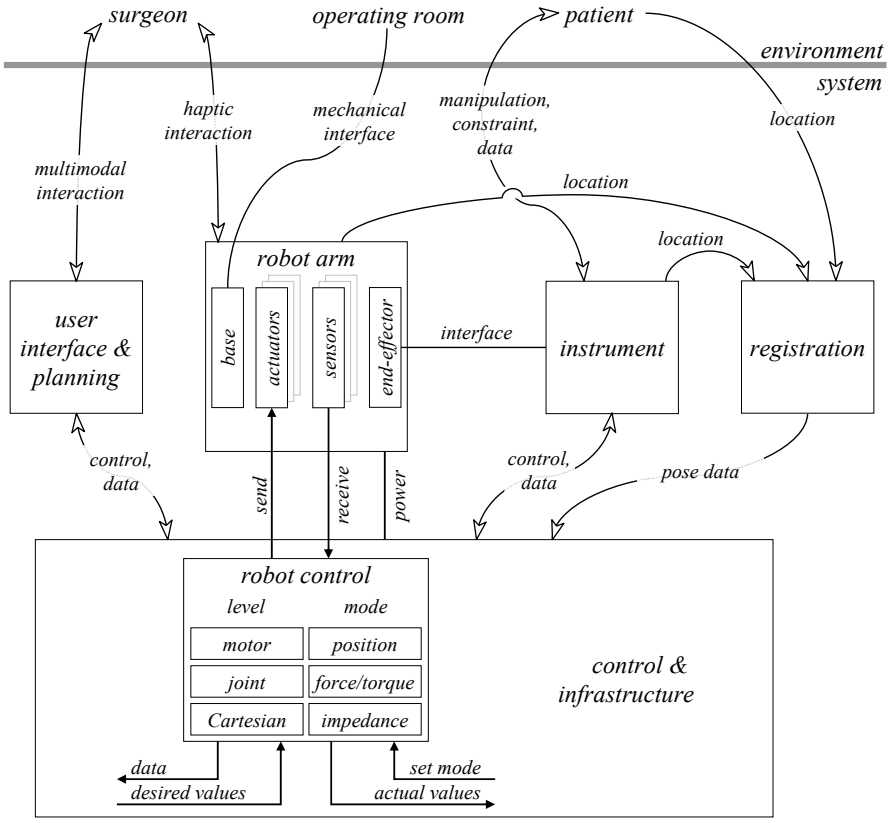

Figure 4.1: Interface abstraction for a surgical robotic system

of the robotic system supplemented with interfaces and a more detailed view on the robot.

The robot arm can be broken down into its base, a set of actuators, sensors, and the end effector. During the setup stage, the robot is connected to the environment of the operating room through its base and a mechanical interface according to the selected mounting option (e.g. cart, operating table). The registration process initially, incrementally, or perpetually references the position of the robot with respect to the patient and planning data. Besides an interface for the power supply, the robot is connected to the control and infrastructure block by a communication interface. This portion of the control and infrastructure block can be named the *robot control*. It interfaces with the other parts of the control and infrastructure with respect to the actual values of the robot's sensors and desired values for the robot's actuators, the possibility of selecting the operating modes of the robot, and an output of miscellaneous data (e.g. status). The robot control can comprise various controllers

(e.g. position control) at different levels (e.g. joint level), transformations (e.g. forward kinematics), as well as functions for initialisation or house-keeping. The robot control sets desired values for the actuators (e.g. motors, brakes) and receives actual values (e.g. positions, torques). The robot arm interfaces at its end effector with the instrument, whereby this interface can comprise power and signal supply for the instrument besides the mechanical connection. If the robot is operated in hands-on robotics mode, an additional interface between the surgeon and robot exists.

The instrument is mounted to the robot and serves as the functional front-end towards the patient. Therefore, it provides manipulation of tissue, acquires data (e.g. endoscopic camera), and is subject to the surgical constraint (e.g. fulcrum point). To enhance accuracy, it can be localised additionally by registration. Like the robot, the instrument is connected to the control and infrastructure block in order to control the instrument and to transfer additional data (e.g. video image of an endoscopic camera). The interface with the robot is mentioned above.

User interface and planning provide a multi-modal, bidirectional (e.g. haptics, visions) interface for the surgeon in order to generate desired values for the system (e.g. planned trajectories, telerobotic commands) and to display actual values (e.g. endoscopic video display).

Registration localises the necessary objects like the patient, robot, and instrument and transfers these poses to the control and infrastructure block to provide actual data. Therefore, the registration is an important component concerning the accuracy of the system. A robotic system cannot benefit from the accuracy of the robot arm without accuracy during the registration.

Control and infrastructure interface with all technical components and generate desired values based on actual values, planning, and user input. Here, component-specific building blocks (e.g. robot control) and blocks for the computation of global data (e.g. distance between two robots, state machines) can interface with each other.

The technical interfaces of the versatile robot can be summarised as follows:

- mechanical (base) interface for the setup of the robot according to different mounting strategies
- mechanical interface for connection of various instruments
- optional signal/ power interface for connection with instruments
- power interface
- control interface

The design of these interfaces should provide safe application, convenient integration, and scalability for future requirements.

4.1.2 Versatility Aspects

In section 3.3 it was shown that the robotic systems considered vary in numerous design aspects. Some of these aspects are supposed to be beneficial for every robotic system (e.g. low weight, joint redundancy); other aspects derive directly from a dedicated application (e.g. payload, accuracy). In order to decide which aspects have an impact on the system's versatility, the author proposes a partitioning of these aspects into three subsets. Subset 1 includes the aspects, which focus on the way the robotic arm is used during the surgical application. The second subset comprises classic performance specifications of robots and the third subset contains physical properties of the robot arm, which result from the applied technologies and the design. For the development of a new robotic arm, the options of subset 1 are selected first, followed by the parameters of the second subset. The third subset is then determined both by subset 1 and 2. For example, if the robotic arms are to be mounted on the operating table (subset 1), this determines the workspace of the robot (subset 2) and the maximum weight of the arm (subset 3) as the maximum payload of a standard operating table is limited:

- subset 1
  - single arm configurations and setups with up to four arms
  - floor, cart, ceiling, operating table mounting
  - dedicated or programmable constraints
  - passive, active, and semi-active operation
  - control-modes: teleoperated, autonomous, or hands-on control of the robot(s)
  - interfacing standard or endoscopic instruments
  - proposed method for collision avoidance (redundant kinematics, restricted workspace)
  - Cartesian and joint level force/ torque control
  - MRI-compatibility
- subset 2
  - workspace (maximum reach, motion capability)
  - payload
  - accuracy

- subset 3
  - kinematics (number of joints, type of joints, etc.)
  - weight
  - size
  - stiffness

For the design of an ideally dedicated system, only one option for each aspect in subset 1 is chosen. In contrast, an ideally versatile robotic arm covers all options of every single aspect in subset 1. The aspects in subset 2 can be considered as scaling factors of robotic arms, directly coupled with the resulting physical properties in subset 3. However, it is not feasible that a robotic arm can be designed covering the whole range of parameters in subset 2 and 3 at the same time. For example, a large workspace always leads to an increased size of the robot. However, a robot having a workspace comparable to the size of the torso of a human patient and a maximum payload derived from the weight of conventional instruments and manipulation forces can be assumed to cover a significant range of applications. This range can be extended by scaling the design of the robot. The main hypothesis of this thesis is therefore:

Versatility hypothesis:
A versatile robot integrates all aspects and variations of subset 1.

For the design of the versatile robot *MIRO*, it is the strategy to integrate all aspects of subset 1 (compare section 4.1.2) with only one exception: the MRI compatibility, although it is a measure for extending the range of applications and, thereby, increasing the versatility. The decision to leave this aspect unconsidered derives from the expertise of the *DLR* in electro-magnetic motors [Lemke and Hirzinger, 2004] and the resulting synergistic effects between different projects at the *DLR*.

The different features of subset 1 are targeted by a versatile approach where possible. Only features which are not feasible to be implemented by a versatile approach (e.g. different hardware interfaces) are targeted with a modular approach. The aspects of subset 2 are chosen to comply with a comprehensive but limited scope of applications. The aspects in subset 3 comprise optimisation goals (reduced size, weight, and complexity).

An important topic in robotic applications which involve close interaction with the human is safety. Regarding the structure of a robotic system, safety aspects are distributed to different levels of the system. The robot platform must integrate

aspects	*robot platform*	*configuration*	*examples*
constraints	six DoF independent motion capability	programmable, application-specific constraints	position controlled fulcrum point
number of robots	single versatile robot	one or multiple instances	four-arm telerobotic system
redundant kinematics	redundant number of joints	application specific nullspace criterion	collision avoidance, singularity avoidance, posture optimisation
control modes	multimodal sensors, high-performance control infrastructure	position, torque, force, impedance control on joint and Cartesian level	hands-on robotics, telerobotics, autonomous applications
accuracy	local (robot) accuracy	system/ application accuracy	registration, navigation
safety	local (robot) safety features	global (system) safety features	plausibility checks
mounting options	low weight, omnidirectional setup of robot's base, generic base interface	adapters for the robot's base (modular approach)	ceiling- or operating table-mounted robots
space consumption	compact and slender design, redundant kinematics	collision avoiding nullspace criterion	multi-arm system with small footprint
instrument interface	universal end effector and wrist design	simple instrument adapters (modular approach)	endoscopic and conventional instruments

Table 4.1: The versatility aspects targeted with the design of the *MIRO* robot.

safety features, which grant deterministic and safe behaviour of the hardware, like safe emergency stop, signal integrity, or surveillance of sensors. On the application level of the robot, a safe operation of the robot arm must be assured and involves for example stable control, plausibility checks (e.g. comparison of actual sensor signals with virtual robot models), or strategies when collisions occur. The last level of implementation for safety features is the configuration level of the entire robotic system. Here, safety topics must be addressed which cannot be covered on the level of a single robot arm, like collision avoidance. Hence, the identified design aspects can be addressed on the level of the robot platform or on a configuration level. Table 4.1 assigns various aspects of the design as they are approached with the *MIRO* robot and their assignment to platform or configuration of the robot.

4.1.3 Definition of Design Goals

In this section the planned system has been outlined. Central design aspects have been identified and partitioned regarding their importance for the aspect of versatility and the application. Based on these findings the design goals for the *MIRO* can be summarised as follows:

- The surgical robotic system is targeted with a modular approach due to the heterogeneity of components.
- The *MIRO* is designed as a versatile robot. Thus, different features, control modes, and kinematic constraints have to be configurable by software to shorten development cycles and to provide in-field configurability. Therefore, the necessary hardware and communication infrastructure for all configurations must be integrated into the robot.
- The generic design of the *MIRO* is targeted to fulfil all features/ aspects of subset 1, excluding MRI compatibility.
- The parameters of subset 2 are chosen for a limited, yet comprehensive range of applications as defined in the later section 4.6. However, the generic design of the *MIRO* must be scalable to extend the range of applications.
- The parameters of subset 3 define optimisation goals regarding minimum complexity (kinematics), low weight, and compact size.
- Only configurations which are not feasible to be integrated into the robot arm or reduce its performance are targeted by a modular approach. This comprises, for example, different adapters for the connection of instruments and the robot base. The adapters are aimed at low complexity and convenient usage for personnel with little or no technical background.

4.2 Design Methodology

Different design methodologies for technical systems have been introduced in the literature. Among these methodologies are the *VDI 2221* standard, defining a step-by-step procedure for the development of technical devices [VDI 2221, 1993]. Other methodologies address certain aspects which appear beneficial for this work, e.g. platform-based design, but are linked to a specific branch of engineering, like electronic design in the approach introduced by Densmore and Davare [Densmore and Davare, 2008]. An adequate methodology for the development of a mechatronic robot is the *Design Methodology for Mechatronic Systems - VDI 2206* [VDI 2206, 2004],

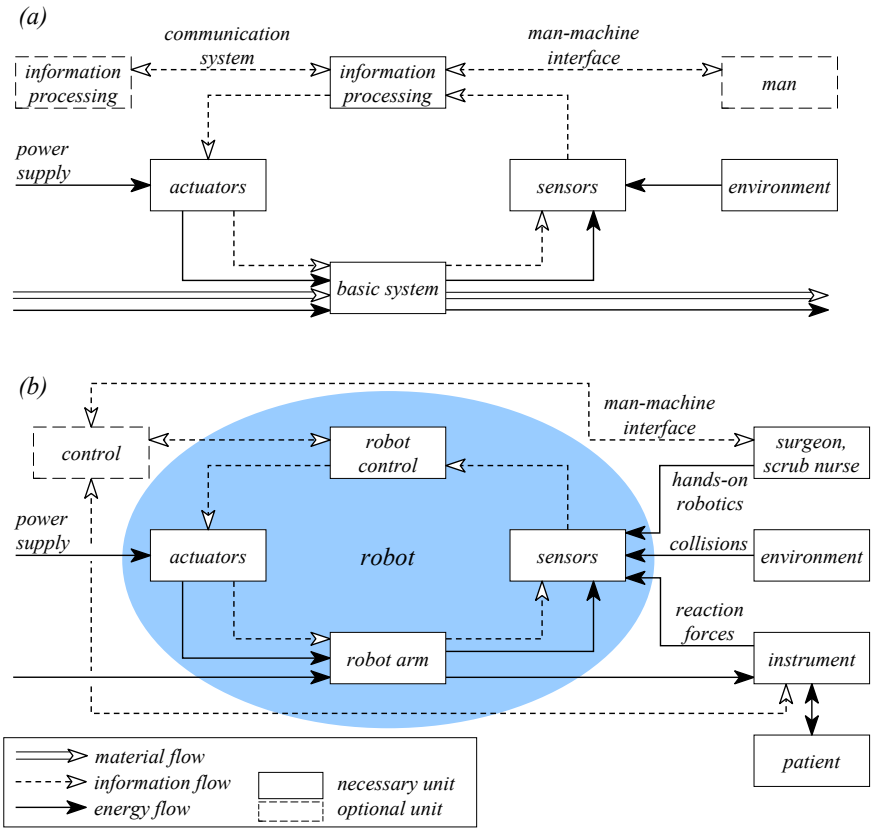

Figure 4.2: Basic structure of a mechatronic system according to *VDI 2206 (a)*, adaptation for the context of surgical robotics *(b)*

as shown with the *ARMAR* robot project [Brudniok, 2007]. The *MIRO* was developed according to the *VDI 2206* and this section describes the adaptation of this methodology.

The *MIRO* integrates at least sensors, actuators, and mechanics. Therefore, it can be characterised as a mechatronic system according to the definitions of mechatronics in the literature [Harashima et al., 1996], [Schweitzer, 1989]. The basic structure of a mechatronic system according to *VDI 2206* is depicted in figure 4.2 *(a)*. The similarity to the interface abstraction for a surgical robotic system as depicted in figure 4.1 is obvious. For the *MIRO* this structure can be interpreted as depicted in figure 4.2 *(b)* detailing the environment of the robot in the surgical domain.

According to the *VDI 2206* standard, mechatronic systems are *"... distinguished by the functional and/or spatial integration of sensors, actors (also known as actuators), information processing and a basic system"* [VDI 2206, 2004].

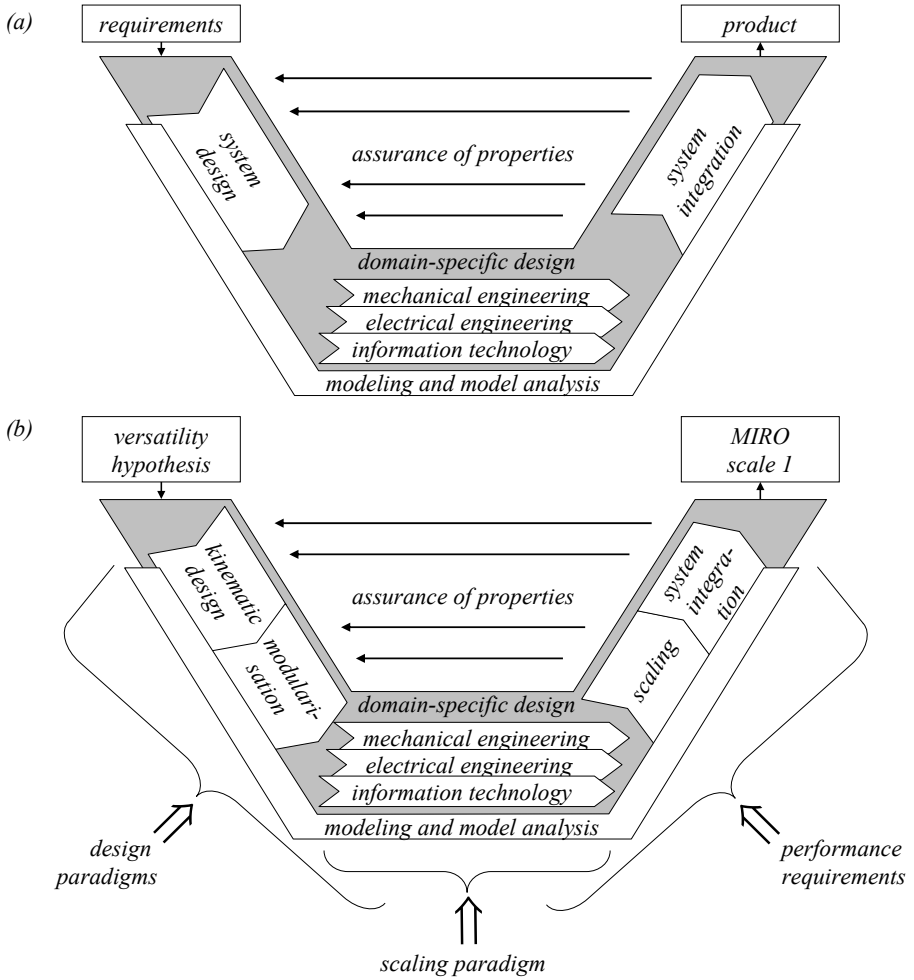

Figure 4.3: *V model* according to the *VDI 2206* standard [VDI 2206, 2004] *(a)*, *V model* interpretation for the design of the *MIRO (b)*

In this sense, mechatronics can be seen as a challenge which integrates various technologies into one system.

Furthermore, VAN BRUSSEL expands this definition to a *"... synergetic cross-fertilization between the different engineering disciplines ..."* [van Brussel, 1996]. This emphasises that solutions in one technical discipline (e.g. electronics) can enhance the design of other parts (e.g. mechanics). This impact is shown, for example, by the effect of integrated electronics on the physical size of robotic joints in the later section 4.3.5.

Another goal of mechatronic design, as formulated in *VDI 2206*, is the creation

of "intelligent" units, i.e. intelligent sensors and actuators. This implicates that integrated units are formed, which can directly connect to the information processing. Regarding the *MIRO*, this is a goal to aspire to for decoupling the development and testing of sub-components like joints, motors, and sensors and demands a modularisation of the system from the start of design.

In order to achieve these goals, *VDI 2206* provides methodologies on general problem-solving cycles (micro level), the *V model* for the overall development cycles (macro level), and process modules for recurrent working steps (e.g. model analysis). In the following, the *V model* according to *VDI 2206* is shown as an example with an interpretation for the *MIRO* development. The central goal in the design of the *MIRO* is its versatility and the possibility of enhancing the range of applications by scaling the generic design. In this sense, the generic design itself lacks the clear performance requirements of a dedicated application. Therefore, the design methodology according to *VDI 2206* has been interpreted for the *MIRO* regarding the *V model*. Figure 4.3 *(a)* depicts the classic *V model* [VDI 2206, 2004] and figure 4.3 *(b)* the interpretation for the *MIRO*.

As stated in the versatility hypothesis, the *MIRO* must be capable of covering all aspects of subset 1, leaving only MRI compatibility unconsidered. The actual scaling parameters for the aspects of subset 2 (workspace, payload, accuracy) are derived from a set of applications. The reduction of complexity (number of joints), weight, and size have been defined as the common optimisation goals for the generic design in subset 3.

In the first step, basic design paradigms for the *MIRO* are defined in section 4.3. These paradigms formulate design rules which are supposed to generally benefit the *MIRO* for application in the surgical domain. These design rules are derived from state-of-the-art manipulator design, the expertise of the research group at the *DLR*, and criteria defined by the author, which are then interpreted and transferred to the domain of surgical robotics. Based on these design paradigms and the versatility hypothesis, the basic concept of the *MIRO* is developed, which mainly comprises the kinematic concept (compare section 4.4). This concept is then modularised, introducing all components and features, which are necessary due to the defined aspects of subset 1 (compare section 4.5). As a result, the system building blocks of the generic design are identified.

At this point, no defined performance requirements for the selection of technologies or design of solutions are available. Therefore, the selection must apply other assessment criteria. As described above, the generic design must be scalable and is targeted at a very compact design. Besides general aspects, like high performance and conformity with the design paradigms, an appropriate criterion for the selection

and design of technologies is therefore the ability to be scaled or the availability of already scaled versions of a certain technology.

If this selection process identifies two different technologies which meet this requirement, the solution which enables the maximum integration is chosen. The reason for this approach is based on the assumption that increasing the size of a mechatronic device is always feasible. In contrast, decreasing the size of a mechatronic design can be limited due to technological boundaries. This can be shown, for example, by the integration of rotary encoders (position sensor) into a robot arm. Such sensors need not to be scaled with respect to the size, workspace or payload of a robot because the measured signal (rotation) does not scale with the size of the robot. The size of these sensors is determined by the applied technology. Therefore, if a sensor has been identified for a certain size of a robot, integration into a larger robot is assumed to always be feasible. This does not apply in the reverse case of downsizing a robot. Consequently, the generic design of a robot must identify technological solutions for the building blocks based on the smallest size of scaling. In other words, if the generic design of a mechatronic system is targeted at being scaled, it is necessary to develop the generic design based on the smallest version of the proposed scaling range. Besides overall performance (e.g. accuracy) and conformity with the design paradigms, the selection of technologies for the building blocks must therefore comply with the scaling paradigm:

Scaling paradigm:
The selected technological solutions for the generic design of the *MIRO* are targeted at maximum integration (size) and the ability to be scaled.

Furthermore, technologies are selected with respect to their potential future development. For example, it can be proposed in analogy to Moore's *law* [Moore, 1998] that computing power in relation to the required footprint increases in the future, but physical limitations (e.g. maximum electric current per copper diameter) persist. Therefore, the selection of technologies must also be conducted in a way which keeps these developments in mind.

After defining the scope of applications (compare section 4.6), performance requirements are derived and the building blocks are scaled and merged to form the *MIRO* prototype. Although such design processes involve iteration loops, the *V model*-based design methodology of the *MIRO* can be abstracted in a sequential way, shown in figure 4.4.

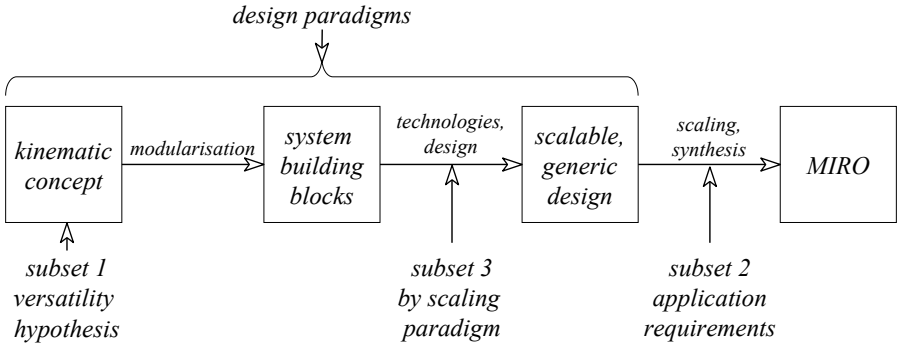

Figure 4.4: Abstracted design workflow for the *MIRO* robot

4.3 Design Paradigms

This section describes five basic design paradigms for the *MIRO*. These paradigms formulate design rules, which are supposed to generally benefit the *MIRO* for the application in the surgical domain.

These design rules are derived from state-of-the-art manipulator design, the expertise of the research group at the *DLR*, and criteria defined by the author. These paradigms describe the way the robot is built, rather than its performance, and have an impact on the robot's versatility, usability, and applicability. The findings are transferred and further developed for the domain of surgical robotics.

The *DLR* has comprehensive expertise in the design of mechatronic lightweight robots (*LWR I* [Hirzinger et al., 1993], *LWR II* [Hirzinger et al., 2000], *LWR III* [Hirzinger et al., 2002]), and robot hands (*DLR-Hand I* [Butterfass et al., 1998], *DLR-Hand II* [Butterfass et al., 2001]) as depicted in figure 4.5.

While the role of the lightweight robot *LWR* as precursor for the *MIRO* is obvious, the *DLR-Hands* have also had a great impact on the design of the *MIRO*. Robot hands can be seen as a multi-robot system integrating multiple serial manipulators (fingers) on a small footprint (palm). Regarding surgical robotic systems with multiple robots (e.g. telepresence), the achievements in the design of robot hands are of great value for the design of the *MIRO*. In this sense, the *MIRO* is in part inspired by both the *LWR* and *DLR-Hand* approaches and technologies. Therefore, these systems and their technologies form the starting point of the *MIRO*.

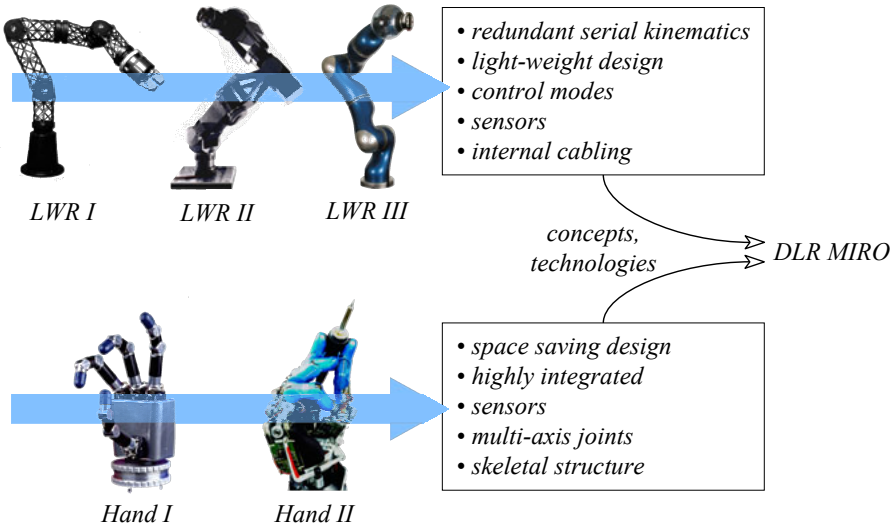

Figure 4.5: Heritage of *DLR* lightweight robots (*LWR*) and robot hands, photos copyright *DLR*

For the conceptual design of the *MIRO* robot five basic design paradigms have been formulated:

- design paradigm 1: lightweight approach
- design paradigm 2: compact and slender design
- design paradigm 3: redundant, anthropomorphic kinematics
- design paradigm 4: integration of sensors
- design paradigm 5: internal cabling and integrated electronics

In the following sections, these design paradigms are explained regarding their derivation and their impact on the system design and the versatility of the robot.

4.3.1 Lightweight vs. Stiffness

Lightweight design in robotics seems to be a tautology, as the reduction of mass and inertia of moving parts is a central design paradigm for all robots. The term *lightweight robot* (compare section 3.2.8) has a different interpretation in the robotics research community and means to go beyond the payload-to-weight ratios of industrial robots.

Robots used in industrial manufacturing processes (compare figure 2.2) are designed to reach a certain pose of the end effector by calculation of the desired joint

angles under the assumption that the links between the joints are ideally stiff. Regarding tasks in a known environment (e.g. stationary objects), this approach is suitable for generating high accuracy without the need for additional sensors. If the outside dimensions (e.g. length and diameter) and material of a robot link are assumed to be fixed, higher stiffness can only be achieved by increasing the cross sectional area and therefore the mass of the link. Today, payload-to-weight ratios of up to 1:5 are feasible, for example, for the *KUKA KR 1000 titan* (payload: 1000 kg, weight: 4690 kg [KUKA, 2010]). Although current developments are increasing the accuracy of industrial robots by modelling the elasticity of the links [Weiss, 2008], this approach is only suitable when all sets of loads applied to the robot (e.g. payload, external loads on the links) are either known or measured (e.g. by the motor currents or sensors).

In contrast, lightweight robots trade the stiffness paradigm in favour of more radical payload-to-weight ratios (e.g. 1:1 with the *LWR III*). Thus, these robots are based on more or less flexible links and joints. Therefore, the pose error of the TCP is partly an accumulation of errors caused by the elasticities of the joints and the links:

$$\Delta \boldsymbol{x}_{elasticity,TCP} = \Delta \boldsymbol{x}_{elasticity,joints} + \Delta \boldsymbol{x}_{elasticity,links} \ . \tag{4.1}$$

The total elastic deflection of the robot is a function of the forces caused by the mass of the robot links ($\boldsymbol{f}_{i,gravity}$), the payload ($\boldsymbol{f}_{payload}$), external loads applied to the links ($\boldsymbol{f}_{i,external}$), for example, in hands-on robotics, and the contact forces of the instrument with its environment ($\boldsymbol{f}_{contact}$):

$$\Delta \boldsymbol{x}_{elasticity,TCP} = \boldsymbol{f}(\Sigma \boldsymbol{f}_{i,gravity}, \boldsymbol{f}_{payload}, \Sigma \boldsymbol{f}_{i,external}, \boldsymbol{f}_{contact}) \ . \tag{4.2}$$

The position error $\Delta \boldsymbol{x}_{elasticity,TCP}$ caused by elasticity can be compensated for by three different approaches:

- Computation of the deflections in the joints and links based on the measurement of the forces and torques in equation 4.2
- Direct measurement of the deflection of the robotic components (e.g. links) with robot-integrated sensors
- Measurement of the actual position of the TCP with external sensors

The strategy for the *MIRO* is based on the first and the third approach. Integrated torque and position sensors are applied to calculate the deflection based on the known or identified elasticity of the robot's components, in order to enhance the accuracy. This approach can be solved completely within the versatile robot component, but requires extensive computation. If higher accuracy is needed in a certain application, the TCP of the robot is tracked by an external pose sensor. Although this approach

requires an additional sensor (e.g. tracking system), it solves the task with relatively low computational effort. Additionally, this approach resembles the way humans perform high precision tasks by closing the position control loop through the observation of the target and their hands. Regarding the modularisation of the surgical robotic system shown in section 4.1.1, this sensor is formed by the registration block through a continuous localisation of the robot's TCP. The gain of system accuracy is limited by the quality (e.g. refresh rate) of such sensors. Therefore, high-precision applications must be performed with lower dynamics of the TCP than applications with a moderate or low accuracy requirement. In the context of surgery, it can be seen that only a few applications in orthopaedics exist, where the target of the operation (anatomic structure) can be assumed as stationary during the operation (e.g. skull bone fixed in a stereotactic frame). In most of the applications the target has to be localised and tracked during an operation, because it cannot be assumed to be stationary (e.g. vertebrae in a spine operation). Therefore, the achievable accuracy of the system is limited by the performance of the registration anyway.

For the *MIRO*, these findings are transferred into the first design paradigm:

design paradigm 1:
The *MIRO* takes an intentionally lightweight approach in order to

- simplify integration and setup in the operating room,
- enable various mounting options, and
- reduce the reflected inertia and thereby the harm in case of collisions.

4.3.2 Slim and Compact Design

Space-saving design appears to be an undisputed design goal. However, this goal needs verification for a surgical robot regarding the trade-off of higher integration effort and thereby complexity and costs. Medical device manufacturers propose concepts and market integrated solutions for the ORs of the future (e.g. *Brainsuite*® by *BrainLAB*, *OR1*™ by *Karl Storz GmbH & Co. KG*). These integrated ORs target optimised workflows and the integration of IT-infrastructure, proposing spacious rooms and more or less equipment from the manufacturer as depicted in figure 4.6 *(a)*.

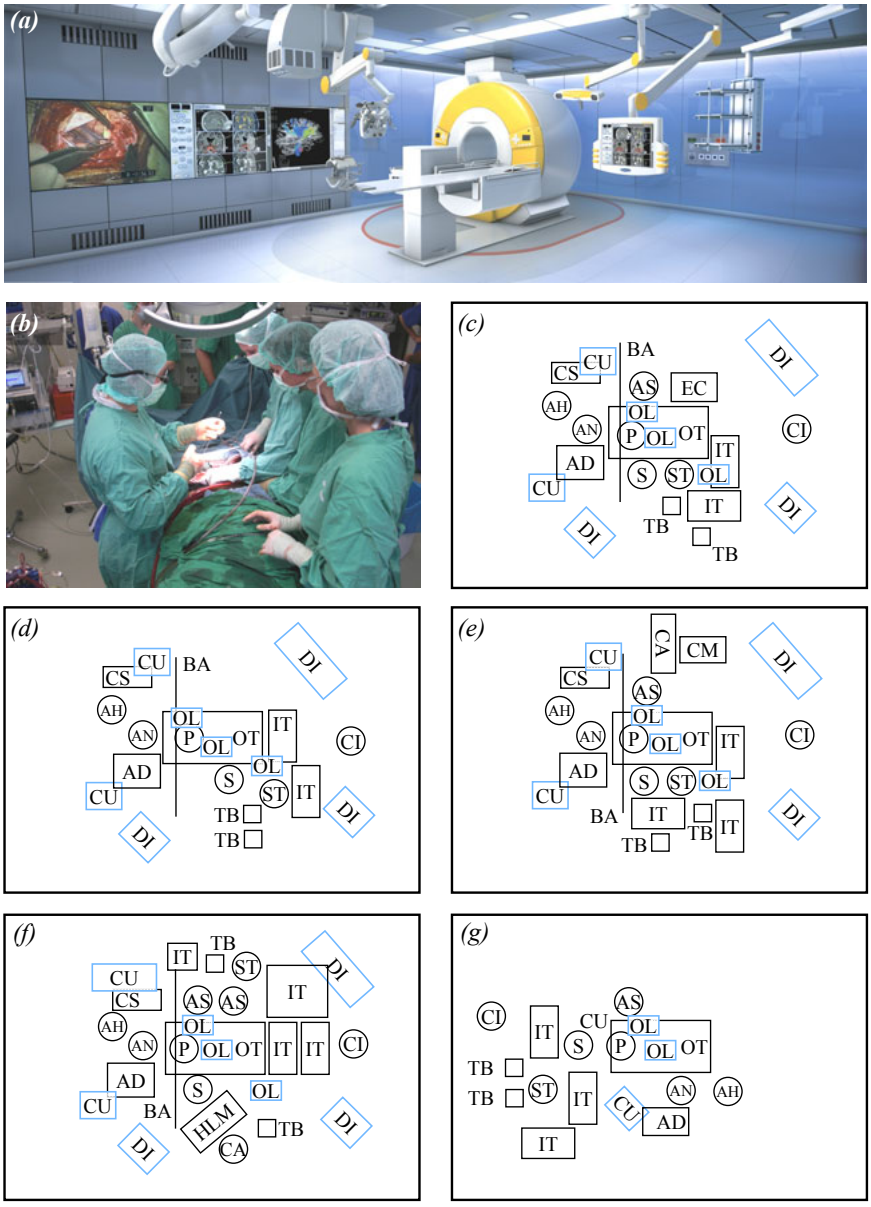

Figure 4.6: Operating rooms: *BrainLAB BrainSUITE® iMRI,* picture courtesy of *BrainLAB AG (a)*, standard operating room scene, photo copyright *DLR (b)*, OR setups for abdominal surgery *(c)*, knee surgery *(d)*, spine surgery *(e)*, heart surgery *(f)*, maxillofacial surgery *(g)*

However, such ORs do not represent the actual situation in clinics worldwide. ORs are still significantly smaller, integrate heterogeneous equipment from different manufacturers, and differ in setup from clinic to clinic, surgical application to surgical application, as well as from surgeon to surgeon. Specifically, the space around the operating table is sparse as depicted in figure 4.6 *(b)*.

A brief research conducted by the *DLR* gathered information on OR setups from four hospitals in Munich, Germany. The data for five different surgical fields (compare figure 4.6 *(c)-(g)*) was collected by surveying surgeons and nurses, visiting empty operating rooms and observing actual operations. The abbreviations used in the figure are explained in appendix C.

Objects standing on the floor have black outlines; ceiling mounted objects are marked in blue. Due to the small number of analysed ORs, the shown layouts must therefore be seen as a sample and are not universally valid. Nevertheless, they depict descriptively the confined space around the operating table and the variety of setups.

To adapt to this confined space, the *MIRO* is targeted at compact and slender dimensions. The robot must adapt to the OR, not vice versa. Eckmann et al. formulated the demand for flexible devices with a small footprint to compensate for the limited space in operating rooms and the need to comply with diverging setups and workflows [Eckmann et al., 2003].

Additionally, compact dimensions and slender design can enhance performance and acceptance of the robot. The confined space cannot only be observed on the OR level, but also on the level of the robotic system, for example, in robotic systems with multiple arms (compare figure 3.9). The trade-off between maximisation of workspaces and danger of collisions is critical. Slender and compact design is therefore essential for high level integration of multi-arm robotic systems. The dimensions of the elbow axis, wrist, and end effector are especially critical and demand small and compact dimensions which conform to proper manipulator design. Therefore, the *DLR* robot hands are an important inspiration for the *MIRO*.

Another important issue is the visual accessibility of the surgical site during an operation (line-of-sight problem) for the surgeon or additional optical devices (e.g. navigation system). This problem can be attenuated by a compact and slender design of the robot. Furthermore, the compact and slender design of the *MIRO* is intended to give an unintimidating, straightforward impression on clinicians in order to improve the acceptance of this technology.

The necessity of compact and slender design for the *MIRO* is formulated in the second design paradigm:

design paradigm 2:
The *MIRO* uses an intentionally slender and compact design in order to

- simplify integration and setup in the confined space of diverging operating rooms,
- reduce the footprint of multi-arm robotic systems,
- enhance the line-of-sight problem for the surgeon and optical devices, and
- enhance the acceptance of the robot with an unintimidating and straightforward look.

4.3.3 Redundant Anthropomorphic Kinematics

One of the most central design decisions in robotics is the type of kinematics. In general, robots with six DoF motion of the end effector can be divided into serial (scara, anthropomorphic), parallel (e.g. STEWART platform-based designs [Stewart, 1965]), and hybrid kinematics (e.g. Delta kinematics with supplemental serial kinematics like the *SurgiScope*® [Michelin, 2004]). Specialised parallel kinematics like pantograph mechanisms are designed for dedicated tasks (e.g. constraints) and are not considered here. SMITH-GUERIN et al. derive a scheme for choosing the kinematics of a medical robot [Smith-Guerin et al., 2008] in the form of a choice organigram. If aspects assumed for the *MIRO* are applied to this scheme (workspace $> 500\,mm^3$, six DoF in task space, No RCM), an anthropomorphic robot with a standard wrist ("...no concurrent axis" [Smith-Guerin et al., 2008]) is proposed. However, this scheme introduces certain decisions based on performance issues like workspace, accuracy, and payload. These aspects have been identified in section 4.1.2 as objectives of scaling and are therefore not reasonable for the kinematic decision of the generic (scalable) design of the *MIRO*. Other publications in literature compare serial manipulators and Parallel-Kinematics Machines (PKM), for dedicated applications. Table 4.2 compares different aspects of parallel and serial kinematics for the field of micromachining [Khalid and Mekid, 2008]. However, the direct application of these findings for the design of the *MIRO* is critical, because they are based on the dedicated application of machining and are therefore not suitable for the idea of a versatile robot. Furthermore, some of the shown ratings in table 4.2 (e.g. equal rating for static stiffness) are questionable.

General associations for PKMs like higher accuracy must be seen critically [Briot and Bonev, 2007], as they neglect linked issues like higher complexity or smaller

property	*serial manipulators*	*parallel manipulators*
working volume/total size	average	poor
vulnerable to errors	poor	good
accuracy	good	average
static stiffness	good	good
axis acceleration (speed)	poor	good
cutting forces (payload)	poor	good
machining of $\leq$ five faces in single setup	poor	average
range of angular motion (reaching to 90°) dexterity	good	average

Table 4.2: Comparison of attributes of parallel and serial kinematics [Khalid and Mekid, 2008]

dexterous workspace. Therefore, the choice of a parallel or serial kinematic chain for the generic design of the *MIRO* must be based on the versatile aspects (subset 1), rather than on general assumptions about performance.

Compared to serial robots, PKMs are commonly associated with attributes like higher accuracy, speed, and stiffness. These attributes are generally desirable and are derived from the fact that most of the drives of the PKM are fixed to the base and that the moving parts (links) do not hold the mass of subsequent drives (motors, gearboxes). Therefore, the inertia of the moving parts and the overall load applied to the links is reduced compared to a serial manipulator. When normalised to the power of the drives, this enables higher stiffness (and therefore accuracy) and/ or higher speeds compared to a serial concept. This advantage is of minor interest for the design of the *MIRO,* as speed requirements in the industry are assumed to differ significantly from the medical field. According to the discussion in section 4.3.1, the demand for high stiffness to achieve good accuracy has already been attenuated for the *MIRO*.

An important aspect of the kinematics, in the case of the *MIRO*, is the overall size or compactness of the robot. Normalised to the maximum of kinematic reach[1], the total dimensions of a PKM are always bigger than those of a serial manipulator.

[1]The maximum kinematic reach is the distance between the first and the last active or passive joint.

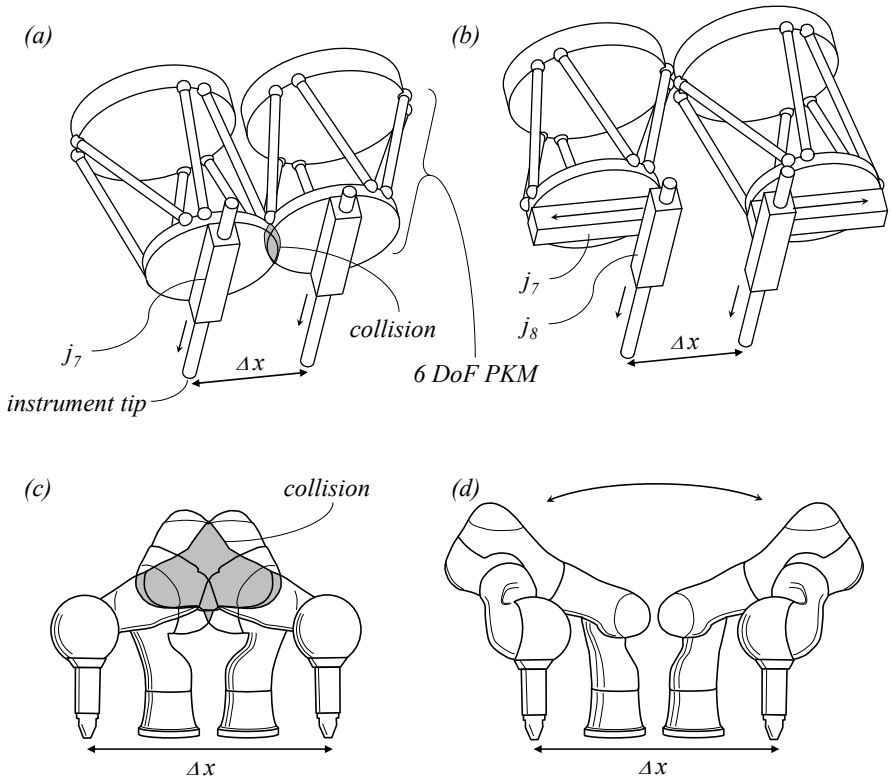

Figure 4.7: Collision avoidance by null-space motion: Collision of the top ring of the *Evolution 1* for a given pose of the instrument tips *(a)*, collision avoidance with a modified *Evolution 1* with an additional linear joint j_7 by a null-space motion *(b)*, Collision of the elbows of two *LWR III (c)*, Collision avoidance by null-space motion of the *LWR III* elbows *(d)*.

This is determined by the fact for a PKM that each of the parallel branches of the kinematics must have at least the same kinematic reach as the compared single serial manipulator. This correlation can be shown descriptively by replacing the legs or branches of a parallel robot by identical serial manipulators, an approach that has been demonstrated with a six DoF parallel robot consisting of three serial manipulators [Chen, 2001]. It is evident that the maximum kinematic reach of this kind of parallel robot cannot exceed the maximum kinematic reach of the single serial manipulator. This finding is moderated for a real system, because the maximum reach of a robot can be increased by adding elongated extensions (e.g. cantilever) at the TCP. In this case the higher payload or stiffness of parallel robots enables longer extensions compared to serial manipulators and thus a larger maximum reach. However, through the spatial arrangement of the branches in a PKM, these machines are always more

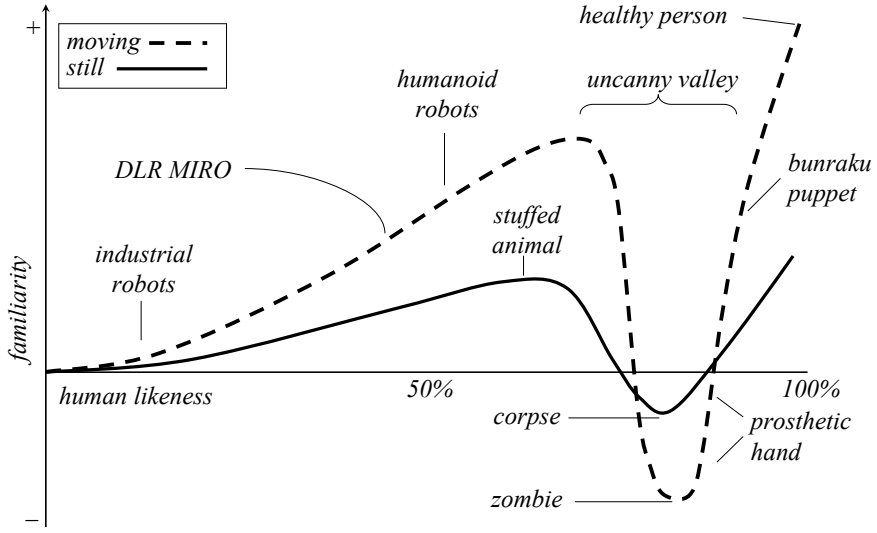

Figure 4.8: Simplified adaptation of the uncanny valley hypothesis chart [MacDorman, 2006]

bulky than single serial manipulators. This attribute conflicts with the defined design paradigm 2, especially regarding system setups with multiple robots.

Another aspect of subset 1 is the possibility of collision avoidance by applying a null-space criterion to a redundant kinematics (compare section 4.1.2). For a robot with six DoF motion of its end effector, this approach requires at least seven actuated joints. Thus, for robots based on a STEWART platform at least one additional joint must be added. As shown with the *Evolution 1* such a kinematic chain can only perform null-space motion along or about the axis of the supplemental joint, depending on whether the supplemental joint is a rotary or a linear axis. The advantage for collision avoidance is therefore limited (compare figure 4.7 *(a)*). For the *Evolution 1* a feasible way would be the integration of an additional orthogonal linear joint at the TCP of the Stewart platform (as depicted in figure 4.7 *(b)*), which would enable null-space motion of the top of the Stewart platform in a planar way. This design would accumulate eight joints. In contrast, the *LWR III* (compare figure 4.7 *(a)*, *(b)*) has shown that with a redundant kinematics integrating only seven joints, significant collision avoidance is possible.

As stated in the preceding section, the acceptance of new technologies is crucial for their success. Although clinicians and OR staff are used to working with technological equipment every day, a robot is a challenge for acceptance because of its more or less autonomous motion capabilities. Robots are used in the OR very closely to

the surgeon and in applications based on hands-on robotics even in direct contact. Therefore, the design of the *MIRO* should stimulate a natural interaction and inspire confidence. The hypothesis of the uncanny valley describes the correlation between the similarity of a robot to a human and its perceived familiarity [Mori, 1970] as depicted in figure 4.8. Thereby an improved similarity of the robot with the human arm regarding the motion capabilities generates an increased familiarity for the user. In other words, the kinematic chain which is the most familiar for a user is that of the human arm. It is assumed that a kinematic chain, which resembles the seven DoF kinematics of the human arm [Zatsiorsky, 1997] results in better acceptance and with it a natural interaction with the robot. However, the kinematic chain must still comply with the other requirements of subset 1 (e.g. interfacing conventional or endoscopic instruments).

The third design paradigm for the *MIRO* can be formulated as follows:

design paradigm 3:
The *MIRO* uses intentionally redundant, anthropomorphic kinematics in order to

- enhance the workspace/size ratio,
- simplify the integration of multiple robots on a small footprint,
- enable null-space criteria for collision avoidance, and
- enhance the acceptance of the robot by a natural understanding of its motion capabilities.

4.3.4 Sensor Integration

The *MIRO* is built for various interaction methods and applications in hard-to-predict environments. Therefore, the robot must enable various control modes as defined in subset 1 (compare section 4.1.2) including position control (e.g. in telerobotic and autonomous applications), joint torque control (e.g. as one possibility to comply with the fulcrum point), and Cartesian force-torque-, as well as impedance control (e.g. for hands-on robotics applications). By this, sensors are needed to enable force/torque control. The classic approach for hands-on robotics shown with the *Hippocrate* or the *OTTO* robot in section 3.2 by adding a force-torque sensor to the TCP is not sufficient for the scope of the *MIRO*, because it cannot provide torque control of a

single joint as needed to imitate passive joints (e.g. to comply with the fulcrum point, compare section 3.1.5). Additionally, this approach limits the haptic interaction of the robot with its environment (e.g. user interaction, collision detection) to the TCP and neglects all other portions of the robot structure. In the case of a redundant robot with seven DoF, this approach would limit the interaction to six Cartesian DoF of the TCP, but would exclude additional haptic interaction for null-space motions. Therefore, the force/torque sensing should enable "full arm" hands-on robotics, which can be established with two different approaches:

- direct measurement of external loads throughout the whole surface of the robot (e.g. by a tactile skin)
- measurement of the resulting forces/torques in the robot joints or structure

The feasibility of direct measurement of the contact forces applied to a robot structure has been shown by WÖSCH and FEITEN [Wösch and Feiten, 2002]. In this setup the robot is covered by a tactile skin with 45 sensors measuring forces and the locations of the contact points. This approach delivers exact information about the external loads without the influence of the robot mass and payload, but requires a large amount of sensor data. However, this approach is not suitable for detecting reaction forces of the surgical instrument with its environment or to enable torque control of single joints.

In contrast, the measurement of loads by the integration of force/ torque sensors into the robot's links or joints accumulates external loads, static and dynamic mass effects of the robot, and the payload. Loads applied to the robot structure cause proportional amounts of torque in one or multiple joints of the robot. Based on the knowledge of the mass properties of the robot (gravitational model), the payload, and the joint angle of the robot, these external loads can calculated and used for torque control on the joint level or force/torque and impedance control on the Cartesian level. This approach has been shown successfully with the *DLR LWRs* [Albu-Schäffer and Hirzinger, 2001] and the *WAM™ Arm*. The main difference between these two systems is the location of the torque measurement along the flux of the drive chain. The *DLR LWRs* integrate additional, dedicated torque sensors between the high-torque side of the reduction gear and the next link. In contrast, the *WAM™ Arm* utilises the motor currents to calculate the joint torques. A central advantage of the second concept is the avoidance of additional dedicated torque sensors, because the motor torques can be derived from measurements of the electric motor currents. On the other hand, unless a direct drive design is possible, joint-sided torques are transmitted by the reduction gears to the motor. To achieve high accuracy in torque measurement, the backdrivability of the gears must be of high efficiency, which limits the selection of available reduction gears. The concept of torque measurement in

the *DLR LWRs* is compatible with every reduction gear regarding the avoidance of parasitic effects (e.g. friction) on the measured torque signal.

Another advantage of dedicated torque sensors is the compensation of elasticities. For an ideally stiff robot only the actual joint angles are necessary to calculate the actual pose of the TCP. As described in section 4.3.1, this paradigm cannot be applied to a lightweight robot with compliant links and joints if high accuracy is necessary. Therefore, two supplemental approaches have been proposed for the *MIRO* (compare section 4.3.1, page 67), one based on robot-integrated load sensors and one on external position sensors.

Given robot-integrated load sensors, the elasticities of the components have to be identified in order to calculate the deflections of the robot due to external loads or its own mass. This can be performed either by calculation (e.g. simulation by finite elements method (FEM)) or by identification in tests. The real-time computation is limited to more or less simple elastic calculations and identification is more promising if the elasticities include complex portions like contact stiffness (e.g. in bearings, gears). In order to compute the deflection of the components based on these identified elasticities, additional sensor information is required to acquire the actual loads on the components. The concept of dedicated joint torque sensors introduced by *LWRs* is one possibility for measuring the load on a joint, to calculate the rotary deflection about the joint axis, and the bending of the robot's links in the plane orthogonal to this axis. However, this concept neglects transverse loads on links, which do not evoke a torque on the preceding joint.

Besides sensors targeted at the force/ torque measurement, a robot must integrate components to acquire the actual positions of the joints. At this point it is assumed that a robotic joint consists of a motor and a reduction gear and that the position of a joint cannot be stored during a power-off period. Basically, two different concepts are available to determine the absolute joint positions:

- motor-sided position sensors or revolution counters combined with joint-sided reference marks and
- joint-sided position sensors.

Due to the ratio of the reduction gear, the position of the motor cannot determine the position of the joint itself. Therefore, the first approach applies reference marks (e.g. an electric switch) at a certain position on the joint side. In order to find the actual position of the joint, an initial reference motion must be performed until the reference mark is reached. In order to avoid mechanical joint limits, usually multiple reference marks are applied near the joint range limits. Once the reference mark is reached, the absolute position of the joint is known and in the following motor-sided

position control is applied. During this reference motion the position of the robot has not yet been determined, which leads to collision risk.

In contrast, the second approach integrates an additional absolute sensor on the joint side, measuring directly the position of the joint. Therefore, the positions of the joints are determined immediately after power-on of the robot. Considering the environment of an operating room, collision avoidance and convenient setup, an initialisation trajectory of the robot for referencing the joints is inappropriate.

The demand of different integrated sensors is formulated in the following design paradigm:

design paradigm 4:
The *MIRO* integrates motor-sided high resolution position sensors, joint-sided position sensors, and joint-sided torque sensors in order to

- enable position, force/ torque, and impedance control on Cartesian and joint level,
- enable position, torque, and impedance control on the joint level,
- avoid the parasitic effects of the reduction gear on the torque measurement,
- measure external loads for full arm hands-on robotics and collision detection,
- receive immediate joint positions after power-on, without initialising trajectory, and
- calculate elasticities due to unknown external loads.

4.3.5 Integrated Electronics and Internal Cabling

The integration of electronics into the robot arm seems to contradict the paradigm of designing a slim and compact robot. Furthermore, the demand for an internal cable conduit appears to be a minor aspect for the design of a robot at first glance. However, this section identifies these aspects as closely interwoven and having an elementary impact on the design of the robot and the feasibility of the preceding design paradigms.

The cable harness of a robot interconnects sensors, actuators, and electronic components. A serial kinematic chain, as proposed in section 4.3.3, determines that parts

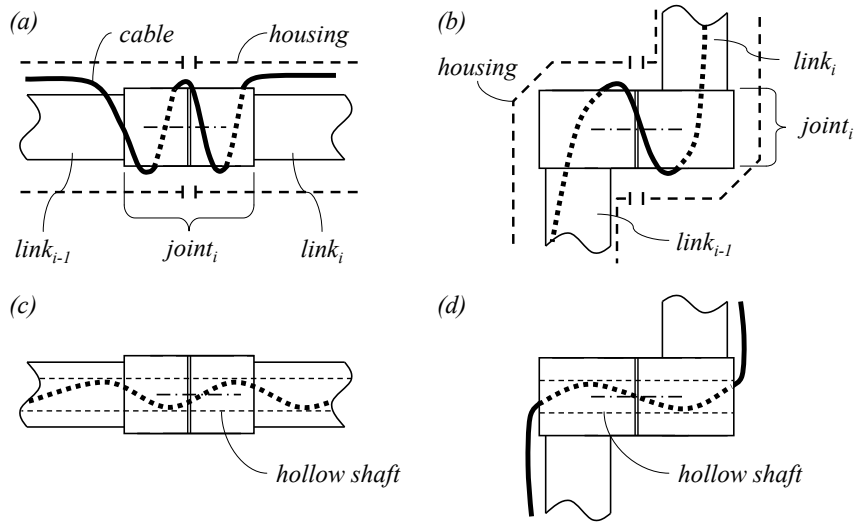

Figure 4.9: Cable routing for bridging revolute joints: external winding with roll joint *(a)* and pitch joint *(b)*, internal cable routing through hollow shaft of a roll joint *(c)* and pitch joint *(d)*

of this cable harness have to bridge moving joints of the robot. This fact can be partly avoided by the application of contact-less transmission (e.g. communication and sensor signals via radio transmission) or completely avoided by sliding contacts like slip rings [Schleifring, 2007]. However, the compact size (diameter) of a cable appears out of reach for the slip ring technology.

According to the design paradigm 3 demanding an anthropomorphic kinematics for the *MIRO*, the following explanations are limited to revolute joints.

To pass a rotary moving joint, two different approaches can be applied as depicted in figure 4.9. Basically, the cable can be wound in a helical or planar way on the lateral area of a joint (compare figure 4.9 *(a), (b)*) or conducted through the joint if a hollow shaft is available (figure 4.9 *(c), (d)*). A major advantage of the first approach is the compatibility with arbitrary joint designs as it does not require a hollow shaft. On the other hand, cable loops on the outside surface of a robot are not acceptable for the *MIRO* for several reasons. In the context of collision avoidance based on a geometrical simulation/ surveillance of the system, the shape of these flexible cable loops is difficult to determine and model. In hands-on robotics applications, cable loops may confuse the surgeon due to their unclear assignment to the robot structure and impact on force/ torque control. Additionally, cable loops and their winding introduce a danger for the hands of the surgeon regarding constriction of fingers. Furthermore, to provide an easy to clean surface for the robot (disinfection) external cables are also

unfavourable. Therefore, an additional housing as indicated in figure 4.9 *(a)* and *(b)*, covering the cables would be indispensable for the *MIRO*.

In contrast, solutions based on a hollow shaft approach require a specialised joint design and limit the range of available components (e.g. hollow shaft reduction gears). On the other hand, disadvantages of the outside cabling version are avoided. For example, as torsion to cables must be avoided, the cables must be wound in a helical way as depicted, which demands longer cables. Although both approaches are feasible for the *MIRO*, the design is based on the hollow shaft approach due to the incompatibility of the other variant with multi-DoF joints, which can be seen in the later section 4.5.

The second aim targets integrated electronics. The electronics of a robot (robot arm and external unit) allows sensors and actuators to interface with the control and infrastructure block as depicted in 4.1.

Therefore, these electronics implement the following objectives:

- generating actuator currents
- receiving sensor signals
- power conversion (e.g. AC operating room supply to DC for electronics)
- communication with the higher-ranking system level
- integration of the robot control
- enabling optional communication with components on the same system level

Physically, the electronics can be modularised and distributed over various locations. Two different locations are possible:

- external, e.g. robot's base or supplemental unit
- internal, in the robot's links or joints

For a standard industrial robot, the electronic components are predominantly located externally, as in the *KUKA KR-C2* controller unit [KUKA, 2004b]. Only indispensable parts (e.g. sensors and signal amplifiers) are located in the robot arm itself. This concept is derived from the integration level of electronics, which excluded integration into the robot arm in the beginning of robotics. Although today's integration level of electronics would enable the integration into the reduced space of a robot arm, this concept seems still more cost effective for industrial robots.

In contrast, the lightweight robots shown in section 3.2.8 are partly targeted at mobile applications. This means that the robot arms are mounted to mobile carriers,

like humanoid robotic systems [Brudniok, 2007] or mobile robots [Görner et al., 2008]. Therefore, the electronic components must be capable of being partly or completely integrated into the mobile system in order to reduce or avoid cable connections to non-mobile system components. Another reason for the integration of electronics into the robot arms is the increased application of sensors in robotic arms. As shown in section 4.3.4 a plurality of sensors must be integrated into the robot arm to provide higher accuracy of lightweight robots or to enable an extended range of control modes. Regarding the scaling of robots according to their performance (e.g. payload), it must be pointed out that the scaling only affects electronic components and cabling, which serve the actuators. All other components, linked to communication, sensors, or control are independent from this scaling.

This fact is critical regarding the design of compact systems like the *MIRO* and can be reduced to an optimisation problem: The integration of electronics into the robot arm is a trade-off between the size (diameter) of the cabling and the space consumption of the integrated electronics. The available space for the integration of cabling and electronics is not homogeneous in a robot arm. The design of a standard industrial robot (compare figure 2.2) depicts the high integration level of the joints and the more or less spacious portions of the robot links. This derives from the fact that joints integrate complex mechanisms (e.g. gears, brakes, bearings) and robot links only consist of structural parts. For the design of a compact and slender robot the effort of miniaturisation of the joints is assumed to be more challenging than the miniaturisation of the links. Therefore, the described trade-off can be transferred to the required space for feeding the cable harness through the hollow shaft of the joint against the available space in the robot links.

The impact of integrated electronics on the diameter of the cable harness is depicted in figure 4.10. The shown cross-sections compare the cable harness conducted through the first joint of the actual *DLR LWR III* (figure 4.10 *(a)*) with a hypothetical *LWR III* with external electronics (figure 4.10 *(b)*). The different cables, their function, and diameters are explained in appendix C, table C.3. The larger diameter of the second variant derives from the large number of sensor and motor cables of the joint j_2 to j_7, which all have to pass j_1. The signals on these cables are EMC-critical regarding immission or emission and must be shielded, which additionally increases the diameter and the rigidity of the cable harness. However, other negative effects of long cables for analogue signals, like power drop or temperature influences remain, which reduce the signal quality, especially regarding sensor signals.

By integrating the electronics into the robot's links, the sensor and actuator signals can be serialised to a common communication. This allows, for example, amplifying and digitising of analogue sensor signals (e.g. strain gauges) near or directly at the

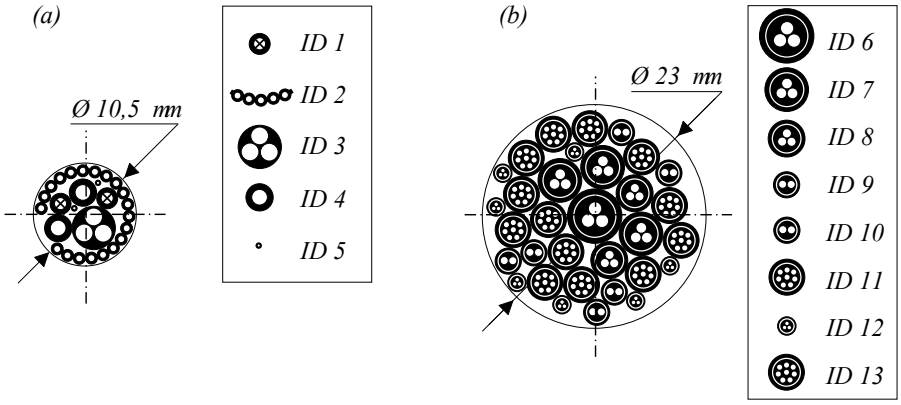

Figure 4.10: Comparison of cable harness cross-section at joint 1: actual *LWR III (a)*, theoretical *LWR III* with external electronics *(b)*.

point of measurement. In order to enhance the signal quality, it is advantageous to reduce the lengths of cables transmitting analogue signals. Additionally, power for the integrated electronics can be supplied by an EMC-uncritical DC supply, which does not require shielded cables, in contrast to conducting a multiplicity of cables transmitting the PWM[2] current for the motors through the whole robot. In this sense, the power supply of the robot joints can also be serialised. Therefore, by integrating electronics into less space-critical portions of the robot (e.g. links), the cable harness can be reduced significantly, which benefits the design of smaller joints. The importance of this correlation increases with the number of sensors and actuators in the robot.

Another advantage of integrated electronics is the possibility of establishing a modular design where sensors and actuators are integrated with their assigned electronics within one physical module. A module can comprise, for example, a robot joint with its preceding link. Such modules enhance the initial testing of robot components before final integration, which is then reduced to the physical connection of the modules and the establishment of the communication between these modules.

On the other hand, the integration of electronic components into the robot arm bears disadvantages. Thermal problems caused by electric losses must be targeted by efficient electronic design and/ or cooling concepts. Regarding the condensed space in the robot arm, accessibility to the electronic components for test or maintenance purposes demands adapted housing and integration concepts. Finally, the high integration level of the electronics caused by the condensed space in the robot arms

[2]Pulse-width modulation is a way to generate a sine-like voltage for an electric motor by pulses with modulated length, but equal amplitude.

demands for specialised designs of the electronics and rules out standard electronic modules (e.g. top-hat rail motor inverters).

Regarding the *MIRO*, the advantages of integrated electronics were rated as decisive in order to achieve the goals formulated in the last design paradigm:

design paradigm 5:
The *MIRO* provides internal cabling and integrates the maximum necessary electronics in order to

- enhance signal quality of sensors,
- reduce EMC problems,
- reduce the size of the cable harness,
- avoid external cable conduits regarding hands-on robotics and collision avoidance, and
- enable operation of integrated joint modules.

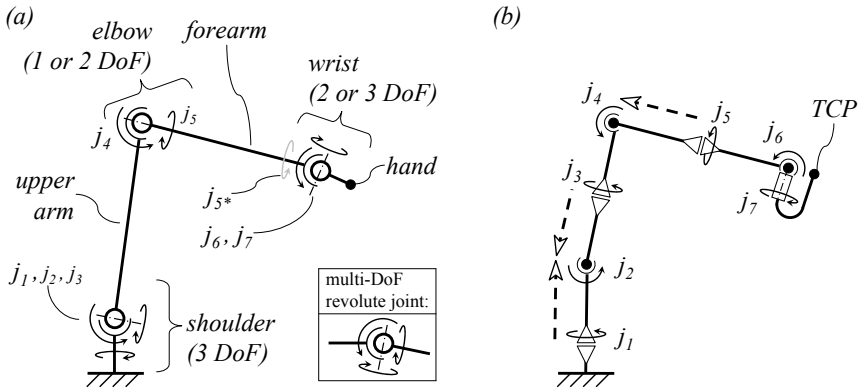

Figure 4.11: The kinematics of the human arm *(a)* and the *DLR LWR III (b).* The graphical abstraction according to the *VDI 2861* standard [VDI 2861, 1988] is supplemented by a new symbol for multi-DoF revolute joints.

4.4 Kinematic Concept

An anthropomorphic kinematics has been defined as a goal in design paradigm 3 for the *MIRO*. Regarding hands-on robotic approaches, the surgeon or the OR personnel interface directly with the robot by haptic interaction. Such modes may comprise the guidance of a surgical tool, initial configuration of the robot during setup or retraction of the robot arm from the surgical site for e.g. changing the instrument. In this sense, the robot does not act exclusively as an output device, but additionally as an input device. Besides the interaction with the TCP, the *MIRO* is aiming at full-arm hands-on robotics, which includes the haptic interaction with all parts of the robot. With this, the motion capabilities of the whole kinematic chain must be comprehensible for the user. Therefore, the central attempt behind the approach of an anthropomorphic look is to establish a kinematics which is intuitive for the user, especially in hands-on robotics applications. The author assumes that a kinematic chain, which resembles those of the human arm, is very natural for the human user.

This section describes the kinematic chain of the human arm and the key aspects which makes it intuitive for the user. This is followed by a description of how this kinematics is adapted for the *MIRO*. Based on the selected kinematic chain, the optimisation of link lengths and joint ranges according to a defined set of applications was conducted [Konietschke et al., 2003b]. This optimisation is not part of the author's research and is therefore described only briefly in the later section 4.6.

4.4.1 The Human Arm

Humanoid robots like *ASIMO* [Sugiura et al., 2006] or *ARMAR* [Brudniok, 2007] apply anthropomorphic kinematics to imitate the human. In contrast, the *MIRO* utilises a kinematic chain resembling those of the human arm to enhance the interaction with the user when applied as a haptic device. The human arm and hand can be seen as the first perceived and most relevant haptic interface of the human with its environment. Therefore, the kinematic chain and their motion capabilities are assumed as to be very familiar for the human operator. Figure 4.11 *(a)* depicts a seven DoF kinematic representation of the human arm [Zatsiorsky, 1997] in comparison to the kinematics of the *LWR III* (figure 4.11 *(b)*).

The main difference between the two kinematics is the accumulation of DoF in the form of multi-DoF joints assigned to shoulder, elbow, and wrist in the human arm. The kinematics of the human arm can be abstracted by a shoulder with three DoF (j_1, j_2 , j_3)[3], the upper arm ($link_3$), an elbow with one or two DoF (j_4, j_5), the forearm ($link_{4*}$ or $link_5$), and the wrist with two or three DoF (j_{5*}, j_6 , j_7).

The assignment of the fifth DoF either as j_5 to the elbow or as j_{5*} to the wrist derives from the complex anatomic design of this DoF with a twisting motion of the two elongated bones forming the forearm (ulna and radius) [Weinberg et al., 2000]. However, the intention of the *MIRO* is not to imitate the mechanics of the human arm, but to generate overall motion capabilities and a look, which resembles those of the human arm. Therefore, this fifth DoF is assumed as an in-line revolute joint and assigned to the elbow[4]. The axes of the joints can be assumed to intersect, forming a spherical joint in the shoulder, a pitch-roll joint in the elbow, and a pitch-yaw joint in the wrist.

Regarding a technical implementation of a seven DoF serial kinematics, the *LWR III* is a good starting point. It applies single-DoF joints, which are connected by more or less identical link lengths. Regarding motion capabilities, this concept equals more or less the kinematics of the human arm, because in-line revolute joints can always be shifted along their axis without impact on the kinematics. For example, the kinematics of the human arm can be accomplished by shifting j_1 and j_3 of the *LWR III* to the location of j_2, and j_5 to the location of j_4 as indicated by the dashed arrows in figure 4.11 *(b)*. Without considering link lengths and joint ranges at this point, the main difference between the two kinematics is the number of links and DoF of joints. With the *LWR III* the number of moving links perceivable by the user adds up to seven. In contrast, the human arm appears to have only three moving links (upper

[3]The enumeration of joint and link indices applied in this thesis conforms with the notation of Denavid-Hartenberg-Parameters according to Yoshikawa [Yoshikawa, 1990] and Craig [Craig, 1986].

[4]Moving a joint towards the base of a robot always reduces the inertia of moving parts and is therefore an undisputed approach.

arm, forearm, and hand). The author assumes that besides the resemblance to the human arm, the reduced number of moving links and the accumulation of DoF in multi-DoF joints simplifies the interpretation and predictability of kinematic motion capabilities for the human user. Another effect of this approach has to be pointed out in relation to design paradigm 5. The space for the integration of electronics into the links is different. With the kinematics in figure 4.11 *(a)*, the space per link increases, but the number of spaces decreases. The relevance of this correlation in relation to the impact on small and slender design will be analysed in section 4.5.

4.4.2 Kinematics of the MIRO

The kinematics of the human arm is chosen as a role model for the *MIRO* because of the assumptions described in the preceding section. This approach complies with the kinematic choice organigram by Smith-Guerin et al. [Smith-Guerin et al., 2008] and is valid regarding the kinematic similarity with the *LWR III* as shown in the preceding section.

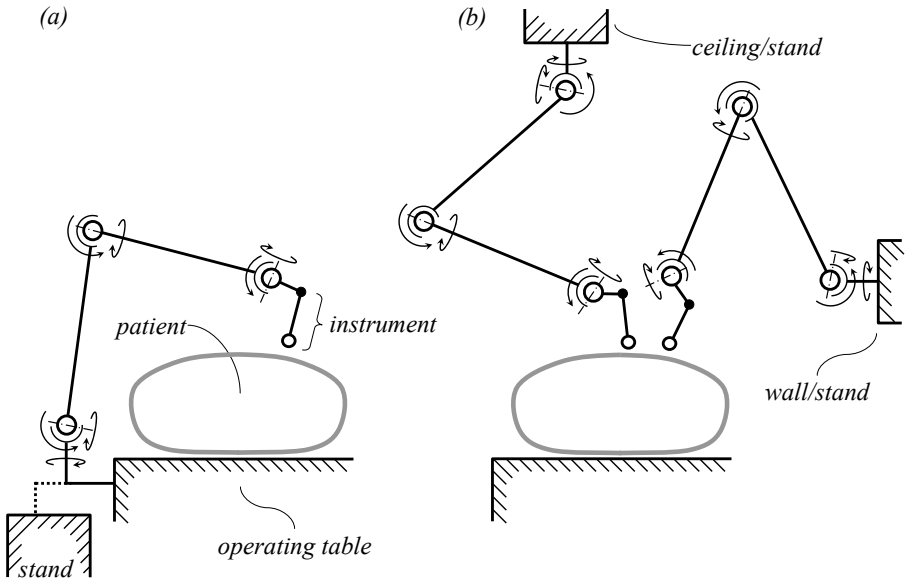

Figure 4.12: Basic arm configurations for the setup options in the OR: vertical upright configuration (operating table mounting or cart) *(a)*, side or vertical hanging configuration (ceiling, wall or stand mounting) *(b)*

However, the human arm kinematics cannot be applied directly to the *MIRO* because of the complexity of the anatomic joints and the wrist design. In the following, the kinematic development of the *MIRO* is structured according to the human arm

into shoulder, elbow, and wrist. To form a very simple and intuitive kinematics, the joint configurations are targeted at orthogonally intersecting axes as in classic robot design.

Regarding the required mounting options of the versatility paradigm, the resulting arm setups can be broken down using spatial orientation of the robot's base. These include vertical upright, vertical hanging, horizontal, and mixed orientations in between, as depicted in figure 4.12).

4.4.2.1 Shoulder

The shoulder of the human arm (*lat. articulatio humeri*[5]) provides three DoF. This joint can be abstracted technically as a ball and socket joint with three orthogonal intersecting axes. Although spherical actuators are an objective in research [Yan et al., 2006], these approaches mainly focus on the design of spherical motors (direct drive), which cannot be applied as a robot shoulder joint regarding the achievable torques in relation to a required compact size. Therefore, the *MIRO* is based on single and 2-DoF joints. The 2-DoF joint designs are more complex than single DoF joints, but enable compact design, reduction of electronic components, and torque-synergy effects between the two DoF. These advantages are clarified in the later section 4.5.

According to the definitions above (three DoF, intersecting axes, single and two-DoF joints), six valid configurations of a shoulder joint are possible utilising single or 2-DoF joints as depicted in figure 4.13 *(a-f)*. These configurations comprise roll-pitch-yaw, pitch-yaw-roll and roll-pitch-roll (like the *LWR III*) sequences, either based on sequences of single DoF joints or combinations of single and 2-DoF joints. Due to the isometric view of the joints, a different abstraction was chosen compared to preceding figures[6].

The pros and cons of the different approaches are minor, because clear criteria for rating are missing at this point. However, it can be stated that a sequence in which a pitch DoF is followed by a single DoF roll joint (compare figures 4.13 *(b)*, *(e)*, *(f)*) has the disadvantage that the pitch joint must hold the weight of the following roll joint. This disadvantage does not apply in the reverse to a roll-pitch sequence if the shoulder design is compact and the centre of gravity of the pitch joint is near the rotation axis of the roll joint.

Additionally, if a vertical upright setup of the robot is assumed, versions *(c)* and *(f)* imply a singularity in the middle of the motion range of j_2 due to the coaxial

[5]The articulating link between humerus (bone of the upper arm) and torso.

[6]Revolute joints are abstracted as cylinders where the cylinder axis is supposed to represent the rotation axis of the joint. The cylinders are depicted as opaque bodies (no hidden lines) to show their orientation in space, but in the case of 2-DoF joints an overlay (transparency) of the two cylinders is applied (no merged bodies).

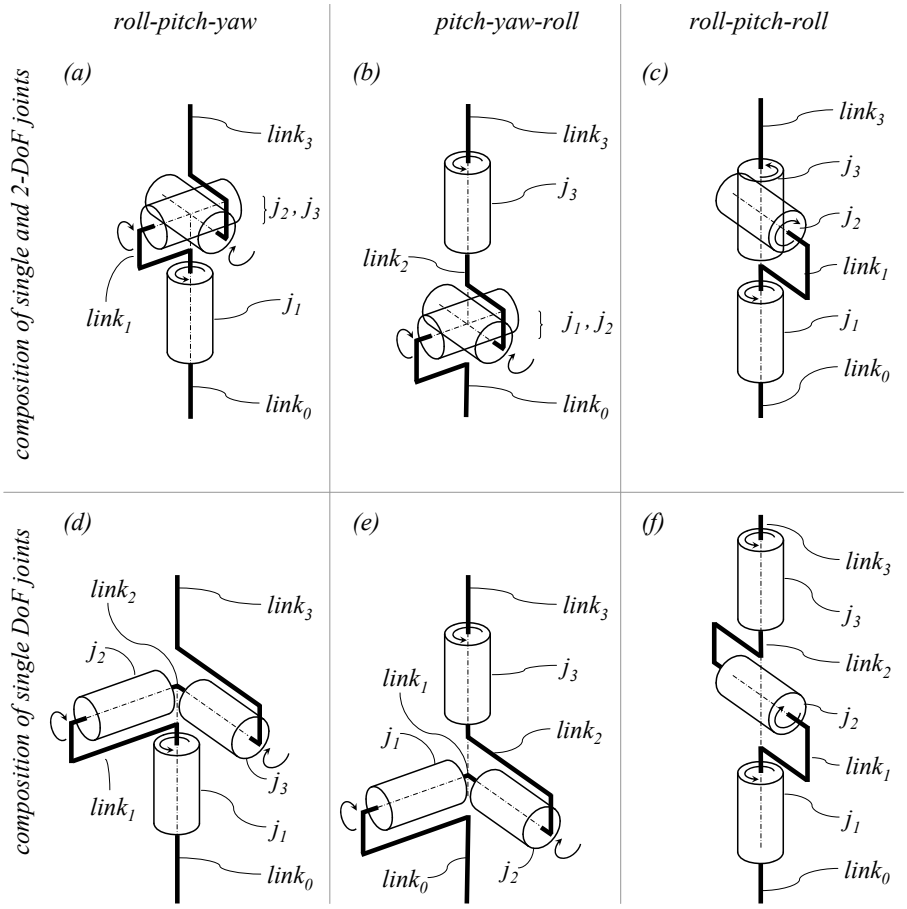

Figure 4.13: Six valid shoulder configurations: roll-pitch-yaw *(a+d)*, pitch-yaw-roll *(b+e)*, roll-pitch-roll *(c+f)*

alignment of j_1 and j_3, as depicted in figure 4.13 *(c)* and *(f)*. This would result in indefinite solutions for the position j_1 and j_3 in the inverse kinematics.

Therefore, the two solutions *(a)* and *(d)* remain. Due to the advantages of 2-DoF joints regarding the reduction of electronic components (compare later section 4.5.3.1), configuration *(a)* is chosen for the shoulder design of the *MIRO*.

4.4.2.2 Elbow

For the design of the *MIRO*, the complex principle of turning the human forearm by twisting *radius* and *ulna* as described in section 4.4.1 are not considered. Therefore, the configuration of the elbow is broken down into a pitch-roll configuration with orthogonally intersecting axes. It must be pointed out here that this choice creates

a singularity (workspace limit) in conjunction with the defined kinematics of the shoulder when the robot arm reaches a completely elongated pose. However, such pose for a robot is rarely chosen for a task.

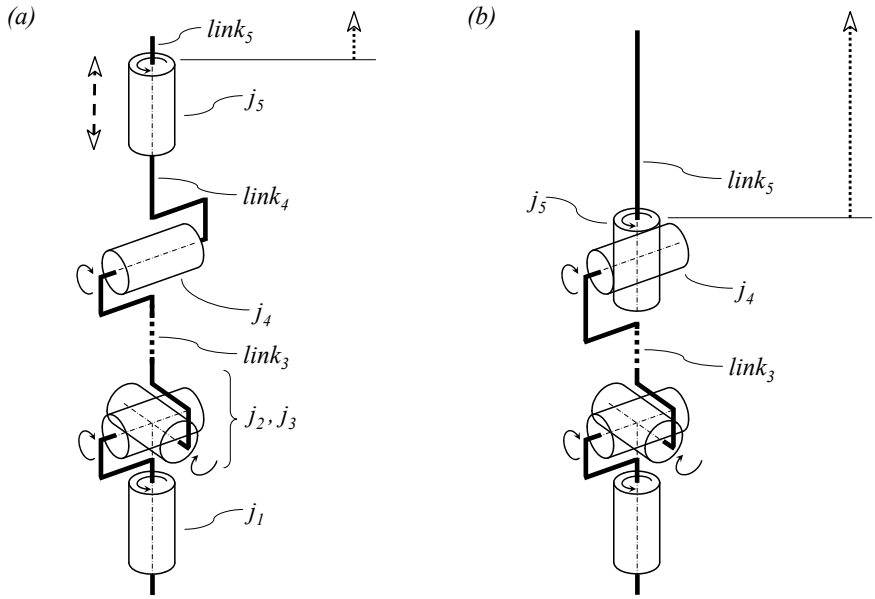

Figure 4.14: Two valid elbow configurations: sequence of single DoF joints *(a)*, 2-DoF joint *(b)*

As a result, the central question persists where the fifth DoF is located. Figure 4.14 *(a)* and *(b)* depict the two possible solutions. Configuration *(a)* is based on single DoF joints. Therefore, j_5 can be located arbitrarily (indicated by the dashed arrow) along the forearm between j_4 and the wrist. The second configuration *(b)* implements the elbow by a 2-DoF joint. Besides the pros and cons of 2-DoF joints (compare section 4.5.3), solution *(a)* shows three major disadvantages. As described in the preceding section, the sequence of a pitch and a roll joint results in a higher torque on the pitch joint. This additional holding torque is decreased when the distance between the centre of gravity of the roll joint and the axis of the pitch joint is reduced. Secondly, the *MIRO* is aiming for a slender and compact design. The importance of compactness increases from the first to the last joint and shifting j_5 towards j_4 is therefore beneficial. At last, the location of j_5 is important for full-arm hands-on robotics. In order to control j_5 through applying an external torque by hand. The user must interact with structures of the robot, which are beyond j_5 and its torque sensor. Only then, the torque sensor of the joint can measure this torque. As indicated in figure 4.14 by the dotted arrows, this portion of the structure is signi-

ficantly larger with configuration *(b)*. Regarding these advantages, configuration *(b)* is best suited and chosen for the elbow design of the *MIRO*.

4.4.2.3 Wrist

The human arm as a model with its pitch-yaw wrist should not be applied directly to the *MIRO*, because the dexterity of the human arm cannot be seen without the hand. Therefore, the wrist of the *MIRO* may differ from the human wrist. The following demands for the wrist of the *MIRO* can be formulated:

- alignment of a revolute joint with the axis of the elongated shaft of a laparoendoscopic instrument
- possibility of removing the laparoendoscopic instrument along its shaft axis from the robot
- possibility of mounting instruments to form a pitch-yaw wrist

A configurability of the wrist design, implementing a supplemental adapter (compare *LWR III*, figure 3.16), in order to form pitch-roll and pitch-yaw configurations of the wrist complies with the first and the third demands defined above. However, this wrist design does not enable removing a laparoendoscopic instrument (e.g. video endoscope) from the patient body if the robot is blocked as discussed in section 3.2.8.

As defined in the versatility paradigm, the *MIRO* must be capable of manipulating laparoendoscopic instruments covering all DoF which can be manipulated from outside of the patient. This includes the rotation of laparoendoscopic instrument about its shaft axis. For example, the *da Vinci® Surgical System* provides a motion range of over 360° about the instrument shaft axis [Hayashibe et al., 2005]. Although it is possible to accomplish this demand with a pitch-yaw wrist by distributing this motion on other roll joints in the arm, this approach results in a large motion envelope. This is depicted in figure 4.15 *(a)* for a rotation of 180° about the shaft axis of the instrument. Furthermore, this approach is not valid regarding a vertical upright configuration of the arm. Such motion range can only be achieved by alignment of a rotary DoF of the robot with the instrument shaft axis. The motion envelope can be reduced if this rotary DoF is located directly at the TCP. Therefore, a pitch-roll joint configuration is selected for the wrist of the *MIRO*. This can be implemented by a sequence of two single DoF joints similar to the configuration depicted in figure 4.14 *(a)* or by a 2-DoF joint as depicted in figures 4.15 *(b)* and *(c)*. The advantages of the 2-DoF joint as formulated in the preceding section on the elbow design also apply to the wrist.

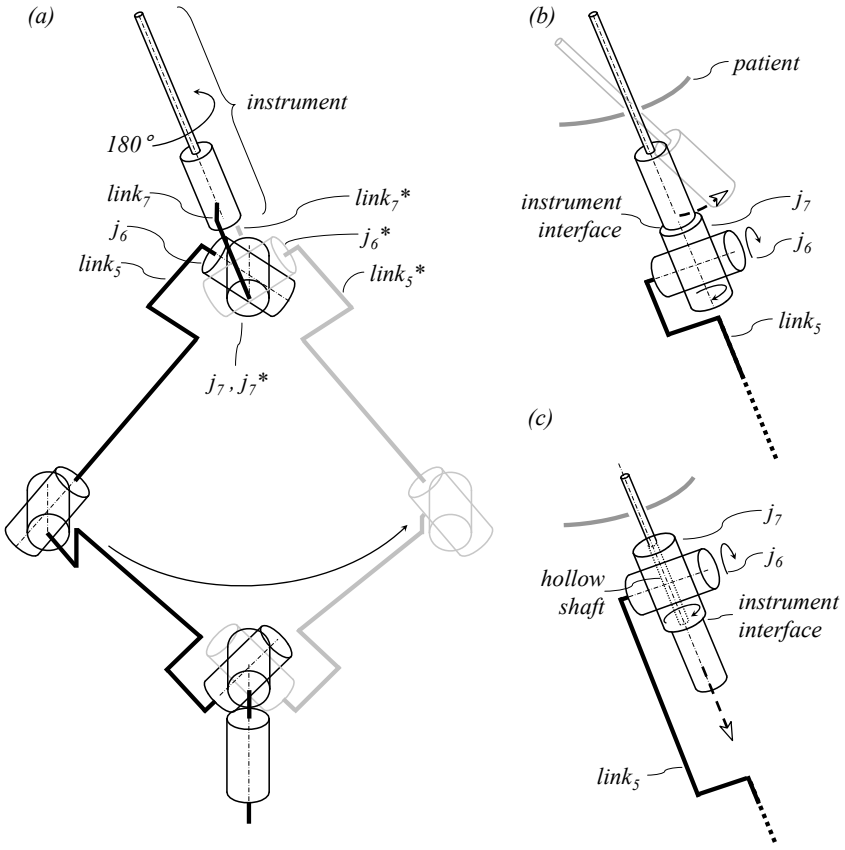

Figure 4.15: Wrist design: arm motion for a 180° rotation of an instrument based on a pitch-yaw wrist *(a)*, classic pitch-roll configuration *(b)*, pitch-roll configuration with hollow shaft *(c)*

Regarding the removal of the instrument from the patient along the instrument shaft axis, the classic pitch-roll configuration (figure 4.15 *(b)*) demands a lateral motion of the instrument after disconnection as indicated with the dashed arrow, if the robot is blocked. This must be avoided in order to prevent harm to the tissue inside the patient (e.g. by scalpel instruments). The configuration depicted in figure 4.15 *(c)* applies the idea of a hollow shaft design for j_7, where the instrument shaft is conducted through the hollow shaft from the rear side of j_7. This way, the instrument can be removed from the patient directly along the shaft axis of the instrument as indicated with the dashed arrow in figure 4.15 *(c)*. However, when the instrument has to be removed in a configuration of the robot where j_7 is aligned with the forearm, as depicted in figure 4.15 *(c)*, the shape of $link_5$ must guarantee the necessary space for

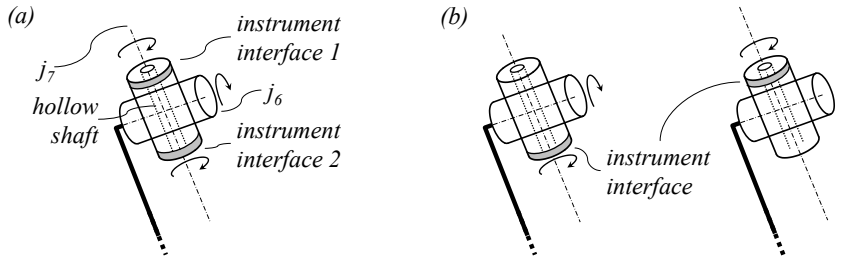

Figure 4.16: Wrist end effector configurations: two instrument interfaces integrated in j_7 *(a)*, single instrument interface with a wide motion range of j_6 *(b)*

the removal of the instrument. Furthermore, the length of j_7 must be designed to be as short as possible, because this length reduces the usable length of the instrument shaft.

As defined above, the wrist design must be capable of using non-endoscopic instruments like lasers, biopsy needles, and osteotomy saws as well. Regarding the usage of guidance for biopsy needles, it can be stated that the alignment of the needle axis and j_7 eliminates one DoF of the system, because the motion about the needle axis is irrelevant. It is trivial to design an instrument adapter which implements an arbitrary orientation of the instrument compared to the joints of the robot wrist. However, the configuration depicted in figure 4.15 *(c)* shows an instrument interface which is not capable of attaching non-endoscopic instruments, because it does not point towards the patient. Figure 4.16 shows the two solutions to solve this problem. The first approach is to integrate two instrument interfaces at both ends of j_7 as depicted in figure 4.16 *(a)* with interface 1 suitable for non-endoscopic instruments and interface 2 for endoscopic instruments. This approach demands duplication of parts, like the interface mechanism. The second approach is based on a wide motion range of j_6, which allows pointing the instrument interface towards the patient or in the opposite direction for endoscopic instruments.

For the wrist design of the *MIRO*, a pitch-roll configuration with hollow shaft design based on a 2-DoF joint is chosen. In order to attach non-endoscopic tools the motion range of j_6 allows for pointing the instrument interface towards the patient. For endoscopic instruments, j_6 can reach a pose where the interface is pointing more or less in the opposite direction. This wrist design of the *MIRO* was granted as a German patent [Hagn, 2004].

4.4.3 Summary on Kinematics Design

The joint configurations of shoulder, elbow, and wrist have been developed in the preceding sections. The generic kinematics of the *MIRO* is therefore represented by a roll-pitch-yaw shoulder, pitch-roll elbow and pitch-roll wrist. Figure 4.17 *(a)* depicts the kinematic chain and table 4.3 *(left)* denotes the Denavit-Hartenberg parameters according to the notation of YOSHIKAWA [Yoshikawa, 1990] and CRAIG [Craig, 1986].

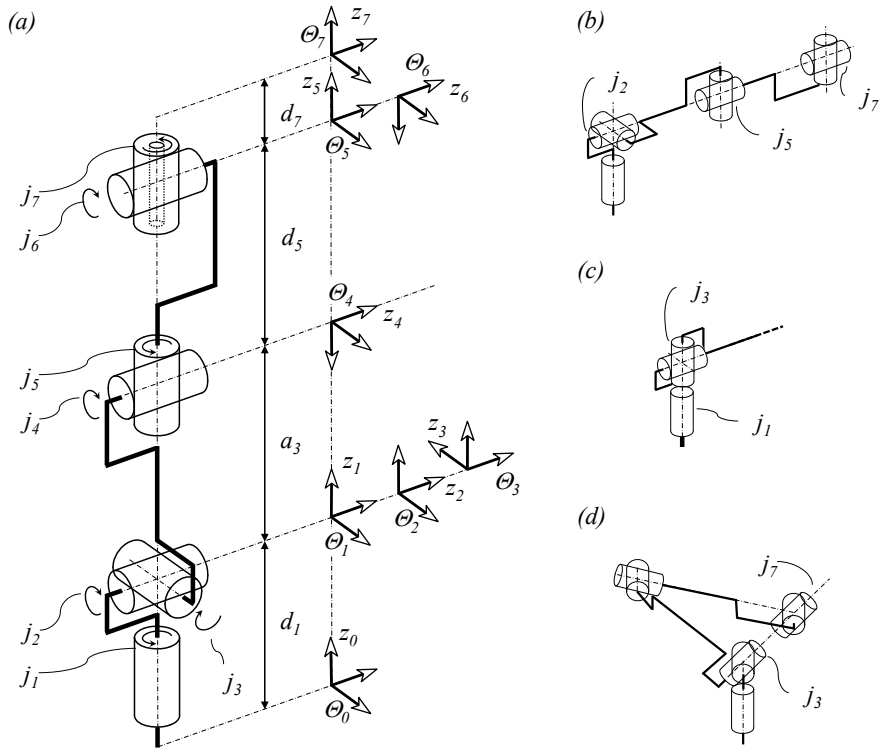

Figure 4.17: Kinematics of the *MIRO (a)*, additional poses with singularities *(b, c)*

Regarding these parameters it can be seen that besides the arbitrary parameters d_1 and d_7, only the lengths of the upper arm a_3 and of the forearm d_5 determine the kinematic lengths. Regarding the scaling of the *MIRO* for larger workspaces, these two parameters represent the sole variables.

Table 4.3 *(right)* determines all theoretical poses where two joints are aligned. Regarding tasks with six DoF and additional constraints (e.g. given pose of the TCP with an applied nullspace criterion for collision avoidance), these aligned joint pairs would represent singularities.

i	a_{i-1}	α_{i-1} [°]	d_i	Θ_0 [°]
1	0	0	d_1	0
2	0	- 90	0	- 90
3	0	90	0	0
4	a_3	- 90	0	90
5	0	90	d_5	0
6	0	- 90	0	0
7	0	90	d_7	0

	aligned joints	*compare figure*
1	$j_1 - j_5$	*4.17 (a)*
2	$j_1 - j_7$	*4.17 (a)*
3	$j_5 - j_7$	*4.17 (a)*
4	$j_2 - j_5$	*4.17 (b)*
5	$j_2 - j_7$	*4.17 (b)*
6	$j_1 - j_3$	*4.17 (c)*
7	$j_3 - j_7$	*4.17 (d)*

Table 4.3: DH-parameters of the *MIRO (left)* and singularities of the generic kinematic design regarding a 7-DoF task *(right)*

However, with respect to the joint motion limits, most of these configurations cannot be reached. The actual singularities of the *MIRO* have been analysed in the optimisation of links lengths and joint ranges, which is shown in section 4.6.

4.5 Mechatronic Concept

The mechatronic concept of the *MIRO* is described in this section from the view point of mechanical engineering. Therefore, it comprises the mechanical concepts of the joints, links, and housings, the selection of mechatronic components (e.g. motors, brakes), and the distribution of electronic components. In order to provide a comprehensive overview of the mechatronic concept of the *MIRO* and in conformity with the chosen design methodology *VDI 2206*, this section breaks down the mechatronic system to its most important hardware building blocks. After that, the selected technological solutions for these building blocks are described. As stated with the scaling paradigm in section 4.2, the selection of technologies for these building blocks cannot be derived from clear parameters of an application. Besides general performance measures, the solutions are selected due to their ability to be scaled and their compactness. For the convenience of the reader, technical solutions which are selected for the *MIRO* robot are indicated with a dash-outlined box in figures throughout the next sections. The description of the building blocks is followed by a section on the specification of performance parameters for a defined set of applications. Finally, the synthesis of the building blocks is described for the *MIRO*.

The surgical robotic system can be structured into the different abstraction levels shown in figure 4.18. Level 0 comprises the entire surgical robotics system. The *MIRO* robot is one instance of level 1, together with for example instruments or user interfaces. Level 2 distinguishes between the robot arm and external components, which are necessary to operate the arm (e.g. power supply, robot control). On level 3 the robot arm is partitioned in sub-modules, for example joint modules (e.g. $miro_{23}$, which is the joint module integrating joint 2 and 3) and level 4 lists the mechatronic building blocks of the sub-modules. The scope in this thesis is on levels 2 to 4, described in the following sections.

In order to form operable sub-components, the arm is modularised into joint modules ($miro_1$, $miro_{23}$, $miro_{45}$, $miro_{67}$)[7], base, TCP, and housing on level 3. This step already introduces a fundamental design decision. Mechanical designs which span the drive chain over multiple joint modules (e.g. tendon driven designs) in order to move actuators towards the robot base cannot be applied. In other words, all components which are necessary to drive the DoF of a joint module must be integrated into it (compare level 4 in figure 4.18). These components are referred to in the following as the building blocks of the joint modules. These building blocks differ from joint module to joint module regarding their size, performance, etc. However, it can be defined at this point that it is desirable to select a single, common technology for a building block, which is then only scaled for each joint module. For example, for

[7]The indices mark the joints integrated into the joint modules.

the selection of motors it is desirable to select one technology, which is then scaled for the different joint modules. The basic electronic design for each joint module can therefore remain and must only be scaled according to the associated motor. In other words it would increase the expense in electronic design to integrate two different motor technologies (e.g. brushless DC and piezo stepper motors).

The following sections comprehensively describe the different building blocks of the *MIRO*, their requirements, selection of technologies, and development of design concepts. The structuring of the next sections is based on the causal path of design decisions, starting with the most fundamental building blocks. Additionally, it must be noted that figure 4.18 is not an absolutely abstract depiction of the system. At this point already it comprises a number of decisions from the design phase (e.g. association of the forearm link to joint module $miro_{67}$).

4.5.1 Structure Design and Housings

One fundamental design issue for the *MIRO* is the choice of the structure design of the robot. Although housings and links are assigned to different modules (compare figure 4.18), they are both discussed in this section due to their dependencies. Integrated joint modules must be connected by links. Besides the function of carrying mechanical loads, these links have been identified as a valuable space for the integration of electronic components (compare section 4.3.5). To provide testing of components it is essential that the electronics cannot only be integrated, but also is accessible e.g. for test probes. Although this demand is worth discussing for a commercial product, it must be stated that the *MIRO* is firstly a research prototype. Integrating new electronic designs therefore demands accessibility to the electronic components during testing of single joints or the integrated robot arm. The following design targets can be formulated for the design of structural links and housing parts for the *MIRO*:

- lightweight and yet stiff structures
- compact and slender design
- ability to integrate electronic components
- accessibility of electronics
- encapsulation (e.g. covers) to provide easy-to-clean surfaces

The last demand directly derives from the requirements in an operating room. In addition to easy-to-clean housings, the *MIRO* will be covered by a sterile drape[8] in

[8] A sterile drape is a disposable, flexible polymer hose used to cover components (e.g. components with electronics), which cannot be (re-)sterilised by common methods like autoclavation, gamma radiation, ethylene oxide, or plasma sterilisation.

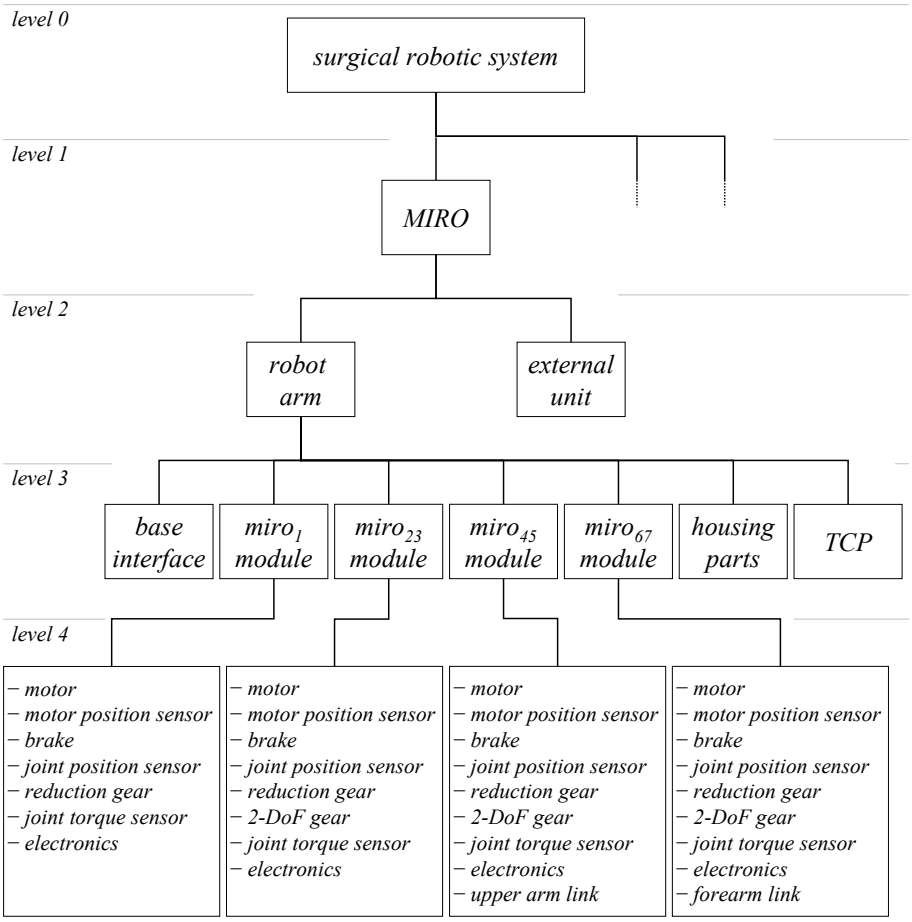

Figure 4.18: Modularisation levels of the *MIRO*

order to prevent contamination of the patient. For the link design of the *MIRO*, five different concepts have been considered, which are shown in figures 4.19 and 4.20 as cross-sections and spatial depictions, exemplarily for the forearm. These concepts are described in the following:

(1) The first concept, depicted in figure 4.19 *(a),* is based on a shell structure with a cutout for the integration of printed circuit boards (PCB). The link part forms the outer surface of the robot together with a similarly shaped cover. A C-shaped, open cross-section is extremely weak regarding torsion.
This can be seen by the ratio of the torsion constants (I_T) of a slit

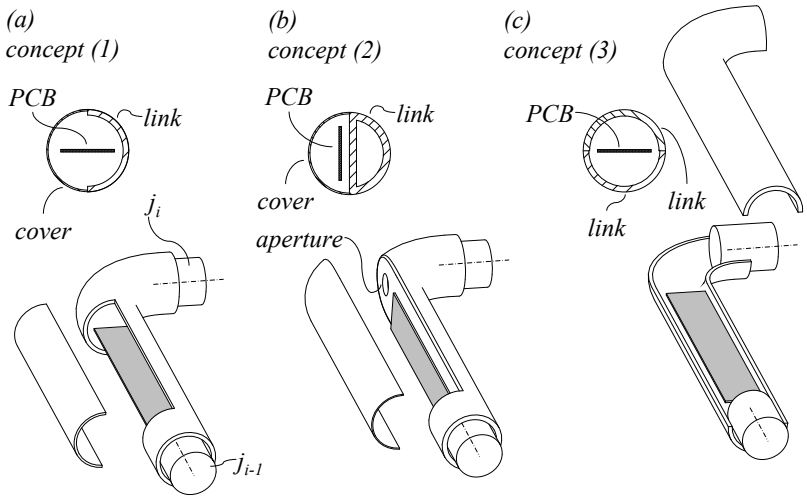

Figure 4.19: Structure design of the *MIRO*: concepts *(1)* to *(3)*

(I_{Ts}) and closed tubular cross-section (I_{Tc}) as defined by SCHNELL et al. [Schnell et al., 1992]:

$$\frac{I_{Ts}}{I_{Tc}} = \frac{1}{3} \cdot \left(\frac{t}{R_m} \right)^2 . \tag{4.3}$$

Regarding an assumed profile with a wall thickness of $t = 2\,mm$ and a radius $R_m = 30\,mm$ of the middle line of the wall, equation 4.3 results in a stiffness ratio of $\frac{I_{Ts}}{I_{Tc}} = 0.0015$. In other words, the closed ring tubular cross-section is 675 times stiffer then the slit version regarding torsion. Therefore, open cross-sections must be avoided.

(2) In order to avoid an open cross-section, the second concept applies a D-shape shell structure with the PCB mounted to the planar outside surface of the link, as shown in figure 4.19 *(b)*. In order to connect the PCB with the joints, an aperture in the shell structure is necessary to feed the cable harness through. It is assumed that this small aperture does not reduce the rigidity of the structure significantly. However, this concept limits the space for PCBs to one or a stack of two boards.

(3) Figure 4.19 *(c)* illustrates concept *(3)*. In order to increase the space for the integration of PCBs and their accessibility, this version utilises a split structure, which forms a tubular shell out of two half-shells. Regarding the relation of mass and moment of area, at the first glance this solution

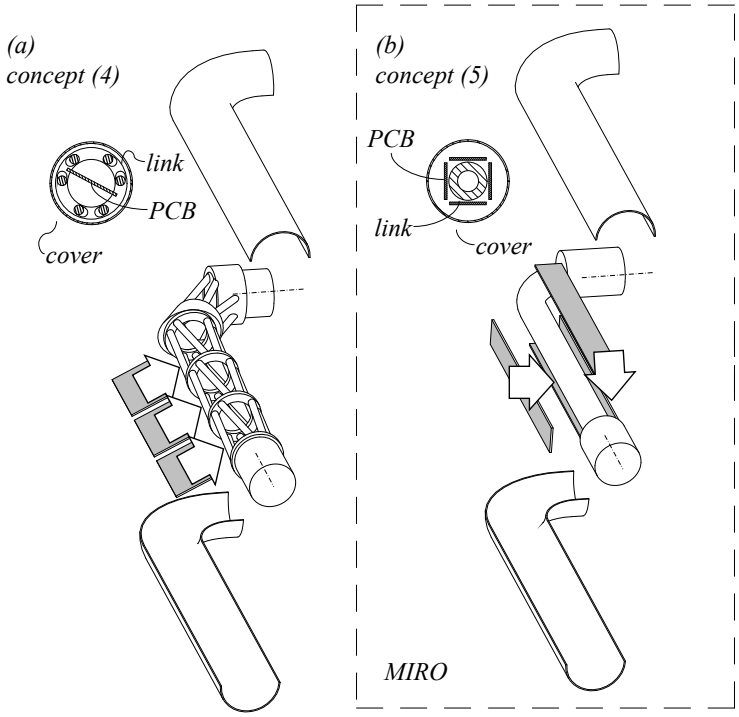

Figure 4.20: Structure design of the *MIRO*: concepts *(4)* and *(5)*

is superior. However, it must be noticed that the rigidity is limited by the connection of the two shell parts (e.g. form fit, bolting). Furthermore, the targeted rigidity is only available if both shells are assembled, but in this case the electronics are not accessible anymore.

(4) Inspired by the STEWART platform kinematics, concept *(4)* (compare figure 4.20 *(q)*) applies a spatial truss structure formed by rings connected by rods. As is apparent in the design of building cranes, this design facilitates a lightweight yet stiff design. It allows the integration of and the access to the PCBs through the spaces between the rods. However, in order to achieve high stiffness, elongated structures ($l \gg d$) must be composed of multiple truss modules. The fragmentation of the electronics then increases and therewith the total size of PCBs due to the necessity of additional electronic connectors interfacing the different PCBs.

(5) The last concept is inspired by the human anatomy itself. The skeletal structure is placed in the centre of the link in analogy to a bone, surrounded tangentially by PCBs (see figure 4.20 *(b)*). The housings have cover

functions and protect electronics and structure from collisions. Additionally, the housings can be designed in a compliant way in order to reduce the severity of impacts with the human. This approach is similar to the use of compliant, polymer cover parts in the cockpits of cars. Although this concept applies a closed cross-section structure, the moment of area is limited by the smaller outer diameter, as shown in appendix C.3. In order to increase the stiffness of the links, a material with high Young's and shear modulus must be selected. However, the possibilities of integrating electronics, their accessibility and the decoupling of structure, electronics, and cover design is superior to all other concepts. With dismounted covers, the rigidity of the link remains unchanged and the entire upper surface of the PCBs is accessible (e.g. for test probes).

The torsion constants of concepts *(2)*, *(3)*, and *(5)* are compared in appendix C.3, showing that $I_{T(2)} > I_{T(3)} > I_{T(5)}$. On the other hand, it can be stated that concept *(5)* shows advantages compared to the other concepts, regarding the scaling paradigm. A scaled version of the PCBs does not evoke changes of the link part, because the PCBs are placed on the outside. Only the covers have to be adapted. In contrast, concepts *(1)*, *(3)*, *(4)*, and partly *(2)* require modifications of the link design to comply with PCBs of other sizes. It can be stated that concept *(5)* largely decouples the design of PCBs and links.

The pros and cons of the concepts are summarised and rated[9] in table 4.4. The skeletal structure of concept *(5)* was chosen for the design of the *MIRO*, based on the advantages described above. However, concepts *(2)* and *(3)* appear as feasible solutions for a future version of the robot, where either the size of electronic components is further reduced or accessibility to the electronics plays a minor role.

structure design concepts	*(1)*	*(2)*	*(3)*	*(4)*	*(5)*
stiffness with covered electronics	−	+	+	+	0
stiffness with uncovered electronics	−	+	−	+	0
space for electronic components	+	0	+	−	+
unconstrained PCB design	0	0	0	−	+

Table 4.4: Rating of the structure design concepts

4.5.2 Single DoF Joint Design

As described in section 4.4.3 the *MIRO* kinematics comprises a single DoF rotary joint for axis one. It pivots $link_1$ about the joint axis of j_1 in relation to the base coordinate

[9] (+ = good, 0 = average, − = poor)

system Θ_0. The design of a single DoF rotary joint is state-of-the art in robotics. A motor is combined with a reduction gear in order to generate the necessary torque. Depending on the motor technology it is additionally equipped with a position sensor, which is needed, for example, with brush-less DC motors for commutation[10]. In order to hold the weight of the following links and joints when the robot is switched off or in case of emergency stops, a joint must be lockable. This can be achieved by the selection of a non-backdrivable reduction gear or by additional brakes. These brakes can be integrated on the joint (high-torque) or on the motor (high-speed) side. Due to the design paradigms 4 and 5 (compare sections 4.3.4 and 4.3.5) $miro_1$ must also integrate a joint-sided position sensor (jps) for the initialisation of the joint, a joint-sided torque sensor (jts), and the possibility of internal cable routing. Besides cables which pass the joint in order to interconnect the joints of the robot, additional cables are necessary to interface the joint-sided sensors of j_1 with its electronics in $link_0$. The electronics comprise all functions needed to actuate motors and brakes based on desired values, read sensor information, and transmit these data to the external robot control components.

This section describes the concepts for the composition of the $miro_1$ module, which comprises the building blocks depicted in figure 4.18. Several basic design decisions regarding the composition can be formulated here:

- To reduce the inertia of the actuated $link_1$, the motor should be integrated in $link_0$.
- Carrying the whole load of the robot, a direct drive (no reduction gear) principle is not feasible.
- If the reduction gear is assumed to be backdrivable, a brake must be integrated for emergency stop and power-off. To reduce the size of the brake, it is integrated on the high-speed (motor) side of the drive chain.
- The length of cables with analogue signals should be short (EMC), moving cables with EMC-relevant signals (e.g. PWM for the motors and brakes) should be avoided.

Three feasible concepts were considered for the design of $miro_1$, which are shown in figure 4.21. All concepts do have in common that the electronics $elec_1$ of $miro_1$ is located in $link_0$ in order to keep the EMC-relevant cabling for the motor and the brakes short and to avoid their conduction through moving parts. Furthermore, regarding the joint-sided sensors (jts_1, jps_1) the requirement of short analogue cabling demands a digital transmission of these sensor values to the joint electronics. In this

[10]Generating currents or voltages to the proper electrical motor phases is called commutation.

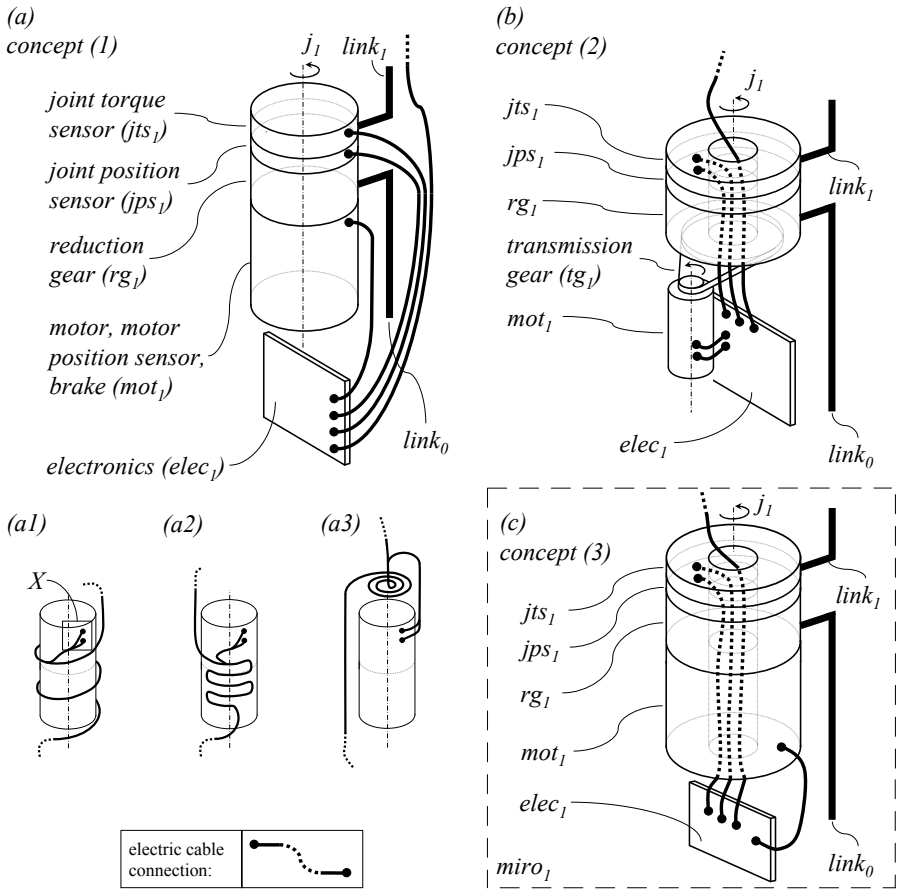

Figure 4.21: Three valid concepts for the design of the $miro_1$ module *(a-c)*, three concepts for an external cable conduit *(a1-a3)*

sense, jts_1 and jps_1 integrate electronic components, which at least amplify and digitise the sensor signal. All three concepts already fulfil the design paradigms 4 (sensor integration) and 5 (integrated electronics and internal cabling) and are rated according to the scaling paradigm, and the design paradigms 1 (lightweight) and 2 (compact, slender design). These concepts are described in the following:

(1) The goal of this concept is to use simple standard components. In order to achieve a compact and slender design, a coaxial composition of the components is chosen, as depicted in figure 4.21 *(a)*. Motor, motor position sensor, and brake form the module mot_1, which is integrated into $link_0$ along with the joint electronics ($elec_1$). The reduction gear (rg_1) connects the high-speed side to the high-torque side of the joint. The joint posi-

tion (jps_1) and joint torque (jts_1) sensor connect the reduction gear with $link_1$. All components do not integrate hollow shafts. The cable harness (indicated by black lines with bullet ends) must therefore be conducted on the outside of the joint (covered by additional housings). The major advantage of this concept is that it does not require hollow shafts for the components and, therefore, offers a big range of applicable components. In this sense, concept *(1)* is superior to the other concepts regarding the scaling paradigm. However, the cable conduit implies a smaller diameter of the building blocks (e.g. motor, gears, and bearings) than with the other concepts, because of the necessary space for the cable harness on the outside. This is critical, because the diameters of motors, brakes, bearings, etc. have a major (non-linear) influence on the maximum torque and stiffness of the components. A detailed derivation of this correlation is shown in appendix C.4.
Three possible configurations for the cable conduit are depicted in figure 4.21 *(a1-a3)*: a spiral coil, a meander, and a flat spiral configuration. All solutions require a significant cable length in order to provide the joint with a large motion range. Therefore, the cables move significantly and need additional guidance components (e.g. anti-kink devices) in order to guarantee a minimum bending radius. Additionally, the cables for the joint-sided sensors (jts_1, jps_1) are connected to the outside of the sensors (compare area *X* in figure *4.21 (a1)*). But this area comprises the high-torque side of the gear and the joint bearing connecting $link_0$ and $link_1$ (not depicted), which makes a radial aperture for the cables difficult.

(2) The second concept applies both standard and hollow shaft components (compare figure 4.21 *(b)*). The mot_1 module is connected to the reduction gear by means of a transmission gear (tg_1). Figure 4.21 *(b)* depicts a belt transmission for this purpose. However, other principles like a spur gear are also feasible. The reduction gear (rg_1), joint position (jps_1), and joint torque sensor (jts_1) utilise a hollow shaft design for the cable conduit. Here, the conduit of the cable harness is shifted to the inside of the joint, which simplifies the cable conduit. Additionally, it enables larger diameters for the reduction gear. The additional transmission gear allows for an adaptation of the torque/speed ratio of the joint additionally to the ratio of the reduction gear. However, the outside diameter of the motor and brake is restricted by the two diameters of the transmission gear and the outside diameter of module $miro_1$. In order to increase the torque of the motor, only its length can be altered. As analysed in appendix C.4,

the maximum torque of motors and brakes only scales linearly with their length but more or less with the square of the diameter.

(3) Figure 4.21 *(c)* depicts the third solution, which is based on the concept of the *DLR LWR* joint modules. It incorporates only hollow shaft building blocks which allow for a complete internal cable routing. Therefore, all components can have a maximum diameter and are only limited by the outside diameter of the joint module. The hollow shaft requirement limits the amount of available components. However, the later sections on reduction gears (4.5.4) and motors (4.5.6) show that the scaling paradigm is not violated by this concept. Also, like concept *(2)* this approach provokes only little motion on a cable harness, compared to concept *(1)*, avoiding significant cable loops.

The pros and cons of the concepts are summarised in table 4.5. The *MIRO* applies concept *(3)* for the joint module $miro_1$, because of the higher torque capacity, the simplified cable conduit and due to the selected hollow shaft reduction gear as well as motor technologies described in the later sections 4.5.4 and 4.5.6.

single DoF joint concepts for $miro_1$	*(1)*	*(2)*	*(3)*
scaling paradigm	+	0	0
torque / size ratio	0	0	+
simplicity of cable conduit	0	+	+

Table 4.5: Rating of the design concepts for $miro_1$

4.5.3 2-DoF Joints

According to section 4.4.3, the *MIRO* integrates 2-DoF joint modules for the shoulder (pitch-yaw), elbow (pitch-roll), and wrist (pitch-roll with hollow shaft). Besides a sequence of two separate single DoF joints as depicted in figure 4.13 of section 4.4.2, such joint modules can be implemented by so-called coupled joints. In the scope of this thesis, coupled joints provide two DoF motion, integrating both motors on the base side of the joint. Coupled joints date back to the beginning of robotics, where the integration of motors and electronics into the robot arm was a major challenge due to the low power/weight ratio of these components. Early robotics deriving from the pure telemanipulation concept therefore shifted as many of these components as possible towards the base of the robot. The torques of the motors were then transmitted to the joints, for example, by rotating shafts, tendons or belt drives.

In order to conduct these torques through a joint j_i to the next joint j_{i+1}, many different mechanisms have been developed [Rosheim, 1989]. These mechanisms try to

- avoid the influence of the motion of j_i on the drive chain of j_{i+1} (e.g. conducting a rotary motion through a pitch-yaw wrist by means of a cardan shaft [Lande and David, 1980]),
- accept the coupling of drive chains and compensate the influence by calculation and control (e.g. conducting a rotary motion through a rotary hollow shaft joint by means of a coaxial rotating shaft), or
- combine the torque of multiple drive chains to drive multi-DoF joints based on differential mechanisms (e.g. pitch-yaw joint based on differential bevel gear [Devol, 1970]).

In contrast, today's technologies allow for the integration of motors and electronics in all joints of a robot. However, these concepts provide significant advantages for the design of 2-DoF joints for the *MIRO* such as:

- reduction of the number of electronic components, cables, and sensors
- compact design
- unlocking synergistic effects regarding the motors, brakes, and gears

These benefits are shown and exemplified in the next sections on the concepts for 2-DoF joint designs for the *MIRO*. Firstly, section 4.5.3.1 derives different coupling mechanisms and develops the design of the $miro_{23}$ joint module. Secondly, the analysed coupling mechanism concepts are adapted for $miro_{45}$ (section 4.5.3.2) and $miro_{67}$ (section 4.5.3.3).

4.5.3.1 Pitch-Yaw Shoulder Concept

As defined in section 4.4.2 the shoulder of the *MIRO* consists of three orthogonal intersecting rotary DoF (j_1, j_2, j_3), provided by the single DoF joint module $miro_1$ (compare section 4.5.2) and a 2-DoF joint module $miro_{23}$. It inclines the upper arm ($link_3$) about the joint axis j_2 and j_3 in relation to $link_1$. In order to drive two DoF two motors are combined with reduction gears to generate the necessary torque and additional gears in order to provide the coupling. Like the $miro_1$ the motors are equipped additionally with position sensors and, in the case of backdrivable joints, with additional motor-sided brakes. According to the design paradigms 4 and 5 (compare sections 4.3.4 and 4.3.5) $miro_{23}$ must integrate joint-sided position sensors and the possibility of integrated cable routing. Like in the preceding chapter, several basic design decisions regarding the composition can be formulated at this point:

- To reduce the inertia of the actuated $link_2$ and $link_3$, both motors should be mounted to $link_1$
- Carrying the weight of a significant portion of the robot and the whole payload, a direct drive (no reduction gear) principle is not feasible
- If the reduction gears are assumed to be backdrivable, brakes must be integrated for emergency stop and power-off
- To reduce the size of the brakes, it is integrated on the high-speed (motor-) side of the drive chain
- The electronics of $miro_{23}$ is mounted to $link_1$ in order to provide short cabling of EMC-relevant signals (e.g. PWM for the motors) and to avoid conducting such cables through moving parts

The demand for compact design needs further interpretation for the $miro_{23}$ module. Among other aims, design paradigm 2 (slender and compact design) aims for a maximum integration of multiple arms on a small footprint. In order to achieve this, the overall size of the robot must be small. Additionally, a small motion envelope of the robot is beneficial in order to avoid collisions. Therefore, design paradigm 2 applies not only to the dimensions and shape of the robot components, but also to their required space when the robot is moving. This aspect is targeted with the term *compact* and can be exemplified with the *LWR III* robot, which has been chosen as a starting point for the *MIRO*. Figure 4.22 *(a)* depicts the roll-pitch shoulder of the *DLR LWR* and the motion envelope (shaded area) due to a rotation about j_1, which is derived from the non-symmetrical design of j_2 in relation to the axis of j_1. Figure 4.22 *(b)* shows the same information for the roll-pitch-yaw wrist of the *DLR LWR*. Due to the more or less rotation-symmetric design of $link_6$ in relation to the axis of j_5, the motion envelope is smaller and more compact. Besides the reduction of the overall size, this effect can be increased with the concept depicted in figure 4.22 *(c)*, where the motion envelope is identical with the robot. This is achieved by the limitation of applied shapes to cylinders and spheres. The design of $miro_{23}$ is therefore targeted at this concept, integrating a spherical, compact geometry.

The following description of different concepts is separated into two steps, starting with the basic concepts of coupling mechanisms (Roman numerals), followed by a more detailed view on the selected concepts (Arabic numerals). The basic idea behind the coupling mechanism is to shift components from $link_2$ towards the stationary link of the joint ($link_1$). This way, the number of PCBs can also be reduced, because components can be shared (e.g. voltage converters or communication nodes). Thereby a more compact design is possible. The derivation of the concepts starts with a serial

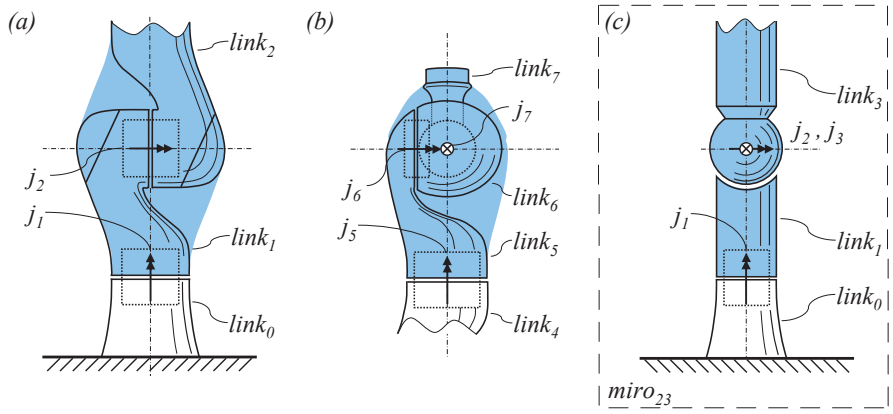

Figure 4.22: Motion envelope of the *DLR LWR* shoulder due to rotation about the axis of j_1 *(a)* and wrist due to a rotation of j_5 *(b)*. Abstracted roll-pitch-yaw shoulder based on a compact, spherical design *(c)*

configuration of two rotary joints (compare figure 4.23 *(a)*), which are similar to the design of $miro_1$. Then, step by step (compare figure 4.23 *(b-d)*), components of j_3 are shifted to the stationary $link_1$. The motor, motor position sensor, and brake are merged into a module mot_i in order to enable testing of integrated modules and to simplify the descriptions. Four different coupling mechanisms *(I-IV)* were analysed:

(I) As described above, concept *(I)* integrates a serial configuration of two single-DoF joints with orthogonal intersecting axes as depicted in figure 4.23 *(a)*. This configuration is state-of-the-art in robotics, for example, in the wrist joints of the *DLR LWR* (compare figure 4.22 *(b)*). Due to the design decision to avoid EMC-relevant cabling (e.g. motor-PWM) through other joints, both joints integrate more or less complete sets of dedicated electronics. For j_3 these electronics must therefore be integrated into $link_2$, next to the mot_3 module[11]. The required space for the electronics and the necessary accessibility still hinder the attainment of the desired goal of the most compact design (compare figure 4.22 *(c)*). The calculation of the joint velocities $\dot{q}_i$ and torques τ_i according to the motor speeds $\dot{q}_{mot_i}$ and torques τ_{mot_i} is trivial[12] and given with the equations 4.4 and 4.5:

$$\begin{pmatrix} \dot{q}_2 \\ \dot{q}_3 \end{pmatrix} = \begin{pmatrix} ratio_{rg_2} & 0 \\ 0 & ratio_{rg_3} \end{pmatrix} \begin{pmatrix} \dot{q}_{mot_2} \\ \dot{q}_{mot_3} \end{pmatrix} , \tag{4.4}$$

[11] It is possible to reverse j_3 in a way that the motor side is located towards $link_3$ and therewith the electronics of j_3 can be integrated in $link_3$. However, such design would add the mass of motor, brake, and electronics to the joint inertia and is not seen as good design practise.

[12] The reduction ratio of a gear is defined as $ratio_{rg_i} = \frac{joint\,revolutions}{motor\,revolutions}$.

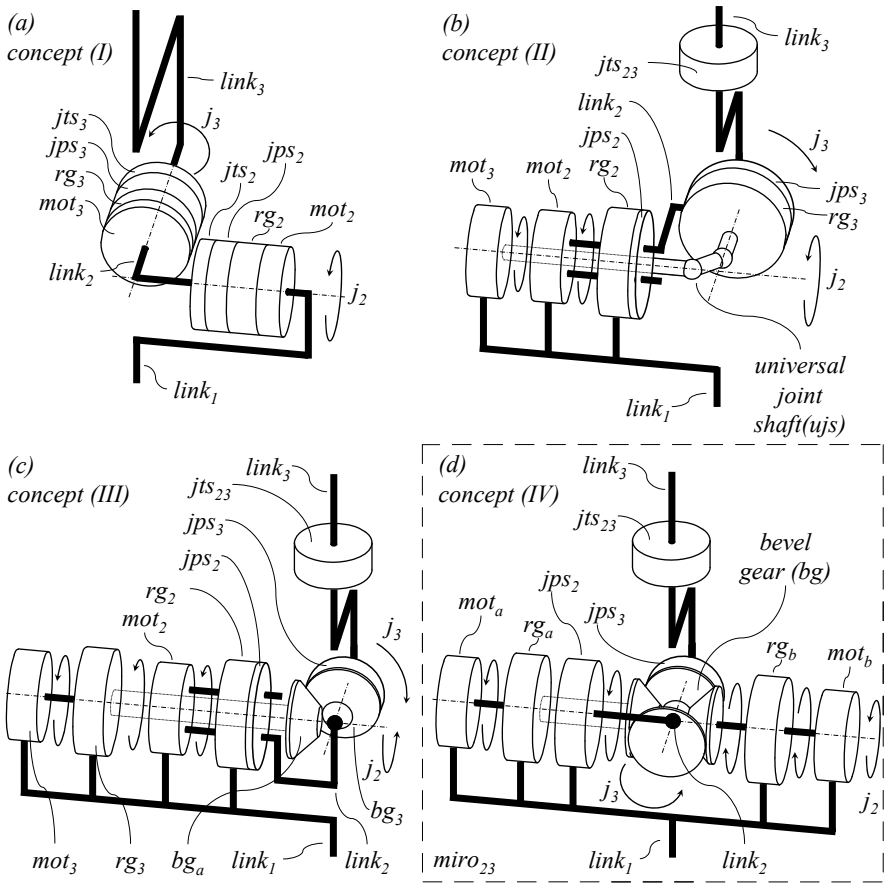

Figure 4.23: Basic concepts of pitch-yaw coupling mechanisms

$$\begin{pmatrix} \tau_2 \\ \tau_3 \end{pmatrix} = \begin{pmatrix} ratio_{rg_2}^{-1} & 0 \\ 0 & ratio_{rg_3}^{-1} \end{pmatrix} \begin{pmatrix} \tau_{mot_2} \\ \tau_{mot_3} \end{pmatrix} . \tag{4.5}$$

(II) In the first step, concept *(II)* (see figure 4.23 *(b)*) moves the motor module mot_3 from $link_2$ to $link_1$. Motor module mot_2 and reduction gear rg_2 stay in place at $link_1$. The motor torque of module mot_3 is transmitted to the reduction gear rg_3, through a hollow shaft design of mot_2 and rg_2 by a universal joint shaft (ujs[13]). The reduction gear rg_3 and the joint position sensor jps_3 remain in $link_2$. By this concept, the motor torque/ position of mot_3 is coupled with the torque/ position of j_2. Therefore, the joint torque sensor jts_2 of j_2 cannot remain where it is in concept *(I)*, because

[13] A universal joint shaft consists of three rotary shafts connected by two universal (cardan) joints. It allows, for example, the transmission of rotary motion between two orthogonal axes.

it would not measure the torque of j_2 alone, but the sum of τ_2 and τ_{mot_3}. Regarding the high frequencies of a motor motion, this must be avoided. Therefore, the joint torques of concept *(II)* are measured by a multi-axis, combined joint torque sensor jts_{23} integrated in $link_3$. In this sense, the sensor measures multiple loads in the structure of the robot. This is a major difference compared to the classic joint arrangement, because the loads applied to this sensor cannot be limited purely to the joint torque as is possible with concept *(I)*. The joint velocities $\dot{q}_i$ and torques τ_i according to the motor velocities $\dot{q}_{mot_i}$ and torques τ_{mot_i} can be calculated with equations 4.7 and 4.6:

$$\begin{pmatrix} \dot{q}_2 \\ \dot{q}_3 \end{pmatrix} = \begin{pmatrix} ratio_{rg_2} & 0 \\ ratio_{rg_2} \cdot ratio_{rg_3} & ratio_{rg_3} \end{pmatrix} \begin{pmatrix} \dot{q}_{mot_2} \\ \dot{q}_{mot_3} \end{pmatrix} , \tag{4.6}$$

$$\begin{pmatrix} \tau_2 \\ \tau_3 \end{pmatrix} = \begin{pmatrix} ratio_{rg_2}^{-1} & -1 \\ 0 & ratio_{rg_3}^{-1} \end{pmatrix} \begin{pmatrix} \tau_{mot_2} \\ \tau_{mot_3} \end{pmatrix} . \tag{4.7}$$

(III) Based on the approach shown above, concept *(III)* (figure 4.23 *(c)*) additionally shifts the reduction gear rg_3 to the static $link_1$. The speed of mot_3 is reduced by rg_3 and transmitted through a hollow shaft design of the other components (j_2) to a 2-part bevel gear (bg), which is introduced as an alternative to the universal joint shaft (ujs). The bevel gear is assumed to offer two advantages compared to the ujs: it allows the transmission of higher torques and a hollow shaft design for the cable conduit. As shown later in this section, the bevel gear is more compact than the corresponding reduction gear rg_3 in concept *(II)* and, therefore, allows for a more compact design of $link_2$. The bevel gears are mounted to $link_2$ pivoted about their rotation axis, indicated by the bullet at one end of the abstracted $link_2$. It is important to notice that the depicted bevel gear is only an abstraction and that it can be implemented in different ways (e.g. gearing, friction, tendons).

Only the joint position sensor jps_2 remains within $link_2$ as it is determined to measure the joint angle directly without the influence of coupling. With this concept a very compact design of $link_2$ can be achieved. As a drawback, joint j_2 also supports the whole torque of j_3, which can be derived from the coupling equations (compare equations 4.8 and 4.9). This concept would always result in oversized j_2 components and is only feasible for applications where $\tau_2 \gg \tau_3$ is desired and the most compact design is necessary. The joint velocities $\dot{q}_i$ and torques τ_i according to

the motor velocities $\dot{q}_{mot_i}$ and torques τ_{mot_i} can be calculated with the following equations:

$$\begin{pmatrix} \dot{q}_2 \\ \dot{q}_3 \end{pmatrix} = \begin{pmatrix} ratio_{rg_2} & 0 \\ ratio_{rg_2} & -ratio_{rg_3} \end{pmatrix} \begin{pmatrix} \dot{q}_{mot_2} \\ \dot{q}_{mot_3} \end{pmatrix} , \tag{4.8}$$

$$\begin{pmatrix} \tau_2 \\ \tau_3 \end{pmatrix} = \begin{pmatrix} ratio_{rg_2}^{-1} & ratio_{rg_3}^{-1} \\ 0 & -ratio_{rg_3}^{-1} \end{pmatrix} \begin{pmatrix} \tau_{mot_2} \\ \tau_{mot_3} \end{pmatrix} . \tag{4.9}$$

(IV) Concept *(IV)* is inspired by the base joint of the *DLR HAND II* [Butterfass, 2000]. It integrates a 4-part bevel gear with all pinions pivoted in $link_2$ as depicted in figure 4.23 *(d)*. Two pinions are connected to the reduction gears rg_a and rg_b and one pinion is connected to $link_3$. The fourth pinion is redundant and can be left out. This differential coupling results in the fact that the motions of the joints j_2 and j_3 cannot be assigned to dedicated motors and gears anymore. Therefore, the drive components are distinguished by the indicators a and b.

Assuming the same reduction ratio for rg_a and rg_b, with both motor modules mot_a and mot_b (and therewith rg_a and rg_b) rotating in the same direction and speed, the pinions of the bevel gear do not mesh with each other and behave like a solid block. This leads to an exclusive rotation of $link_2$ (and therefore $link_3$) about the axis of j_2. In contrast, if the motors rotate at the same speed, but in opposite directions, this results in an exclusive rotation of $link_3$ about the axis of j_3. Regarding the coupling mathematics for joint velocities $\dot{q}_i$ and torques τ_i (see equations 4.10 and 4.11 [Butterfass, 2000]), for example, the joint torque τ_2 of j_2 is generated by the sum of both reduction gear torques, if τ_3 is zero. This applies in the reverse to the other DoF. The joint velocities $\dot{q}_i$ and torques τ_i for this concept calculate as follows:

$$\begin{pmatrix} \dot{q}_2 \\ \dot{q}_3 \end{pmatrix} = \begin{pmatrix} \frac{1}{2} \cdot ratio_{rg_a} & \frac{1}{2} \cdot ratio_{rg_b} \\ -\frac{1}{2} \cdot ratio_{rg_a} & \frac{1}{2} \cdot ratio_{rg_b} \end{pmatrix} \begin{pmatrix} \dot{q}_{mot_a} \\ \dot{q}_{mot_b} \end{pmatrix} , \tag{4.10}$$

$$\begin{pmatrix} \tau_2 \\ \tau_3 \end{pmatrix} = \begin{pmatrix} ratio_{rg_a}^{-1} & ratio_{rg_b}^{-1} \\ -ratio_{rg_a}^{-1} & ratio_{rg_b}^{-1} \end{pmatrix} \begin{pmatrix} \tau_{mot_a} \\ \tau_{mot_b} \end{pmatrix} . \tag{4.11}$$

In order to simplify the interpretation of the coupling equations, figure 4.24 illustrates these correlations graphically for all concepts. For this comparison identical motors and reduction gear ratios ($ratio_{rg_i}$) for all concepts and DoF are assumed. The range of joint velocities $\dot{q}_i$ based on the motor velocities $\dot{q}_{mot_i}$ are depicted in figure 4.24 *(a)*.

Figure 4.24 *(b)* depicts the analogous correlation for the joint torques τ_i according to the motor torques τ_{mot_i}. The graphs for concepts *(I)* and *(IV)* in figure 4.24 *(a)* and *(b)* are adapted from BUTTERFASS [Butterfass, 2000].

Concept *(I)* allocates for both DoF independently the maximum speed ($\dot{q}_{mot_{i\,,\,max}} \cdot ratio_{rg_i}$) and maximum torque ($\tau_{mot_{i\,,\,max}} \cdot ratio_{rg_i}^{-1}$). In contrast, concepts *(II)* to *(IV)* show that these parameters are always affected by both joints. Regarding concept *(II)* it is apparent that it differs only minor from concept *(I)*. Depending on the direction of rotation, minor speeds or torques are either subtracted from or added to the maximum torques and speeds. This derives from the fact that only the motor mot_3 has been shifted from $link_2$ to $link_1$.

In contrast, concept *(III)* shows the impact of moving additionally the reduction gear rg_3 to $link_1$. When both joints rotate in positive or negative direction, the torques of both motor-gear units add up. In contrast, if the joints rotate in opposite direction, the joint torques are reduced significantly. This applies in an inverted way to the correlation of motor and joint speeds.

Concept *(IV)* creates symmetrical speed and torque ranges due to the differential bevel gear and the symmetric design. Regarding the achievable joint torques it is striking that this concept provides a larger torque range than concept *(I)*. As stated above, this design doubles the maximum torque of one joint, if the torque of the other joint is zero. In contrast, the maximum joint speed of one joint can only reach those of concept *(I)* if the speed of the other joint is again zero. Concept *(IV)* can be seen therefore as an additional reduction gear (speed reducer). In contrast to the other coupling mechanisms, concept *(IV)* is independent of the motion direction of the joints.

Figure 4.24 *(c)* and *(d)* depict the inscribed ranges, if the maximum joint torque/ speed of both joints is demanded independently. It is common sense that these ranges need not to be necessarily square-shaped ($\tau_{2,max} \neq \tau_{3,max}$).

As a conclusion on these results, it can be stated that concept *(II)* has similar performance characteristics as concept *(I)*. Concept *(III)* additionally moves the reduction gear rg_3 to the stationary link and enables thereby the most compact design of $link_2$ of all concepts. It will be shown in the later section 4.5.3.3 that this concept fits perfectly for the wrist design of the *MIRO*.

However, concept *(III)* is not feasible for the shoulder joint of the *MIRO*, due to the substantially smaller range of torques and speeds compared to concept *(IV)*. Concept *(IV)* reduces the size of $link_2$ significantly compared to concept *(I)* by avoiding electronic components in $link_2$. There, the differential mechanism integrates another speed reduction.

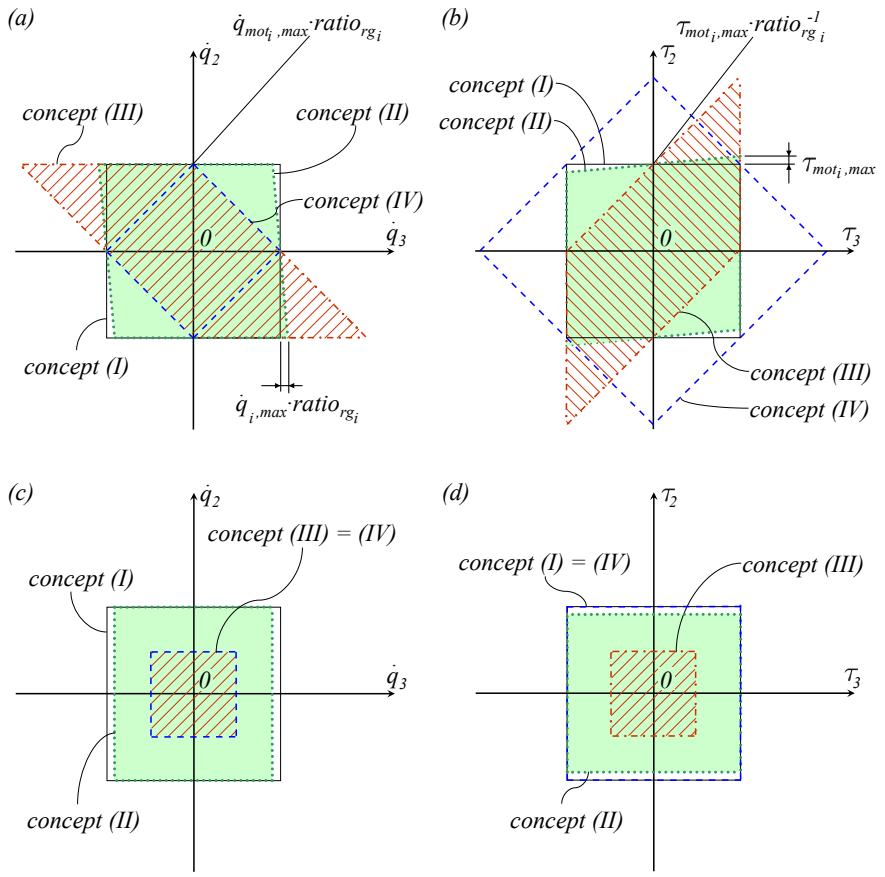

Figure 4.24: Graphical representation of joint velocity *(a)* and torque ranges *(b)* for the pitch-yaw shoulder concepts. This representation is based on identical motors and reduction gears for all concepts and DoF. The ranges for concept *(I)* and concept *(IV)* are depicted by outlines, concept *(II)* by outline and shading, concept *(III)* by outline and hatching. Graphs *(c)* and *(d)* depict the available joint velocity and torque ranges for the different concepts, if no dependency between j_2 and j_3 is desired. Adapted partially from Butterfass [Butterfass, 2000]

According to the findings, concept *(IV)* is suited for joints where one of the two DoF continuously demands a higher load or speed than the other DoF. Here, torque ranges beyond the limits of concept *(I)* can be explored. However, this design does not determine which of the two DoF applies the higher loads and leaves this decision accessible and configurable even during operation of the robot. Regarding the assumed basic arm configurations defined in section 4.4.2 (compare figure 4.12), this characteristic appears to be extremely beneficial for the vertical upright and the wall-mounted (horizontal) configuration. In these given configurations, one of the pitch-yaw DoF of

the shoulder holds most of the weight of the following joints and links. For this requirement, concept *(I)* would be modified with a more powerful motor and gear for this predominant DoF. In contrast, this can be achieved with concept *(IV)* by common parts for both motors and gears. By shifting motors, brakes and reduction gears to $link_1$ and due to the fact that the maximum torques and speeds of the two DoF can be adapted by common parts, this concept accords with the scaling paradigm.

The $miro_{23}$ module applies the differential coupling mechanism *(IV)* due to the advantages described above regarding explorable torque ranges and because of the assumed compact dimensions of this joint design. The rating of the different concepts is summarised in table 4.6.

coupling mechanism concepts for $miro_{23}$	*(I)*	*(II)*	*(III)*	*(IV)*
compactness of $link_2$	−	0	+	0
scaling paradigm	−	0	+	+
symmetry of transmission	+	0	−	+
torque range	+	0	−	+
velocity range	+	0	+	−

Table 4.6: Rating of the coupling mechanism concepts for $miro_{23}$

The following paragraphs describe the two design concepts (Arabic numerals) for $miro_{23}$, which evolved from the selected coupling mechanism *(IV)*, differing mainly in the transmission principle of the bevel gears and the distribution of the drive components in $link_1$. From this point on, the level of detail of the concepts presented is too high to be shown in the isometric way applied in the preceding illustrations. Therefore, all following sections in this chapter additionally also apply the technical drafting style common in mechanical engineering. The mechanisms are thereby depicted in one or multiple planar views, which correspond to each other according to the first angle projection ([DIN 6-1, 1986]). Additionally, in the following illustrations the components (e.g. motors, gears) are depicted in their actual shape and size in the design of the *MIRO*. Two different mechanical concepts *(1, 2)* for $miro_{23}$ are shown in the following:

(1) Grebenstein introduced a tendon-driven pitch-yaw joint based on the coupling mechanism concept *(IV)* [Grebenstein, 2005].
This in-house concept groups the components of the 2-DoF joint in two layers as depicted in figure 4.25 *(a)* in order to comply with the desired compact design of $miro_{23}$. The lower layer which is connected to $miro_1$ integrates the motor modules mot_a, mot_b, the reduction gears rg_a, rg_b, and conical pinions pin_a, pin_b (all depicted as solid bodies and therefore

not sketched as cross-sections). This layer therefore comprises all components for generating the torque of the robot joint.
The upper layer integrates two pinions (pin_{def-a} and pin_{def-b}), which are pivoted about a shaft, which is fixed to $link_1$. Additionally, $link_2$ can pivot about this shaft, which represents j_2. Two additional conical pinions (pin_{23} and pin_{free}) are pivoted on $link_2$. Pinion pin_{23} is connected by an arc-shaped stirrup to the joint torque sensor jts_{23} and thereby to $link_3$. The rotation axis of pin_{23} is represented by j_3. In order to avoid collisions, the size and shape of the stirrup are determined by a sphere, indicated with the dashed outline in figure 4.25 *(a)*. As a result of this cardan design, $link_3$ can pivot about j_2 and j_3. To actuate the two DoF, concept *(1)* applies tendons. These tendons (e.g. steel cables) are connected with their terminals with one end to pin_a or pin_b. The other end is connected to pin_{23} or pin_{free}. The two remaining pinions pin_{def-a} and pin_{def-b} serve only to deflect the tendons.
As with the example depicted in figure 4.25, tendon u terminates at one end at pin_a, then loops around pin_{def-a} and then terminates at pin_{23}. In contrast, tendon v also terminates at pin_a and is looped around pin_{def-a}, but then terminates at pin_{free}. This cross-assignment applies in reverse for cables x and w. If the motors rotate in the same direction, for example, only the tendons u and w transmit a force to pin_{23}, which results in a torque about j_2. Additionally, u and w form an equilibrium on pin_{23}, preventing a torque about j_3. If the motors rotate in opposite directions, for example, only the tendons x and u transmit forces. In this case tendon u directly evokes a torque on pin_{23} about j_3. Additionally, tendon x evokes a torque on the free-running pinion pin_{free}, which alone would not result in a torque about j_3. But pin_{free} is connected to mot_a by tendon v, which therefore transmits the torque of pin_{free} to mot_a and thereby supports the torque of this motor. In order to simplify the understanding of this complex coupling mechanism, figures 4.25 *(b)* and *(c)* depict isometric, abstracted views of the concept. Figure 4.25 *(b)* depicts the involved tendons u and w for a rotation about j_2 and figure 4.25 *(c)* the involved tendons u, w, x for a rotation about j_3 (F_{mot_i} is defined as the force on the tendon evoked by mot_i). With four tendons both rotation directions about both joint axes can be actuated. The joint position sensors jps_2 and jps_3 are integrated in places where the relative motion between $link_1$ and $link_2$, as well as $link_2$ and $link_3$ can be captured directly.As defined with the coupling mechanism concept *(IV)*, design concept *(1)* therefore

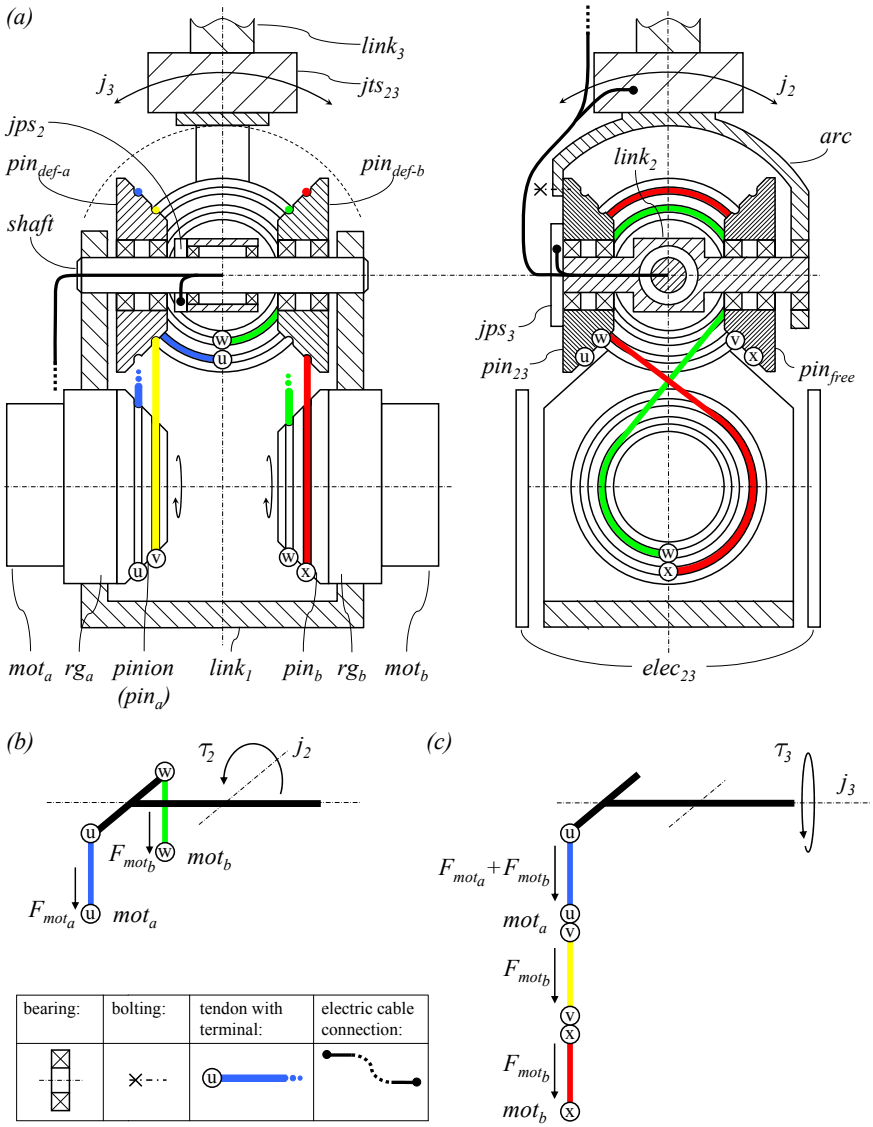

Figure 4.25: The $miro_{23}$ design concept *(1)*: two cross-section views of the tendon driven differential concept *(a)*, rotation about j_2 *(b)*, rotation about j_3 *(c)*

adds the torques of both motors for j_2 or j_3, when one torque of these DoF is zero. This concept enables an inherent backlash-free differential gear if adequate pretensioning of the tendons is guaranteed and has been patented in Germany [Grebenstein, 2005]. Due to the independent mo-

tion capabilities of the joint-sided pinions, the cables do not glide on the pinions and the friction of the joint assembly results only from the bearings. However, the tendons are guided on different diameters of pinions (cp. tendons u and w in figure 4.25 *(a)*) and must therefore withstand different loads. In order to avoid this asymmetry the prototype of this joint (compare section 4.7) doubles the number of tendons. Then, every tendon pair loops about the same average diameter.
A prototypical implementation of this concept (compare appendix D.1) showed certain disadvantages. A cable conduit on the outside of the joint in the form as shown with the concept of $miro_1$ (compare figure 4.21 *(a1-a3)* in section 4.5.2) is not feasible for $miro_{23}$ due to the combined motion ranges of both joints and the resulting length of a cable loop. Additionally, an external cable loop would be difficult regarding the design of housings. One possible path for an internal cable conduit is indicated in figure 4.25 *(a)*. *Shaft* and $link_2$ must therefore be designed as hollow shafts (not depicted). However, the relative motion between *shaft* and $link_2$ makes this approach difficult. Furthermore, this does not really enhance the design of the housings, because of the tendons between $link_1$ and $link_2$, which hinder a separate encapsulation of both links. Additionally, the motion range of this concept is limited by the contact arc of the tendons on pin_{23}, pin_{free} (e.g. $\pm 45°$ for j_3), which is further reduced by the size of the tendon terminals. Furthermore, the recurring readjustment of the tendon tensions due to creeping of the tendons and the overall stiffness turned out to be disadvantages in this concept. Regarding the scaling paradigm, the torque of this 2-DoF joint can be scaled easily by the integration of other motors and gears, which is feasible, because of the adaptable distance between the two layers. However, this results in higher loads on the tendons, which have to be adapted in their diameter and/or quantity.

(2) Concept *(2)* structures $miro_{23}$ in two layers, similar to the preceding concept. As depicted in figure 4.26 *(a)* the lower layer (interfacing $miro_1$) integrates only the motor modules mot_a, mot_b. The motor torques τ_{mot_i} are transmitted to the upper layer by transmission gears tg_a, tg_b. Since the motor motion is multi-turn, the approach of tendons, as shown with concept *(1)*, is not applicable (compare section 4.5.4.2). The transmission gears tg_a, tg_b must therefore be implemented, for example, by multiple spur gears, a chain drive, or a favourable timing belt transmission gear, as depicted in figure 4.26 *(a)*.

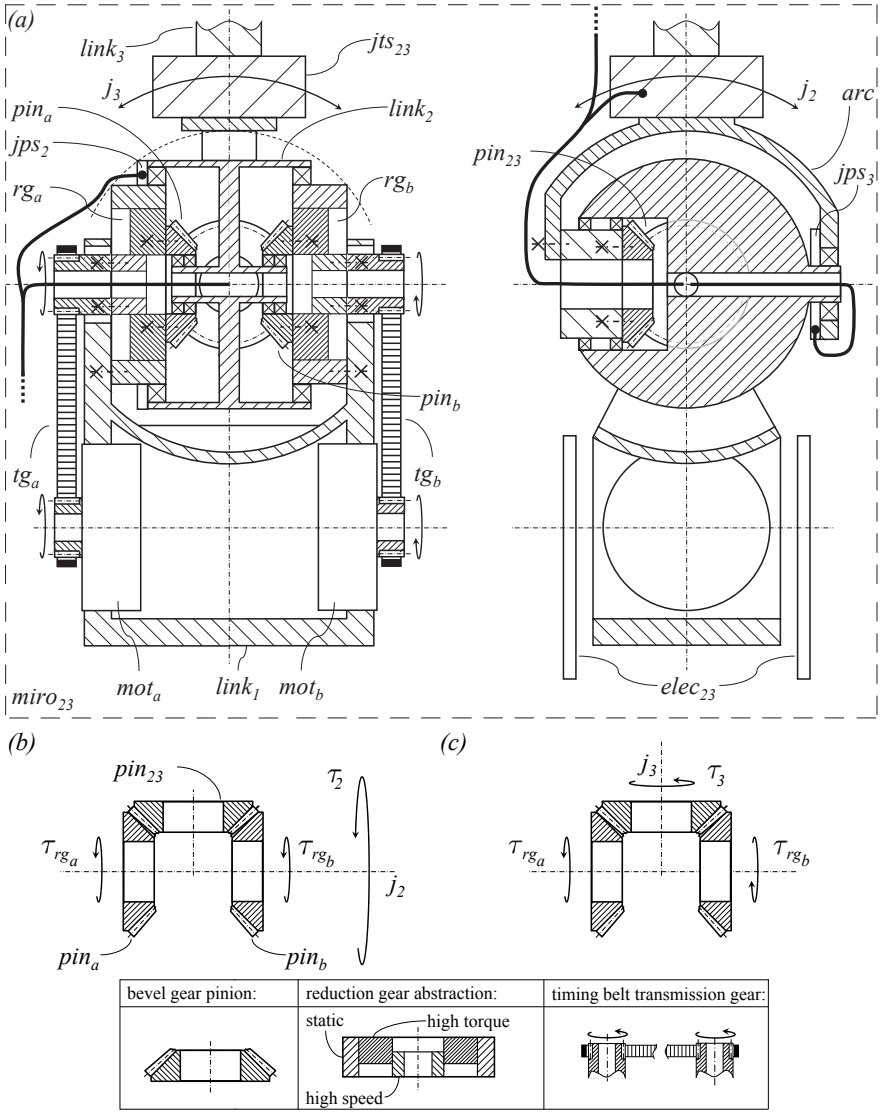

Figure 4.26: The $miro_{23}$ design concept *(2)*: two cross-section views of the bevel-gear differential concept *(a)*, rotation about j_2 *(b)*, rotation about j_3 *(c)*

The transmitted motor velocities are then reduced by two reduction gears (rg_a, rg_b) attached to $link_1$ by their static portion. The high-torque sides of these reduction gears are then connected to bevel-gear pinions (pin_a, pin_b). In contrast to the preceding concept, these pinions are im-

plemented as geared bevels meshing a single pinion pin_{23}. Due to the possibility of transmitting torques in both directions of rotation by the gearing (in contrast to tendons, which can only apply forces in one direction), the fourth pinion (compare pin_{free} in concept *(1)*) is not needed and can be left out. The principle of this differential bevel gear has been already explained in the preceding paragraph on the coupling mechanism concept *(IV)*. Additionally, figures 4.26 *(b)* and *(c)* show the correlation between the rotation of the bevel gears and the two DoF of the joint graphically. Like the preceding concept, this design allows for a compact, spherical portion of the upper layer (indicated by the dashed outline in figure 4.26 *(a)*), by moving the motors to the lower layer. One advantage of this concept is the possibility of encapsulating $link_1$, $link_2$, and $link_3$ separately, due to the absence of tendons connecting the moving $link_2$ and the static $link_1$ (cp. concept *(1)*). Additionally, the bearing concept enables a hollow shaft design for the internal cable routing. Furthermore, the motion range of the two DoF is not limited by the differential gear as it is in concept *(1)*. Although it is a challenge to achieve a backlash-free bevel gear assembly, it does not need any readjustment during the lifetime of the joint, unlike tendons. Like concept *(1)*, this concept can be scaled for other joint torques, by other motors, reduction gears, and timing belt transmission ratios. However, the integration of bigger reduction gears and thereby bigger bevel gears in the upper layer results always in an increased size of the spherical portion.

The decisive pros and cons of the two concepts are summarised in table 4.7. Both concepts can be scaled easily regarding the scaling paradigm and enable a high level of integration. The *MIRO* applies concept *(2)* for the joint module $miro_{23}$, because of the simplified housing and cable conduit design, the larger motion range, and the reliability of bevel gears in comparison to tendons over the lifetime of the joint (e.g. no readjustment of pretensioning).

2-DoF joint concepts for $miro_{23}$	*(1)*	*(2)*
scaling paradigm	+	+
simplicity of cable conduit	0	+
simplicity of housings	−	+
motion range	0	+
reliability of coupling mechanism	0	+
simplicity of backlash-free coupling mechanism	+	−
stiffness	−	0

Table 4.7: Rating of the design concepts for $miro_{23}$

4.5.3.2 Pitch-Roll Elbow Concept

The elbow of the *MIRO* consists of two orthogonally intersecting rotary DoF (j_4, j_5), implemented by the 2-DoF joint module $miro_{45}$. In relation to the upper arm ($link_3$), it inclines the forearm ($link_5$) about the joint axis j_4 and rotates it about j_5. In order to drive two DoF, two motors are combined with reduction gears to generate the necessary torque and additional gears in order to provide the coupling. Like in the preceding joints, the motors are additionally equipped with position sensors, and in the case of backdrivable joints with additional motor-sided brakes, forming motor modules. According to the design paradigms and like the preceding joint concepts, $miro_{45}$ must integrate joint-sided position sensors (jps), joint-sided torque sensor (jts) and the possibility of integrated cable routing. The basic design decision formulated for $miro_{23}$ (cp. first paragraph in section 4.5.3.1) apply here also:

- To reduce the inertia of the actuated $link_5$, both motors should be mounted to $link_3$.
- Carrying the weight of the whole forearm, joints j_6, j_7, and the payload, a direct drive (no reduction gear) principle is not feasible.
- If the reduction gears are assumed to be backdrivable, brakes must be integrated for emergency stop and power-off.
- The electronics of $miro_{45}$ are mounted to $link_3$ in order to provide short cabling of EMC-relevant signals (e.g. PWM for the motors) and to avoid conducting such cables through moving parts.

The demand for a compact design as formulated for the $miro_{23}$ is interpreted for the $miro_{45}$ module as follows. The size of $miro_{45}$ and its motion envelope are targeted to be small in order to enable a maximum integration of multiple arms on a small footprint (cp. design paradigm 2). Basically, two different design approaches are feasible for a pitch joint. The first approach is based on an asymmetric swingarm-like design as it is applied in the *DLR LWR III* (cp. figure 4.27 *(a)*). The second solution applies a symmetric fork-joint design, as depicted in figure 4.27 *(b)*. As indicated in figure 4.27 *(a)*, the asymmetric swingarm-like design can enable a large motion range for j_4 due to the shape of $link_3$ and $link_4$. In contrast, the motion range of j_4 based on the symmetric fork-joint concept is limited by the distance between the fork ground and j_4, as indicated in figure 4.27 *(b)*. Although it is possible to increase this distance to enlarge the motion range, the later section 4.5.9 on the upper arm link will show that the indicated motion range depicted in figure 4.27 *(b)* is sufficient for the *MIRO*. Furthermore, increasing this distance leads to a fragmentation of the upper arm into two portions. This fragmentation hinders the integration of electronic components in

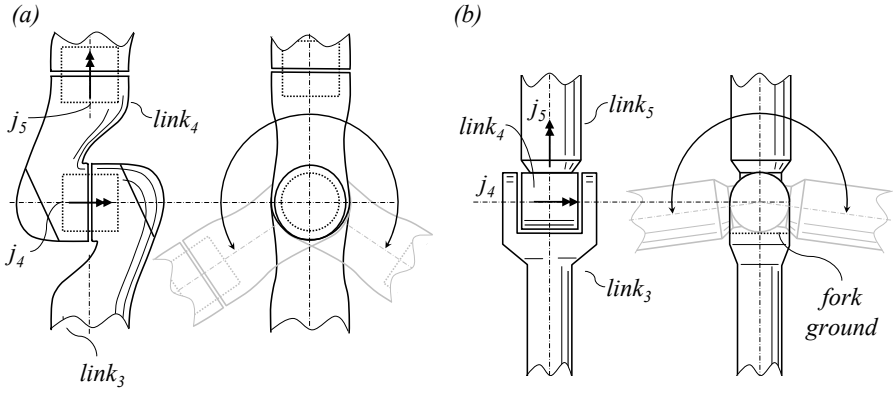

Figure 4.27: Two different approaches for the design of a pitch-roll joint configuration: asymmetric swingarm-like design *(a)*, symmetric fork-joint design *(b)*

the upper arm. However, neither of these two concepts can be excluded at this point and their compatibility with the coupling mechanism concepts has to be considered.

Regarding the coupling mechanisms identified in the preceding section on $miro_{23}$, it is trivial to convert all pitch-yaw configurations to pitch-roll joints, by attaching the following link ($link_5$) coaxial with the driven side (j_5) of the coupling mechanism instead of an orthogonal assembly (cp. $link_3$ is orthogonal to j_3 in all concepts for $miro_{23}$ in section 4.5.3.1). Therefore, all coupling mechanisms (*II-IV*) identified in the preceding section can also be applied to $miro_{45}$.

Regarding the assumed basic configurations of the *MIRO* (cp. section 4.4.2), it is apparent that the presumable maximum torques of j_4 and j_5 differ significantly. The pitch DoF must hold and manipulate the weight of the forearm, joints j_6 and j_7, the complete payload (e.g. instrument), as well as external manipulation forces. In contrast, the torque of j_5 is mostly independent of the gravitational effects of other robot parts and derives mainly from the inertia of these parts and external manipulation forces. This demand fits perfectly with the differential coupling mechanism concept *(IV)* (cp. concept *(IV)* in section 4.5.3.1, figure 4.23 *(d)*). Furthermore, using this coupling mechanism for $miro_{45}$ allows for some synergistic effects, like common parts for $miro_{23}$ and $miro_{45}$.

Although the differential coupling concept is applied in $miro_{23}$ in the form of a fork-joint design, it is feasible to modify this concept in order to achieve an asymmetric swingarm-like design. Figure 4.28 *(a)* depicts a swingarm-like and figure 4.28 *(b)* a fork-joint design. Both concepts adapt the coupling mechanism *(IV),* selected for $miro_{23}$, for a pitch-roll configuration.

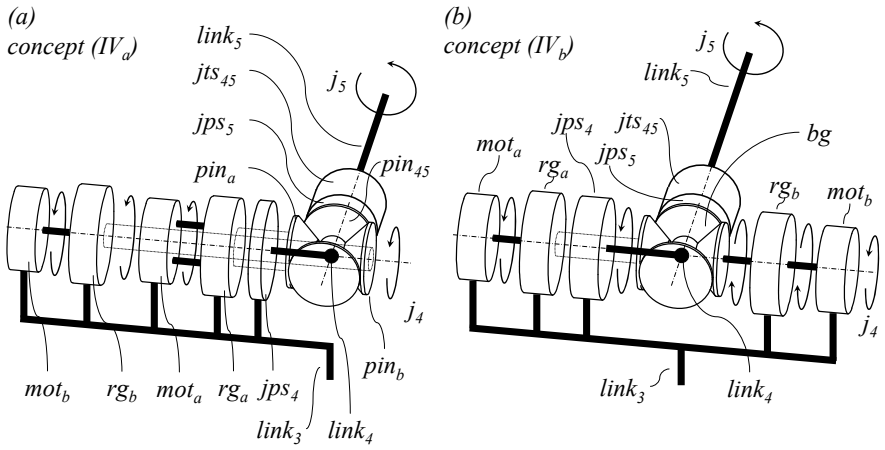

Figure 4.28: Two concepts of pitch-roll couple mechanisms based on a differential mechanism: swingarm-like configuration *(a)*, fork-joint design *(b)*

The following explanations are limited to the necessary modifications compared to $miro_{23}$:

(IV_a) The swingarm-like, pitch-roll *(IV_a)* modification of coupling mechanism *(IV)* is depicted in figure 4.28 *(a)*. In order to implement the roll DoF, $link_5$ is coaxially connected to pinion pin_{45}. The joint torque sensor jts_{45} and the joint position sensor jps_5 are also located here. Motor mot_b and reduction gear rg_b are shifted to the other joint side where the components with indicator a are integrated. The connection between the high-torque side of reduction gear rg_b and pinion pin_b is then implemented by an additional torque-tube, coaxial to the hollow shafts of the components with the indicator *a*.

(IV_b) The second concept (see figure 4.28 *(b)*) uses the same fork-joint design as selected for $miro_{23}$. Again, $link_5$ is coaxially connected to pinion pin_{45} in order to attain the roll DoF (j_5). The joint torque sensor jts_{45} and the joint position sensor jps_5 are aligned with pin_{45} as well.

Therefore, the differential coupling mechanism *(IV)* can be applied to both design concepts: the swingarm-like and the fork-joint design. For both approaches the coupling mechanism equations given in section 4.5.3.1 apply also (compare equations 4.10 and 4.11). Furthermore, this coupling mechanism is implemented by a geared bevel assembly, according to the same reasons as described for $miro_{23}$. Table 4.8 summarises the decisive reasons for the selection of the coupling mechanism and a gearing

concept	*decisive reasons*
differential coupling mechanism *(IV)*	higher torque of j_4 compared to j_5
	symmetry of transmission
	compactness of $link_4$
geared bevel assembly	larger motion range compared to the tendon-based concept
	common parts for $miro_{23}$ and $miro_{45}$

Table 4.8: Decisive reasons for the selection of the geared bevel differential mechanism concept for $miro_{45}$

of the bevel pinions. A more detailed view on the swingarm-like and the fork-joint design in the next paragraph will lead to the decision pertaining to these design aspects. In the following, coupling concept (IV_a) is itemised in the mechanical concept *(1)* and coupling concept (IV_b) in the mechanical concept *(2)* for $miro_{45}$:

(1) Figure 4.29 depicts a more detailed view of the swingarm-like joint design based on the selected coupling mechanism *(IV_a)* in form of a cross-section. Compared to $miro_{23}$, the index position of $link_4$ is rotated by 90° about j_4. The joint position sensor jps_5, the joint torque sensor jts_{45} and $link_5$ are then coaxially connected to pinion pin_{45} in order to implement the roll DoF (j_5). Motor mot_b, reduction gear rg_b and transmission gear tg_b are shifted to the other joint side, where the components with indicator a are integrated. In order to connect the high-torque side of reduction gear rg_b with the corresponding bevel-gear pinion pin_b, an additional torque tube is integrated, aligned with the hollow shafts of the other components. One drawback to this approach is that this torque tube must run through the centre of the bevel gear assembly. This space is intended for the cable conduit. Due to the relative rotary motion between the torque tube and $link_4$, a more complicated path for the cable conduit must be chosen as indicated in figure 4.29. Additionally, the torque tube reduces the available diameter of the cables.

(2) Figure 4.30 shows the adaptation of the bevel-gear differential mechanism *(IV_b)* for the $miro_{45}$ pitch-roll joints, based on a fork-joint design. Like the preceding concept, the index position of $link_4$ is rotated by 90° about j_4 and the joint position sensor jps_5, the joint torque sensor jts_{45} and $link_5$ are coaxially connected to pinion pin_{45}. Besides this, the design is identical to $miro_{23}$. As depicted in figures 4.30 *(b)* and *(c)* the mechanism enables rotation about j_4 and j_5 as described in the preceding

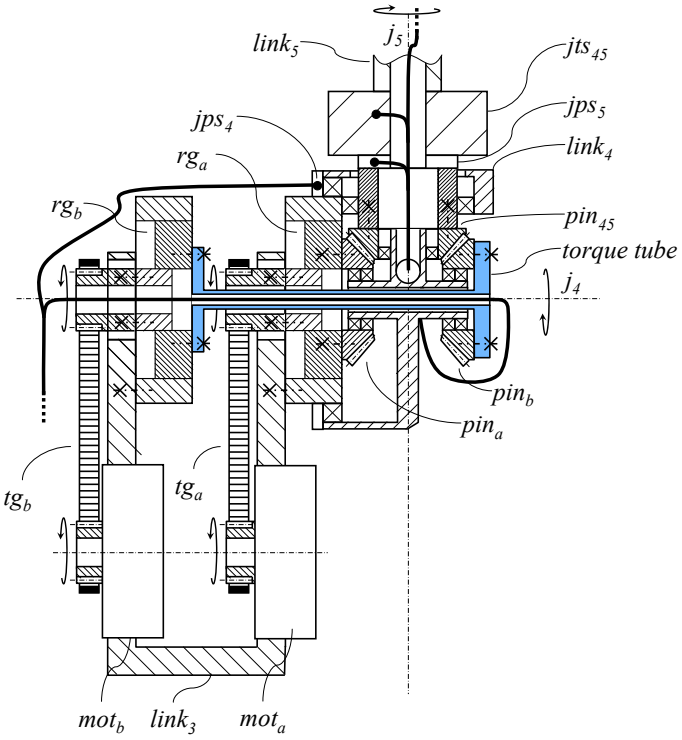

Figure 4.29: The $miro_{45}$ design concept *(1)*

section on the $miro_{23}$ module. The cable conduit from $link_4$ to $link_5$ is provided by a hollow shaft design of pin_{45}, jps_{45}, jts_{45}, and partially $link_5$. The integration space for the joint electronics $elec_{45}$ (not depicted in figure 4.27) is in the upper arm link ($link_3$) and described in the later section 4.7.

Despite the similarities of these concepts with the shoulder pitch-yaw joint, this joint module has one major difference when compared to $miro_{23}$, regarding the joint torque sensor. Due to the integration of the joint torque sensor beyond the rotary DoF j_5, its orientation is not fixed in relation to joint axis j_4. In order to measure the torque about j_4, the sensor concept must take therefore the rotary position of j_5 into consideration. The solution to this requirement is described later in the according section 4.5.5 on the joint torque sensors.

Still, both design approaches appear feasible for the $miro_{45}$ module. However, due to the disadvantage of a more complex cable conduit and the only minor advantage of the swingarm-like design regarding the motion range, the *MIRO* applies the fork-joint design for $miro_{45}$. Table 4.9 summarises the reasons for this decision.

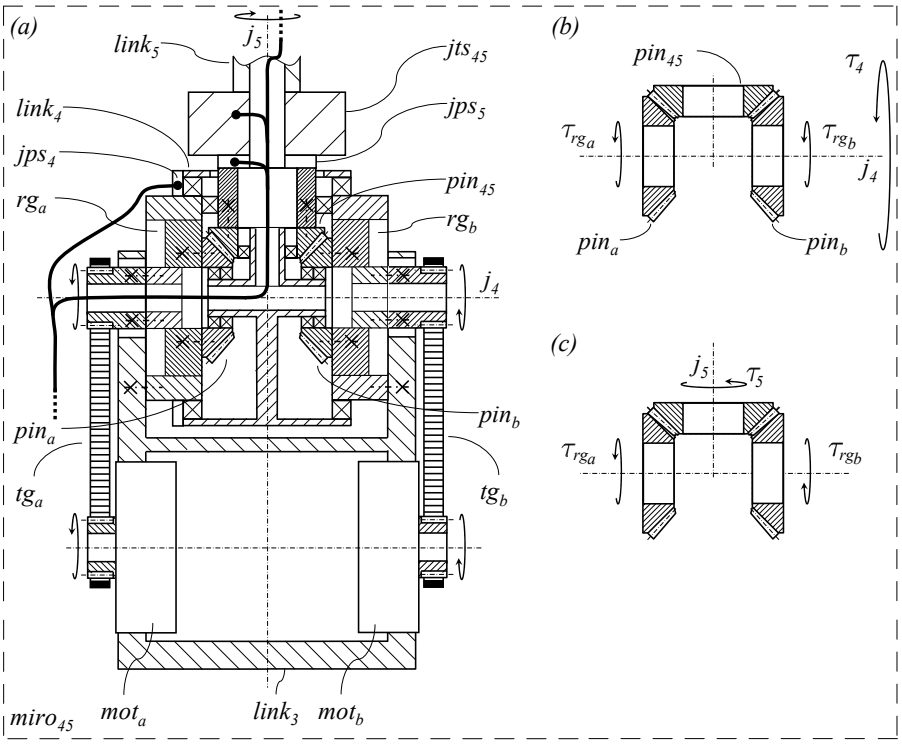

Figure 4.30: The $miro_{45}$ design concept *(2)*: cross-section view *(a)*, rotation about j_4 *(b)*, rotation about j_5 *(c)*

2-DoF joint concepts for $miro_{45}$	*(1)*	*(2)*
simplicity of cable conduit	0	+
motion range	+	0
stiffness	0	+

Table 4.9: Rating of the design concepts for $miro_{45}$

4.5.3.3 Pitch-Roll Wrist Concept

As defined in section 4.4.2 the wrist of the *MIRO* consists of two orthogonal intersecting rotary DoF (j_6, j_7), provided by the 2-DoF joint module $miro_{67}$. In relation to the forearm ($link_5$), it inclines the TCP ($link_7$) about the joint axis j_6 and rotates it about j_7. Besides motors, motor position sensors, brakes, and reduction gears, $miro_{67}$ integrates joint-sided position sensors (jps), joint-sided torque sensors (jts), and the possibility of integrated cable routing like the preceding joints.

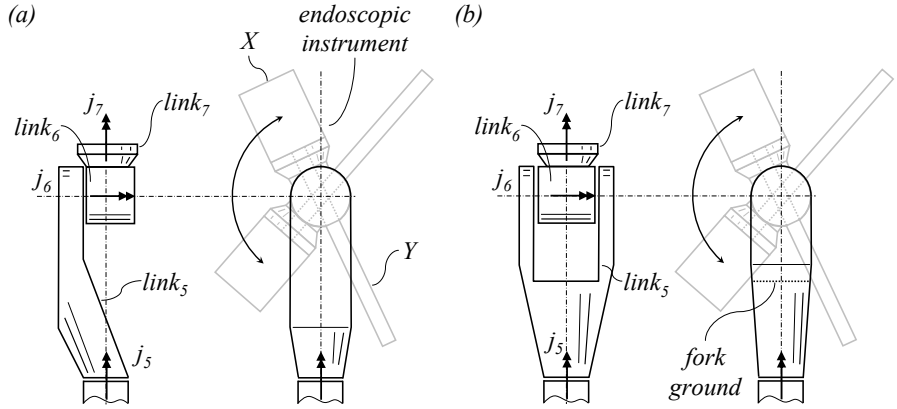

Figure 4.31: Two different approaches for the design of a pitch-roll wrist joint configuration: asymmetric swingarm like design *(a)*, symmetric fork-joint design *(b)*

The basic design decisions for $miro_{67}$ can be formulated as follows:

- To reduce the inertia of the actuated links, both motors should be mounted to $link_5$.
- If the reduction gears are assumed to be backdrivable, brakes must be integrated for emergency stop and power-off.
- The joint motion ranges and the compactness of the joint module are the main optimisation goals.
- The design must enable the mounting of endoscopic instruments as described in section 4.4.2.3.
- The electronics of $miro_{67}$ is mounted to $link_5$ in order to provide short cabling of EMC-relevant signals (e.g. PWM for the motors) and to avoid conducting such cables through moving parts.

The size of $miro_{67}$ as well as the motion envelope is targeted to be small. This requirement, which was formulated for the other joints as well, has an increased importance for the wrist joints. The wrists of multiple robots must be operated within a small spatial volume, for example in telerobotic approaches. Compact dimensions therefore enhance the workspace of the robots. Furthermore, a compact design has positive effects on the line-of-sight problem, giving better visual access to the patient's body.

With the same number and type of DoF as $miro_{45}$, both basic design approaches, which have been described in section 4.5.3.2 are feasible for $miro_{67}$. The first approach

is based on an asymmetric swingarm-like (cp. figure 4.31 *(a)*) and the second on a symmetric fork-joint design as depicted in figure 4.31 *(b)*. Both illustrations show the demand for a large motion range of j_6, which is derived from the fact that the endoscopic instrument has two portions, the electronics module (compare indicator X in figure *4.31 (a)*) and the shaft (see indicator Y), which can collide with parts of the robot.

Basically, the same joint ranges are possible with both approaches. These ranges are limited by the interference of $link_5$ with portions (shaft or electronics module) of an endoscopic instrument. Regarding the integration of electronics in $link_5$, the fork-joint design fragments the available space more than the swingarm-like design. However, a decision for or against one of the two concepts is not applicable at this point. Therefore, both approaches are analysed in the next paragraphs.

Regarding the identified coupling mechanisms, all three concepts which have been explored for $miro_{23}$ can be transferred to a pitch-roll configuration. Combined with the options of fork-joint or swingarm-like design, the following four coupling mechanism concepts (IV_a, IV_b, II_a, and III_a) are feasible for the $miro_{67}$ joint module:

(IV_a) The first concept (see figure 4.32 *(a)*) applies the differential coupling mechanism *(IV)* to a swingarm-like design. This approach and the description of the mechanism is identical to concept *(IV_a)* for $miro_{45}$ (compare page 122). In order to enable the swingarm-like design, motor mot_b and reduction gear rg_b are shifted to the joint side of components with the indicator *a*. The connection of the high-torque side of reduction gear rg_b and the corresponding bevel-gear pinion pin_b demands an additional torque tube co-aligned with j_6. Therefore, this torque tube crosses the joint axis j_7 and thereby excludes the mounting of an endoscopic instrument as proposed earlier in this section.

(IV_b) The second concept applies differential mechanism *(IV)* to a fork-joint design as depicted in figure 4.32 *(b)*. It is identical to the selected coupling mechanism (IV_b) for $miro_{45}$. Therefore, the description of this mechanism formulated for $miro_{45}$ (cp. concept *(2)* page 122) also apply here. In contrast to the preceding concept, the mounting of an endoscopic instrument through a hollow shaft of j_7 is feasible. The coupling equations for this mechanism have already been formulated in the section 4.5.3.1 (compare equations 4.10 and 4.11).

(II_a) This concept modifies the coupling mechanism *(II)* introduced in section 4.5.3.1 for a pitch-roll configuration as depicted in figure 4.32 *(c)*.

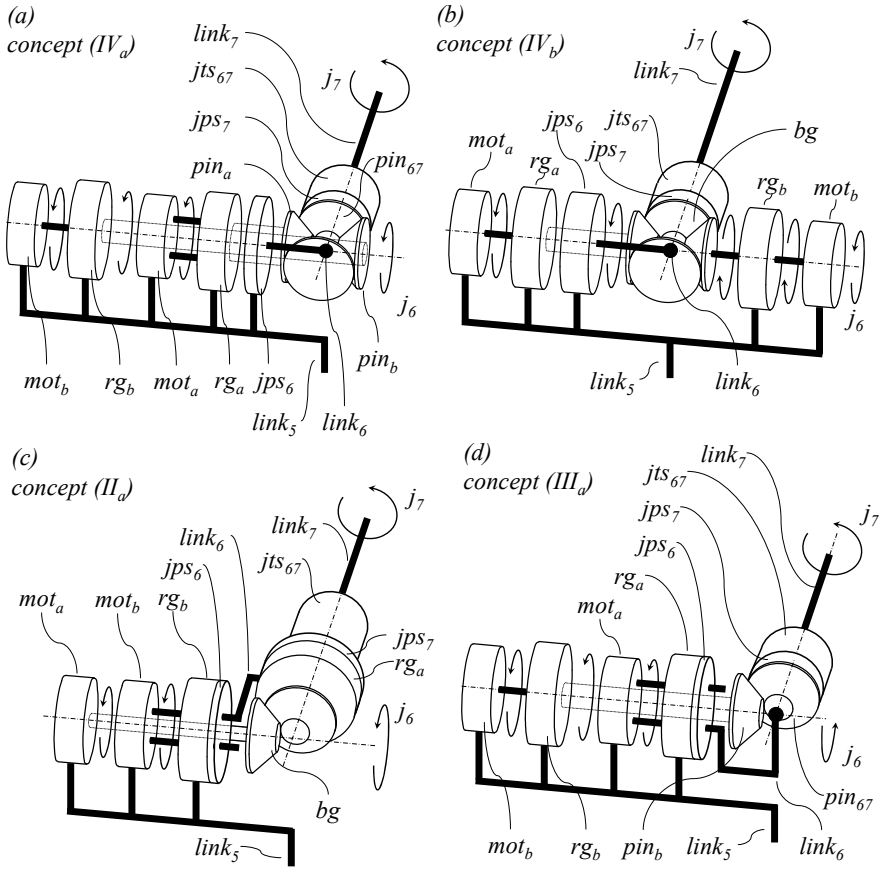

Figure 4.32: Four coupling mechanism concepts for $miro_{67}$: differential swingarm-like design *(a)*, differential fork-joint design *(b)*, universal shaft based swingarm-like design *(c)*, swingarm-like design based on a two-part bevel-gear assembly *(d)*

There, in order to remove the motor mot_a from $link_6$, it is integrated in $link_5$ and connected to its corresponding reduction gear rg_a by means of a universal shaft. The universal shaft would result in the same problem as the torque tube of concept (IV_a), because it eliminates the possibility of a hollow shaft design for j_7 and therewith the mounting of an endoscopic instrument as required for $miro_{67}$. It is therefore replaced by a two-part bevel gear (compare figure 4.32 *(c)*) transmitting the motor torque τ_a to reduction gear rg_a. However, this design still integrates the reduction gear rg_a in $link_6$. The hollow shaft of this reduction gear must have a large enough diameter not only for conducting the cables, which connect the joint sided sensors (jps_7, jts_{67}) with the joint electronics $elec_{67}$ (inte-

grated in $link_5$), but also to bear the shaft of the endoscopic instrument. Although the maximum torque of j_7 is comparably small, the size of the hollow shaft would demand for an oversized reduction gear (regarding the torque), which conflicts with the desired goal of compact dimensions of the joint. Therefore, this concept is not feasible for $miro_{67}$.

(III_a) Figure 4.32 *(d)* illustrates the last concept, which applies the coupling mechanism *(III)* (cp. section 4.5.3.1) for a swingarm-like pitch-roll configuration. The motor mot_b and reduction gear rg_b are positioned on the other side of the joint (side of components with the indicators a). In contrast to concepts (IV_a) and (II_a), mounting an endoscopic instrument as required is feasible. The coupling equations given in the section 4.5.3.1 also apply (compare equations 4.8 and 4.9).

Therefore, two coupling mechanism concepts for the $miro_{67}$ remain. Coupling mechanism (III_a) is only feasible with a swingarm-like design. In contrast, coupling mechanism (IV_b) demands a fork-joint design. Although coupling mechanism (IV_b) enables a larger usable joint torque space, compared to mechanism (III_a), it must be stated at this point that the maximum loads on $miro_{67}$ are substantially smaller than on the other joints[14]. In contrast, the demand for compactness is higher for $miro_{67}$ than for any other joint.

During the design of $miro_{67}$ the hollow shaft diameters of reduction gears turned out to be a major bottleneck. The search for available reduction gears (see section 4.5.4.1) did not result in available reduction gears adequate for the comparably small torques of j_6 and j_7, the accompanying small dimensions, and a hollow shaft design large enough in diameter for the required cable conduit. In order to avoid oversized reduction gears for the sole reason of providing a sufficient cable conduit, the two following concepts integrate the reduction gears in a way that cables do not need to be conducted through their hollow shafts. In analogy to the tendon-driven concept for $miro_{23}$ (compare section 4.5.3.1), both concepts integrate the reduction gears on the lower layer together with the motor modules. In order to connect the high-torque side of the reduction gears with the upper layer, both concepts apply transmission gears. Regarding the comparably small torques of j_6 and j_7 this approach appears feasible.

[14] The loads on joints j_6 and j_7 derive almost completely from the payload and not from the weight of robot components.

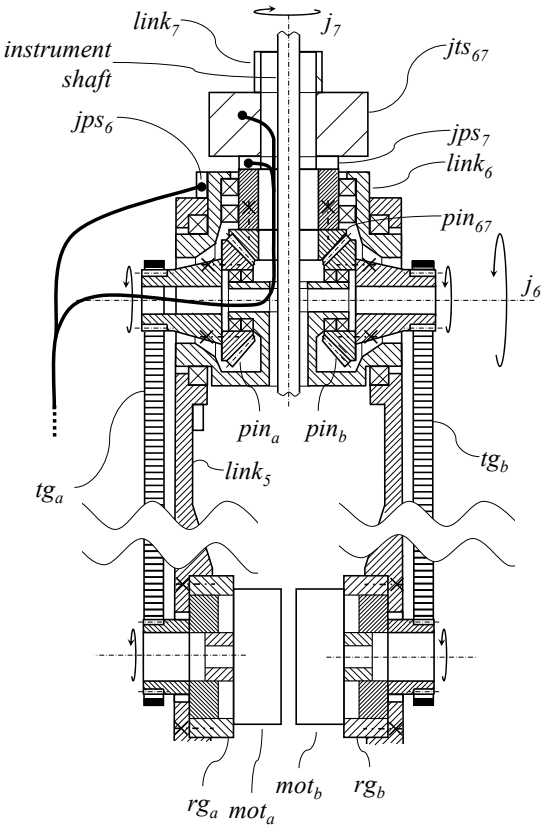

Figure 4.33: The $miro_{67}$ design concept *(1)*

The mechanical concept *(1)* described in the following is based on coupling mechanism (IV_b) and concept *(2)* on coupling mechanism (III_a), respectively:

(1) As shown in figure 4.33, design concept *(1)* for $miro_{67}$ is based on the coupling mechanism (IV_b) combined with a fork-joint design. As described above, both motor modules (mot_a, mot_b) and the reduction gears (rg_a, rg_b) are integrated into the lower layer of the joint. The high-torque sides of the reduction gears are connected to the corresponding bevel pinions pin_a and pin_b by means of transmission gears tg_a and tg_b. Therefore, the motors and gears can be placed anywhere along the forearm of *MIRO*. The two pinions pin_a and pin_b mesh with the third pinion pin_{67}, which evokes the same 2-DoF motion capabilities as described with $miro_{45}$. As it was shown in the preceding 2-DoF joint concepts, the joint torque sensor jts_{67} connects the driven pin_{67} to the following $link_7$. In order to comply with

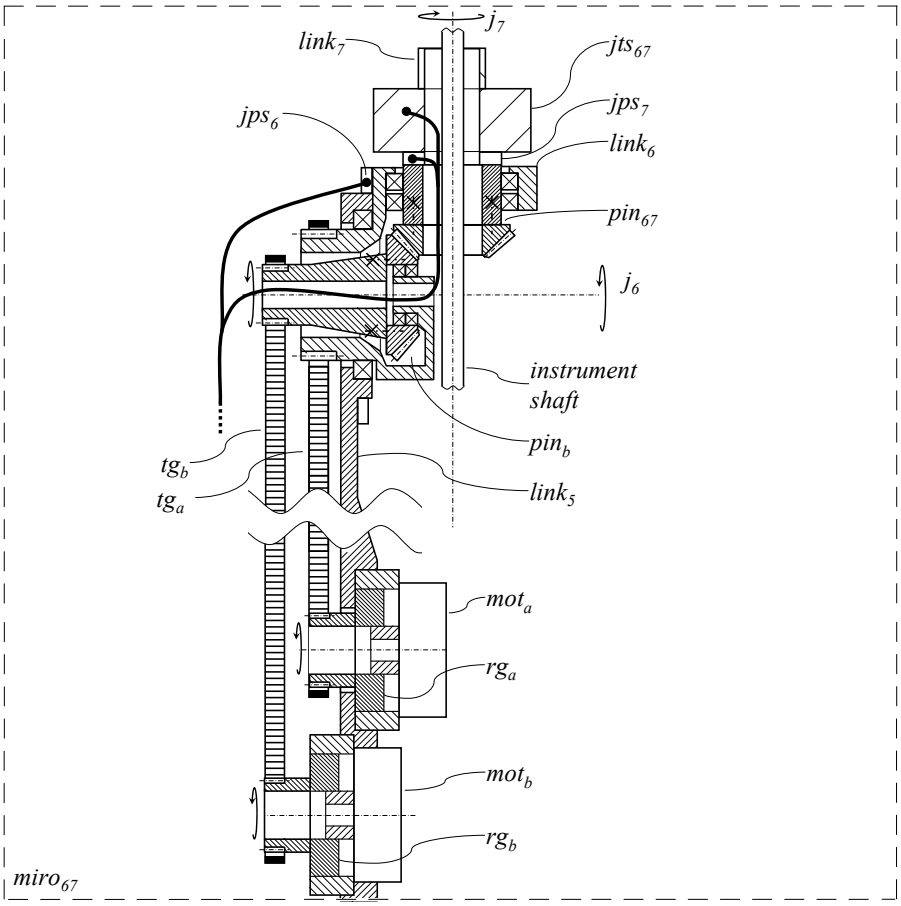

Figure 4.34: The $miro_{67}$ design concept *(2)*

the requirement of mounting an endoscopic instrument, the shaft of the instrument and the cables, which connect the joint sided sensors (jps_7, jts_{67}) share the same space in the hollow shaft of j_7.

(2) The second concept applies coupling mechanism (III_a) to a swingarm-like design as depicted in figure 4.34. In order to reduce the size of the joint and to use the elongated space in the forearm ($link_5$), the two drive modules ($mot_i + rg_i$) are staged in two different layers. The high-torque side of reduction gear rg_a is connected directly to $link_6$ by a transmission gear tg_a.
In contrast, the torque of reduction gear rg_b is transmitted by transmission gear tg_b to the bevel pinion pin_b, which meshes with bevel pinion pin_{67}.

The integration of the joint sided sensors (jps_6, jps_7, jts_{67}) is identical to the preceding concept *(1)*.

Both concepts represent valid solutions for the design of $miro_{67}$. Concept *(1)* enables a larger usable joint torque space, due to the differential coupling mechanism. However, the maximum torques of j_6 and j_7 are substantially smaller than those of the other joints, due to the very small portion of robot components whose masses have to be moved by j_6 and j_7. In contrast, concept *(2)* enables the most compact design of $link_6$. Additionally, concept *(2)* does not fragment the forearm in the same way as the fork-joint design of concept *(1)*, which simplifies the integration of the joint electronics. Therefore, concept *(2)* is chosen as design concept for $miro_{67}$ (compare table 4.10).

The swingarm-like design of $miro_{67}$ combined with a hollow shaft of j_7 for the optimised use of laparoscopic instruments was chartered as German patent [Hagn, 2004].

2-DoF joint concepts for $miro_{67}$	*(1)*	*(2)*
explorable torque range	+	0
motion range	+	+
compactness of $link_6$	0	+
simplicity of electronics integration into $link_5$	0	+

Table 4.10: Rating of the design concepts for $miro_{67}$

4.5.4 Gears

The joint concepts introduced in the preceding sections demand different gear concepts for speed reduction, torque transmission, and coupling mechanisms. This section summarises these demands, analyses briefly the available gear technologies regarding their applicability and identifies the technologies applied to the *MIRO* robot. This selection is limited to commercially available or modified reduction gears and does not consider novel gear designs.

4.5.4.1 Reduction Gears

Reduction gears are used in robotic arms to generate the demanded joint torques based on the motor torques. This is necessary, because the torque-speed ratio of e.g. electric motors does not comply with the desired torques and velocities of robot joints.

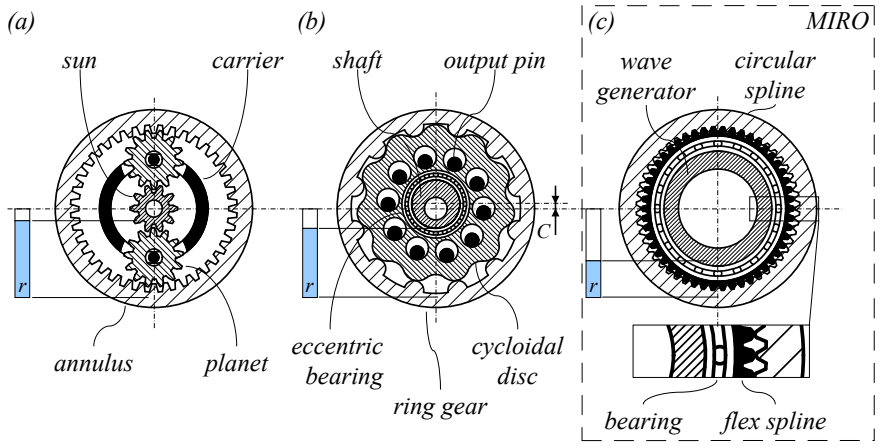

Figure 4.35: Three reduction gear principles: planetary speed reducer *(a)*, cycloidal speed reducer *(b)*, Harmonic Drive reduction gear *(c)*

Regarding the *MIRO* the following basic demands can be formulated according to the design and scaling paradigms:

- compact dimensions
- availability in a comprehensive range of torques and sizes
- hollow shaft design for joints j_1 to j_5
- near-zero backlash in order to enhance the accuracy of the robot[15]

In contrast to reduction gears in industrial robots, the demand for high rotary stiffness is only minor for the *MIRO* due to design paradigm 1 (lightweight design). Specifically, the hollow shaft requirements combined with the desired compact dimensions reduces the amount of available reduction gears significantly. Three different technologies can be seen as state-of-the-art reduction gears in robotics (compare figure 4.35):

Planetary Gearheads Reduction gears based on the planetary or epicyclic principle integrate a central gear (sun) meshing multiple surrounding gears (planets), which are pivoted in a common carrier (compare figure 4.35 *(a)*). The planets again mesh an outer ring gear (annulus). If the carrier is fixed in rotation and the sun is used as the input of the reduction gear, the annulus can be used as the gear output.

[15]Backlash of reduction gears results in an undetermined relation between motor and joint position. Furthermore, regarding torque control of joints it may lead to unstable torque control.

The speed reduction ratio $ratio_{rg,\,planetary}$ of the planetary gear is then calculated according to the number of teeth of sun z_S and annulus z_A:

$$ratio_{rg,\,planetary} = \frac{z_S}{z_A} \tag{4.12}$$

In order to enable significant reduction ratios, the sun must be significantly smaller than the planets. Therefore, the radial range *(r),* which is relevant for the torque amplifying function of the gear (indicated by the blue column *(r)* in figure 4.35 *(a)*), starts at a comparably small diameter. This conflicts with the hollow shaft requirement and thus no significant range of commercial hollow shaft planetary gearheads is available. A second possibility for increasing the reduction ratio is to couple multiple stages of planetary gears in series. Regarding available planetary gearhead product ranges (e.g. *MAXON GP* series [Maxon, 2009a]), this second approach is chosen very often in order to provide different reduction ratios for a certain gear size. This way, the number of stages and thereby the length of the reduction gear are a function of the reduction ratio.

Cycloidal Drives These reduction gears integrate a central input shaft with an eccentric bearing (eccentricity C) as depicted in figure 4.35 *(b)*. The cycloidal disk is pivoted on this bearing and meshes with the gearing on its perimeter with a ring gear. The number of teeth z_C of the cycloidal disc and z_R of the ring gear are different. Due to a rotation of the input shaft and the described gearing, the cycloidal disk moves in an eccentric, cycloidal way. The output of the gear is designed by multiple co-located pins, which roll in bores of the cycloidal disc. The speed reduction of this gear principle is calculated by the ratio between the number of teeth z_C of the cycloidal disc and z_R of the ring gear:

$$ratio_{rg,\,cycloidal} = \frac{z_R - z_C}{z_C} \tag{4.13}$$

Therefore, the reduction ratio is more independent of the size of the input shaft compared to the planetary gearheads. Typical available cycloidal drives are offered with more than one reduction ratio option for each size (e.g. the *RV-C* series can be ordered with two different reduction ratios for each size). The relevant radial portion *(r)* (compare blue column in figure 4.35 *(b)*) for the speed reduction of the cycloidal gear starts at a larger inner diameter. The possibility of use with hollow shaft designs should therefore be higher compared to planetary gearheads. However, no significant range of compact cycloidal reduction gears with hollow shaft design is available today (e.g. the *NABTESCO* hollow shaft *RV-C* series starts at an outside diameter of 147 mm (type *RV-10C*) [Nabtesco, 2009]).

Harmonic Drive Gears Reduction gears based on the Harmonic Drive principle [Musser, 1959] are very popular in lightweight robots, for example, in the *DLR LWR III* [Albu-Schäffer et al., 2007a] or the *Mitsubishi PA-10* [Kennedy and Desai, 2003]. In contrast to the preceding gear technologies, Harmonic Drive gears apply not only rigid components, but also a part which is elastically deformed. This part, the flex spline, is a thin-walled cup-shaped body with a gearing on its perimeter as depicted in figure 4.35 *(c)*. The rotary input of a Harmonic Drive gear consists of an elliptical disc with an elliptical ball bearing, together forming the wave generator. A rotation of the wave generator deforms the flex spline to an ellipse and thereby its gearing meshes the circular spline with the transverse portion. If the circular spline is assumed as stationary, the wave generator represents the input (high-speed side) and the flex spline the output (high-torque side) of the reduction gear. The number of teeth z_C of the circular spline and z_F of the flex spline differ by two ($z_C - z_F = 2$), which causes the speed reduction of this gear principle. The ratio of the speed reduction is calculated as follows [Lauletta, 2006]:

$$ratio_{rg,\,Harmonic\,Drive} = \frac{z_F - z_C}{z_F} \tag{4.14}$$

Due to the thin wall of the flex spline, the main speed-reducing function of this gear technology (indicated by the blue column *(r)* in figure 4.35 *(c)*) is located at a larger diameter compared to the preceding gear principles. The hollow shaft design is only limited by the conjugate diameter of the elliptic wave generator bearing and the design of the bottom portion of the cup-shaped flex spline.

Table 4.11 compares typical parameters of the reduction gear technologies presented, based on the available product ranges of three manufacturers: *MAXON* (planetary gearheads), *NABTESCO* (cycloidal drives), and *HARMONIC DRIVE AG* (Harmonic Drive gears). However, it must be stated at this point that the ratings shown are focused on the specific demands of the *MIRO*. Therefore, and due to the reduced scope of only three manufacturers, this comparison is barely exhaustive and cannot be seen as a general rating of these gear technologies.

Harmonic Drive gears were chosen as reduction gear technology for all joints of the *MIRO* robot. The combination of hollow shaft design throughout all gear sizes with the availability of small scales is the major advantage of this gear technology compared to the other candidates. The availability of up to six different reduction ratios for each gear size (identical diameter and length) complies with the scaling paradigm. The torque-speed ratio of joints can therefore be adapted by exchanging the reduction gears without modification of additional parts. Furthermore, the selected reduction gears manufactured by the homonymous *HARMONIC DRIVE AG* are available as

	planetary gears [Maxon, 2009b]	*cycloidal drives [Nabtesco, 2009]*	*Harmonic Drive [Harmonic Drive, 2008]*
typical minimum reduction ratios	1 : 3.5 (*GP 42* series)	1 : 10.7 (*GH* series)	1 : 30 (*HFUC* series)
typical maximum reduction ratios	1 : 6285 (*GP 32* series)	1 : 258 (*RD-C* series)	1 : 160 (all series)
typical minimum backlash	15 arc-min (*GS 16 VZ* series)	1 arc-min (*RV-C* series)	1 arc-min* (*CSD* series)
availability of hollow shaft designs	−	0	+
availability of small versions	+	−	+
available repeated peak torque range	0.002 - 250 Nm	58 - 8820 Nm	1.8 - 9180 Nm (*HFUS* series)
reduction ratios per diameter and length	2 - 4 (*GP 32 BZ* series)	6 (*RV-E* series)	6 (*HFUC* series)

* lost motion

Table 4.11: Typical parameters of reduction gear technologies

	planetary gears	*cycloidal drives*	*Harmonic Drive*
backlash / lost motion	−	+	+
range of hollow shaft versions	−	0	+
availability of small versions	+	−	+

Table 4.12: Ratings of reduction gear concepts

component sets, which allow a higher level of integration compared to *gear units*[16].

Table 4.12 shows the decisive reasons for the selection of Harmonic Drive reduction gears for the *MIRO*.

4.5.4.2 Transmission Gears

The *MIRO* 2-DoF joint concepts demand the transmission of rotary motion between unaligned, parallel axes. In contrast to $miro_{23}$ and $miro_{45}$, where the transmission

[16]Gear units are ready-to-use reduction gears integrating own housings and bearings. Regarding the integration into a robot joint, which already integrates joint-sided bearings and housings, these parts are redundant. In contrast Harmonic Drive component sets only comprise wave generator, flex spline and circular spline.

gears are supposed to transmit the motor torques (low) and speeds (high), the $miro_{67}$ transmission gears must transmit the output torques (high) and velocities (low) of the reduction gears. Regarding the *MIRO* the following basic requirements can be formulated according to the design and scaling paradigms:

- near-zero backlash in order to enhance the accuracy of the robot
- multi-turn ($miro_{23}$ and $miro_{45}$: $\geq$ 200 revolutions, $miro_{67}$: $\geq$ two revolutions)
- availability in a comprehensive range of axes offsets
- compact dimensions and low friction

For the transmission gears in the *MIRO*, three different transmission principles have been taken into consideration. In order to simplify the comparison, the following descriptions are based on a 1:1 transmission ratio.

Closed-loop tendon drives In order to transmit rotary motion between two parallel axes, a closed-loop tendon drive as depicted in figure 4.36 *(a)* represents a valid solution. The two tendon pulleys are integrated with the desired parallel offset A. Tendon u is terminated at one end with pulley a and at its second end with pulley b. As tendons can only transmit forces in one direction, a second pulley v must be applied in a mirrored form for the transmission of torque in the other rotary direction.

In order to provide multi-turn rotation ability, the tendons loop the pulleys multiple times ($loops_a$, $loops_b$). The maximum revolutions of this transmission gear is given by the sum of tendon loops on $pulley_a$ and on $pulley_b$. Therefore, this principle should not be applied for transmitting the motor rotation in $miro_{23}$ and $miro_{45}$, due to the large number of cable loops on the pulley. However, regarding the small number of revolutions (≤ 2) in $miro_{67}$ this approach appears feasible.

Furthermore, this transmission principle fulfils the scaling paradigm in an ideal way: for given pulley diameters ($\varnothing D_{pa}$ and $\varnothing D_{pb}$), every axis offset can be implemented simply by adapting the cable lengths. In order to enable higher transmissible torques, the diameter of the tendons can be increased. In order to adjust the necessary pretensioning of the tendons, either the rotary position of the tendon terminals on the pulleys must be adjustable or an additional pulley must be added. Tendon-based transmission is inherently backlash-free if an adequate pretension of the tendons can be implemented. Furthermore, it has no ripple due to the absence of gearing. However, the experiences with the prototypical tendon-based coupling mechanism $miro_{23}$ (compare appendix D.1) showed that the design of a miniature tendon pretensioning mechanism and its adjustment is not trivial.

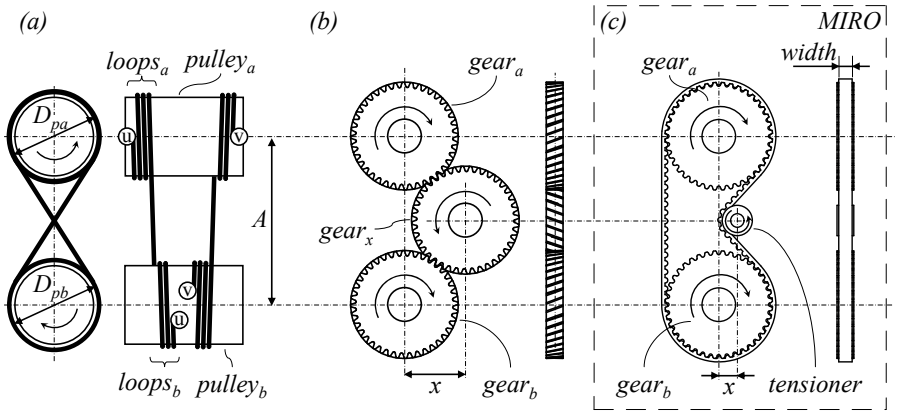

Figure 4.36: Three transmission gear principles: closed-loop tendon drive *(a)*, spur gear *(b)*, timing belt *(c)*

Spur gears A very simple way to transmit rotary motion between parallel axes is the application of an n-stage spur gear assembly. Although it is possible to implement such transmission with only two gears, this limits the variation of possible axis offset, because the gear diameter is determined by the incremental number of teeth and the modul (size of the teeth). Furthermore, this approach would result in a spacious design for large axis offsets. Therefore, an assembly consisting of three spur gears as depicted in 4.36 *(b)* appears to be more advantageous and allows a stepless specification of the axis offset by adapting parameter x. In contrast to the preceding approach, the spur gear inherently enables multi-turn rotation. It can be designed backlash-free by the application of helical gearing, which additionally reduces the acoustic noise of the transmission gear significantly in contrast to straight-cut gearing. In contrast to the closed-loop tendon drive, the spur gear enables higher stiffness of the transmission but introduces ripple due to the gearing.

Timing belts The third concept can be seen as a combination of the first two approaches. The transmission gear is implemented by means of a timing belt, which loops around two gears. Like the tendon-based solution, it integrates a flexible component, which allows a more compact design than the spur gears. In fact, timing belts integrate steel tendons in the polymer matrix and have therefore similar stiffness compared to tendons. On the other hand, it inherently enables massive multi-turn rotation in contrast to the tendon-based approach. In order to implement the prescriptive pretensioning of the timing belt and to enable different axis offsets based on determined belt lengths, an additional tensioner can be applied, as shown in figure 4.36 *(c)*. Like the spur gears, the timing belts introduce ripple due to the gearing, but due to the

	tendon-based gear	*3-stage spur gear*	*timing belt*
multi-turn ($\leq$ 200 revolutions)	−	+	+
multi-turn ($\leq$ two revolutions)	0	+	+
simplicity of adjustment	−	0	+
compactness	+	−	+
robustness	0	+	+
rotary stiffness	0	+	−
simplicity of scaling the axes offset	+	0	+
low ripple	+	−	0

Table 4.13: Rating of transmission gears

polymer material this effect is smaller. With precision manufacturing of the gear teeth, this transmission technology can be machined with near-zero or even zero backlash[17]. In order to increase the transmissible torque, the width of the timing belt is the only parameter besides the gear diameter. However, based on experience with the tendon-based coupling mechanism for $miro_{23}$ (compare section 4.5.3.1 and 4.7), the simplicity of this transmission gear regarding assembly and adjustment is striking.

All three concepts can be implemented with near-zero backlash transmission and can be scaled easily for changing torque requirements, which complies with the scaling paradigm.

Regarding the transmission of motor torques in $miro_{23}$ and $miro_{45}$ only the spur gear and the timing belt concepts are feasible, because of the requirement of massive multi-turn ($\leq$ 200 revolutions). Both concepts allow a near-zero backlash transmission, although this demand is of minor importance for the transmission of the motor position, due to the downstream reduction gears. Because of the very compact design and the simplicity regarding the adaptation to demanded axis offsets, the *MIRO* applies timing belts as transmission gears for $miro_{23}$ and $miro_{45}$. Thereby, the pretensioning of the belt is implemented by a tensioner on an eccentric shaft, as depicted in figure 4.35 *(c)*.

[17]Standard timing belt gears apply a small amount of backlash in order to reduce abrasion of the belt in high-speed applications.

For the torque transmission in $miro_{67}$ basically all three transmission gear principles are applicable and the differences turned out as minor. Despite the presumed higher rotary stiffness of the spur gear and the inherent ripple-free transmission of the tendon-based approach, the $miro_{67}$ integrates timing belt transmission gears. During the design phase of $miro_{67}$, the timing belt approach enabled a more compact design than the spur gear. Regarding the comparably large axes offset and the desired compact dimensions of $miro_{67}$, the spur gear approach would result in at least a 4-stage spur gear assembly for tg_b (compare figure 4.34). Compared to the tendon-based approach, the timing belt allows a simpler, yet more robust pretensioning mechanism. In contrast to the pretensioning approach for $miro_{23}$ and $miro_{45}$, which apply an additional tensioner, the position of the motor-reduction gear modules of $miro_{67}$ (compare figure 4.34) can be changed within a small range in order to provide the pretensioning of the belt.

Table 4.13 summarises the pros and cons of the described transmission gear solutions with the focus on the requirements and spatial constraints of the *MIRO*.

4.5.4.3 Bevel Gears

All 2-DoF concepts developed integrate bevel gears, which transmit comparably high torques between two orthogonal intersecting axes. In order to achieve a backlash-free transmission, the assembly is implemented in the form of high precision[18] spiral bevel gears based on the *GLEASON* system [Jones and Ryffel, 1984]. To compensate for manufacturing tolerances, the positions of all bevels are adjustable by the application of laminated steel shim foils.

The main intention behind the application of the coupling mechanisms in the *MIRO* 2-DoF joints is to reduce the size of the joints. All coupling mechanisms introduced shift the motor of the second joint and its electronics to the stationary link, which leads to a compact design. Furthermore, the bevel-gear coupling concepts additionally shift all reduction gears to the stationary link. This results in an additionally reduced size as described in the following paragraph.

Comparing the two coupling mechanisms *(II)* and *(IV)* introduced for $miro_{23}$ (compare section 4.5.3.1, page 108), these concepts differ mainly in the fact that concept *(II)* still integrates the reduction gear rg_3 in $link_2$ and concept *(IV)* shifts all reduction gears to stationary $link_1$ by integrating a 3-part differential bevel gear in $link_2$. Figure 4.37 compares the size of the desired spherical portion of $miro_{23}$ for these two approaches based on concrete specifications.

[18] Grinded with quality 5 according to DIN 3965, modul 1.400 .

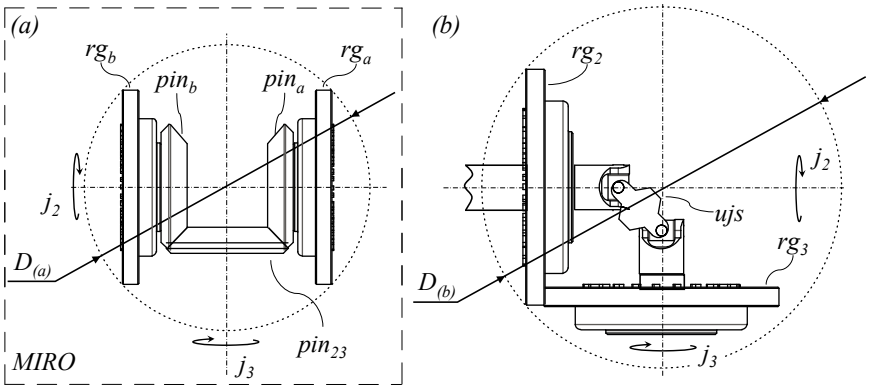

Figure 4.37: Spatial comparison for $miro_{23}$ of coupling mechanism *(IV)* based on a differential bevel gear *(a),* with coupling mechanism *(II)* leaving the reduction gear rg_3 integrated in $link_2$ *(b)*

Both joint configurations are targeted at a maximum and concurrent torque of $\tau_2 = \tau_3 = 90\,Nm$, thus leaving the additional usable torque space of coupling mechanism *(IV)* unconsidered (compare 4.5.3.1, figure 4.24 *(b)*).

Regarding the differential coupling mechanism *(IV),* the maximum torques of the reduction gears $\tau_{rg_a} = \tau_{rg_b}$ are calculated according to the coupling equations (equation 4.11) for this mechanism as follows:

$$\tau_{rg_a} = \tau_{rg_b} = \frac{\tau_{2,3}}{\sqrt{2}} = \frac{90\,Nm}{\sqrt{2}} = 63,6\,Nm \tag{4.15}$$

As depicted in figure 4.37 *(a)*, coupling mechanism *(IV)* therefore integrates two *CSD-20-160-2A-GR-BB*[19] reduction gears manufactured by *HARMONIC DRIVE* with a momentary peak torque limit of 64 Nm [Harmonic Drive, 2008]. This allows for a spherical space for the integration with a diameter of $D_{(a)} \approx 103\,mm$.

With coupling mechanism *(II)*, the reduction gear rg_3 remains in $link_2$ as depicted in figure 4.37 *(b)*. The torque of the corresponding motor mot_3, which is integrated into the stationary $link_1$, is transmitted to rg_3 by a universal joint shaft (*ujs*). In order to achieve the desired output torque, both reduction gears must output the desired 90 Nm. This demands for the next scale of *CSD* reduction gears (*CSD-25-50-2A-GR-BB*, with 127 Nm momentary peak torque limit [Harmonic Drive, 2008]), which results in a spherical space with a diameter of $D_{(b)} \approx 130\,mm$.

The differential mechanism based on the bevel-gear assemblies can therefore reduce the size of joints. However, in the comparison shown, it has to be pointed out that the difference in size is derived mainly from the stepped scaling of available reduction

[19] *Harmonic Drive* component set, size 20, reduction rate 1:160, enlarged hollow shaft option (BB).

gears. Furthermore, the speed-reduction effect and additional usable torque space of coupling mechanism *(IV)* are not considered in this comparison.

4.5.5 Joint Torque Sensors

As defined in design paradigm 4, the *MIRO* integrates joint-sided torque sensors in order to establish hands-on robotics applications, sense impacts with its environment, and benefit the control of the joints (e.g. vibration damping). Although it is feasible to derive the joint torques from the motor currents, this approach has disadvantages like the parasitic effects of transmission and reduction gears (e.g. friction). Therefore, dedicated joint-sided torque sensors are applied.

This section clarifies the design of the torque sensors regarding the applied technology and adaptation in the *MIRO* joints. The following requirements can be formulated for the design of the joint torque sensors (jts) of the *MIRO*:

- absolute torque measurement (no initialising after power-on)[20]
- single- (jts_1) and multi-DoF torque measurement (jts_{23}, jts_{45}, jts_{67})
- adaptable design regarding geometry and torque range
- high bandwidth for vibration damping
- hollow shaft design
- compact dimensions (sensor and processing electronics)

The design of force and/or torque sensors is a comprehensive field of research. Most approaches measure the deformation of a body caused by the exerted force or torque. The body is thereby deformed within the limits of its elastic range (HOOKE's law) in order to achieve a linear relation between the deformation and the load exerted. Regarding the measurement of joint torques, this body must be integrated into the flux of forces/torques of the robot. Therefore, the elasticity of the sensor body has a major impact on the stiffness of the robot and the sensor elasticity must be reduced to a minimum. The different physical principles which have been considered to sense the deformation of the body therefore aim at the measurement of very small deformations.

[20] This demand excludes sensors based on the piezo-electric effect.

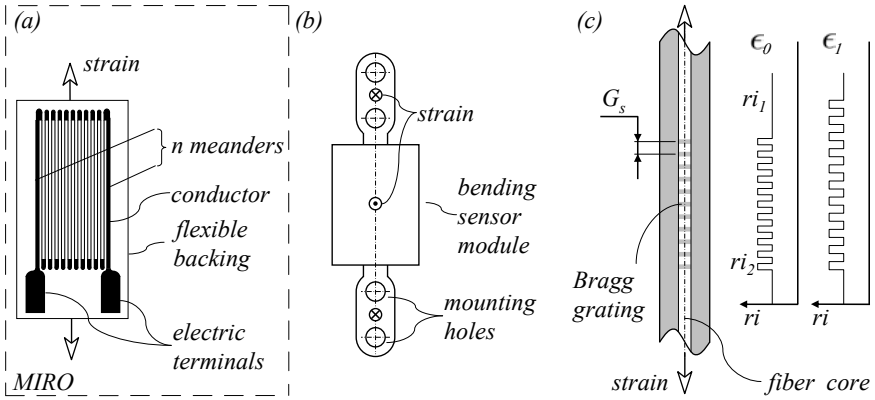

Figure 4.38: Principles for the measurement of small deformations: foil strain gauge *(a)*, *NCTEngineering GmbH* stand alone bending sensor module based on inverse magnetostriction *(b)*, fibre optical BRAGG grating sensor *(c)* (note: depictions *(a)*, *(b)*, *(c)* have different scales)

Strain Gauges The electrical resistance R $[\Omega]$ of a conductor is composed by its cross-section area A $[m^2]$, length l $[m]$ and the electrical resistivity ρ $[\Omega m]$ of the material:

$$R = \rho \cdot \frac{l}{A} \tag{4.16}$$

Strain Gauges apply this principle for the measurement of strain. In order to increase the change in resistance in relation to the deformation of the sensor body (gauge factor), the conductor is shaped in the form of a meander as shown in figure 4.38 *(a)*. Thereby, the elongation of the sensor body results in n-times the elongation and n-times the reduction of the cross-section area of the conductor. The resistance of the strain gauge can be measured by the voltage change of a WHEATSTONE bridge circuit. The most common types of strain gauges are foil strain gauges, which consist of a metallic conductor on a flexible insulator tape. These gauges are applied mechanically to the sensor body by bonding with an adhesive and are connected to the electronics by unencumbered, thin wires. Force/ torque sensors based on strain gauges are very popular in robotics (e.g. joint torque sensors in the *DLR LWR III*) due to the adaptable design of the sensor body, the comprehensive range of different strain gauges, and the comparably simple design of the signal processing electronics. Strain gauges are available with compensation for dedicated sensor body materials and defined temperature ranges.

Inverted Magnetostriction JOULE identified that ferromagnetic materials change their shape when a magnetic field is applied, though their volume remains constant. This effect is known as magnetostriction [Hering et al., 1989]. By inverting this effect, a mechanical deformation of a ferromagnetic body results in a change of its magnetisation. This correlation can be applied to the design of torque or force sensors, as introduced e.g. by GARSHELIS for automotive transmission applications [Garshelis et al., 1997]. The central advantage of this approach is that only the material of the sensor body needs to be determined (e.g. 50NiCr13 [NCTEngineering, 2006]) and the geometric shape can be chosen almost arbitrarily. Furthermore, the magnetisation change of the sensor body can be measured contact-free by sensor coils, which enables torque measurement of rotating components (e.g. motor shafts). This technology has been transferred to commercially-available sensor products, e.g. by *NCTEngineering GmbH*, Germany. The first products targeted integrated single-DoF torque, force, angle, or position measurement. Regarding the requirement of multi-DoF torque measurement, as formulated for the *MIRO*, a constellation of multiple single-DoF sensors appears to be feasible. Such single-DoF sensors, like the *standalone (SA) bending sensor module* by *NCTEngineering GmbH* (compare figure 4.38 *(b)*) have been introduced as made-to-order products *[NCTEngineering, 2006].* Furthermore, this sensor element can also be ordered in a version measuring two DoF, which simplifies the design and assembly of multi-DoF sensors.

Fibre Bragg Grating Sensors Optical sensors based on BRAGG grating apply light for sensing the strain of a sensor body, instead of an electric current like the preceding principles. The sensor element consists of a single-mode optical fibre with an inscribed periodic modulation of the refractive index (compare figure 4.38 *(c)*). This grating is implemented by means of a high-power ultraviolet light source (UV laser) and is called BRAGG grating. Incoming light is partially reflected by and transmitted through these fringes. Regarding the reflected light, the particular wavelength λ is reflected substantially more than others, which equals the BRAGG wavelength of the grating. For the unstrained condition ϵ_0 of the fibre, the BRAGG wavelength λ_0 is given by equation 4.17, with the grid spacing G_s and average refractive index ri_{av} of the fibre core[21] [Kreuzer, 2008]:

$$\lambda_0 = 2 \cdot ri_{av} \cdot G_s \ . \tag{4.17}$$

If the wavelength λ matches λ_0 the reflections at each fringe are in phase and thereby accumulate to a strong signal. Other wavelengths result in reflections at the fringes with different phases and therefore cancel each other out. By the mechanical

[21] $ri_{av} = \frac{ri_1 + ri_2}{2}$

deformation ϵ_1 of the fibre, the grid spacing G_s changes as illustrated in figure 4.38 *(c)* and the BRAGG wavelength changes to λ_1. This results in a shift of the reflected wavelength, which is directly related to the strain of the fibre and thereby of the sensor body. By analysing the wavelength of the reflected light peaks (e.g. by means of an interferometer), this principle can be applied as a strain sensor. The central advantage of this concept is the robustness of the signal transmission regarding large fibre lengths and electro-magnetic hazard. However, the complexity and size[22] of suitable processing electronics eliminates the possibility of integration into the *MIRO* robot, demanding a dedicated external component for signal processing.

All principles shown can be applied to the measurement of strains and therefore to torques or forces. The optical approach based on BRAGG gratings promises comparably low-cost sensor elements (fibres), but still demands a large processing component, which cannot be integrated into a robot arm. A separate external cabinet integrating this processing component would result in the demand for numerous fibres conducted through the arm and a multiplicity of voluminous fibre connectors. Furthermore, KREUZER's research showed that this technology still cannot fully compete with metal strain gauges in terms of precision [Kreuzer, 2008], especially regarding temperature compensation. Therefore, this approach is not feasible for the *MIRO*.

Sensors based on the inverted magnetostrictive effect and strain gauges enable very compact sensors and signal processing components, and comply with the scaling paradigm. However, the compact dimensions of a strain gauge still have not been achieved by the magnetostrictive sensor. At the point of time, when the sensor design of the *MIRO* was determined, no commercial sensor based on this principle was available. Today, the range of available standard strain gauges is still substantially larger than those of magnetostrictive torque sensors. Regarding the motion ranges and speeds of the robot joints, the advantage of contact-free measurement offered by the magnetostrictive principle is secondary. However, the simplicity in design and the assumed stiffness (steel sensor body) are very promising.

The *MIRO* applies state-of-the-art metal strain gauges as sensor elements of the joint torques sensors, due to their very small size and simple, compact signal-processing electronics. Strain gauges are available in a comprehensive range of standard elements, enabling an optimised, in-house design of integrated multi-DoF sensors. Furthermore, the *Institute of Robotics and Mechatronics* of the *DLR* has notable expertise in the design of strain gauge sensors and their processing electronics[23].

[22] A typical interrogator for optical strain gauges is the *DI410* of *HBM Measurement*, Germany, realising a 1 kHz sampling rate for four separate channels. The dimensions of this component are 269 mm x 128 mm x 132 mm.

[23] Strain gauge based force torque sensors are applied e.g. in the *DLR LWR II* [Hirzinger et al., 2000], *LWR III* [Hirzinger et al., 2002], and *Hand II* [Butterfass et al., 2001].

	metal strain gauges	*magneto-strictive sensors*	BRAGG *grating sensor*
compactness of sensor element	+	0	+
compactness of signal processing	+	+	−
feasibility of adapted sensor designs	+	+	+
robustness regarding temperature	+	+	−
robustness regarding magnetic fields	+	0	+
range of available off-the-shelf elements	+	0	0
effort for assembling a multi-DoF sensor	0	+	−

Table 4.14: Rating of torque sensor principles

Table 4.14 summarises the rating of the three described sensor principles. It must be noted that the rating results shown are related to the dedicated requirements of the *MIRO* robot and cannot be seen as a general rating of these technologies.

The previous paragraphs identified strain gauges as a technical solution for the measurement of strains. In the following, the designs of the integrated sensors for the different joints of the robot are described. Figure 4.39 shows an abstracted view of the *MIRO* and the distribution of joint torque sensors. The alternating colours yellow and green indicate the demarcation between links.

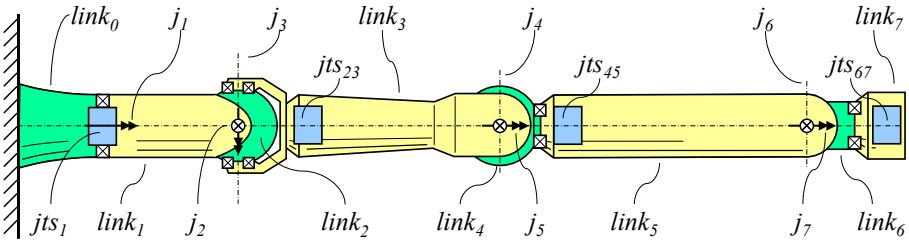

Figure 4.39: Overview of the joint torque sensor integration in the *MIRO* (bearings of j_2, j_4, and j_6 not depicted)

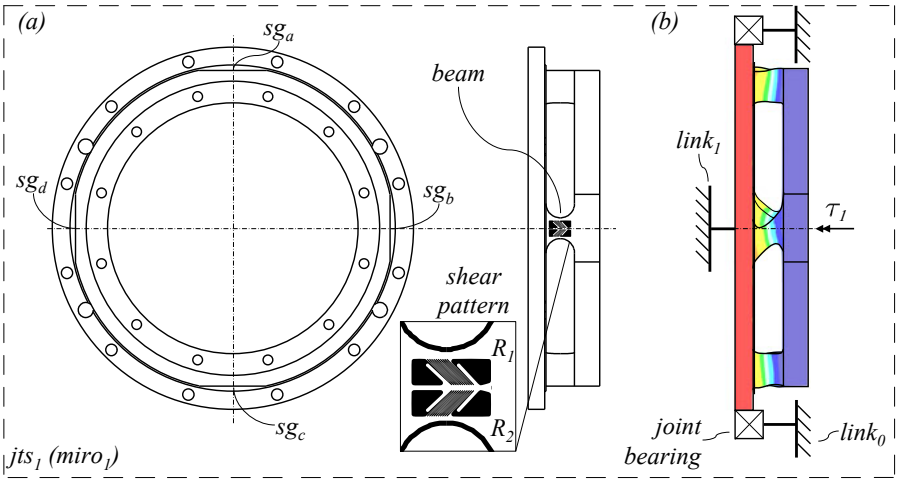

Figure 4.40: Single-DoF torque sensor concept for jts_1 ($miro_1$): two orthogonal views *(a)*, scaled deformation of the sensor body due to a joint torque τ_1 *(b)*

By this, two different joint torque sensor types for the *MIRO* can be distinguished:

- jts_1: The torque sensor of $miro_1$ is integrated between $link_0$ and $link_1$. The joint bearing shores external loads and only the joint torque is applied to jts_1 (classic torque sensor).
- jts_{23}, jts_{45}, and jts_{67}: These multi-DoF torque sensors are integrated into the next link (structural load sensor), beyond the last bearing of the couple joint. By this, all external loads are applied to the sensor bodies.

The next sections describe the design of the sensor bodies and the application of the strain gauges in detail.

4.5.5.1 Torque Sensor for $miro_1$

Joint j_1 of the *MIRO* is a single-DoF rotary joint and transmits the joint torque of reduction gear rg_1 to $link_1$. Based on the joint concept (compare section 4.5.2), it must integrate a hollow shaft design. Regarding the flux of forces and torques, this sensor is inserted between the reduction gear and the joint bearing (compare figure 4.40 *(b)*). Therefore, only the joint torque τ_1 is introduced to the sensor and other loads are supported by the joint bearing. In this sense, the sensor concept is similar to the joint torque sensors of the *DLR LWR III* [Hirzinger et al., 2002].

Figure 4.40 *(a)* shows the monolithic aluminium sensor body of jts_1 which is basically composed of two concentric ring bodies connected by four beams. Four

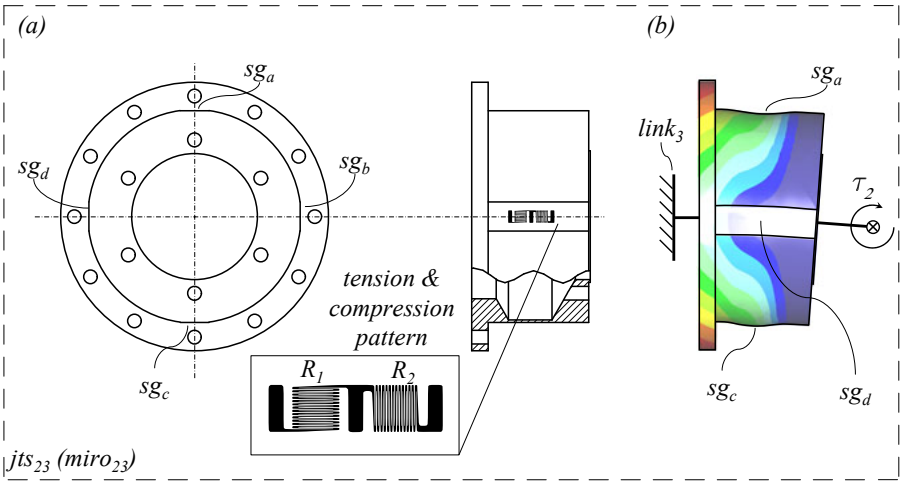

Figure 4.41: The 2-DoF torque sensor concept for jts_{23} ($miro_{23}$): two orthogonal views *(a)*, scaled deformation of the sensor body due to a joint torque τ_2 *(b)*

metal strain gauge elements (sg_a to sg_d) are applied to planar, exterior surfaces of these beams. The torque τ_1 of j_1 results in a deformation of the beams as indicated in figure 4.40 *(b)*. The dimensioning of the beams is optimised by FEM[24]. The maximum rated peak torque $\tau_{1,max}$ of j_1 thereby results in a maximum stress of up to approximately 50% of the yield strength of the sensor body material. Therefore, the sensor has an overload capacity of 100%. The shear-pattern strain gauges are applied to measure this deformation. Each of these strain gauges integrates a 90° arrangement of two single resistors (R_1, R_2). Two strain gauges on opposite sides (e.g. sg_b and sg_d) form a full bridge, consisting of four resistors. With a total of four strain gauges, the jts_1 sensor measures the joint torque τ_1 with two full bridges in a redundant way. The associated processing electronics are described in the later section 4.5.12. Regarding the scaling paradigm, variations of the maximum torque of this sensor can be achieved by adaptation of the beams' dimensions and are therefore feasible.

4.5.5.2 Torque Sensor for $miro_{23}$

The demands regarding the torque measurement of joints j_2 and j_3 differ significantly from those of joint j_1. The selected 2-DoF coupling mechanism (compare section 4.5.3.1) impedes a single-DoF dedicated torque sensor for each DoF due to the differential principle. Regarding the flux of torques in this mechanism, both joint

[24]FEM is the abbreviation for Finite Element Method

torques "appear" simultaneously at the joint-sided bevel-gear pinion (pin_{23}). Due to the joint bearing, the first part where both torques can be measured is the arc-shaped stirrup (compare figure 4.39). In order to allow a simple, rotation-symmetric shape of the sensor and to achieve a certain level of modularity at this point (exchangeable sensor), the joint torque sensor of $miro_{23}$ is designed as an additional component connecting the stirrup with $link_3$. Therefore, this sensor must measure two torques perpendicular to its rotation axis (bending).

Figure 4.41 *(a)* depicts the concept of the joint-sided torque sensor jts_{23} of $miro_{23}$. The aluminium sensor body has a tubular shape with flanges at both ends for integration into the robot structure. Four metal strain gauge elements (sg_a to sg_d) are applied to exterior planar surfaces of the sensor. The dimensioning of the wall thickness is optimised by FEM to approximately 50% of the yield strength of the material[25] at the maximum rated peak torques $\tau_{2,max}$ and $\tau_{3,max}$. Strain gauges with two single orthogonal resistors are applied, designed to measure tension and compression along their longitudinal axis.

The torques τ_2 and τ_3 of $miro_{23}$ result in a bending of the sensor body. Exemplarily, this deformation is shown in figure 4.41 *(b)* for τ_2. Due to this deformation sg_a gets stretched (its resistance R_1 increases) and sg_c is being compressed (decrease of R_1). The resistances R_1 of the other strain gauges sg_b and sg_d change in the same way and compensate for change of the total length of the sensor body. Resistors R_2 compensates for shear forces. Therefore, sg_a and sg_c form a full bridge for the measurement of τ_2, sg_b and sg_d for τ_3. Other loads on the sensor, e.g. forces along the rotation axis of the sensor body are compensated for by this transducer arrangement. With a total of four strain gauges, the jts_{23} sensor measures the joint torques τ_2 and τ_3 without redundancy. However, this could easily be accomplished by additional strain gauges. Regarding the scaling paradigm, the arguments given for jts_1, also apply here.

Although this sensor is designed to have a hollow shaft, the joint design does not require this characteristic for the internal cable conduit, as the cable harness of the robot passes on the outside of the sensor (compare figure 4.26, on page 117). It must be noted that the point of measurement of jts_{23} has a significant spatial distance to the joint axes j_2 and j_3 (see figure 4.41 *(b)*), which can be seen as the main difference to the concept of jts_1. This results in the following consequences:

- external loads on parts of the robot, which are located between the sensor and the joint axes (e.g. stirrup) are not measured
- the control of this joint must take this distance into consideration

[25] This results in an overload capacity of 100%.

Regarding hands-on robotic applications, the first issue take precedence because it results in an absence of haptic interaction with these parts of the robot. For example, applying forces to the stirrup of $miro_{23}$ does not result in an impedance-controlled motion of the arm. However, experience with the *MIRO* prototype proved that this disadvantage is negligible because of the small amount and size of "insensitive" portions of the joint. The impact of the distance between sensor jts_{23} and the joint axis on the control is described in the later section 4.5.12.

4.5.5.3 Torque Sensors for $miro_{45}$ and $miro_{67}$

The elbow and wrist of the *MIRO* robot are both composed of 2-DoF pitch-roll joints. Therefore, the same torque sensor concept with a different scale can be applied for these joints. Like the torque sensor jts_1, the torque sensors jts_{45} and jts_{67} must integrate a hollow shaft design. Due to the coupling mechanism, jts_{45} and jts_{67} must be integrated between the joint-sided bevel gear of the differential mechanism and the following link. Therefore, the torque sensors jts_{45} and jts_{67} rotate about the roll joint axes j_5 and j_7, respectively (joint rotation angles q_5, q_7). Consequently, the torque about the pitch joint axes j_4 and j_6 cannot be measured directly by the sensors. To solve this problem, sensors jts_{45} and jts_{67} are designed to measure three orthogonal torques, whereby the torque about the longitudinal axis equals the torque of the roll joint (τ_5, τ_7). The two other (bending) torques (τ_x, τ_y) can be seen as an orthogonal vector pair, as depicted in figure 4.42, for example, for the jts_{45} sensor. In order to compute the actual torque τ_4, the vector addition of τ_x and τ_y is projected onto the direction of j_4. Furthermore, a second torque $\tau_{\perp 4}$ is computed, which represents the transverse moment on the joint. Although this torque cannot be applied for the control of this joint, it can be used for the compensation of transverse elasticities. Like the preceding sensors, jts_{45} and jts_{67} are optimised to grant an overload capacity of 100%.

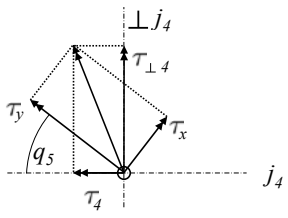

Figure 4.42: Torque sensor jts_{45}: transformation between the measured torques τ_x, τ_y and τ_4

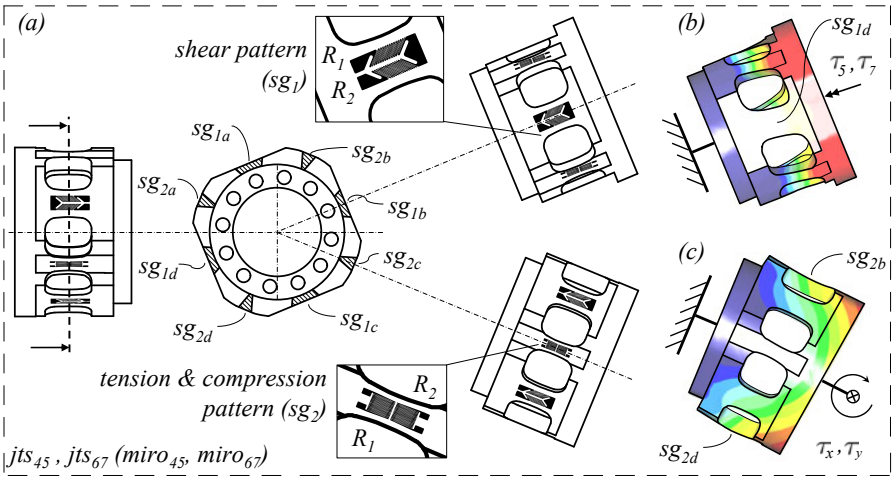

Figure 4.43: The 2-DoF torque sensor concept for jts_{45} ($miro_{45}$) and jts_{67} ($miro_{67}$): four views of the sensor *(a)*, scaled deformation of the sensor body due to a joint torque τ_5 respectively τ_7 *(b)*,scaled deformation of the sensor body due to a bending torque τ_x or τ_y.

The sensors jts_{45} and jts_{67} must measure one rotary torque (τ_5, τ_7) like jts_1 and two orthogonal bending torques like jts_{23}. The design of the sensors therefore merges the concepts of jts_1 and jts_{23}. Figure 4.43 *(a)* shows multiple views of jts_{45} and jts_{67}, which are basically composed of two concentric ring-shaped flanges connected by a total of eight beams (compare cross-section view in figure 4.43 *(a)*). Four of the beams are equipped with strain gauges for the measurement of shear strain (sg_{1a} to sg_{1d}). These strain gauges measure the rotary torque (τ_5, τ_7). The resulting deformation is illustrated exaggeratedly in figure 4.43 *(b)*. Thereby, the strain gauges sg_{1d} and sg_{1a} (opposite side) measure this deformation. The torque about the roll axis (τ_5, τ_7) is therefore measured by two full bridges and is redundant. In contrast, τ_x and τ_y are each measured with one full bridge.

Tension- and compression-sensitive strain gauges (sg_2) are applied to the other four beams, to measure the two bending torques τ_x, τ_y (compare figure 4.43 *(c)*). The explanations regarding the scaling of the sensors and the offset between the point of measurement and the actual joint axis, given in the preceding sections, also apply for this sensor design.

4.5.5.4 Overload Protection of Torque Sensors

As described above, the sensor bodies of the joint-sided torque sensors are optimised for an overload capacity of 100%. Beyond this limit, the plastic deformation of the

sensor bodies is evoked. Although overload protection in the form of mechanical end stops is feasible [Sporer and Hähnle, 2003], the *MIRO* joint-sided torque sensors reject this approach because of the following assumption. Preventing overload of the torque sensors is feasible during the operation (power-on state) of the robot due to collision avoidance, proper planning, knowledge of loads (e.g. payload), and, last but not least, torque sensing. In contrast, the handling of the robot in a clinic during setup, cleaning and storage is not monitored. Therefore, improper handling can cause overloads on robot components. Regarding the mechanical flux in the robot, this can result in damage of the reduction gears, differential bevel gears, torque sensors, structure links, and housings. It must be anticipated that such damage will remain undetected and the robot will thereafter be used in an operation. Therefore, the torque sensors are designed as the weakest link in the mechanical flux, because only they enable the detection of former overloads. For example, a plausibility check after power-on can be performed, where a comparison of the virtual robot model with the actual values of the sensors identifies plastic deformations. However, if this approach turns out not to be feasible in clinical practise or incompatible with emerging safety standards, it is feasible to equip the sensors with a mechanical overload protection.

4.5.6 Motors, Motor Position Sensors and Brakes

Motors, motor position sensors, and safety brakes of the *MIRO* are mechatronic components forming the drive side of the joints. Due to their adjacent integration and relation to the electronics, the selection of technological solutions for these components is tightly interwoven.

4.5.6.1 Motors

The application of motors which convert electricity to mechanical power has been state-of-the-art technology in robotics since its beginning. However, other principles are applied in robotic systems as well, like artificial pneumatic muscles for anthropomorphic robot hands (e.g. *Dexterous Hand* by the *SHADOW ROBOT COMPANY* [Shadow Robot Company, 2003]), fluidic actuators (e.g. *Fluid Hand* by the *Institute for Applied Computer Science, Forschungszentrum Karlsruhe* [Schulz et al., 2001]), or even liquid-fuelled anthropomorphic arms [Fite et al., 2006].

Artificial pneumatic or fluid muscles are applied mainly because of their compact size and weight in combination with high strength. Nevertheless, these systems apply the fluid or pneumatic-actuation technology as an intermediate step of power transformation between electric power and mechanical power, due to the common availability of electric power. Therefore, systems applying these technologies mostly integrate

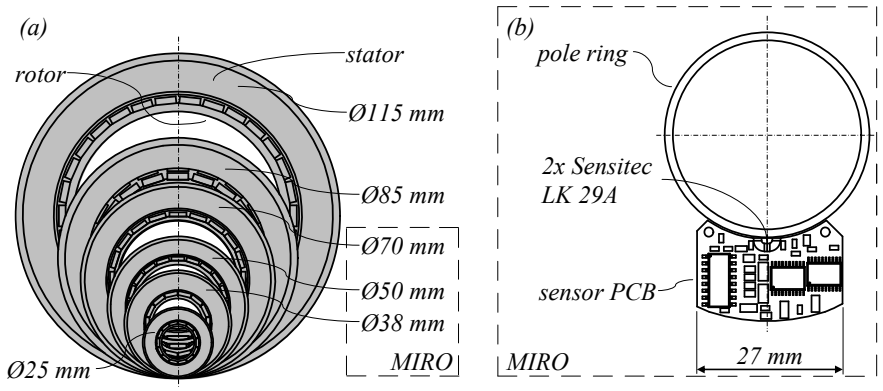

Figure 4.44: Diameter range of the *ILM* motor *(a)*, the MR-sensor for commutation *(b)*

additional electricity-driven components like compressors or pumps for pressurising the medium. The major benefit of these technologies is the possible distribution of the components. The large and heavy devices for transforming electric power to, for example, pressurised gas, can be located almost arbitrarily, for example in stationary parts of the system. Only the compact and lightweight actuators which generate mechanical power based on the pressurised gas must be integrated into moving parts of the robotic system. Often, these actuators are then even coupled with a tendon-based transmission to work with moving links. This appears to be a valuable benefit regarding design paradigm 2 (compact design) of the *MIRO*. However, artificial muscles as indicated by their name are mainly targeted at the generation of linear motions and forces [Festo, 2008]. In order to enable pivot motions, these muscles are applied according to the principle of leverage. Therefore, they are mainly applied in pitch or yaw joints (e.g. finger joints of robot hands), but only rarely for rotary joints. This correlation is different with electric motors, which are applied mainly as rotary drives and rarely as linear motors in robotics. Regarding the rotary joints of the *MIRO* and their required large motion range, the application of artificial muscles is assumed not to be beneficial for the *MIRO*.

The *MIRO* robot integrates electric rotary motors for the actuation of the joints. Although multiple principles of electric motors are feasible like ultrasonic, piezo, or magnetostrictive motors, the *MIRO* applies the *ILM*[26] synchronous motor, a technology developed in-house, due to synergistic effects in electronic design and control.

The *ILM* motor was developed at the *DLR, Institute of Robotics and Mechatronics* with a specific focus on the demands of lightweight robotics [Dietrich et al., 2003].

[26]ILM is the german abbreviation for “Innen Läufer Motor” (english: inrunner motor).

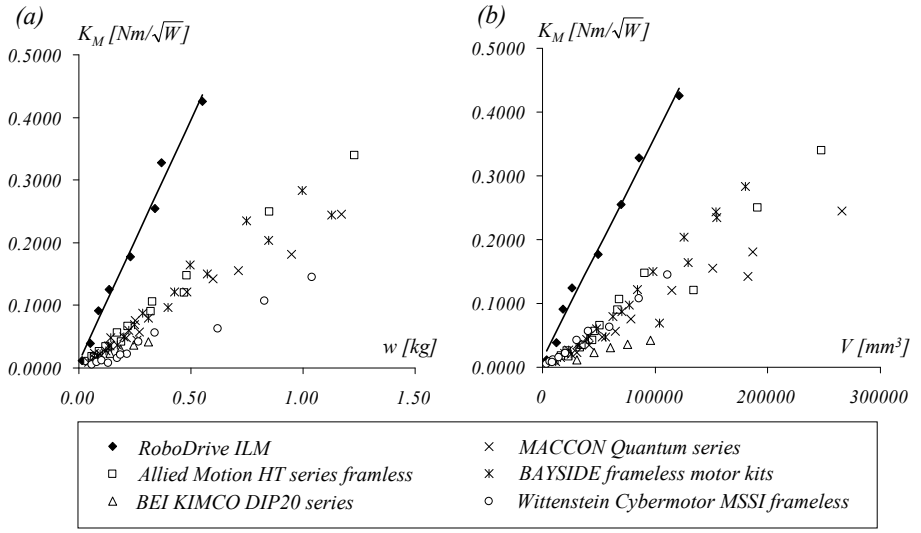

Figure 4.45: Comparison of various BLDC motors: motor constant K_M with respect to weight w $[kg]$ *(a)*, motor constant K_M with respect to volume V $[mm^3]$ *(b)*

These demands can be formulated in the same way for the *MIRO* and comprise:

- minimised weight of active mass, in order to comply with the lightweight approach and to enhance the motor dynamics,
- reduced electric losses in order to reduce the generated waste heat,
- hollow shaft design ($miro_1$), and
- enhanced torque-to-size ratio regarding the design paradigm 2.

The *ILM* motor (compare figure 4.44 *(a)*) is a permanent-magnet synchronous motor and consists of a stator with individual windings for each pole connected separately or as blocks to the energy supply. The poles are embedded in a polymeric matrix. The rotor is implemented as an inrunner with permanent magnets on the perimeter of a metal ring. The numbers of poles of the stator and of the rotor differ by at least one. In order to enhance the torque-to-weight ratio and to reduce the electric losses, the *ILM* was optimised regarding the shape of the laminated stator stack, the number of poles, as well as the number of windings [Lemke and Hirzinger, 2004]. Furthermore, size and torque for each size have been optimised regarding compatibility to Harmonic Drive gears with corresponding dimensions. Figure 4.45 depicts a comparison of the *ILM* motors with other available frameless BLDC motors regarding the motor constant K_M $[^{Nm}/\sqrt{W}]$ with respect to the weight w $[kg]$ and to the volume V $[mm^3]$ (compare

data in appendix C.5). The motor constant is a direct indicator for the torque of the motor scaled to the electrical power. The calculation of the motor volume already subtracts the volume of the hollow shaft.

Figures 4.45 *(a)* and *(b)* show descriptively the high torque-per-weight and volume of the *ILM* motors. However, it must be stated that this is only a brief and barely exhaustive comparison with a special focus on the size and weight of the motors. Furthermore, the concept of the *MIRO* is not limited to the integration of the *ILM* motors and other BLDC motors can be applied as well. For motors with a voltage rating from 24 V to 48 V and the same pole pair number as the *ILM*, even the motor position sensor and the *MIRO* electronics can be applied without changes.

The *ILM* motor technology was transferred to a commercial product, manufactured by *RoboDrive*, Germany. Basic specifications and dimensions are listed in tables C.5, C.6 in appendix C.4 and in table C.11 in appendix C.5. The *ILM* is available as frameless kit, leaving the design of bearings, housing, and shaft open to the designer of the robot. Therefore, a high level of integration can be achieved.

Regarding the demonstrated efficiency of the *ILM* motors, the range of available sizes and torques and the exchangeability with other BLDC motors, this design decision complies with the scaling and design paradigms.

4.5.6.2 Motor Position Sensors

The integration of motor position sensors pursues two main targets. First, due to the brushless design of the motors, the motor position is needed as commutation signal. The commutation of the motor is the process which switches the motor currents for the stator windings in relation to the actual position of the permanent magnetic field of the rotor (rotor position). Second, the motor positions combined with the gear ratios are used in the control of the *MIRO* to determine the joint positions. Therefore, a high precision motor-position sensor is advantageous for both, the electric control of the motor and the control of the robot.

The in-house developed MR-Sensor is specifically tailored to the demands of the *ILM* motor technology (e.g. hollow shaft, robustness, accuracy, pole counts). The frameless sensor kit consists of a circuit board mounted on the stationary part of the motor (stator) and a thin polymer (*TROMADUR*®) or ferrite ring, which is integrated on the rotating shaft of the motor (compare figure 4.44 *(b)*).

In contrast to the mechanical angle of the motor (α_{mec}), the MR-Sensor is supposed to measure the electrical angle of the stator in respect to the rotor (α_{elec}), which is needed for the commutation of the motor. One mechanical revolution of the motor (rev_{motor}) relates to the electrical revolution (rev_{elec}) with $n_{pole\,pairs,mot}$, the number of pole pairs of the motor, as follows:

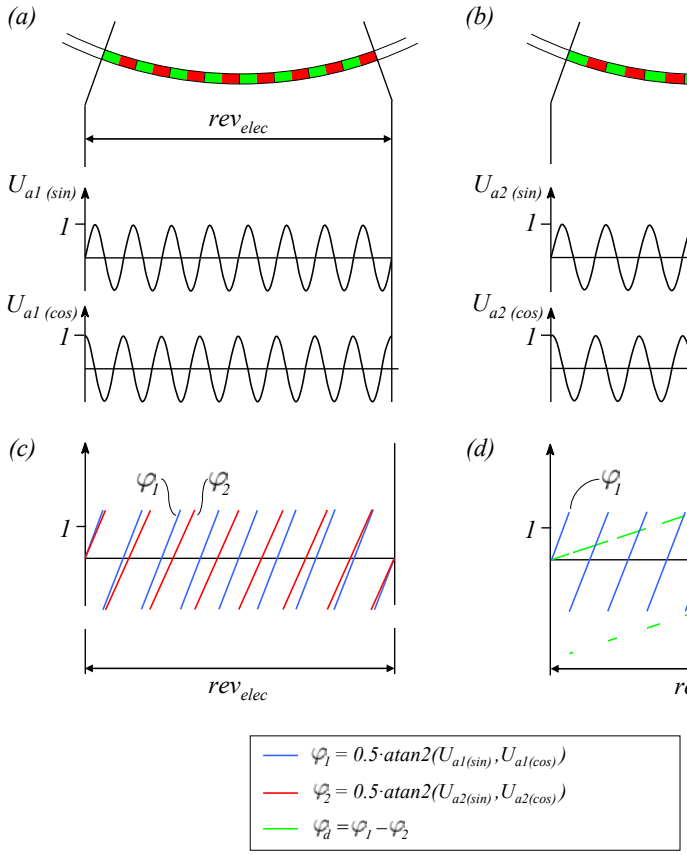

Figure 4.46: Voltage signals of the MR-sensor during one electrical revolution: eight pole pairs per electrical revolution *(a)*, seven pole pairs per electrical revolution *(b)*, calculated angle signals of both tracks *(c)*, angle signal of track 1 and subtraction of both angle signals *(d)*

$$rev_{mec} = n_{pole\,pairs,mot} \cdot rev_{elec} \tag{4.18}$$

In order to initially provide the absolute position within the electrical period, without the necessity of phase-finding procedures[27], the MR-sensor PCB integrates two magnetoresistive sensor chips (*Sensitec LK 29A* [Sensitec, 2007]) and the pole ring has two separate magnetisation tracks 1 and 2. The sensor chip measures the gradient (not the amplitude) of the pole ring's magnetic field passing by. Thus, it is

[27]If the motor position sensor is implemented as an incremental sensor, it does not provide the electrical angle initially. Therefore, phase-finding procedures "learn" the electrical angle by e.g. forcing a certain commutation and evoking an initial motor motion.

comparably robust regarding the distance between sensor and pole ring. The gradient of the magnetic field evokes a change in the electrical resistance of a ferromagnetic material, which is measured by two WHEATSTONE bridges on the chip. Thereby, a passing magnetic pole results in a sine and a cosine signal. Figure 4.46 *(a)* shows the sensor output voltages ($U_{a1\,(sin)}$ and $U_{a1\,(cos)}$) for a pole ring track with eight pole pairs per electrical revolution. The two magnetisation tracks 1 and 2 of the pole ring have different numbers of magnetic pole pairs within an electrical revolution (compare figure 4.46 *(a)* and *(b)*). By composition of the sine and cosine signals of each track, the angle signals φ_1 and φ_2 are calculated (see figure 4.46 *(c)*). These angles show the absolute position of the sensor in relation to a single dedicated pole pair of the corresponding magnetic track. To enable absolute position sensing (α_{elec}) in relation to the complete electric revolution ($rev_{elec,}$), the *nonius principle* is applied. For this, the nonius signal φ_d is computed, as shown in figure 4.46 *(d)*, which is used to identify the actual pole pair within the electric revolution. The combination of φ_1 (angle in relation to pole pair) and φ_d (identified pole pair) results in absolute position measurement within rev_{elec}.

The pole rings are available in corresponding diameters and pole counts for all *ILM* motors and the MR-sensor PCB integrates a communication interface based on the *BiSS* protocol [iC Haus, 2008] for the connection with the *MIRO* electronics. The MR-sensor was transferred to a commercially available product manufactured by *RoboDrive GmbH*, Germany, rated with an accuracy of $\pm 0.06°$ (mechanical revolution) at speeds up to 7000 rpm.

4.5.6.3 Brakes

As defined in sections 4.5.2 and 4.5.3 on the different joint concepts, the *MIRO* integrates motor-sided brakes because of the backdrivability of the coupling mechanisms and the Harmonic Drive gear. The brakes have different aims. First, the brakes must hold the robot exactly in its pose when the system is electrically powered off. Otherwise, the mass of robot links and payload would backdrive the robot joints, moving the arm in uncontrollable postures and to mechanical motion range limits of the joints. This would result in a deadlock situation, regarding software safety thresholds at both ends of the motion range of joints. Second, the brakes are applied to perform emergency stops of the robot. It must be stated clearly that normal stop procedures, for example when the robot must maintain a certain pose during an application, are performed by the motors and not by the brakes.

The brakes require a failsafe design and must block joint motion during power-off phase. In order to avoid storage of electric energy for this purpose, the braking action must be performed by a passive solution and releasing the brakes by an active

approach. Regarding the use of electro-magnetic motors and sensors, the robot already integrates various electrical components. Consequently, the safety brakes of the *MIRO* base on an electro-mechanical actuation for releasing the brake and mechanical springs for braking. In order to achieve a smooth stop of the motor at any rotary position, the *MIRO* applies friction-based brakes instead of form-fit locking brakes.

Regarding the high integration level of the joints, only $miro_1$ allows a more or less commercial, off-the-shelf brake. This joint module integrates the electro-magnetic spring-applied safety brake *RSM-70* manufactured by *Chr. Mayr GmbH & Co. KG*, Germany. However, other safety brakes like the *ROBA-stop* series [Mayr, 2008] are also applicable. Figure 4.47 *(a)* depicts the *RSM-70* brake. The stationary part integrates copper windings (coil), which evoke an electro-magnetic force on the spring-supported brake $disc_a$. The rotating hub is connected to the motor shaft (not depicted) and contacts the brake pad by a tooth geometry. Due to the serration between these two parts, they are coupled regarding rotation, but the pad can still move axially in relation to the hub. If no current is applied to the coil, multiple springs press $disc_a$ and the brake pad against the stationary $disc_b$. Therefore, two contact surfaces are used for braking. Due to the friction between the different materials and the force of the springs, two equal friction forces $F_{friction}$ are evoked, which result in a brake torque of $\tau_{RSM-70} = 0.55\,Nm$ acting against the rotary torque of the hub (compare descriptions in appendix C.4, page 253). By applying an electric current to the coil, an electro-magnetic field evokes, according to LORENTZ, an attracting force on the ferromagnetic $disc_a$ which releases the brake against the spring force.

In order to achieve a more compact brake, $miro_{23}$, $miro_{45}$, and $miro_{67}$ apply a plunger-coil actuator designed in-house, depicted in figure 4.47 *(b)*. By applying a current, the coil generates an electro-magnetic field which evokes an attraction force ($F_{actuator}$) on the ferromagnetic plunger of up to 14 N (24 VDC, 0.5 A). The compact dimensions of the actuator enable a very tight integration, for example, in the motor modules of $miro_{23}$ and $miro_{45}$ as depicted in figure 4.47 *(c)*. Here, the motor, motor position sensor (not depicted), and the brake are integrated into a module in order to simplify identification of parameters and testing. The housing of this module incorporates a central stationary tubular portion on which the rotor of the motor is pivoted with bearings. Inside this tubular portion, the brake actuator is integrated. If no electric current is applied to the brake actuator coil, the integrated spring presses the braking pad (*Raybestos® R-211* polymer, $\mu_{R-211,\,steel} = 0.6$) which is not rotating against the rotating motor shaft, which results in the desired braking torque (e.g. 0.1 Nm for the two brakes in $miro_{45}$). By applying an electric current to the coil, an electro-magnetic field evokes a force on the plunger, which releases the brake against the spring force. The compact design of the integrated motor-brake-

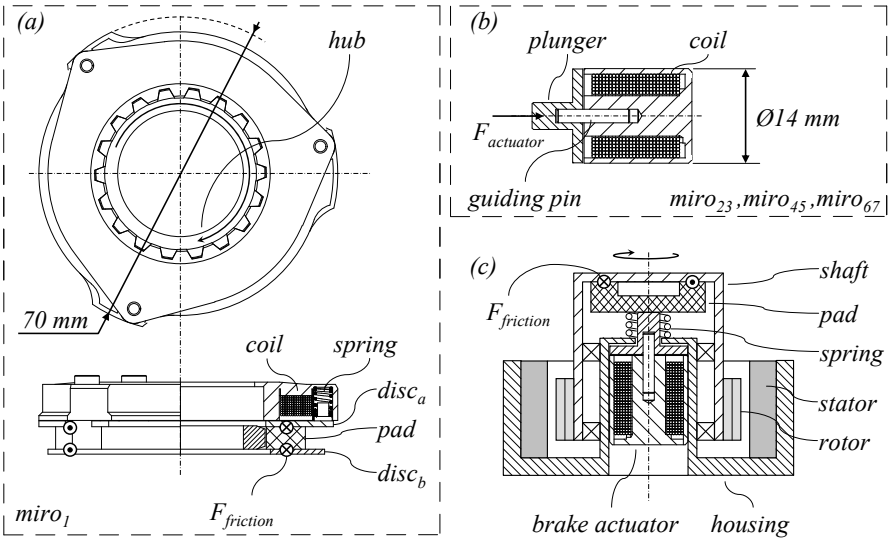

Figure 4.47: Brakes of the *MIRO* robot: *MAYR RSM-70* for $miro_1$ *(a)*, brake actuator for $miro_{23}$, $miro_{45}$, $miro_{67}$ *(b)*, simplified depiction of the brake actuator integration in $miro_{23}$ and $miro_{45}$ *(c)* (note: drawings *(a)*, *(b)*, and *(c)* have different scaling)

module is possible due to the hollow shaft design of the *ILM* motor.

Both brake types enable compact design and can be scaled regarding their braking torque. The *MAYR RSM-70* can be replaced by a range of *ROBA-stop* types with higher braking torques. The brake design of the other joints, involving the brake actuator designed in-house, can be scaled by various parameters without profound changes of other components. Among these are the diameter of the braking pad/disc, the number of friction contacts, and the length of the brake actuator. With this, the selected braking technologies comply with the design paradigms (e.g. compact design) and the scaling paradigm.

4.5.7 Joint Position Sensors

As described in the preceding section 4.5.6.2, the *MIRO* integrates absolute position measurement of the electric motor angles. The measured positions are very accurate due to the following transmission by the reduction gear. The robot control (e.g. joint position control) is based on these motor-sided sensors. However, the absolute joint positions cannot be directly derived from these data because of the multiplicity of electric rotations per mechanical revolution of the motor, the reduction gear ratios, and the coupling mechanisms of the joints. As stated with the design paradigm 4 (sensor integration, section 4.3.4), it is required to immediately receive the joint positions

after power-on of the robot, without the necessity of an initialising trajectory. Therefore, the *MIRO* additionally integrates joint-sided rotary position sensors to provide the initial posture of the robot and to enable monitoring of the motion range limits of the joints. The description of design paradigm 1 (lightweight design, section 4.3.1) already showed that the intended lightweight approach for the *MIRO* can result in a elastic deflection of the robot links due to internal and external loads. Therefore, the joint positions alone are not sufficient to enable high accuracy Cartesian applications and additional external system components (e.g. optical tracking system) are necessary for such applications. Thus, the accuracy demand of the integrated joint-sided position sensors can be rated as average. Due to the complex and compact design of the coupling mechanisms and the demand of measuring the different joint positions directly, without calculation of the coupling mechanisms, the possible locations for the joint-sided position sensors are sparse and divergent. Furthermore, the desired compact dimensions of the joints demand adaptable dimensions of these sensors to comply with the available space. In this regard, integrated COTS[28]-sensor units (e.g. encoder) with housings, bearings and determined mechanical interfaces are not feasible. The requirements for the joint-sided position sensors can therefore be formulated, as follows:

- absolute position measurement
- hollow shaft design
- compact and adaptable design
- average accuracy (at comparably low sampling rate)
- robustness

Sensing the relative position of two objects can be done by applying various physical principles. For the *MIRO*, two different state-of-the-art sensor concepts have been considered for the measurement of the joint positions.

Optical Absolute Encoder The basic principle of rotary optical position sensors comprises a light source, a receiver and a coded rotating transmitter or reflector disc. This disc integrates areas which enable (I) or disable (O) the transmission/reflection of the light from the source to the receiver. Incremental sensors integrate a multiplicity of light-absorbing radial lines on a circular track of the reflecting or transparent disc. A rotation of the disc results in a switching of the receiver signal, which can be counted and thereby the rotary angle can being computed. However, in order to enable an

[28] Commercial Off-The-Shelf product

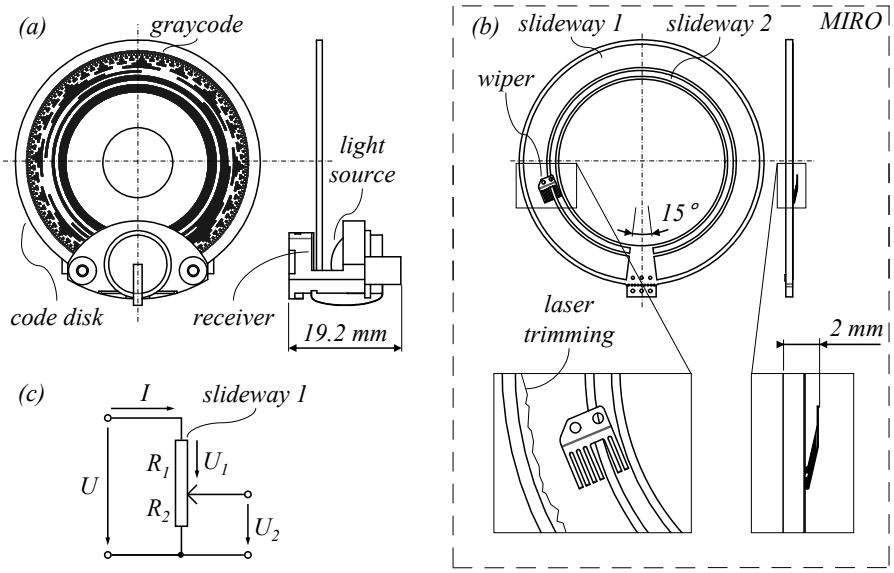

Figure 4.48: Rotary joint position sensors: *NEMO2, OPTOLAB Microsystems (a)*, custom conductive plastic potentiometer *(b)*, voltage divider *(c)* (Note: drawings *(a)* and *(b)* have same scaling)

absolute position measurement, this simple approach is not feasible. Absolute optical position sensors therefore apply a more complex coding of the disc. A very popular solution is the *graycode* principle named after Frank Gray, where the disc integrates multiple circular tracks with different optical encoding. The signal of each track represents thereby a digit of a binary word, which relates directly to the rotation angle of the disc (compare appendix C.6).

A very compact absolute-position encoder based on the optical graycode principle is the *NEMO3* sensor by *OPTOLAB Microsystems* [Optolab Microsystems, 2006]. This sensor consists of a stationary part integrating the light source, receiver and interface electronics, and a transparent graycode code disk (polymer). The sensor achieves a remarkable absolute resolution of 16 bit at a $1\,\mu s$ cycle. However, in-house tests with the parent version *NEMO2* (compare figure 4.48 *(a)*) showed a strong sensitivity of the optical path regarding particles like dust or lubricants. Therefore, an additional encapsulation of the sensor in the *MIRO* would be necessary, protecting the sensor from lubricants and dust. Regarding the integration level of the joints, this requirement hinders the achievement of the most compact design.

Conductive Plastic Potentiometer This sensor technology is based on the correlation between the electrical resistance and the length of a conductor. The electrical

resistance R [Ω] of a conductor is calculated by a given cross-section area A [m^2], length l [m], and the electrical resistivity ρ [Ωm] of the material (compare equation 4.16 in section 4.5.5). Potentiometers do not physically change the length of the conductor. The conductor with a dedicated length is tapped by a sliding contact (e.g. wiper), which can be moved along the conductor. If the cross-section area A and the electrical resistivity ρ vary along the length of the conductor, the resistance $R(x)$ at the tap position x is calculated by equation 4.19:

$$R(x) = \int_0^x \rho\,(x) \cdot \frac{1}{A(x)} dx \ . \tag{4.19}$$

Increasing x therefore always results in a gain of resistance and the function of the resistance $R(x)$ is therefore strictly increasing. Figure 4.48 *(b)* depicts a custom conductive plastic potentiometer designed for j_7 of $miro_{67}$. The sensor consists of a PCB with two conductive slideways and a metallic wiper, which short-circuits the two slideways at a variable rotary position. The two components are mounted to the opposing sides of the moving joint, whereby the wiper must be integrated into and electrically isolated from conductive parts of the joint. A rotation of the joint therefore moves the wiper along the slideways. Slideway 1 is connected with both ends and slideway 2 with one end to the electronics implemented in the form of a voltage divider. The full resistance of slideway 1 is comparably high (e.g. $R_{slideway\,1} = 30\,k\Omega$ in the *MIRO*) and that of slideway 2 is negligible ($R_{slideway\,2} \ll R_{slideway\,1}$)[29]. The resulting voltage divider is depicted in figure 4.48 *(c)*. For a given supply voltage U, known total resistance of slideway 1 ($R_1 + R_2$) and a measured voltage U_2, the resistance of R_2 calculates as follows [Kuchling, 1989a]:

$$R_2 = \frac{R_1 + R_2}{U} \cdot U_2 \ . \tag{4.20}$$

R_2 relates directly to the wiper position and is a direct measure of the rotary angle of the position sensor. Due to manufacturing tolerances (e.g. thickness of the slideways) this function is not linear. Therefore, conductive plastic potentiometer manufacturers offer the option of laser trimming of the slideways, which cuts off a circumferential portion of e.g. slideway 1 by means of a laser. The outline of the laser cut is calculated from a resistance measurement during a rotation of the sensor monitored by a reference (high accuracy) encoder. Therefore, a linearity of $\pm 0.1\%$ can be achieved [Metallux, 2006]. However, the correlation between R_2 and the rotary

[29] Both slideways apply usually the same conductive material in order to balance the abrasion and achieve high dependability of the wiper contact. In order to eliminate the resistance of slideway 2, an additional layer underneath with high conductivity is integrated to short circuit the conductive material of slideway 2.

angle is not known, as it is with the digital optical encoder. Gain and offset of the sensor must be calibrated. Although every change in position of the wiper results in a change of the resistance and by this the sensor resolution is theoretically infinite (analogue sensor principle), the accuracy and resolution is limited by the electric signal processing (signal-to-noise ratio), thermal effects, remaining non-linearity, and elastic deformation of the wiper.

Regarding figures 4.48 *(a)* and *(b)*, which have equal scaling, the compact size of the conductive plastic potentiometer is apparent. Although the *NEMO3* sensor by *OPTOLAB Microsystems* is available in a more compact version (*NEMO3 - Super Flat Module*), the overall thickness of only 2 mm of the conductive plastic potentiometer is unmatched. However, it must be stated at this point that the *NEMO* sensors already integrate the signal processing electronics with a digital communication interface. The necessary space for these electronic components must be added to the conductive plastic potentiometer. According to design paradigm 5 (internal cabling), the distance between the electronics and the potentiometer must be very short and the applied cabling must be shielded for EMC reasons. Furthermore, this sensor principle does not enable 360° rotation or multi-turn (e.g. 345° maximum rotary range in the *MIRO* as depicted in figure 4.48 *(b)*). However, the design of the PCB and thereby the slideways is only limited by the wiper geometry (minimum widths and offsets of the slideways), which provides a large design space and therewith the feasibility of adapted designs for the dedicated spatial requirements in the *MIRO*. Due to the scraping contact of the wiper with the slideways, this technology is very robust against contamination with lubricants[30], which additionally enables integration close to reduction gears without the necessity of sealed encapsulations.

Table 4.15 summarises the decisive differences of both sensor concepts with a special focus on the demands (design paradigms) of the *MIRO*. Therefore, the decision balances high accuracy at high speeds and multi-turn ability on one hand, with compact dimensions and robustness against contamination on the other. Regarding the demands formulated in the beginning of this section, a very high accuracy is of minor interest due to the fact that the absolute joint position cannot be applied for Cartesian position control. Furthermore, the multi-turn capability would only benefit rotary joints and in this case is limited by the internal cable harness. Although it is feasible to adapt the design of the code discs of the optical sensor to dedicated constraints (e.g. realisation of a larger hollow shaft, circular segment shaped discs), this adaptation is simpler for the conductive plastic potentiometers, due to the applied manufacturing process[31]. Regarding the advantages of robustness and very compact,

[30] This does not comprise a general assumption on the chemical resistance of the applied materials.
[31] The production of conductive plastic potentiometers is based on a standard PCB manufacturing

as well as adaptable design, the *MIRO* applies custom conductive plastic potentiometers for joint position sensing in all joints. However, for future versions of the robot it might be interesting to apply the joint-sided position sensor for closed-loop control of the joints. Then, the demand for a sensor concept with higher accuracy, like optical position sensors or a modified MR-sensor (compare section 4.5.6.2) comes to the fore.

	optical position sensor NEMO3	*MIRO potentiometers*
resolution	16 bit @ 1 MHz	13 bit @ 3 kHz
absolute measurement	+	+
multi-turn	+	−
robustness regarding contamination	−	+
compactness	0	+
feasibility of adapted designs	0	+

Table 4.15: Rating of joint position sensor principles

4.5.8 Base Interface

The base interface mechanically connects the robot with its environment. Most robots, like industrial robots, are designed for the possibility of mounting the robot arm to the floor as depicted in figure 4.49 *(a)*.

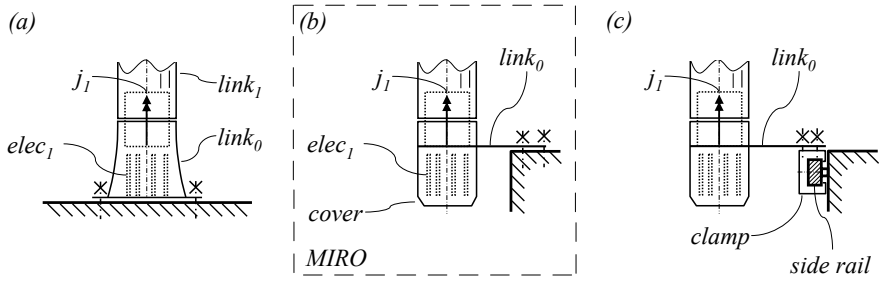

Figure 4.49: The $link_0$ concept: turret-like design *(a)*, lateral interface design *(b)*, adaptation of the lateral design for mounting the robot to the side rails of an operating table *(c)*

Therefore, these concepts apply a turret-like design of $link_0$ with fastening bores for the connection to the floor. Regarding the integration and accessibility (maintenance) of the electronics $elec_1$ of $miro_1$, the tubular design of $link_0$ demands radial apertures, which reduces the stiffness or increases the weight of $link_0$. Furthermore,

process. The slideways are applied to the PCB by thick-film printing.

the necessity of mounting the *MIRO* to the floor is not a given in the OR. As a result, the *MIRO* applies a lateral mechanical interface $link_0$ as it is illustrated in figure 4.49 *(b)*. Thereby, a structural part with a radial lever is connected directly to the stationary side of j_1. This lever can be equipped with various mechanical interfaces to mount the robot to stands, ceiling support systems, or the side rails of an operation table[32] (see figure 4.49 *(c)*). The electronics $elec_1$ is protected by an unencumbered cover, which can be removed completely to gain access to the electronics (compare figure 4.49 *(b)*). However, if floor mounting is necessary (e.g. for identification of parameters during testing of the robot) the implementation of an additional turret-shaped adapter is feasible.

4.5.9 Upper Arm Link

As described in section 4.5.1 on the structure design of the *MIRO*, the elongated links of the upper arm and forearm are based on a skeletal concept consisting of internal load-carrying structures surrounded by electronics and covered by housings. In order to compensate for the low geometrical moment of inertia and torsion constant of the central load-carrying structure, a material with a high Young's modulus is chosen to increase the stiffness of these parts. In contrast to common materials in lightweight design like aluminium or carbon fibre laminates, the *MIRO* applies *STARCERAM® S:SSiC* ceramics manufactured by *H.C. Starck Ceramics*, Germany, for the structural part of $link_3$. This pressureless sintered silicon carbide material has a density of 3.1 g/cm^3 [H.C. Starck Ceramics, 2009], which is slightly higher than aluminium (e.g. 2.7 g/cm^3 for AlZnMgCu1.5 [Aluminium-Zentrale, 1988]), but with 395 GPa an approximately 5.5-times higher Young's modulus (70 GPa for technical aluminium alloys [Aluminium-Zentrale, 1988]). By this, the material is suited to compensate for the reduced low geometrical moment of inertia and torsion constant of $link_3$ regarding stiffness. Furthermore, this ceramic material shows a very small coefficient of thermal expansion of $4.5\,[\cdot 10^{-6}K^{-1}]$ [H.C. Starck Ceramics, 2009] compared to aluminium (e.g. $23.4\,[\cdot 10^{-6}K^{-1}]$ for AlZnMgCu1.5 for temperatures between 20 to 100°C [Aluminium-Zentrale, 1988]). Regarding the dissipation of waste heat from the electronics integrated into the robot links, this results in a significantly lower thermal dilation of the link parts. This thermal aspect of the application of ceramics as parts for robot structures has been filed as German patent (pending) [Hagn, 2005].

However, two major disadvantages are introduced by the ceramic material. First, this material is not ductile and therewith very sensitive to mechanical impacts. Se-

[32] Operating tables integrate side rails for the mounting of accessories like e.g. limb posturing devices or instrument trays. The design of these rails is standardised and corresponding clamps available.

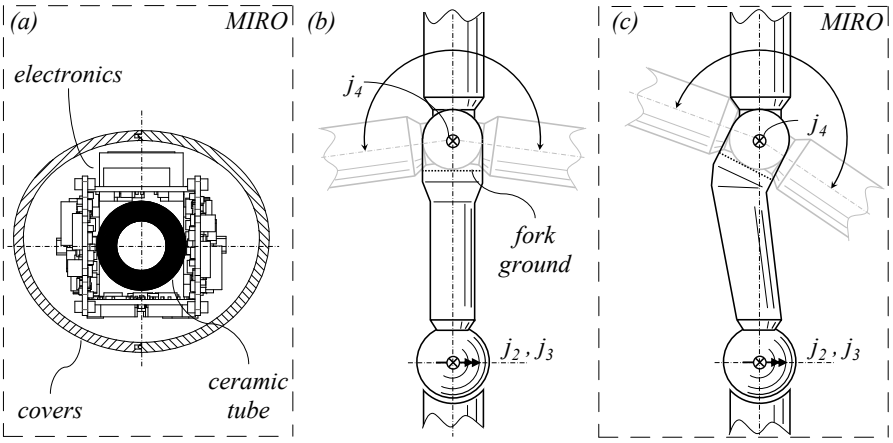

Figure 4.50: The $link_{34}$ concept: cross-section view of $link_3$ *(a)*, symmetric concept for $link_3$ *(b)*, geometrical tilt of $miro_{45}$ to achieve an asymmetric motion range of j_4 *(c)*

cond, the manufacturing process of sintering results in a significant shrinking of the green body[33] and the sintered part. As a consequence, exact geometrical tolerances are difficult to achieve directly and additional manufacturing processes like grinding are needed. Regarding the fitting position as depicted in figure 4.50 *(a)*, the ceramic part is well-protected against mechanical impacts by the surrounding housings and the electronic components[34]. In order to achieve a comparably simple geometric part, $link_3$ is composed of grinded tubular ceramics with bonded aluminium flanges at both ends as mechanical connections to the joint modules $miro_{23}$ and $miro_{45}$.

Another aspect in the design of $link_3$ derives from the motion range of joint j_4. As described in the earlier section 4.5.3.2 on the concept of $miro_{45}$, this 2-DoF joint is designed in the form of a fork-joint, which basically results in a symmetric and limited motion range for j_4. Regarding the basic configurations of the *MIRO* in a surgical application (compare figure 4.12, section 4.4.2), a symmetric joint range of the elbow as shown in figure 4.50 *(b)* is not essential. The location of the patient and therefore the effective workspace, is fixed in relation to the base of the robot. Hence, an asymmetric design was chosen for the *MIRO* (compare figure 4.50 *(c)*), enlarging the motion range of j_4 in one direction (towards the patient) and reducing it in the other direction (away from the patient). To achieve this and to comply

[33]Ceramic powder is consolidated to the desired shape, which is called a green body. The final part results from firing the green body at high temperatures.

[34]In the opinion of the author it is important that in case of a major crash of the robot with its environment, the integrity of the robot structure and electronics is more important than those of housings.

with the kinematics design defined in section 4.4.3, $link_3$ is kinked, which inclines $miro_{45}$ to a certain angle (compare figure 4.50 *(c)*). In the final design of the *MIRO*, joint j_4 has a mechanical motion range of $+127°/-57°$ instead of $\pm 92°$. Despite this asymmetric range, the intersecting points formed by j_2, j_3 (centre of shoulder) and j_4, j_5 (centre of elbow) still lie on the axis of j_1, as defined in the kinematics design (compare figure 4.17, section 4.4.3).

4.5.10 Forearm Link

The descriptions on the structure design given in the preceding section 4.5.9 for $link_3$ apply likewise for $link_5$. Therefore, the same tubular design for the structural part and surrounding arrangement of electronics and housings is chosen for $link_5$. Due to the comparably low weight of the wrist and short length of the tubular portion, the advantages of a ceramic part is negligible and the *MIRO* applies a cheaper aluminium part for the structure of $link_5$. However, a replacement of this aluminium part with a ceramic version is simple.

Regarding the impact of $link_5$ on the motion range of joint j_6, $link_5$ integrates a kink as well, which results in the form of a swingarm-like design. This aspect has already been described in section 4.5.3.3 (compare figure 4.31 *(a)*).

4.5.11 Sterile Drape and TCP Interface

The robot interfaces with instruments which must remain sterile during an operation. In other words, the robot must not contaminate the instruments with microbiological agents such as bacteria, fungi, or viruses. Furthermore, all robot surfaces must prevent the contamination of the sterile operating room staff (e.g. scrub nurse). Regarding the technologies available for sterilising devices, four different solutions can be regarded as state-of-the-art methods:

- radiation sterilisation
- chemical sterilisation
- heat sterilisation
- plasma sterilisation

All methods apply physical or chemical media, which kill microbiological agents. The radiation sterilisation thereby applies large dose of radiation (e.g. up to 2.5 Mrad of gamma radiation by a ^{60}Co source), chemical sterilisation utilises, for example, the toxic ethylene oxide (C_2H_4O). Heat sterilisation is based on the application of high temperatures (steam sterilisation: 121-135°C, dry heat sterilisation: 160-180°C). The

plasma sterilisation process generates gas radicals, which kill microbiological agents [Wintermantel and Ha, 2009].

All methods presented are difficult to apply for the sterilisation of a complex mechatronic device like the *MIRO*. Methods involving heat significantly limit the range of compatible materials (e.g. polymers for housings) and electronic components. Gamma radiation can have a negative impact on electronic components. VUJISIC et al. examined the effect of gamma irradiation on programmable read-only memories [Vujisic et al., 2007]. The gamma irradiation caused irreversible faults, for example, in EEPROMs[35]. In order to apply this sterilisation method, a significant shielding of electronic components would be recommended. Furthermore, it is not a very common procedure for re-sterilisation in clinics due to comparably high costs. For the application of chemical sterilisation processes the housings of the robot must prevent infiltration of toxic substances into the robot, in order to avoid corrosion of mechanical components and damage to electronics. The plasma sterilisation is very effective regarding surfaces and operates at low temperatures, but is very limited regarding undercuts of the object [Wintermantel and Ha, 2009]. As a consequence, the *MIRO* is not sterilised itself, but covered by a sterile drape like many other medical devices. This drape consists of a sterile, disposable polymer hose, which covers the robot, and additional bonded parts, which are necessary to attach it to the instrument interface. These parts are described in the following paragraphs.

The TCP flange of the robot serves as the connection to the surgical instruments. As defined in the versatility paradigm, it must enable the connection of laparoscopic instruments. This aspect has been further examined in section 4.4.2.3, resulting in the selection of a hollow shaft design of joint j_7. The demands for the TCP flange ($link_7$) comprise:

- hollow shaft design
- ability to cover the interface with a sterile barrier
- backlash-free and failsafe mechanical connection of instruments
- avoidance of difficult-to-clean surfaces
- simple and low cost sterile (disposable) parts
- optional signal and power interface for instruments
- optional electric- and/or software-controlled locking and releasing of instruments

[35]EEPROM: abbreviation for Electrically Erasable Programmable Read-Only Memory

The last requirement needs further explanation. In order to enable future projects which target automated change of instruments, it is necessary that the mechanical connection between the instrument and the robot can be established and released by software. This eliminates manual locking mechanisms like bolting (e.g. [DIN ISO 9409-1, 2004]) or manual quick changing adapter solutions (e.g. *MGW* series by *GRIP GmbH*, Germany [Grip GmbH, 2009]), which are the state-of-the-art solution in robotics. One possibility to adapt such quick changing adapter solutions for automated tool changing is to achieve the necessary actuation of the locking mechanism by the robot joints itself. For example, the robot would move the instrument to a shelf where the instrument is retained in its position, but free in one DoF of rotation. Then the robot would perform a certain rotation about this free DoF. One portion of the quick changer system (such as a lever), which hooks to the shelf is then actuated by this robot motion and thereby releases the instrument (e.g. *WGS Quick-Lock Quick Changer* by *Wemo Automation AB*, Sweden [WEMO Automation, 2009]). A central advantage of this approach is the application of existing actuators (robot joints) instead of the integration of additional actuators. However, the additional motion of the robot for locking/ releasing the instrument introduces new constraints regarding collision avoidance, as well as necessary torque and motion range. Therefore, the TCP instrument interface of the *MIRO* avoids this motion of the robot for locking/ releasing the instrument, by utilising an additional, integrated actuator.

Transmitting forces and torques between the robot and the instrument can be implemented by various physical principles. Regarding the demand for switching this connection, three approaches appear feasible: form-fit, friction, and magnetism. Although friction-based connections are very common in an operating room, for example, to connect an instrument to a stand by clamping, it requires comparably high actuation forces if the surfaces cannot be assumed dry and clean (e.g. contamination with blood). Assuming the worst case of lubricated surfaces (e.g. by lipids) the coefficient of friction between two steel parts would drop to $\mu_0 = 0.13$ [Kuchling, 1989b], which would demand a contact (actuator) force of 230 N to hold a payload of 30 N. Due to the uncertainty of the actual coefficient of friction and the comparably high actuation forces for the worst case, this approach is not considered for the TCP interface of the *MIRO*.

Figure 4.51 depicts the two technical solutions, based on form-fit and magnetic principles, which have been considered for the instrument locking mechanism of the *MIRO*. Only those parts of the sterile barrier are depicted which are relevant for the function of the mechanical locking mechanism. Other portions of the drape (e.g. covering of the hollow shaft) are described later in this section.

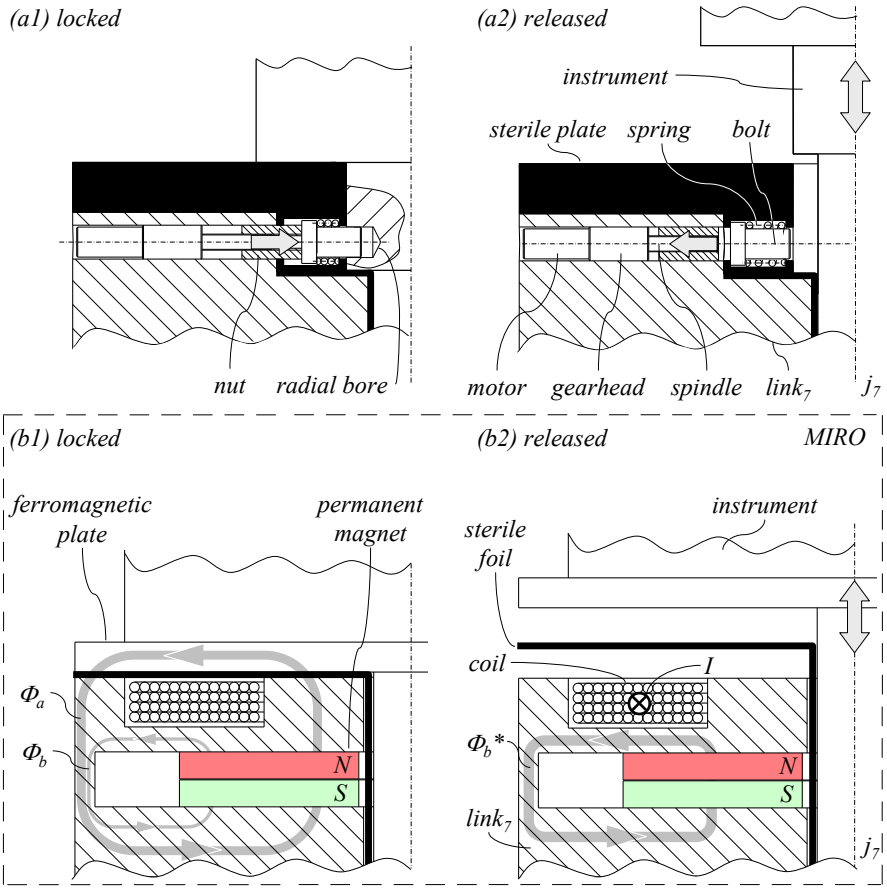

Figure 4.51: Half cross-section views: form-fit instrument interface mechanism *(a1, a2)*, electromagnetic interface *(b1, b2)*

The first concept (see figure 4.51 *(a1, a2)*) is based on an actuated form-fit connection between the TCP and the instrument. The central problem here is that both components must be separated completely from each other by the sterile enclosure in order to avoid contamination of the sterile instrument. The non-sterile $link_7$ of the robot integrates one or multiple linear actuators consisting of a motor, gearhead, spindle, and nut. These actuators are integrated in such a way that their motion axis points radially towards the shaft of the instrument. The sterile barrier at this point consists of a sterile plate which integrates spring-loaded bolts. Figure 4.51 *(a1)* shows the established connection between the TCP, the sterile barrier, and the instrument. The form-fit between these three parts is achieved by the bolts which are part of the sterile barrier and fit into corresponding bores of the instrument, as well as by the

spindle nut which holds the bolt in position. Combined with the form fit between the instrument and the hollow shaft of the robot, the instrument can be fixed in all six DoF. In order to avoid backlash of this connection, the bolts and corresponding bores can be shaped conically. To release the instrument from the robot, the linear actuators move in the opposite direction range limit and the bolts return to their rest position due to the spring forces (compare figure 4.51 *(a2)*). If the gearhead combined with spindle and nut is not backdrivable, the locked and released states can be maintained without consuming electric power. The required maximum force of the linear actuators results only from the spring forces and possible friction effects. Therefore, miniaturised linear actuators like the *smoovy*® series by *Dr. Fritz Faulhaber GmbH & Co. KG* can be applied [Faulhaber, 2009] to comply with the requirement of compact design. However, this approach still requires precision manufacturing of the parts to a significant extent to guarantee a backlash-free connection and to avoid the danger of seizing. Regarding the fail-safe demand of this design, the connection is locked even during power failure, but seizing of the mechanism or failure of the actuator can prevent removing the instrument in an emergency case. An additional mechanism would be necessary to manually push back the bolts for release.

The second approach applies a magnetic coupling between the instrument and the TCP as depicted in figure 4.51 *(b1, b2)*. The TCP integrates a combination of a permanent magnet and an electromagnet. The instrument simply integrates a ferromagnetic plate and the sterile barrier is implemented as a thin foil. The fixation of the instrument is achieved by the magnetic field of the permanent magnet, which is composed by Φ_a and Φ_b, where $\Phi_a \gg \Phi_b$ and Φ_a evoking an attraction force on the ferromagnetic plate of the instrument (compare figure 4.51 *(b1)*). Therefore, this connection is failsafe regardless of the operational state of the robot (e.g. power-off). To achieve a high attraction force, the thickness of the separating barrier must be reduced to a minimum. In order to release the instrument, a current I is applied to the coil of the electromagnet, which creates a counterpole magnetic field, forcing the magnetic flow of the permanent magnet to Φ_b* as depicted in figure 4.51 *(b2)*. Therefore, this locking mechanism only requires electric power for a short period while releasing the instrument. However, the magnet generates a force in a single direction. Hence, the TCP, the sterile barrier and the instrument must integrate an additional form-fit connection, which bears the other load directions. This form-fit is implemented by a prismatic joint with one free DoF, which is aligned with the attraction force direction of the magnet. The advantages of this mechanism are the absence of moving parts (robustness against seizing) and the very simple design of the sterile barrier and the mating part of the instrument. Furthermore, it allows a smooth surface for the TCP avoiding difficult-to-clean undercuts or bores. Therefore,

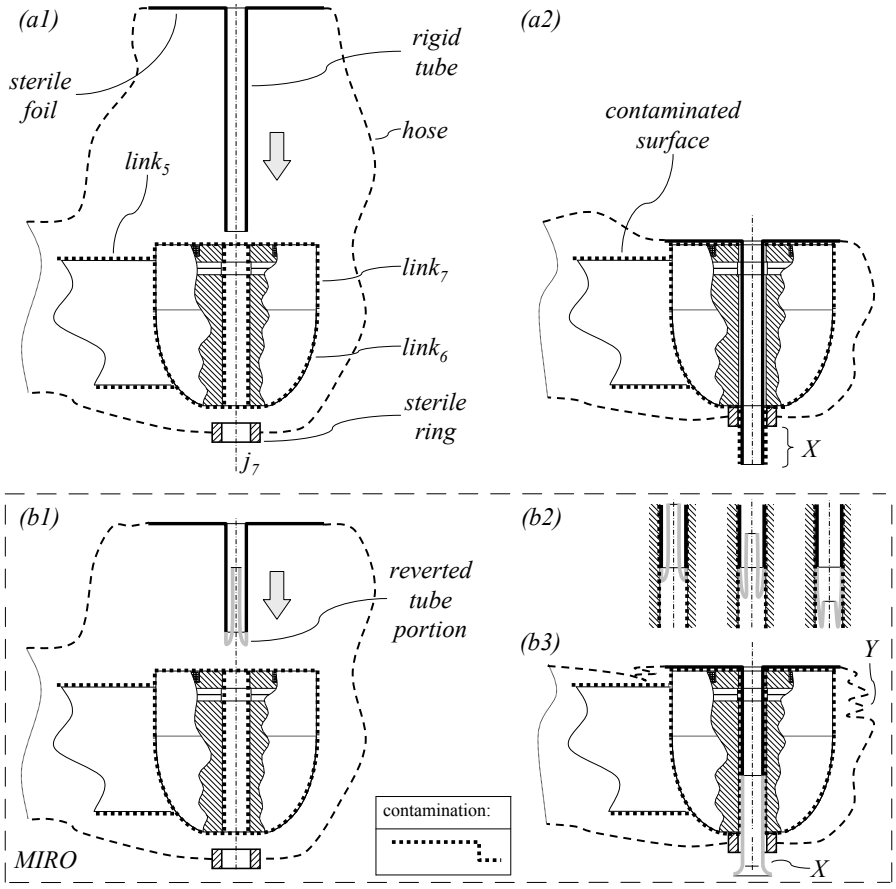

Figure 4.52: Design of the sterile drape: rigid tube for covering the hollow shaft *(a1, a2)*, flexible, reverted tube for covering the hollow shaft *(b1, b2, b3)*

the *MIRO* uses the described approach based on a holding magnet with electrical switch-off. The prototypical implementation of this magnetic instrument holder in the *MIRO* (sized Ø32x16 mm) achieves an attraction force of well above 100 N despite a sterile barrier thickness of 0.05 mm (maximum holding force of 160 N without sterile barrier).

As mentioned above, the sterile barrier must not only cover the TCP, but the entire surface of the robot, including the hollow shaft of joint j_7. It comprises a sterile plastic hose which covers the robot links, the described sterile foil for the TCP, and a portion which prevents contamination of laparoscopic instrument shafts by the non-sterile hollow shaft of j_7. The concept illustrated in figure 4.52 *(a1, a2)* utilises a rigid tube to cover the hollow shaft, which is connected to the sterile foil of the

drape. The contamination of the interior surface of the hollow shaft is indicated in figure 4.52 *(a1)* by the dotted lines. The rigid tube is slipped through the hollow shaft of j_7 and fixed to an additional sterile ring of the drape (compare figure 4.52 *(a2)*). By moving the rigid tube through the hollow shaft of j_7, the tip portion (compare designator X in figure 4.52 *(a2)*) of the tube becomes contaminated, which must be avoided. Therefore, the design is modified as shown in figure 4.52 *(b1, b2, b3)*, dividing the tube into a rigid and a very flexible part (e.g. rubber silicone). The tube is then inserted as shown in figure 4.52 *(b1)*, whereby the flexible part of the tube is turned to the inside. When the rigid part is fitted to the joint, the flexible part is turned inside out as shown in the sequence in figure 4.52 *(b2)*. This way, surfaces of the tube which come in contact with contaminated surfaces stay in their position. The tip portion X is protected against contamination and remains sterile. This concept has been applied for as a patent [Hagn, 2009]. The dimensions of the sterile hose must be large enough in order to create a crimped portion (compare designator Y in figure 4.52 *(b3)*), which enables the unaffected rotary motion of the TCP.

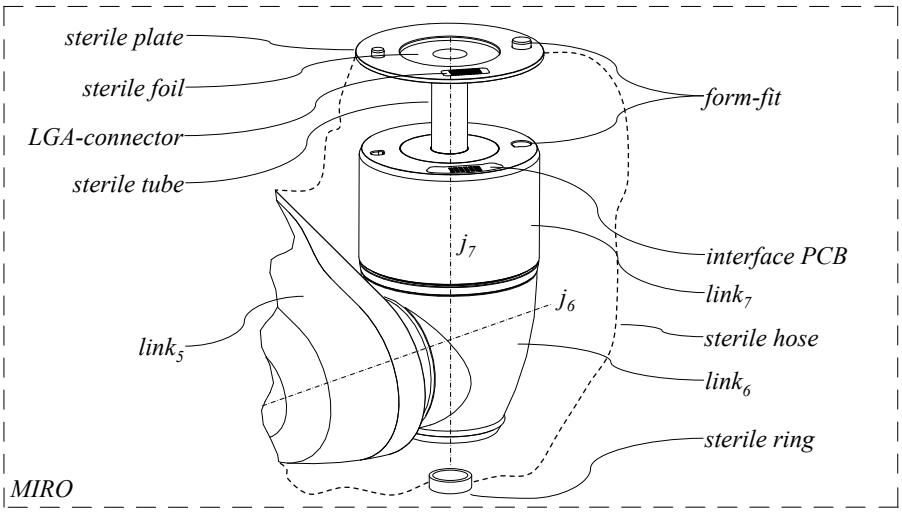

Figure 4.53: Design of the *MIRO* TCP ($link_7$) with sterile drape

Figure 4.53 depicts the final design concept of the *MIRO* TCP. The sterile drape consists of the described sterile foil, ring, hose, tube, and a sterile plate. This plate integrates two simple pins for the form-fit between robot and instrument. To establish an optional power and signal connection between *MIRO* and an instrument, an electric connector is also integrated. In order to avoid surfaces which are difficult to clean, the electric interface of the *MIRO* and the instrument uses simple PCBs with flat gold pads. The disposable drape integrates the actual connector, which consists of

an array of two-sided metal springs (5x10 positions) embedded in a plastic insulator. These kinds of connectors are usually applied for testing of LGA[36] components. In the *MIRO* prototype, this interface will establish high-speed communication (*SpaceWire*) and power supply (24 VDC) for instruments.

4.5.12 Electronics

This section briefly describes the partitioning of the electronic components and their distribution in the *MIRO* robot. The descriptions given in this section relate to the *MIRO* design, representing the latest developments. The following functions can be defined for the electronics of the *MIRO*:

- readout of the motor position sensor signal
- commutation, current feed, and torque control of the motors
- current feed and control of the electromagnetic safety brakes
- readout of the joint position sensor signals
- readout of the joint torque sensor strain gauges
- readout of auxiliary sensors (e.g. temperature, current monitoring)
- communication of sensor and actuator signals within a joint module
- communication between the joint modules and the external control component
- generation of required voltage levels based on the supply voltage of the robot
- current feed and control of the electromagnetic instrument interface
- optional communication with actuated instruments
- optional power supply of actuated instruments
- failsafe emergency stop of the actuators

These functions must be partitioned and distributed within the robot in order to comply with the following requirements formulated for the *MIRO*:

- short analogue cabling and shielding of signals (EMC)
- small diameter of the cable harness
- creation of operable sub-modules

[36]LGA: abbreviation for Land Grid Array

- compact dimensions and seamless integration into the robot
- simple exchangeability of electronic components (maintenance)
- easily accessible electronics (testing)

These requirements therefore suggest a certain modularity of the electronic components. On the other hand, modularity hinders the most compact design of the electronic components due to the necessity of additional interfaces between the electronics (e.g. cables, connectors). However, a more granular breakdown of the electronic components benefits the adaptation to available spaces. The *MIRO* robot therefore has two levels of operable sub-modules, besides the level of the fully integrated robot (level 2, compare figure 4.18, page 97) and single PCBs. Level 4 comprises sensors with their signal processing electronics and actuators with their corresponding power inverter electronics. Level 3 of modularisation includes operable integrated joint modules (e.g. $miro_{23}$). Besides backplanes, the electronic components of the *MIRO* are partitioned into the following PCBs:

- $elec_{communication}$: This electronic component establishes the communication between the four joint modules and the external robot control. Inside one joint module, it interfaces with the different sensor signal processing electronics and the motor/brake electronics. Furthermore, it supplies all sensors with the necessary electric power. Every joint module integrates one $elec_{communication}$.
- $elec_{power\,supply}$: This electronics generates all necessary voltage levels in a joint module based on the DC supply voltage of the robot. Every joint module integrates one $elec_{power\,supply}$.
- $elec_{motor,brake}$: Based on the motor position provided by the motor position sensor (mps), this electronic component executes the commutation and the torque control of a BLDC motor (mot). The required torque for the motor is thereby received from the communication electronics ($elec_{communication}$). Furthermore, it generates the current to release the brake. The electronic components on this PCB are supplied by the power electronics ($elec_{power\,supply}$). In contrast, the electric power for the motor is tapped from a separate motor supply cable harness in the robot. This power line can be cut off by a binary e-stop communication. Thereby, in case of an emergency stop, all electronic boards remain powered on and only the motors and brakes are switched off. All joint modules with two motors ($miro_{23}$, $miro_{45}$, $miro_{67}$) integrate two of these electronic modules, $miro_1$ only one.

module	*location*	$elec_{base}$	$elec_{communication}$	$elec_{power\ supply}$	$elec_{motor,brake}$	$elec_{potentiometer}$	$elec_{strain\ gauges}$	$elec_{TCP\ driver}$
base	$link_0$	1						
$miro_1$	$link_0$		1	1	1			
	$link_1$					1	1	
$miro_{23}$	$link_1$		1	1	2			
	$link_2$					1		
	$link_3$					1	1	
$miro_{45}$	$link_3$		1	1	2			
	$link_4$					1		
	$link_5$					1	2	
$miro_{67}$	$link_5$		1	1	2	1		1
	$link_7$					1	2	

Table 4.16: Distribution and quantities of electronic components in the *MIRO* robot grouped according to joint modules

- $elec_{potentiometer}$: This module integrates the signal processing (A/D) electronics based on a WHEATSTONE bridge circuit for one conductive plastic potentiometer and interfaces with the communication electronics.

- $elec_{strain\ gauges}$: This electronics integrates the signal processing (A/D) electronics based on WHEATSTONE bridge circuits for two full bridges of strain gauges. It interfaces with the communication electronics. The implementation of these electronics allows for stacking multiple instances of this component, sharing the same interface with the communication electronics (cascading). This feature is applied, for example, in the joint torque sensor jts_{67} of $miro_{67}$. There, two electronics for processing the strain gauges ($elec_{strain\ gauges}$) and one potentiometer electronics ($elec_{potentiometer}$) are merged to make a sensor module.

- $elec_{TCP\ driver}$: Only the $miro_{67}$ joint module integrates this electronic component, which is connected to the joint communication node ($elec_{communication}$). It pursues two main functions: generating the current for unlocking the electromagnetic instrument interface and switching the optional supply voltage for the instruments. Both functions are triggered by the communication electronics. The implementation of this component is pending.

- $elec_{base}$: This electronics simply changes the physical layer of the robot communication from fibre optics (between robot and external robot control unit) to a copper physical layer (within the *MIRO*).

Table 4.16 summarises quantities and distribution of the electronic components in the *MIRO* robot. An illustration of the physical distribution of the electronics in the *MIRO*, as well as a description of the electronics design is given in the later section 4.7.6.

4.6 System Parameters

The preceding sections of this chapter described the design concepts of the *MIRO* in detail. Regarding the selected design methodology, these concepts have been developed in order to comply with the versatility hypothesis, as well as the scaling and design paradigms. As a result, a generic design of the *MIRO* has been derived, which fulfils the following requirements:

- single arm configurations and setups with up to four arms
- floor, cart, ceiling, operating table mounting
- dedicated or programmable constraints
- control-modes: teleoperated, autonomous, or hands-on control of the robot(s)
- interfacing standard and endoscopic instruments
- proposed method for collision avoidance (redundant kinematics, restricted workspace)
- Cartesian and joint level force/ torque control

Furthermore, the design concepts target an anthropomorphic (7-DoF) kinematics and the most compact size. Regarding the necessary design parameters of a robot, the following criteria have not yet been analysed and need to be defined for the final design of the *MIRO* prototype:

- workspace (maximum reach, motion capability)
- payload
- accuracy
- dynamics
- weight

According to the descriptions in 4.2, these specifications must be derived from applications and serve as concrete scaling parameters for the robot. The research group has identified a set of surgical techniques which span diverging requirements for the robotic system. Thereby, a set of worst-case specifications can be compiled, which is intended to cover a comprehensive range of additional applications.

The following applications have been selected for the *MIRO* robot:

1. minimal invasive surgical applications
   (a) coronary bypass graft operation
   (b) operations at the mitral and aortic valve
   (c) correction of atrial septal defects
   (d) resection of the gallbladder (cholecystectomy)
   (e) vermiform appendix removal (appendectomy)
   (f) surgical correction of inguinal hernias (hernioplasty)
   (g) explorative laparoscopy
2. orthopaedic applications
   (a) drilling of holes for pedicle screws in vertebral bodies for osteosynthesis
   (b) osteotomy utilising laser
3. neurosurgical applications
   (a) brain biopsy

The minimally invasive applications require for a multi-arm system for bimanual operation, complying with the constraint of the fulcrum point. Thereby, the robot arms are controlled mainly in a telerobotic (position control) mode. Konietschke et al. identified three minimally invasive operation as having the largest workspace [Konietschke et al., 2003b]. Figure 4.54 illustrates these three workspaces with dimensions in millimetres. For the *MIRO*, the coronary applications are intended to be supplemented by a method for the compensation of the heart motion introduced by Ortmaier and thereby enabling operation on the beating heart [Ortmaier, 2003]. This requires certain dynamics of the robot.

The orthopaedic applications comprise two different approaches. Drilling of holes at the vertebrae is intended for a hands-on robotics approach, where surgeon and robot guide the drill machine in conjunction. Based on preoperative planning and intraoperative navigation, the robot limits the motion capabilities to a desired path towards the target. Then the instrument is held aligned with the planned bore axis and the drilling is performed by the surgeon. In contrast, the osteotomy of bone tissue with a laser enables more complex cutting trajectories compared to classical instruments, like saws. In order to benefit from this advantage, the robot is intended to perform these trajectories autonomously.

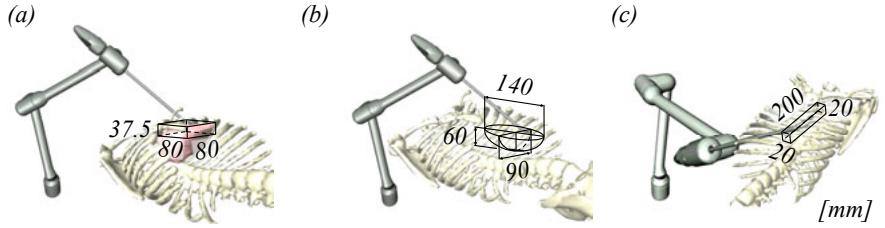

Figure 4.54: Three minimally invasive surgery workspaces with dimension *[mm]*: coronary bypass *(a)*, abdominal procedures *(b)*, left internal mammary artery harvesting *(c)* [Konietschke et al., 2003b]

The biopsy application is intended for a hands-on robotics approach, which integrates the robot arm with an intraoperative navigation system providing the concurrent positions of the patient and the robot TCP. In this sense, this application is similar to the pedicle screws application. However, the required accuracy is significantly higher. The research group at the *DLR* derived the open design parameters for the *MIRO* robot based on these applications, which are described in the following paragraphs. A more detailed description on the applications is given in chapter 5 on the results.

4.6.1 Link Lengths

The kinematic concept of the *MIRO* robot has been developed in section 4.4.3, comprising the type, location, and orientation of joints. This design still leaves the following parameters undefined:

- length of the upper arm (a_3)
- length of the forearm (d_5)

These open parameters have been researched by KONIETSCHKE et al. [Konietschke et al., 2003b]. Based on the selected applications, typical workspaces have been identified and joint motion ranges were derived from the mechanical concept. The optimisation of the robot link lengths was then conducted by utilising genetic algorithms and subsequent gradient-based methods. The applied quality criteria for the optimisation comprised the accuracy and manipulability of the end effector (instrument), the minimised size of the robot and the insensitivity of the results against uncertainties of the robotic setup. Based on the results of this optimisation, the link lengths of the *MIRO* have been determined as shown in table 4.17. Due to the motion range limits, only one singularity can be derived from the possible joint alignments (compare section 4.4.3) identified for the *MIRO* robot: if the pose is completely upright,

i	a_{i-1} $[mm]$	α_{i-1} [°]	d_i $[mm]$	Θ_0 [°]	q_i [°]
1	0	0	232.6	0	± 162.5
2	0	-90	0	-90	± 41
3	0	90	0	0	± 41
4	310	-90	0	90	$-41/+117$
5	0	90	385	0	± 162.5
6	0	-90	0	0	± 160
7	0	90	66.2	0	± 162.5

Table 4.17: DH-parameters and joint motion ranges of the *MIRO*

joint j_1, j_5, and j_7 are aligned. However, this pose represents a workspace limit and is not sensible for applications. Regarding applications in minimally invasive surgery utilising instruments with two additional DoF (compare 3.2.1), the kinematic chain integrates nine DoF. Then, only two singularities remain within the workspace of the *MIRO* [Konietschke et al., 2006a].

4.6.2 Payload

A central performance criterion of robot arms is the maximum payload which can be applied to the end effector flange. Regarding industrial standard robots (compare section 2.1.4), the payload is the central scaling parameter for entire families of products, besides the maximum reach. The necessary payload derives from the weight of the instruments and the manipulation forces. It determines the dimensions of motors, electronics, gears, brakes, structural parts, and torque sensors. Regarding the selected applications, the drilling of holes for pedicle screws was identified as the most challenging application for the *MIRO* concerning the maximum payload. In-house experiments with the *DLR LWR II* robot and various state-of-the-art surgical drilling machines have been conducted to determine the magnitude and distribution of reaction forces resulting from cutting the bone tissue [Döbele, 2008]. As a result, a maximum payload of 3 kg for the robot was identified as a sufficient limit, also for all other selected applications. This parameter has been applied to the scaling of the robot regarding the whole workspace, thus enabling even higher payloads in subsets of the workspace.

4.6.3 Position Resolution

As discussed in section 4.1.1 and 4.3.1, the total accuracy of a surgical robotic system is influenced by a significant number of parameters. Among these are the uncertainties of the patient's position and of the robotic setup. Therefore, additional system

components providing the registration of patient and robot are necessary in surgical applications. If this registration is applied to the TCP, the absolute position accuracy of the robot can be left unconsidered. If this initial correlation between the TCP and the target is established, the accuracy of the robot is determined by its position resolution (smallest position step). Regarding the selected applications, this parameter has been derived from the minimally invasive coronary bypass application. A smallest position step of 0.1 mm for the TCP position and 0.5° for the rotation was defined for the *MIRO* [Ortmaier et al., 2006].

During the design of the robot's hardware, this demand mainly influences the selection of position sensors. The position control of the joints is based on the motor position sensor instead of the joint position sensor. The motor position sensor resolution is thereby enhanced by the following gear reduction. As described in section 4.5.6.2, a high resolution motor position sensor was selected, which grants a rotary position accuracy of ±0.06°, which, in combination with a reduction gear applying a 1:100 reduction ratio, would result in an accuracy of ±0.0006° of the joint, in contrast to 0.04 ° resolution[37] of the joint-sided conductive plastic potentiometers *jps* (compare section 4.5.7). However, the repeatability of the robot is influenced by additional factors besides the sensor accuracies. Among these are the transmission quality of gears (e.g. position hysteresis), friction (e.g. stick-slip effects), and manufacturing tolerances of structural parts (deviation of the DH-parameters). Therefore, methods of calibration, identification, and control have a significant impact on the aspired accuracy of the robot, which will be described in the later section 4.7.6.

4.6.4 Dynamics

In contrast to hands-on robotics applications and autonomous applications where low speeds are desired for safety reasons, the minimally invasive scenario has been identified as the most challenging field of applications regarding the dynamics of the robot. The proposed method of motion compensation in beating heart surgery [Ortmaier, 2003] superposes the dynamics of the heart onto the instrument motions. The maximum speed of the instrument tip has therefore been set to 60 mm/sec [Konietschke et al., 2003a]. The dynamics of the robot is scaled by the principle of leverage due to the fulcrum point. A desired speed of the instrument's tip results in a higher speed of the robot. Therefore, the final design of the *MIRO* aims for a significantly higher maximum speed of up to 500 mm/sec in a subset of the entire workspace.

[37] The joint-sided position sensor with the largest motion range in the *MIRO* enables 345° and implements a position resolution of 13 bit.

The reduced inertia of moving parts due to the lightweight approach, high-performance motors, and the design of efficient electronics have been identified as the central measures to achieve this goal.

4.6.5 Weight

As described in the preceding chapters, the lightweight approach targets at various mounting options of the robot including multiple-arm mounted to the operating table. Therefore, the maximum payload of an operating table is a decisive criterion for the targeted maximum weight of the robot arm. According to anthropometric data, the maximum weight of a patient can be derived from the 95th percentile of the male human, which is 102.5 kg (age 41-60) [Jürgens, 2004]. The maximum payload of operating tables ranges from 135 kg to 360 kg, according to brief survey on operating tables (compare appendix C.2). Regarding a three-arm robotic system the weight of a single *MIRO* should not exceed 10 kg, in order to enable the application with a significant amount of existing operating tables.

4.6.6 Stiffness

The overall stiffness of the robot has been identified as an optimisation criterion (subset 3) in section 4.1.2 and not derived from the applications. The reason for this decision was discussed in section 4.3.1 on design paradigm 1. In the following paragraphs, this approach is further examined in relation to surgical applications.

The Cartesian stiffness is often associated with a quality that is important for the accuracy of the robot. In fact, a higher stiffness reduces the elastic deflection $\Delta\mathbf{x}_{elasticity,TCP}$ at the TCP due to mass properties of robot and payload, as well as external forces. Section 4.3.1 showed already methods for compensation of this deflection. However, these methods are limited regarding dynamics, as measuring of forces and positions, computation of models, and appropriate control of the joints need time. Disturbances with higher dynamics for example by an oscillating saw or impacts still lead to pose errors of the TCP. A lower stiffness can increase this error and one way is therefore to target a higher stiffness by design. However, this does not result automatically in a higher accuracy in the application. The following explanations question the approach of gaining accuracy in surgical applications by increased stiffness of the robot.

In applications for treatment of soft tissue the pose of the targeted anatomic structure (e.g. blood vessel) is not static or even known at the beginning of the operation. The surgeon localises the structure intraoperatively by means of vision (e.g. endoscope, ultrasound) and guides the instrument in relation to this view. With

this telerobotic approach, the absolute accuracy and stiffness of the robot are of minor importance, in contrast to the capability of fine motion control of the robot (position resolution) and good vision. In applications which target rigid anatomic structures like in orthopaedic surgery, the robot system is applied to perform more or less autonomously tasks according to preplanned data. Here, a robot can enhance the accuracy by its mechanical stiffness if the pose of the targeted anatomic structure (bone) is fixed in relation to the robot. However, a direct mechanical fixation of the bone is only applicable for larger anatomic structures like the femur or the skull bone (stereotactic frame). Regarding the application of drilling holes for pedicle screws for example, the vertebra is embedded in elastic muscular tissue and cannot be clamped rigidly in relation to the robot due to its fragility and size. By this, the pose of the vertebrae changes during the operation, particularly due to the forces and vibrations during drilling, as well as aspiration, and it must be localised continuously. This data can be used to control the robot accordingly, within the range of its dynamic capabilities. For this approach, the overall stiffness of the robot is inferior in contrast to its dynamics.

Therefore, the *MIRO* was not designed to a certain Cartesian stiffness value. However, link and joint components where optimised regarding their stiffness within the scope of the lightweight and compactness demand.

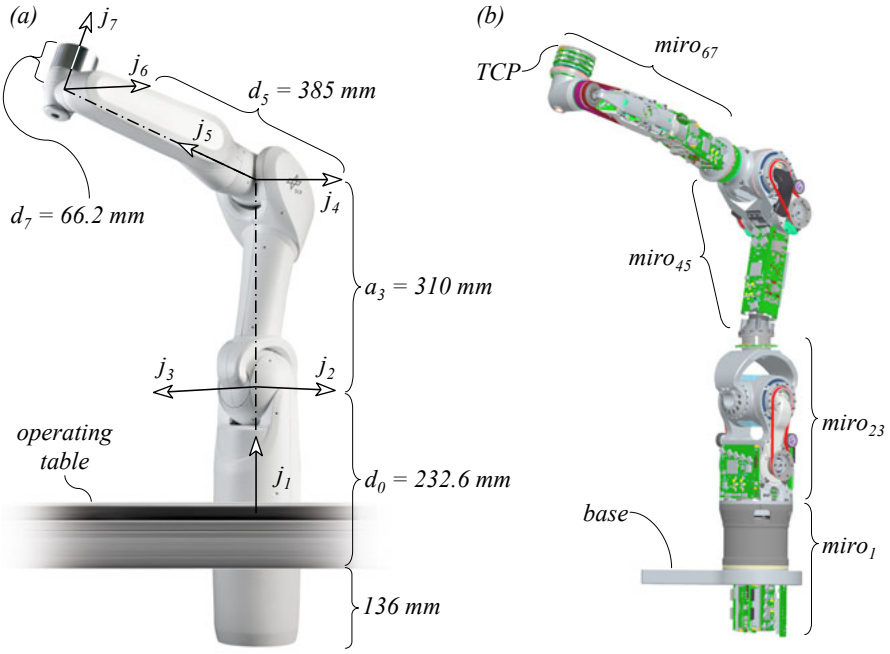

Figure 4.55: The *MIRO* robot arm, photo copyright *DLR (a)*, rendering of the *MIRO* (without housings) with denoted joint modules *(b)*

4.7 DLR MIRO Prototype

Figure 4.55 *(a)* shows the *MIRO* prototype [Hagn et al., 2008a][38]. A single arm weighs 9.8 kg without the interface cable for the external control unit, and has a maximum payload capacity of 3 kg. Maximally extended, the total physical arm length adds up to 1130 mm. The robot arm is based on a skeletal structure (compare figure 4.55 *(b)*), which makes the arm fully operational without the additional polymer housings. During integration and testing, this proved to be a valuable advantage.

On modularisation level 3 (compare section 4.5), the robot arm consists of four joint modules ($miro_1$, $miro_{23}$, $miro_{45}$, $miro_{67}$), the base ($link_0$), the TCP ($link_7$) and the housings. The following paragraphs describe the technical implementation of the concepts developed, followed by a brief description of the electronics and control design.

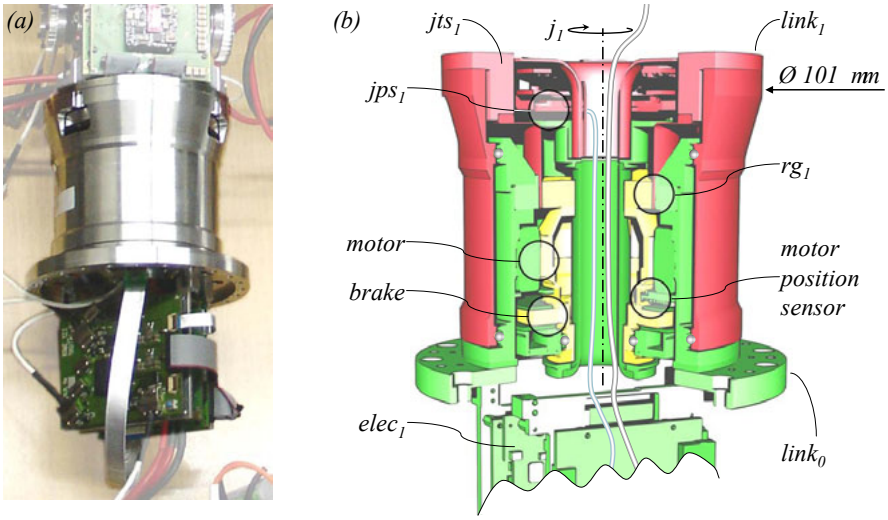

Figure 4.56: The $miro_1$ joint module *(a)*, rendered cross-section (90°) view with stationary parts highlighted in green, joint side in red, high-speed motor parts in yellow *(b)*

4.7.1 Joint Module $miro_1$

The first DoF of the *MIRO* is implemented by a single-DoF rotary joint module ($miro_1$), as depicted in figure 4.56 *(a)*. In order to provide a operable sub-component, the joint module integrates all necessary mechanical and electronic components to operate this DoF. The load on this joint is mainly derived from the inertia of the following links and joint modules. The torque caused by static loads (weight of the payload and subsequent robot parts) is mainly present in horizontal (for example, wall-mounted) robot setups.

Based on the conceptual design, it integrates hollow shaft components, utilising a central conduit (compare figure 4.56 *(b)*) for the cables connecting the joint electronics ($elec_1$) with the joint-sided sensors (jps_1, jts_1) and the next joint module ($miro_{23}$). The stationary portion of the joint (marked in green in figure 4.56 *(b)*) integrates the motor, the motor position sensor, and the spring-applied safety brake, which are connected to $elec_1$. The joint position sensor (jps_1) and joint torque sensor (jts_1) are integrated into the moving portion (compare red-coloured parts in figure 4.56 *(b)*). The tube of the cable conduit is applied to bring the rotary position of the stationary portion to the moving side of the joint. The *Harmonic Drive* reduction gear (rg_1, 1:160) connects to the stationary and moving side of the joint.

[38]This publication was honoured with the *Outstanding Paper Award 2009* of the *Emerald Literati Network*.

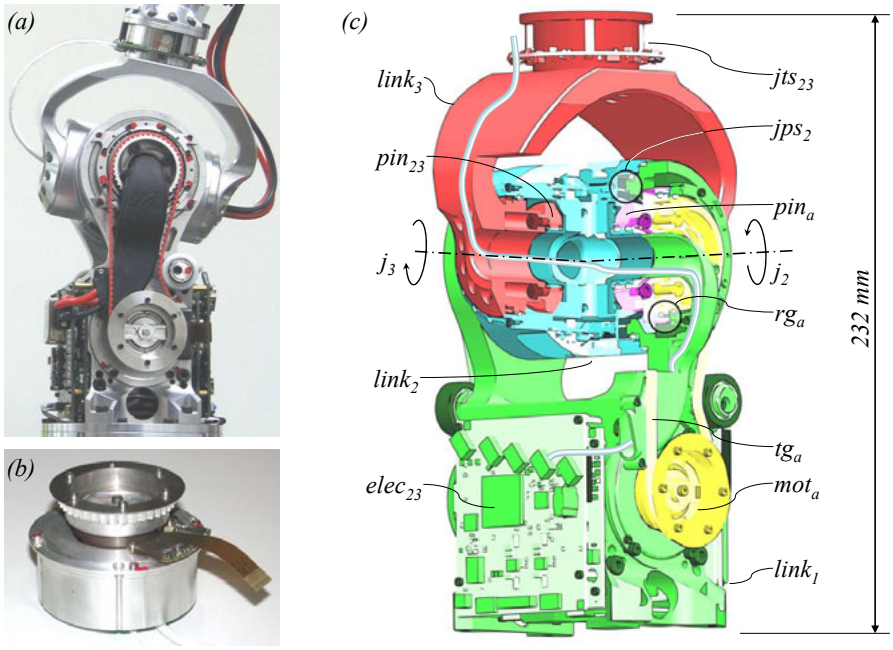

Figure 4.57: The $miro_{23}$ joint module *(a)*, motor module (*mot*), integrating motor, motor position sensor, brake, and timing belt gear *(b)*, rendered view (differential gear portion as cross-section) with stationary parts ($link_1$) highlighted in green, parts coupled with $link_2$ in blue, joint-sided parts ($link_3$) in red, high-speed motor parts are shown in yellow *(c)*

The compact joint module (diameter $\varnothing D_a$=101 mm) weighs 1.6 kg including the electronics and has a maximum torque of 82 Nm (rated peak torque of the reduction gear[39]) within a rotary motion range of 325° (software limit).

4.7.2 Joint Module $miro_{23}$

The pitch-yaw DoF of the *MIRO* shoulder are implemented by a couple joint with two DoF based on design concept *(2)* (see page 116). The $miro_{23}$ module (depicted in figure 4.57 *(a)*) integrates all necessary components to provide full testing and operation of the joint module.

The module is structured in two layers, whereby the lower layer integrates two motor modules (compare figure 4.57 *(b)*) and the joint electronics ($elec_{23}$) in $link_1$. All stationary parts of this joint module are highlighted in green in figure 4.57 *(c)*. The motor module integrates a motor, motor position sensor, brake, and the timing

[39] All other components are rated with more than 100 Nm peak torque.

belt gear as described in the section on the conceptual design (compare section 4.5.6.3, figure 4.47 *(c)*). The torques of the motors are transmitted to the input side of the reduction gears (rg) in the upper layer by means of timing belts (tg). All high-speed components (motor rotor, timing belt, wave generator of the *Harmonic Drive* gear) are highlighted in yellow. The high-torque side of the reduction gears connect to the bevel-gear pinions (pin_a, pin_b) highlighted in magenta, which mesh the single bevel-gear pinion pin_{23} connected to $link_3$. All bevel-gear pinions are pivoted in $link_2$ (blue colour) and form the differential coupling mechanism.

By selecting hollow shaft components for the upper layer of the joint, central conduits for the cable harness are formed as depicted in figure 4.57 *(c)*. In order to change the timing belts without having to disconnect the cable harness, an additional cable conduit is integrated underneath the timing belt. The joint position sensors (jps_2, jps_3) and their electronics are integrated in $link_2$, the 2-DoF joint torque-sensor in $link_3$.

The joint module $miro_{23}$ weighs 2.4 kg and implements two DoF in a spatial size similar to the single-DoF $miro_1$. The maximum torque simultaneously available for both DoF is limited to 90 Nm by the rated peak torque of the reduction gears. However, in order to enhance the sensitivity in impedance control mode, the joint torque sensor was optimised to a maximum torque of 50 Nm, which proved sufficient for the selected applications. Although each DoF is capable of $\pm 90°$ motion separately, the coupled motion, the housings, and software limits reduce the motion range to $\pm 41°$ for each DoF[40].

4.7.3 Joint Module $miro_{45}$

The elbow DoF (j_4, j_5) and the upper arm of the *MIRO* are integrated into the $miro_{45}$ joint module. The coupling joint adapts the differential bevel-gear concept implemented in $miro_{23}$ for a pitch-roll configuration of the DoF. Therefore, a large amount of identical or similar parts can be used.

The electronics ($elec_{45}$) of this module are attached to the outside of the stationary upper arm (compare figure 4.58 *(a)*). As shown in figure 4.58 *(c)*, the motor modules (mot_a, mot_b) are integrated into the lower layer of the joint and are based on the same design (compare figure 4.57 *(b)*) as the motor modules in $miro_{23}$, but with a different scaling. The motor torque is transmitted by timing belts (tg_a, tg_b) to the reduction gears (rg_a, rg_b) in the upper layer of the joint module. The high-torque sides of the reduction gears connect to the bevel-gear pinions (pin_a, pin_b) pivoted by $link_4$ and mesh the joint-sided bevel-gear pin_{45}, which is pivoted by $link_5$.

[40] The motion range of one DoF is 90° if the other DoF is in zero position. If both DoF are controlled independently, the motion ranges are ±60° for both joints without housings.

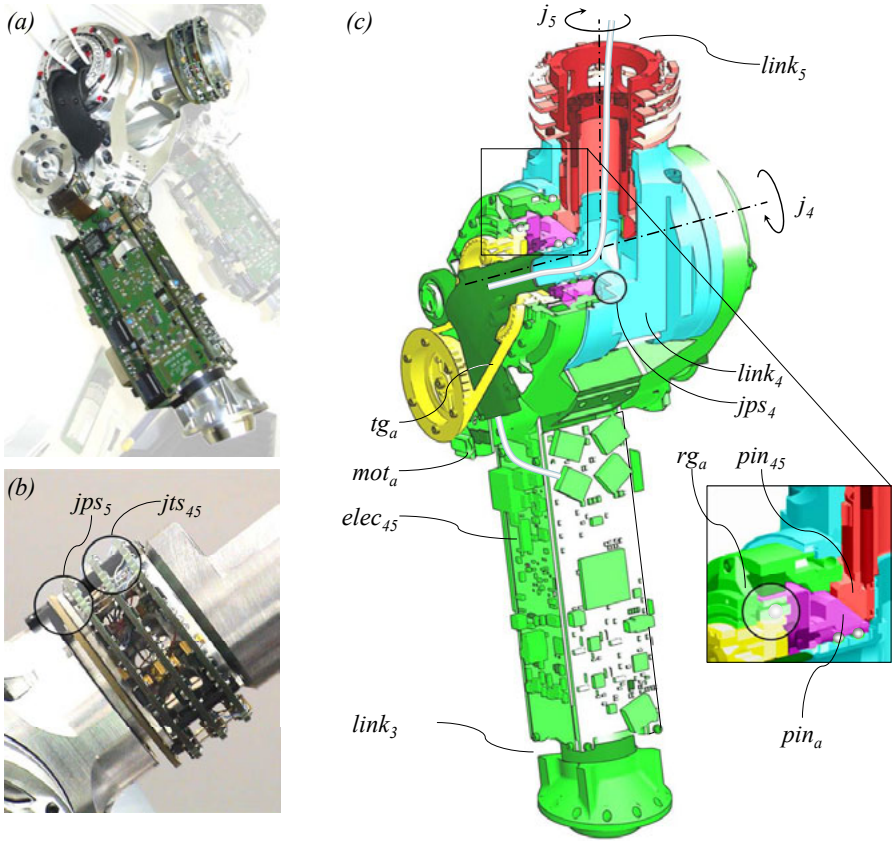

Figure 4.58: The $miro_{45}$ joint module *(a)*, module integrating the joint-sided torque and position sensors (jts_{45}, jps_5) *(b)*, rendered view (differential gear portion as cross-section) with stationary parts ($link_3$) highlighted in green, parts coupled with $link_4$ in blue, joint-sided parts ($link_5$) in red, high-speed motor parts in yellow *(c)*

This results in the pitch-roll motion capabilities described in section 4.5.3.2. The joint position sensor jps_4 is integrated into $link_4$. The 3-DoF torque sensor (jts_{45}) and the joint position sensor (jps_5) are integrated into a single module (compare figure 4.58 *(b)*).

The joint module integrates a central conduit for the cable harness, which is formed by hollow shaft components (e.g. reduction gears, torque sensor) for the differential portion of the joint (compare to the stylised cable harness in figure 4.58 *(c)*).

The $miro_{45}$ joint module weighs 1.95 kg and has a mechanical motion range of $-65°/+135°$ for j_4 and $\pm 172.5°$ for j_5. The range for j_4 is designed to be asymmetric because the location of the patient and, therefore, the effective workspace (patient) is fixed in relation to the base of the robot (compare section 4.5.9). This motion range

asymmetry was achieved by tilting the joint mechanism in relation to the upper arm. The housings and software end-stop monitoring reduce these motion ranges to $-41/+117°$ (j_4) and $\pm 162.5°$ (j_5). Due to the coupling mechanism approach, this joint module is capable of a maximum torque of 110 Nm e.g. for j_4 if the torque of j_5 is zero, and vice versa. Furthermore, 77 Nm can be achieved for both DoF simultaneously. Because of the selected applications, the torque range has been limited and the joint torque sensor (jts_{45}) was optimised to a nominal torque range of up to $\tau_{4,max}$=30 Nm and $\tau_{5,max}$=4.5 Nm.

4.7.4 Joint Module $miro_{67}$

In order to optimise the workspace and reduce the risk of collisions, the last portion of the robot aims at the most compact design (see figure 4.59 *(a)*). The $miro_{67}$ module represents the pitch-roll wrist of the *MIRO* and integrates the forearm with all electronics necessary to fully operate the joints j_6 and j_7. In contrast to the preceding 2-DoF joints, this module is based on the coupling mechanism concept (III_a) (compare section 4.5.3.3) and applies a swingarm-like design instead of the fork-joint structure. A more slender design and increased motion ranges have been achieved, but as a trade-off, a smaller torque range results.

The electronics of this module ($elec_{67}$) are attached to the outside of the forearm, which is kinked in the plane spanned by j_5 and j_6 in order to provide a large motion range for j_6. This stationary portion of the joint (see parts which are highlighted in green in figure 4.59 *(c)*) also integrates the joint position sensor jps_6 and two drive modules consisting of a motor, motor position sensor, brake, reduction gear, and timing belt pulley (compare figure 4.59 *(b)*). In contrast to the preceding couple joints, the drive modules are not integrated coaxially, but in two different distances to joint axis j_6 to achieve a more slender design of the forearm. The two modules are coupled by the braking mechanism, where the two brake actuators connect to the single rhomboid brake calliper. The springs press the calliper onto the two brake discs if no current is applied to the brake actuators. Therefore, both motors can only be stopped simultaneously, which is acceptable regarding the coupled joint approach [41]. The first drive module (mot_a, rg_a) transmits its torque by means of a timing belt (tg_a) directly to the belt pulley of $link_6$, resulting in the pitch DoF (these components are highlighted in blue in figure 4.59 *(c)*). The other module transmits the torque of the reduction gear by a second timing belt (tg_b) to a 2-part bevel-gear assembly, which is pivoted in $link_6$ (highlighted in magenta). There, the bevel gear pin_b meshes with the joint-sided pin_{67}, which results in the roll motion DoF.

[41] The control of only a single motor of a couple joint is not reasonable.

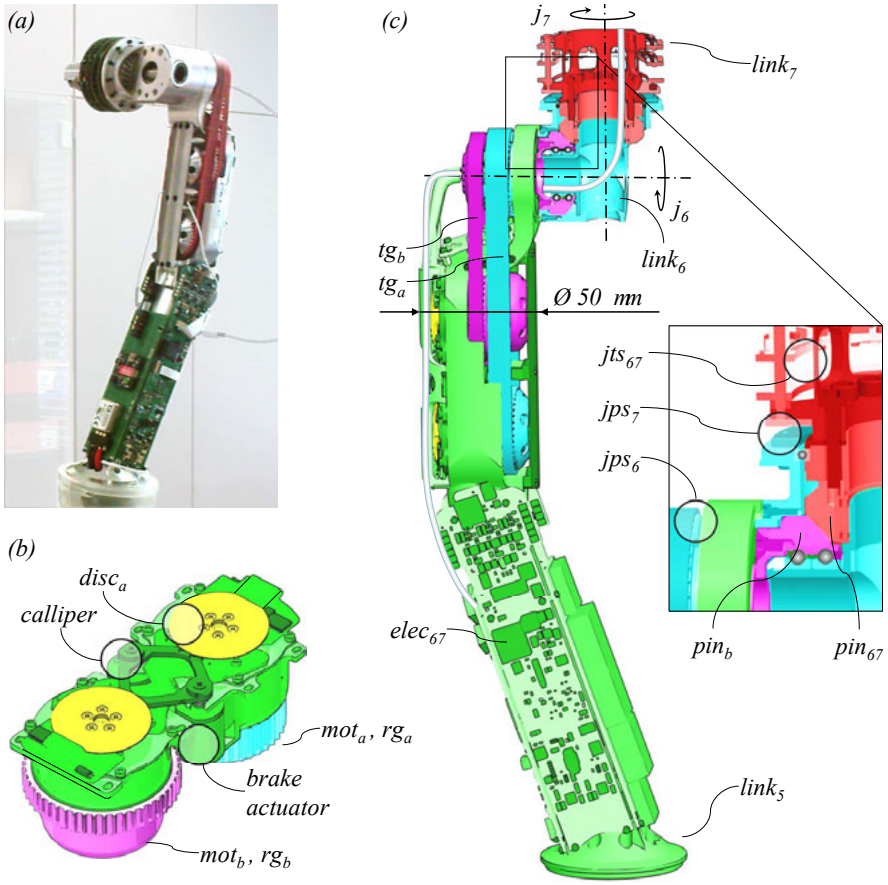

Figure 4.59: The $miro_{67}$ joint module *(a)*, drive modules (mot_i, rg_i) of $miro_{67}$ *(b)*, rendered view (bevel gear portion as cross-section) with stationary parts ($link_5$) highlighted in green, parts coupled with $link_6$ in blue, joint-sided parts ($link_7$) in red, high-speed motor parts in yellow *(c)*

In analogy to $miro_{45}$, the torque sensors (jts_{67}) and position sensors (jps_7) are integrated into a contained module connecting to the TCP module.

The hollow shaft design of the wrist mechanism pursues two goals. The first is to provide a conduit for the cables connecting the electronics ($elec_{67}$) to the TCP flange and the joint-sided sensors. Second, the portion of the hollow shaft which is aligned with j_7 allows for the mounting of laparoscopic instruments in the designated way (compare section 4.4.2.3). This aspect is described in more detailed in the next section.

The $miro_{67}$ joint module weighs only 1.28 kg and has a mechanical motion capability of $\pm 172.5°$ for both DoF. However, the monitoring of the end stops limits

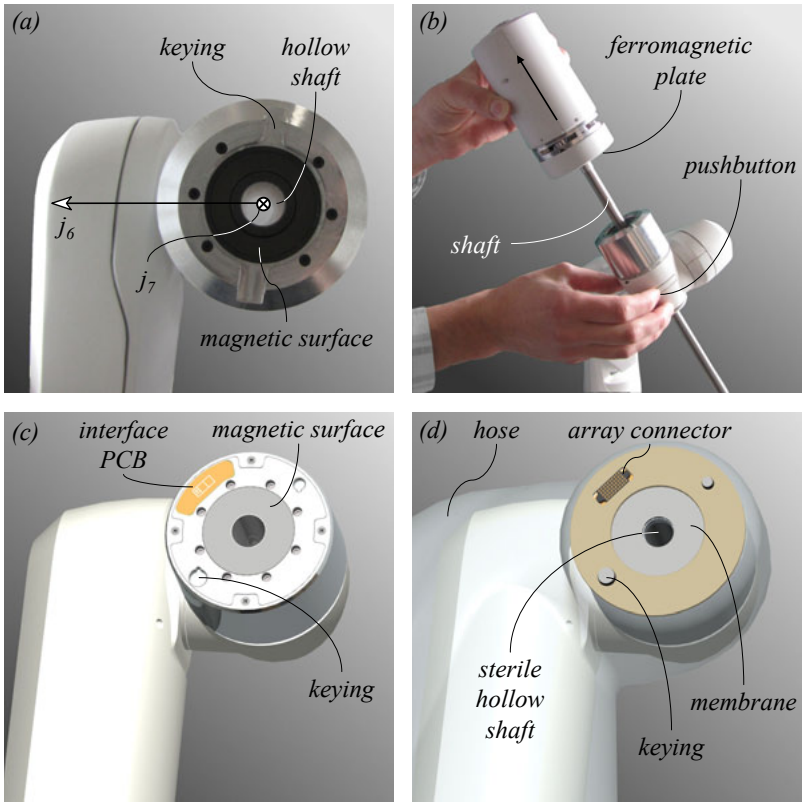

Figure 4.60: Current implementation of the TCP flange *(a)*, detaching a laparoscopic instrument from the *MIRO (b)*, rendering of the new TCP flange design *(c)*, rendering of the draped TCP flange *(d)*

the motion range to ±160° for j_6 and ±162.5° for j_7. The drive modules output a maximum torque of 5 Nm each. Due to the coupling mechanism concept, the maximum torque is limited and the joint-sided torque sensor (jts_{67}) is optimised to $\tau_{6,max}$= 4 Nm and $\tau_{7,max}$= 1 Nm.

4.7.5 End Effector TCP

The TCP module connects the robot with the instrument. Figure 4.60 *(a)* shows the current implementation of this interface in the *MIRO* robots, with the contact surface of the electro-magnetic quick changer, the form-fit keying for the instrument, and the hollow shaft. Figure 4.60 *(b)* illustrates the convenient exchange of a laparoscopic instrument. To enable the use of an instrument, it must be equipped with a ferromagnetic plate of the defined shape. By pressing a switch, a current is applied to the

coil of the electro-magnetic changer and the instrument can be removed. To attach an instrument, it must be moved into the correct position and orientation (form-fit) to snap it to the TCP by the force evoked by the permanent magnet.

Furthermore, figure 4.60 *(b)* shows the achieved compactness of the *MIRO* wrist assembly. The hollow shaft of the TCP, which represents a part of the housing of the robot, enables the use of instruments with a shaft diameter of up to 10 mm.

Figure 4.60 *(c)* depicts the completed design of a new interface version, whose integration into the *MIRO* prototypes is pending. This interface includes all functions of the design concepts described in section 4.5.11. It utilises the electro-magnetic holding magnet for holding and releasing the instrument. Keying provides the exact orientation between TCP, sterile drape, and instrument. Furthermore, a communication and power interface for the instruments is integrated. Figure 4.60 *(d)* shows the TCP equipped with the relevant parts of the sterile barrier. In order to achieve the smallest gap between the electro-magnet of the TCP and the ferromagnetic plate of the instrument, a thin metal membrane is integrated into the sterile barrier. Furthermore, the sterile barrier integrates the connector for the communication and power interface. To obtain easy-to-clean surfaces on the robot and instrument sides, this connector uses an array of double-sided spring probes. The interface PCBs of the robot and instrument can be achieved by planar gold contacts (landers).

4.7.6 Electronics and Control

Partitioning and distribution of the electronic components in the *MIRO* robot arm have already been described in section 4.5.12. The central goals in electronics and control design for the *MIRO* can be summarised as follows:

- high level of integration of electronic components in the robot arm in order to achieve a compact design and seamless integration into the robot's mechanics
- partitioning of electronic components to enable testing of sub-modules
- realtime communication with high bandwidth and low latency to enhance control of the robot
- configurability and scalability for the implementation of new communication or control approaches

The electronics and control design of the *MIRO* were not part of the author's research work. In order to provide a complete view of the *MIRO* robot, electronics and control implementations are described briefly in the following paragraphs, with a focus on their peculiarities.

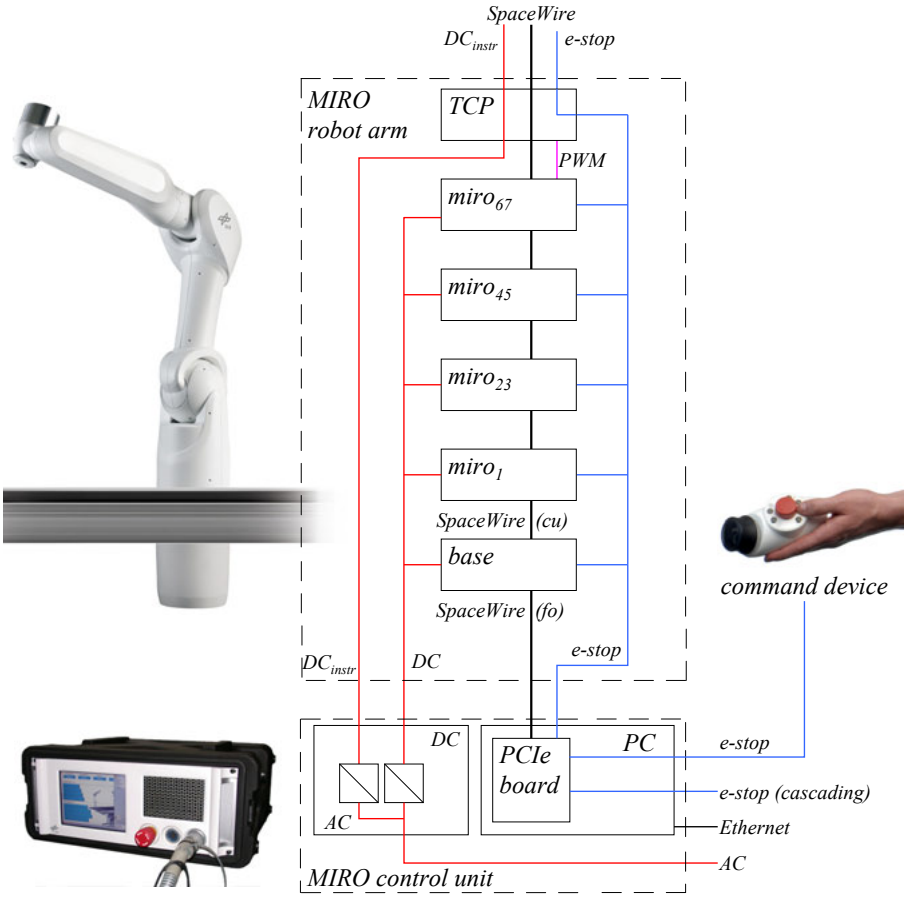

Figure 4.61: Abstracted network plan of the communication and power supply of the *MIRO* robot and the external *MIRO* control unit (modularisation level 2-3), photos copyright *DLR*

Figure 4.61 illustrates the electric connections of the system on the levels 0 to 3 according to the defined modularisation levels (compare section 4.5). The external *MIRO* control unit comprises the components to generate the 48 VDC power supply for the robot arm, a standard PC equipped with a PCIe board for the communication with the robot arm, and electronics for routing e-stop signals to a handheld command device. The *MIRO* control unit is embedded into the surgical robotic system by a real-time Ethernet communication. The communication of the external unit with the robot arm, as well as of the joint modules with each other utilises a high bandwidth (1 Gbit/s), configurable communication based on an in-house adaptation of the *SpaceWire* standard [ECSS, 2003]. There, the connection between control unit

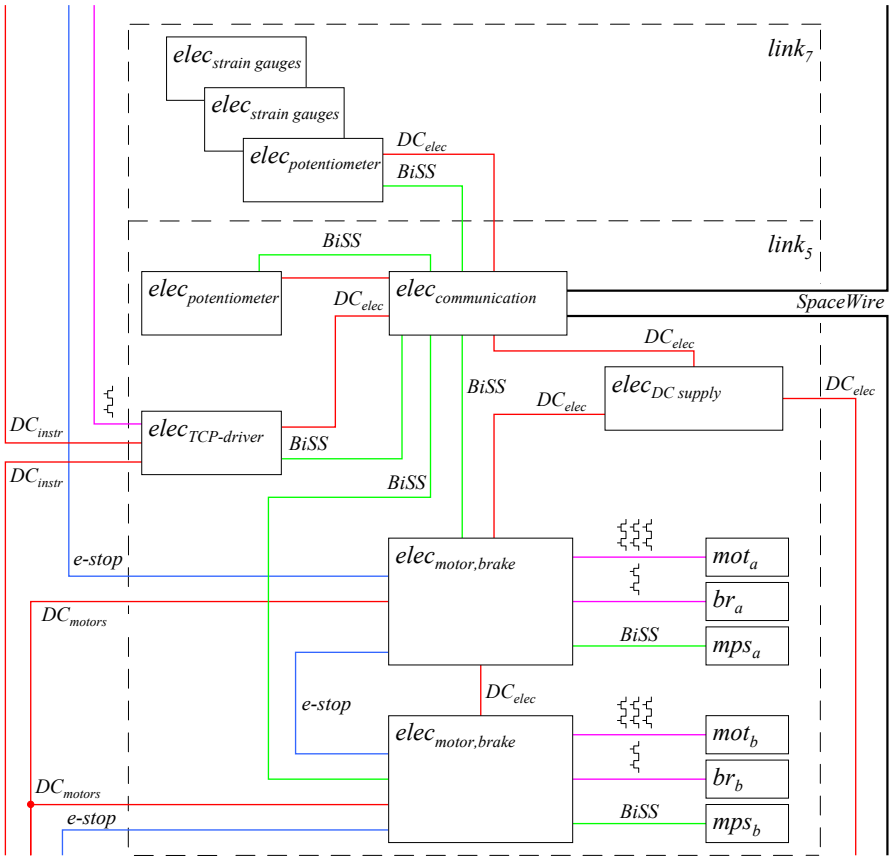

Figure 4.62: Composition of joint electronics for $miro_{67}$ (modularisation level 4)

and robot applies fibre optics for galvanic decoupling and the physical layer of the communication inside the robot arm is based on copper. Furthermore, the binary e-stop signal connects the same components and ensures failsafe emergency stop of all actuators. Additionally, an interface at the TCP is proposed which integrates SpaceWire communication, e-stop signal, and DC supply for instruments.

The next modularisation level 4 comprises all components within a joint module and is illustrated exemplarily for $miro_{67}$ in figure 4.62. The main electronic components like the two motor and brake electronics ($elec_{motor,brake}$), communication electronics ($elec_{communication}$), and DC conversion ($elec_{power\ supply}$) are located in the stationary $link_5$. The sensor electronics $elec_{potentiometer}$ and $elec_{strain\ gauges}$ are integrated near the corresponding sensor element. As an example, the multi-DoF joint torque sensor is integrated into $link_7$ and therefore its electronics as well. Besides DC supply of the electronic boards and the PWM for motors and brakes, the electronic

components are connected via the *BiSS-C* communications standard [iC Haus, 2008]. *BiSS* is a standard specialised for sensor and actuator communication, with the possibility of cascading multiple members and implementation on a small footprint physical layer. Regarding the electronics for the joint torque sensor this cascading option is used to combine two $elec_{strain\,gauges}$ to a stack, which communicates with the other electronics by a single connection. The e-stop signal interconnects all motor and brake electronics for switching off the electric power. Furthermore, figure shows the pending TCP interface electronics ($elec_{TCP-driver}$), which switches the DC interface at the TCP.

Communication and electronic components of the different levels of modularisation are intentionally targeted at different requirements. In the robot joints, where the available space is limited, components are very specialised and highly integrated. To illustrate the condensed space and the tight integration, figure 4.63 shows the physical distribution of the electronics in the *MIRO*.

Consequently, general-purpose architectures are applied to embed the robot into the entire system in order to add flexibility. Besides single electronic boards, this multi-level communication concept establishes sensors, actuators, as well as integrated joint modules as operable sub-modules.

The current implementation of the robot control is based on a 3 kHz control cycle. Thereby, the latency of communication and computation always stays well within the limit of one control cycle (i.e. 333 μs). Figure 4.64 illustrates the layered software architecture of the *MIRO*. Besides functionality which observes the hardware of the robot (joint state observer) and communication, only the motor torque control is implemented in the robot arm's electronics, with motor current control cycles of 20 kHz for $miro_1$ to $miro_{45}$ and 100 kHz for the smaller motors of $miro_{67}$. In order to enhance further development and expandability, all other control algorithms are implemented on an external general-purpose, scalable architecture (standard PC platform running the real-time OS *QNX Neutrino RTOS*). This approach allows the development of the control with tools like *Mathwork's Matlab Simulink* and enables efficient algorithm and application development.

The hardware abstraction layer (*HAL*) establishes a functional separation (compare figure 4.64) between the robot arm and its control design environment. The *HAL* provides the control designer with a representation of a complete current-controlled robot in the form of a *Simulink* block, presenting all sensor values as floating point SI values. Furthermore, the *HAL* integrates all features that are not provided by the hardware directly, but result from the identification of the robot (e.g. sensor-value calibration). For further reading, more detailed descriptions of the electronic and communication concepts of the *MIRO* are given in literature [Nickl et al., 2009], [Jörg

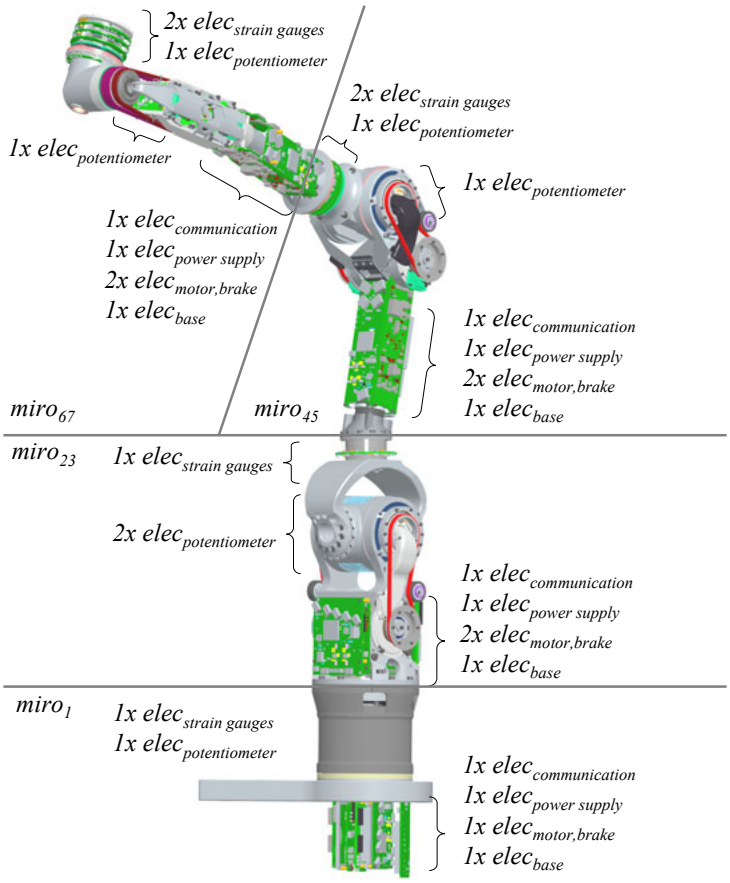

Figure 4.63: Physical distribution of electronic components in the *MIRO* with assignment to joint modules

et al., 2006], [Hagn et al., 2008a].

Besides motor torque control, all other control algorithms are designed utilising *Mathwork's Matlab Simulink* and the *aRD* software framework [Bäuml and Hirzinger, 2006], enabling automatic generation of real-time code and its distribution to one or multiple *QNX* hosts. The *MIRO* robot can be operated in two main control modes, which are selected by the application.

In the classical position control mode, the robot follows the commanded trajectory in Cartesian or joint coordinates as accurately as possible and is controlled to overcome external disturbances. This mode is applied in tasks which require exact positioning, such as laser cutting or biopsy. Thereby, the main challenge comes from the elasticities introduced by the lightweight approach of the *MIRO*. Based on the control design of the *DLR LWR III*, the *MIRO* control applies a flexible joint model and a state

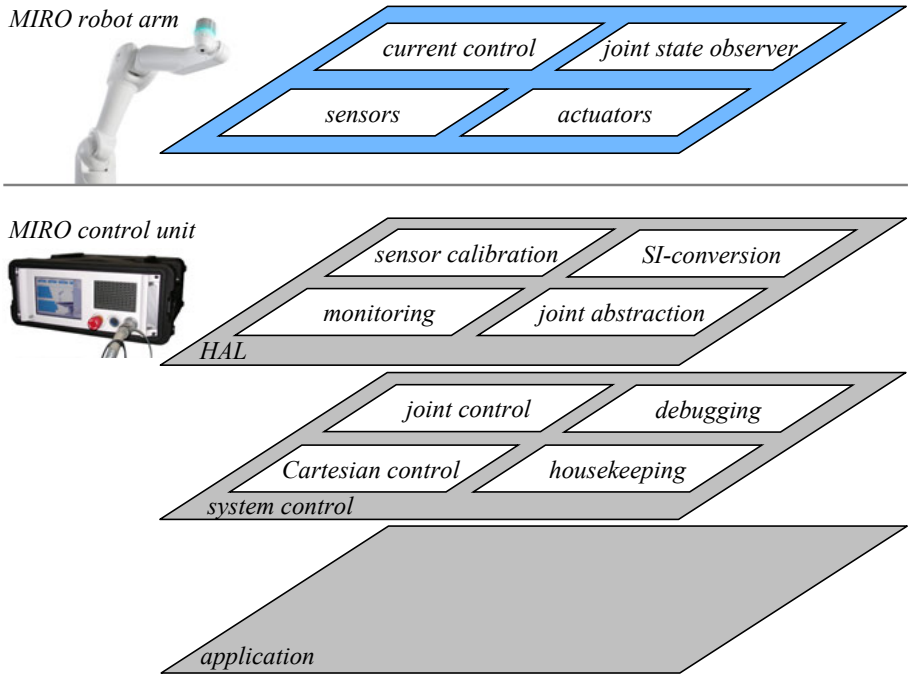

Figure 4.64: The layered *MIRO* software architecture, photos copyright *DLR*

feedback controller with the states given by motor position q_{mot} and velocity $\dot{q}_{mot}$ as well as the joint torque τ and its derivative $\dot{\tau}$.

In contrast to the *DLR LWR III*, the 2-DoF joints introduce not only a coupling regarding the positions, but also of the elasticity and damping matrix. For this purpose, multiple input and output controllers (*MIMO*) have been designed [Le-Tien et al., 2007]. The transformation of positions and torques between motor and joint coordinates are established according to the coupling mathematics described in sections 4.5.3.1, 4.5.3.2 and 4.5.3.3.

The second operation mode is a compliant one, i.e. the so-called *soft robotics* approach [Albu-Schäffer et al., 2007c]. Here, the robot can be manually guided to a desired position or on a desired trajectory. The interaction forces between user and robot are thereby measured with the integrated joint torque sensors (jts). The weight of the robot components and instruments are taken into consideration by exact modelling of these masses and their inertia (gravity compensation). The location of the joint torque sensors in the following link (compare section 4.5.5) requires the masses between the joint axis and the sensor be subtracted, as they are not captured by the sensor. The joint-level torque controller reduces the effects of friction and provides the torque needed to hold the robot and instrument in its posture. By

applying virtual springs and dampers to parts of the robot (e.g. TCP), the degree of free motion accessible to the user can be limited. This can be applied to avoid collisions with other objects, but also to establish a haptic output of desired paths.

For further reading, more detailed descriptions on the control design of the *MIRO* are given in literature [Le-Tien, 2010].

Chapter 5

Results

The preceding chapters described the methodology, central design decisions, conceptual design, and the implementation of the concepts in the form of the *MIRO* robot. The total range of possible applications for the robot is difficult to prove. Instead, this chapter summarises past and ongoing test implementations in different prototypical applications, covering all defined versatility aspects. These applications are developed by the *DLR* medical robotics research group and external research partners, and are not part of the author's research. However, these implementations are described to give experts in the surgical domain a descriptive impression of the capabilities and limitations of the introduced *MIRO* robot as a thought-provoking push for future applications. This chapter is concluded by a summary of the identified characteristics and performance measures of the *MIRO* robot.

5.1 Navigated Biopsy

This application was tested with the *KineMedic* (compare appendix D.2), a predecessor of the *MIRO*, which already integrated parts of the concepts for the *MIRO*. Among these corresponding aspects are the coupling mechanisms of joint j_{23} and j_{45}, the overall dimensions, as well as the kinematic chain. Regarding the formulated versatility hypothesis (compare section 4.1.2), this application covers multiple aspects:

- single arm configuration
- programmable constraints
- semi-active, hands-on operation interaction
- interfacing with conventional instruments

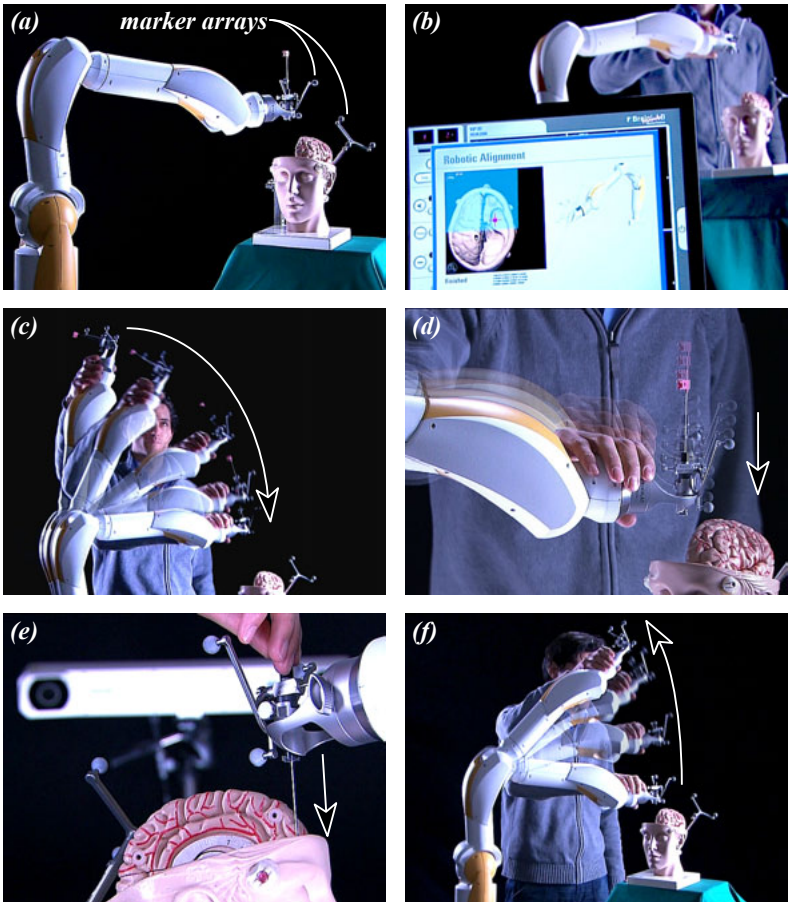

Figure 5.1: Prototypical implementation of a robot-assisted navigated biopsy with the *KineMedic (a)*, position control of patient and robot *(b)*, approach step 1 *(c)*, approach step 2 *(d)*, manual feeding of the biopsy needle *(e)*, retraction mode *(f)*, original video courtesy of *KUKA*

- programmable workspace restrictions
- position and impedance control on Cartesian level

The robotic setup integrates one *KineMedic* robot and robot control (see figure 5.1 *(a)*) with a prototypical intraoperative navigation system (*VectorVision*®) of *BrainLAB AG*, Germany (graphical user interface depicted in figure 5.1 *(b)*). The implementation is targeted at performing a biopsy of lesions in the human brain. In order to extract tissue specimens, for example for the pathological examination regarding benignity or malignancy, a needle with a small cavity is inserted into the tumour. The high precision of this action enables the diagnosis of smaller lesions and, thereby,

benefits early treatment. In the setup presented, the location of the lesion is identified in a preoperative step, using tomographic data of the patient. A prototypical *VectorVision*® system of *BrainLAB AG* was utilised as the tool for this preoperative planning as well as for the intraoperative registration of the patient (and the lesion) according to a defined world coordinate system. To achieve this, the system integrates an optical tracking system, consisting of a stereo camera pair and optical marker arrays. One or multiple of these marker arrays can be applied to objects (e.g. skull bone of the patient) and are tracked by the camera system for their pose. In contrast to the conventional application of such navigation systems in the operating room where the positioning and insertion of the biopsy needle is performed manually by monitoring the location of needle and lesion utilising a graphical representation, this implementation setup applies robotic assistance for this step. This way, false interpretation of the graphical representation is eliminated and accuracy is enhanced. For this purpose, the instrument which comprises a guide jacket for the biopsy device, is equipped with an additional optical marker array (compare figure 5.1 *(a)*). With this, the optical tracking system establishes a continuous localisation of the lesion in relation to the instrument guided by the *KineMedic*. Inevitable uncertainties introduced by the setup (e.g. positioning of the robot base) are reduced significantly. By connecting the tracking system to the robot control, this data has been used to control of the robot. However, remaining position errors persist which result from the registration process, the resolution and frame rate of the tracking system, as well as from the remaining position control error of the robot.

Although the use of a robot here suggests a completely autonomous execution of the biopsy, this implementation utilises a semi-active, hands-on approach in order to give maximum control of the actions to the doctor. The workflow is therefore structured in sequenced steps applying a state machine and different control modes of the robot:

1. The robot is operated in impedance control mode and freely manoeuvrable in all directions. The doctor has full control of the arm and can check the accessibility of the surgical site and identify possible collisions with other objects.

2. By switching manually to a second mode, the impedance control limits the free motion along a trajectory towards a defined point on the planned needle insertion path above the patient (pre-positioning). This haptic guidance is enabled by applying virtual fixtures in the form of different Cartesian stiffness to the TCP. Furthermore, the orientation of the instrument is aligned automatically with the insertion path of the biopsy needle (compare figure 5.1 *(c)*).

3. By switching to the next mode, the impedance control enables free motion only along the insertion path of the needle (compare 5.1 *(d)*). This motion is blocked and the system is switched automatically to the next mode when the position is reached, where the length of the (not equipped) biopsy needle combined with the guide jacket results in a proper alignment of the needle cavity with the tumour.

4. In this mode the doctor releases the robot, which then autonomously performs the fine positioning. Due to the small and slow motions, this autonomous action is acceptable regarding collision avoidance and safety.

5. The robot then holds its position by applying impedance control with maximum Cartesian stiffness[1]. The doctor then inserts the biopsy needle into the guide jacket and performs the biopsy manually (compare figure 5.1 *(e)*) while receiving the natural feedback of occurring forces. In this sense, the robot is applied as a passive holding arm, providing the proper alignment of the needle towards the lesion and limiting the insertion depth. If the tissue specimen is checked, the user switches manually to the next step.

6. The safe removal mode inverts step 3, limiting the free motion of the robot to the direction away from the patient (compare figure 5.1 *(f)*). When a distance of 100 mm is reached, the system switches automatically to the next mode.

7. The robot arm is now freely manoeuvrable again (as in mode 1). However, in order to avoid collisions with the patient, a horizontal virtual wall above the patient is imposed.

This application combines multiple control modes of the robot. Changes in the workflow can be easily implemented in order to adapt it to other demands or applications, like the very similar approach of positioning a drill machine correctly for placing pedicle screws in spine surgery [Ortmaier et al., 2006]. By applying an external position sensor (tracking system), which continuously measures the pose of the TCP in relation to an anatomic target, uncertainties deriving from the robotic setup and the compliance of the robot can be reduced significantly. The position accuracy of the robot proved adequate for the application, targeting a spherical shaped lesion of 1 mm diameter. However, the experiment showed that the tracking systems applied for intraoperative navigation systems lack adequate sampling rates (e.g. 30 fps) and real-time characteristics (e.g. non-deterministic latencies up to 150 ms) for its application as position sensors in dynamic position control modes of the robot (control cycle 3 kHz).

[1] This mode could be replaced by a classical position control mode.

For further reading, KONIETSCHKE et al. introduce a more detailed description of the robot-assisted biopsy application presented [Konietschke et al., 2006b].

5.2 Ultrasound Transducer Guidance

Within the ongoing *ASTMA* project funded by the *German Research Foundation* (DFG), the *DLR* research group and the ICCAS (Innovation Center Computer Assisted Surgery, University Leipzig, Germany) applies a single *MIRO* robot for force-controlled guidance of an ultrasound transducer [Vázquez et al., 2008].

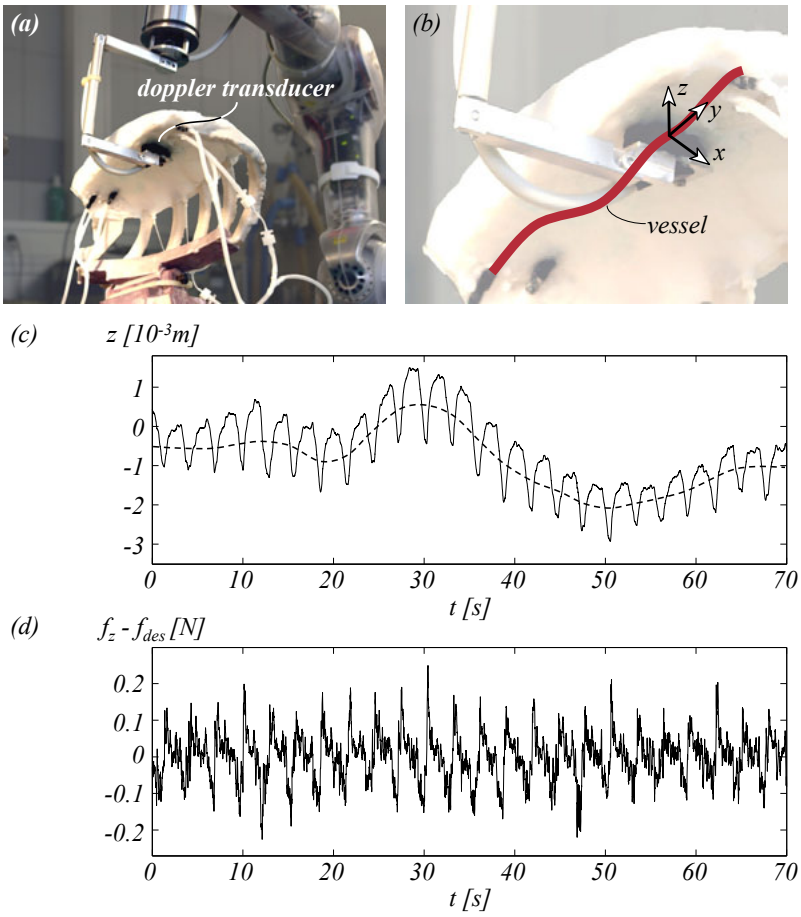

Figure 5.2: Preliminary setup for Doppler guidance with an open-chest phantom developed by *ICCAS (a)*, stylised blood vessel *(b)*, position of the transducer in z-direction over a period of 70 seconds *(c)*, force deviation in z-direction *(d)*, photos copyright *DLR*

This setup (compare figure 5.2 *(a)*) is intended to assist the surgeon during the task of harvesting the left internal thoracic artery (LITA) for coronary artery bypass grafting (CABG). The artery is surrounded by tissue and is not visible. The robot guides an endoscopic Doppler transducer in order to localise the artery and its shape to provide data for the manual or robot-assisted dissection of the vessel. Due to the unknown shape of the surfaces and the vulnerability of the vessel, the *MIRO* robot applies force control in the z-direction (compare figure 5.2 *(b)*) to maintain physical contact between transducer and tissue. The computed localisation of the vessel within the Doppler images controls the *MIRO* to keep the transducer positioned on the vessel (x-direction). The motion along the vessel (y-direction) can be influenced by the surgeon by exerting forces to the robot by utilising Cartesian impedance control. The controlled stiffness is determined from the ultrasound data and the force measured between transducer and tissue.

As the robot is only used during short steps of this operation, it is mounted to a mobile stand, which can be easily removed. It applies methods of visual servoing and force control for a semi-active, hands-on approach. Due to the absence of an adequate endoscopic Doppler probe with force-sensing capabilities at this point, first tests are carried out with a prototypical Doppler instrument on a C-shaped holder (compare figure 5.2 *(a)*) in an open chest procedure and apply the torque sensors of the *MIRO* for measuring the contact force. Figure 5.2 *(c)* plots the motion in the z-direction of the *MIRO* during travelling along the vessel for a period of $70\,s$ in a first in-vivo porcine test conducted at *UniversitätsSpital Zürich,* Switzerland. The inside shape of the chest is indicated by the dashed approximation curve superposed by a more dynamic motion (0.3 Hz), which is due to the respiration. Figure 5.2 *(d)* shows that the error of the contact force in z-direction ($f_z - f_{des}$) is within a range of only ± 0.2 N. Regarding the composition of this Cartesian force computed from multiple joint torque sensors and its exposure to various disturbances (e.g. robot dynamics, elasticities of the instrument), this result shows descriptively the sensitivity (resolution) of the *MIRO* force-sensing. In order to achieve high absolute accuracy of the force sensing, ongoing research aims at a calibration of the entire robot arm.

5.3 Accuracy Evaluation for Laser-Osteotomy Applications

The surgical task of cutting bone tissue (*osteotomy*) is present in many surgical procedures. Basically, most of these operations remove bone tissue (e.g. to remove bone metastases), correct deformations (e.g. correction of hip dysplasia), or prepare the site for implants (e.g. artificial knee joint).

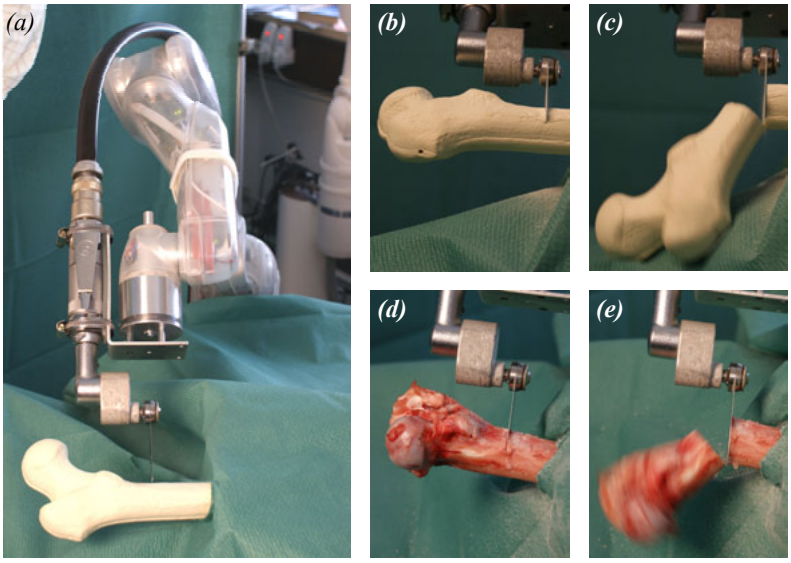

Figure 5.3: Preliminary tests of the *MIRO* guiding an oscillating bone saw for osteotomy *(a)*, cutting of a *Synbone* femur phantom *(b, c)*, cutting of a porcine femur *(d, e)*, photos copyright *DLR*

Besides a desired geometric accuracy of the osteotomy according to the therapy planning, minimising the loss of healthy bone tissue, and avoiding harm to surrounding tissue (e.g. necrosis caused by heat or particles) are challenging. The application of a robot for guiding the tool can enhance the geometric accuracy, whereas the other two demands are determined more or less by the tool. Three different tool principles for cutting bone tissue are relevant in robot-assisted osteotomy: milling [MAKO, 2009], sawing [Moctezuma de la Barrera, 1995], and laser ablation [Burgner et al., 2009]. All principles have advantages and disadvantages, which are not subject of the thesis at hand. Milling and the use of oscillating saws have not been performed as applications for the *MIRO* so far, as corresponding surgical applications are not the subject of current research projects at the *DLR*. However, a first preliminary test with an oscillating bone saw (compare figure 5.3 *(a-e)*) showed that despite its low payload compared to e.g. the *Evolution 1* and the compliant design, the *MIRO* can cope with the forces introduced by the oscillating actuation of the saw and the cutting. Nevertheless, an evaluation regarding the achievable accuracy with the *MIRO* is pending.

The advantages of applying a laser system for osteotomy comprise the absence of reaction forces due to the contact-free principle and the possibility of complex cutting trajectories. The first advantage enables the application of lightweight and compliant

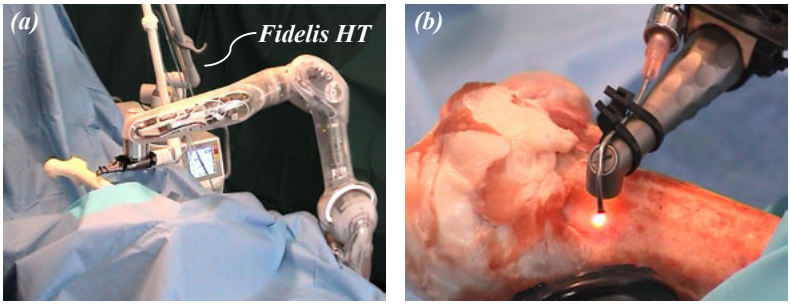

Figure 5.4: Setup integrating a *MIRO* arm with a *Fotona Fidelis HT* surgical laser *(a, b)*, photos copyright *DLR*

robot arms, as dynamic forces and torques disturbing the accuracy of the robot are absent. In contrast, the second advantage can be amplified by the use of robots, as they are intended for accurately following a commanded trajectory. Regarding the scope of applications for the *MIRO*, guiding a laser for osteotomy can be seen as a challenging application regarding accuracy. Figure 5.4 *(a, b)* depicts first tests of the *MIRO* robot with a surgical laser system (*Fotona Fidelis HT*, Er:YAG, 1 Joule, 12 Hz) for cutting *Synbone* phantoms and porcine femurs, carried out in cooperation with the *University Hospital rechts der Isar,* Munich. The passive laser mirror arm is coupled to the TCP flange of the *MIRO*. These tests proved the compatibility of the *MIRO* with the kinematics of the passive laser mirror arm and the workflow consisting of the impedance-controlled positioning of the robot followed by autonomous operation during cutting. In this simple setup, the additional load on the *MIRO* caused by the mirror arm was approximated by a constant load at the TCP for the gravity compensation. Regarding the position control mode (cutting) and the small workspace, this simplification is acceptable for first tests. However, in a later application, mass and inertia of the mirror arm kinematics must be computed properly.

However, the geometric quality of cutting bone tissue with a laser is subject to many disturbances, like inhomogeneity of bone tissue or contamination of the optical lens[2].

By this, the resulting cut geometries of the conducted tests are not satisfactory to approve the applicability of the robot for this technique. In order to identify the applicability of the *MIRO*, only its position accuracy has a relevant influence on the geometric result of the laser cut. Therefore, the accuracy of the *MIRO* robot was

[2]In-house tests of the *FOTONA Fidelis HT* with a porcine shoulder blade revealed that the ablation ratio varied between 1.6 and 3.7 mm^3/sec, due to the inhomogeneity of bone tissue (level of water absorption). Furthermore, the contamination level of the optical laser lens had a significant impact on the ablation ratio.

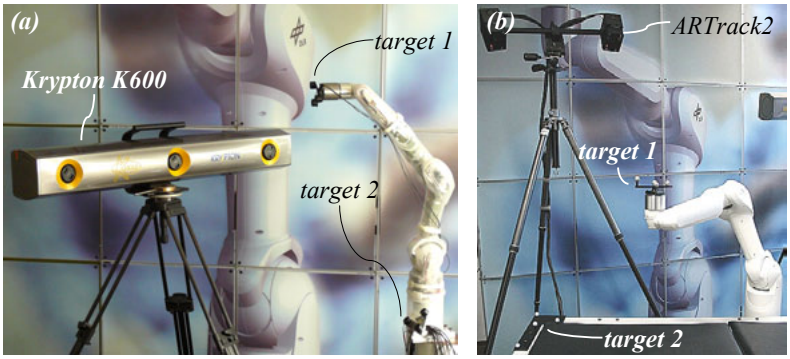

Figure 5.5: *MIRO* setups integrating external position sensors: calibration setup utilising a *Krypton K600* measurement system *(a)*, closed-loop position control setup integrating a *ARTrack2* tracking system *(b)*, photos copyright *DLR*

analysed separately without the laser system.

In order to increase the accuracy of the robot, enhanced calibration and compensation methods must applied and the resulting accuracy is measured with a setup integrating an external optical tracking system (*Krypton K600* by *Metris*®, Germany). At a maximum distance of up to 3 m, this camera system can localise marker targets (active LEDs) with an accuracy of 0.1 mm [Metris, 2009]. Two tracking targets have been applied: to the *MIRO* TCP and one to the robot's base (compare figure 5.5 *(a)*). First, the actual Denavit-Hartenberg parameters of the *MIRO* were identified. Due to manufacturing tolerances e.g. the link lengths deviate from the kinematic concept, which results in a position error when computing the forward and inverse kinematics. Second, an elastic compensation based on measured joint torques and the mass properties derived from the robot CAD model was implemented. As a result a remaining error of smaller then 0.498 mm (standard deviation: 0.259 mm) for the position accuracy and of up to 0.2 mm for the position repeatability was identified. The tests were carried out according to the appropriate standard for industrial robots [ISO 9283, 1998], with 60 different poses throughout the whole workspace. Although this result is remarkable for a lightweight robot[3], a more precise calibration of the joint torque sensors (jts), exact identification of the real mass properties, and modelling of the link elasticities are proposed to further enhance the accuracy of the *MIRO* robot.

Besides the accuracy of the robot arm, the system accuracy can be enhanced through additional sensors. In applications based on pre-planned data, the pose of an anatomic target structure in the operating room must be registered in relation to the robot. For this purpose, technical systems are used which measure the location of the

[3]In comparison, the repeatability of a *KUKA KR 16* has a remaining position error of $\pm 0.1\,mm$ [KUKA, 2004a].

patient or anatomic structures. Such systems can be applied to measure additionally the actual pose of the TCP. Therefore, the *MIRO* was integrated with an *ARTrack2* optical tracking system (*Advanced Realtime Tracking GmbH*). Based on an infrared stereo camera, retro-reflective markers are localised with 60 Hz. A set of pre-calibrated marker targets was attached to the TCP and the base (compare figure 5.5 *(b)*). The tracked position of the TCP was applied to the robot position control in the form of observer feedback, in order to compensate the actual position error. For commanded trajectories (velocity < 0.01 m/s) the *MIRO* is able to follow these trajectories with an error smaller than 0.1 mm, which is within the sensor resolution of the external tracking system [Tobergte et al., 2010].

Regarding the applicability of the *MIRO* robot for laser osteotomy procedures, it can be summarised that with closed-loop position control utilising an external tracking system, a positioning accuracy of 0.1 mm can be provided. It must be stated at this point that other steps within an application, like the registration of anatomic structures, introduce significant errors[4]. Therefore, the identified accuracy of the *MIRO* robot is more than sufficient for these applications.

Beyond accuracy, the convenient impedance-controlled pre-positioning of the *MIRO* as well as the compact dimensions of the setup have been rated as important benefits by the physicians.

[4] A survey of three optical navigation systems revealed a mean target registration error of 1.00 mm as best result for localisation of the patient (skull) in maxillofacial surgery [Strong et al., 2008]

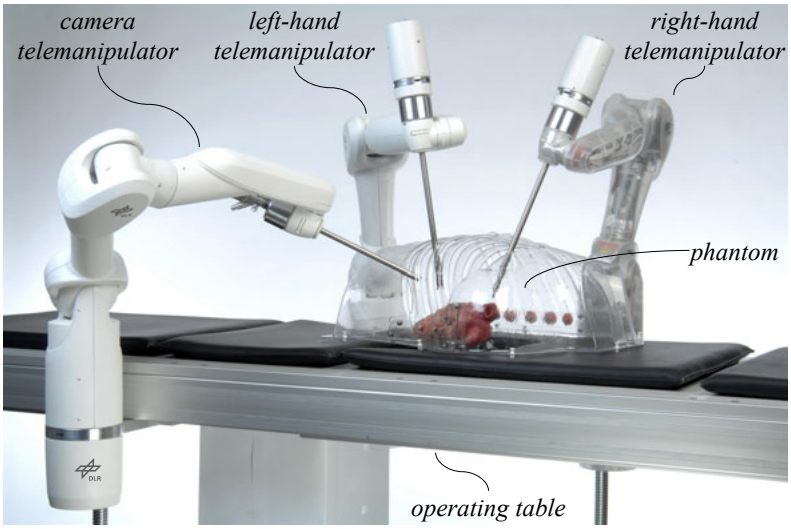

Figure 5.6: *DLR MiroSurge* telerobotic system: telemanipulator side with three *MIRO* arms, equipped with laparoscopic instruments, photo copyright *DLR*

5.4 MiroSurge Telerobotic System

This robotic system for telesurgery is developed within the *MiroSurge* project funded by the *Bavarian Science Foundation* (*BFS*). Aimed at establishing a platform for research in the field of endoscopic telesurgery, the modular system design places a great deal of emphasis on configurability regarding the number and arrangement of components, application of different control methods, design of workflows, and distribution of computing power. The *MiroSurge* project addresses various research topics, which comprise:

- integration of a three-arm, bimanual telerobotic system for laparoscopic surgery
- instruments and interfaces providing force feedback
- enhanced planning systems for robot setup optimisation
- application of visual servoing techniques to compensate for the motion of the beating heart

The current configuration integrates three *MIRO* robots with laparoscopic instruments as telemanipulators (compare figure 5.6). The system benefits from the design optimisation of the *MIRO* robot regarding the requirements of minimally invasive surgery [Hagn et al., 2008b]. As most steps of the operation are intended to be covered by applying the robotic system, the *MIRO* robot arms are mounted to the operation

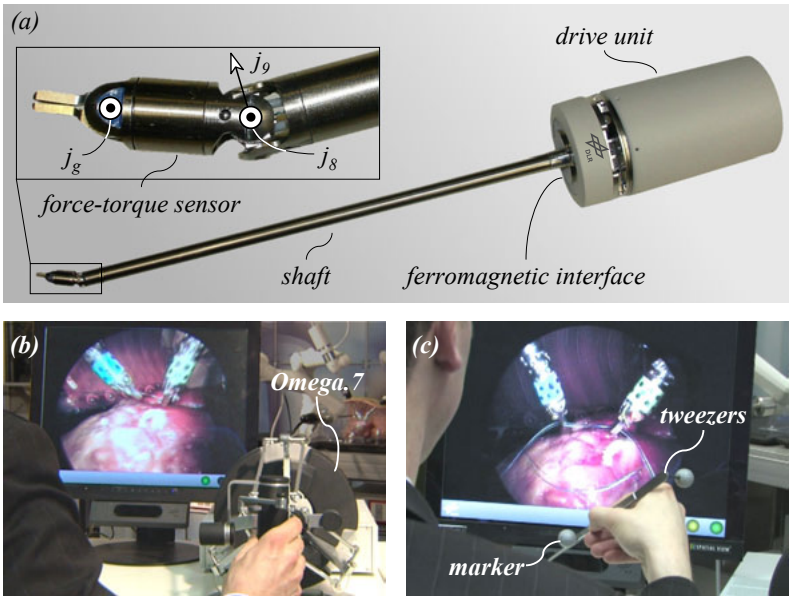

Figure 5.7: Actuated laparoscopic instrument *(a)*, surgeon console applying haptic interfaces with force feedback *(b)*, control of the robotic system by the use of optical tracked conventional instruments *(c)*, photos copyright *DLR*

table, which is feasible due to their low weight of 10 kg. For specialised operating rooms, which are dedicated to the *MiroSurge* robotic system, FRUMENTO et al. alternatively propose a ceiling-mounted system, for motorised positioning of the robots above the operating table [Frumento et al., 2006].

One *MIRO* arm is equipped with an endoscopic stereo camera, provided by *Richard Wolf GmbH*, Germany. The two other *MIRO* robots are intended for bimanual manipulation and interface with laparoscopic instruments [Seibold et al., 2008] developed in-house. Besides the actuated functional DoF (e.g. gripper j_g), these instruments integrate two additional actuated joints (j_8, j_9) near the tip of the instrument (compare figure 5.7 *(a)*), enabling six DoF motion inside the patient. Furthermore, these instruments integrate a miniaturised 6-DoF force-torque sensor and additional force-sensing of the functional DoF (e.g. gripping force). A new generation of instruments (*DLR MICA*), which connects to the *MIRO* communication and power supply directly at the TCP flange (compare section 4.60) is under development [Thielmann et al., 2010]. Besides avoidance of distracting external cables, this new design aims at the seamless integration of the actuated instrument into the communication and control of the *MIRO* and the possibility of automated procedures for changing instruments.

The telemanipulator portion of the system is controlled by the surgeon from a remote console. One configuration of this console integrates bimanual haptic interfaces (*Omega.7*, *Force Dimension*, Switzerland) providing six DoF motion and one DoF for commanding the functional DoF (see figure 5.7 *(b)*). The three translatory DoF as well as the functional DoF integrate actuators. In combination with the telemanipulators, this enables six-DoF control of the instrument tips and the haptic feedback of the gripping and manipulation forces. Another configuration (compare figure 5.7 *(c)*) applies conventional surgical instruments (e.g. tweezers) equipped with retro-reflective markers, which are tracked by an external optical tracking system, to control the Cartesian motions of the instrument tips. This approach does not provide haptic feedback. However, it is assumed to improve the natural interaction with the system due to the surgeon's familiarity with this interface and due to the reduced inertia.

To provide a visual sensation of the operating site in 3D, the endoscopic stereo camera is connected to an autostereoscopic display (*SeeFront 3D*, Germany).

The setup of the robotic system in the operating room is planned according to preoperative data (e.g. MRI/CT-scan of the patient) as introduced by KONIETSCHKE. After definition of the surgical site and proposition of trocar locations by the surgeon, this tool computes the ideal positions of the robot's bases in order to avoid joint motion limitations, singularities, and collisions [Konietschke, 2008]. The intraoperative registration of the patient utilises the *DLR 3DMo*, a handheld multi-sensory optical digitiser [Suppa et al., 2007], which is localised by an optical tracking system or mounted directly to the TCP flange of one *MIRO* robot, operating in impedance-control mode (compare figure 5.8 *(a)*). After registration of the resulting patient-surface scan with the preoperative planning, a refinement of the setup planning is computed and the ideal positions for the robots are determined. Together with the trocar positions, this data is displayed by applying a handheld laser projector [Konietschke et al., 2007]. In the current implementation of the robotic system, the *MIRO* robots are operated in different control modes:

- mode 1: In the initial step after setup, the *MIRO* robots move in Cartesian position control mode from their parking pose towards a location above the planned insertion points (compare figure 5.8 *(b)*). The orientation of the TCP is controlled in a way which aligns j_7 with the trocar axis.

- mode 2: The system then switches to impedance control mode, enabling a hands-on interaction (see figure 5.8 *(c)*). The Cartesian rotations of the TCP are blocked in order to maintain the alignment of instrument and trocar. This mode is used to insert the instruments into the patient (figure 5.8 *(d)*).

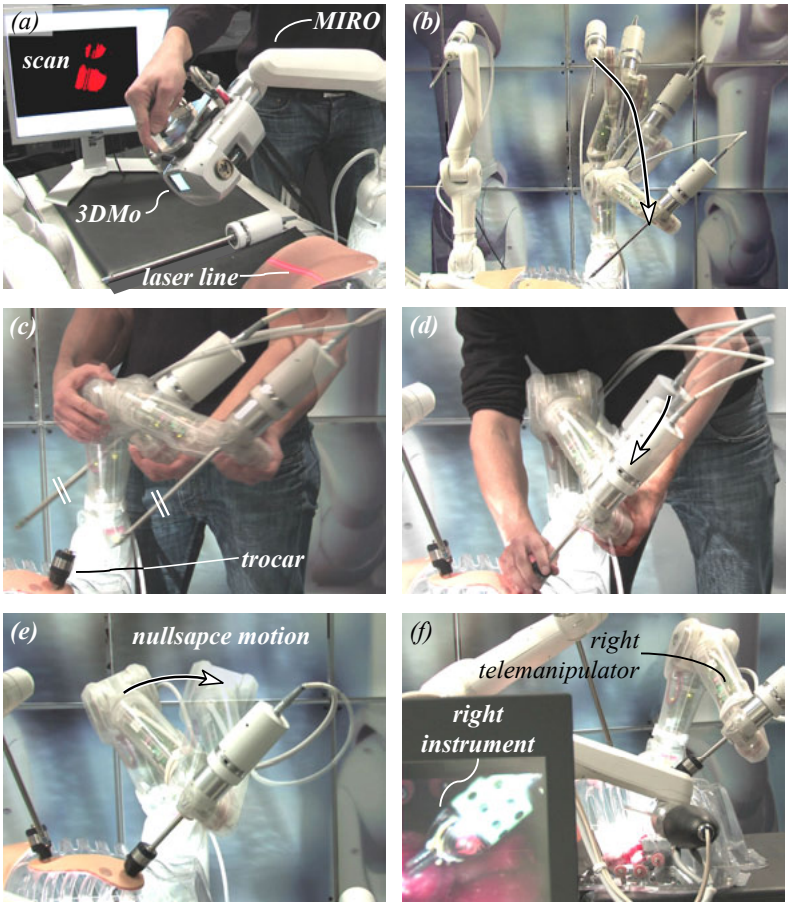

Figure 5.8: *MiroSurge* setup procedure: patient registration applying a laser range scanner (*DLR 3DMo*) mounted to the TCP flange of the *MIRO (a)*, initial approach in position-control mode *(b)*, impedance-controlled guiding of the robot with blocked Cartesian rotations *(c)*, impedance-controlled insertion of the instrument *(d)*, position-controlled nullspace motion of the *MIRO* elbow *(e)*, established teleoperation connection *(f)*, photos copyright *DLR*

- mode 3: The telemanipulators are hooked up to the operator side for telerobotic control. The *MIRO*s perform a null-space motion, which increases the distance between their elbows in order to avoid collisions (compare figure 5.8 *(e)*). Then, the bilateral position control scheme introduced by Tobergte et al. is established [Tobergte et al., 2009], which is structured in lower (fast) and higher (slow) layers (compare figure 5.9). Abstraction levels for decoupled design are thereby created. Layer 1 establishes the joint control for all devices separately. Layer 2 provides Cartesian control of the devices. A *MIRO* with the attached

instrument forms a telemanipulator (nine DoF) and the Cartesian control is established for the instrument tip pursuant to the restrictions of the fulcrum point. The third layer (bilateral teleoperation) combines an operator device (e.g. right *Omega.7*) with the corresponding telemanipulator (right *MIRO* with instrument) to a one arm master-slave system for bilateral teleoperation with force-feedback (compare figure 5.8 *(f)*). The fourth layer controls the multi-arm coordination for bimanual teleoperation and interfaces with all vision sensors. By applying a foot switch, the operator can alternatively connect its input devices with the third *MIRO* to control the endoscopic camera.

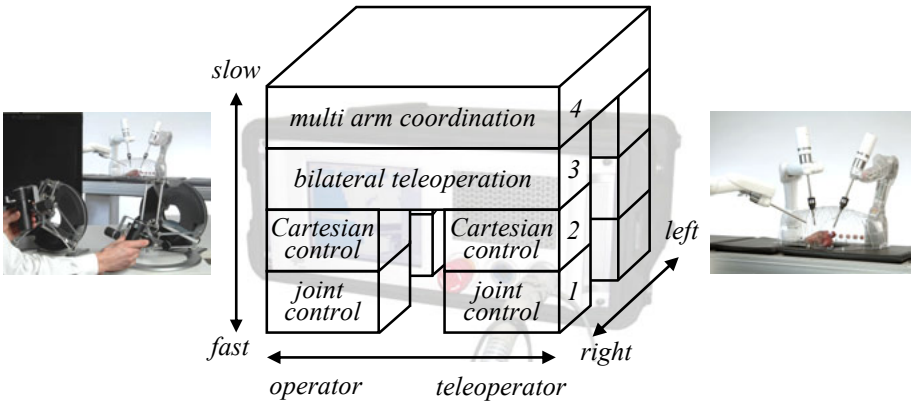

Figure 5.9: Simplified representation of the architecture for bimanual remote control of the *MiroSurge* system, picture copyright *DLR*

- mode 4: The heart beat compensation mode optionally extends the preceding mode 3 to compensate for motions of organs by applying visual servoing approaches. In the *MiroSurge* project, this is implemented, for example, for compensation of the heart's motions in cardiosurgery. Natural landmarks on the heart surface are extracted and tracked in the images of the endoscopic camera. To enhance the robustness, this position data is combined with other sensor data (patient's respiration) and online prediction methods [Ortmaier et al., 2005]. The resulting position frame of the heart surface can be overlaid with the motions commanded by the operator in order to compensate for the heart's motions.

Regarding the desired versatility, the *MIRO* applies the following aspects and features in the current *MiroSurge* configuration:

- multi-arm configuration
- operating table mounting
- programmable constraints (fulcrum point)
- active operation
- control modes: teleoperated and hands-on control of the robots
- interfacing with endoscopic instruments
- null-space motion and programmable workspace restrictions for collision avoidance
- Cartesian level impedance and position control

In the *MiroSurge* system the *MIRO* robots are mounted to the rail of an operating table.

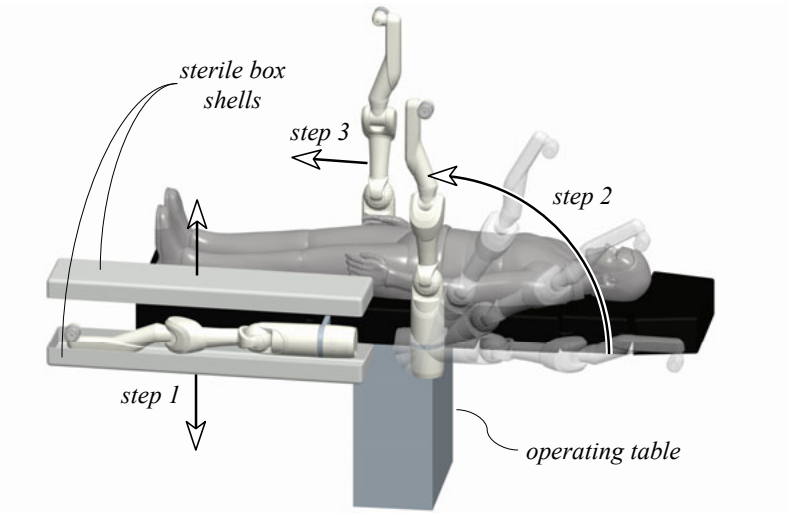

Figure 5.10: Proposed procedure for attaching the *MIRO* to an operating table, integrating an additional passive joint between rail clamps and robot base

In order to save setup time, it is desirable to attach the robots to the operating table before positioning the patient on the table. Therefore, the author proposes a procedure where the robots are boxed while they are attached horizontally to the side

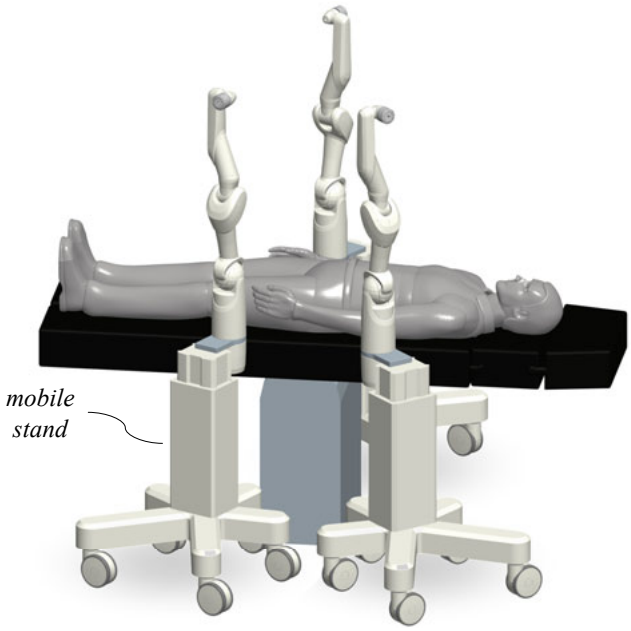

Figure 5.11: Setup utilising single mobile stands for operating the three *MIRO* robots

rails of the table by clamps, as indicated in figure 5.10 (step 1). In this step, the *MIRO* robots are already draped and contained in sterile boxes. This horizontal arrangement of the robot leaves sufficient room for moving the patient onto the operating table. Then, the two half-shells of the box are removed and the robot is brought into an upright or intermediate position (compare with figure 5.10, step 2). To enable this setup motion, an additional passive, lockable joint between the rail clamps and robot base is proposed. In step 3, the robot is positioned along the rail. Another setup possibility is illustrated in figure 5.11, where each robot is mounted and operated on a single mobile stand.

Although the current *MiroSurge* system applies three *MIRO* robots, configurations with four or more robot arms are feasible. Due to the approach of complying with the fulcrum point constraint by active control of the redundant kinematics, the invariant insertion point can be located within a significant range inside the robot's workspace.

Therefore, the necessary DoF for the setup of the robot's base can be reduced, which simplifies the design of the robot-setup positioning components. This is an important result of the *MIRO* design and shows significantly the difference to RCM approaches like the *da Vinci® Surgical System*. For the operating-table-mounted option, chosen for *MiroSurge*, the single DoF along the side rails is sufficient for the setup. The main advantage of the operating-table-mounted option is that the table

height can be adjusted without consideration of the robot control. However, a more convenient way for the setup is the integration of the robots into a mobile stand.

Figure 5.12 *(a, b)* depicts a setup of three *MIRO* robots on the smallest possible footprint. If the robot bases are aligned in a row as depicted in figure 5.12, a closest distance of 115 mm between the wrist centre points (intersection of j_6 with j_7) is reachable. This compact footprint has a base width of 388 mm and results from the following design aspects of the *MIRO*:

- zone 1: Absence of interference geometries regarding rotations of j_1, achieved by the more or less rotation-symmetric shape of $miro_1$ and $miro_{23}$.
- zone 2: Possibility of nullspace motions of the elbow ($miro_{45}$), due to the redundant number of joints.
- zone 3: Compact design of the wrist ($miro_{67}$).

The setup shown in figure 5.12 is intended for operations, where the ports for the instruments must be located very close to each other (e.g. Slawin and Kella propose a distance of 80 to 100 mm between each port for robotic radical prostatectomy [Slawin and Kella, 2005]). The scene rendered in figure 5.13 illustrates a compact three-arm setup mounted on a mobile stand proposed for urological operations, like the endoscopic extraperitoneal radical prostatectomy [Stolzenburg et al., 2007]. This setup can be easily expanded by additional robot arms mounted to this mobile stand, to the operating table, or an additional mobile cart. Due to the low weight of the *MIRO* robots, setups mounted to the ceiling are also feasible, either by application of a motorised ceiling support system as proposed by Frumento et al. [Frumento et al., 2006] or by integrating a passive, lockable off-the-shelf system like the *Draeger AGILA* (compare figure 5.14). However, for ceiling-mounted options, besides the applicable payload[5], vibrations and stiffness of the support system are critical issues. For both the ceiling-mounted and mobile stand version, the table height and configuration of the table top must be taken into consideration by the robot control.

It is obvious that the different setups introduced in this section can be adapted for other surgical procedures and numbers of robots. For further reading on other parts of the *MiroSurge* system (e.g. preoperative planning), the author proposes the following publications: [Hagn et al., 2009] and [Konietschke et al., 2009].

[5] *Draeger AGILA* ceiling mounted support system: 120 kg payload [Dräger, 2007]

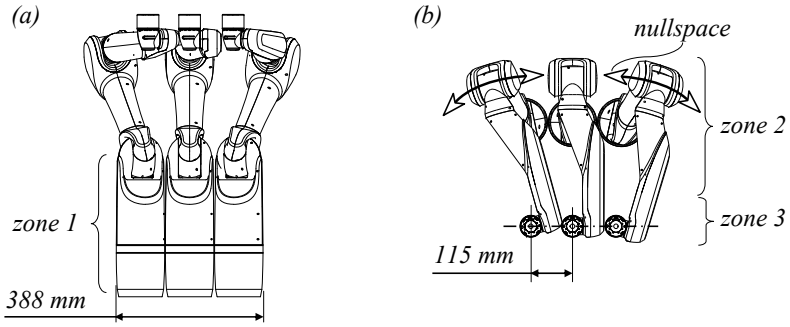

Figure 5.12: *MiroSurge* three-arm configuration with smallest footprint: front view *(a)*, top view *(b)* (note: the depicted views do not apply the first angle projection method)

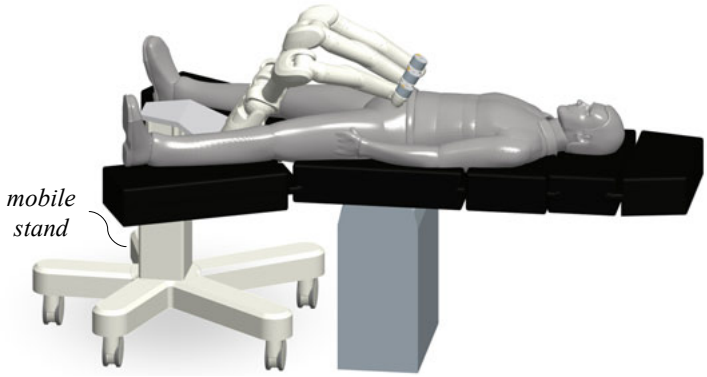

Figure 5.13: Three *MIRO* robots integrated on a single mobile stand

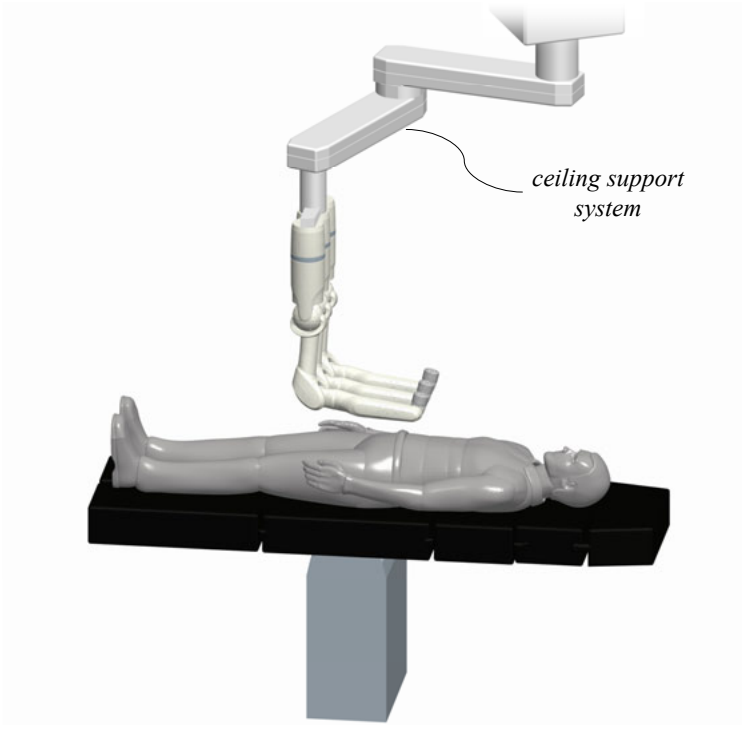

Figure 5.14: Setup integrating a ceiling-support system

5.5 Conclusion on the Results

The preceding sections introduced example implementations of the *MIRO* robot in prototypical applications, which cover all aspects defined in the versatility paradigm (except MRI-compatibility). The results can be summarised as follows:

- The biopsy application (section 5.1) showed the value of the hands-on robotics capabilities of the robot. The surgeon is always in full control of the system, only those tasks which are absolutely necessary (fine positioning of the biopsy device) are covered by an autonomous mode.

- The application of force-sensitive guidance of an ultrasound transducer showed the applicability of the *MIRO* in applications, where the interaction forces of the robot with tissue are critical. Therefore, an additional force-torque sensor at the TCP is not necessary. Furthermore, the experiences during the first clinic trials proved the benefit of the *MIRO*'s compact design, as the robot arm integrates seamlessly alongside the surgeon in the crowded environment of the operating room.

- The experiments for robot-guided laser osteotomy showed remarkable repeatability for a lightweight robot with a remaining position error of $\leq$0.2 mm and in closed-loop position control utilising an external tracking system a remaining position deviation of below 0.1 mm. Therefore, the *MIRO* is applicable in a wide range of medical applications where accurate positioning of instruments is required.

- The *MiroSurge* system showed the feasibility of setups integrating multiple *MIRO*s on a small footprint, enabled by the compact design and the possibility of null-space motion. Furthermore, the availability of impedance control turned out to be a comfortable opportunity for positioning the robots during the setup procedure. The capability of complying with the fulcrum point by control reduces the necessary number of DoF for positioning the robot's base. Finally, the wrist and end effector design proved to be compatible with the requirements introduced by endoscopic instruments.

Figure 5.15 depicts the workspace of the *MIRO* robot and table 5.1 summarises the central design characteristics and performance data.

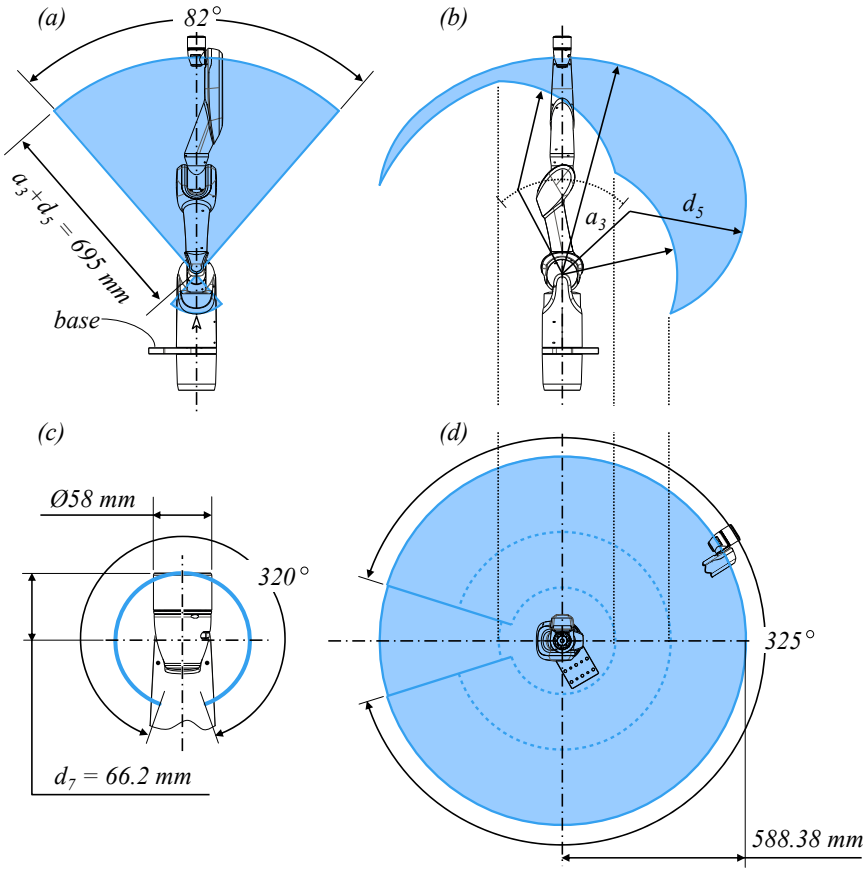

Figure 5.15: *MIRO* workspace: motion volume of the wrist centre (intersection of j_6 with j_7) generated by actuation of j_2, j_3, j_4 *(a)*, planar range of motion of the wrist centre generated by actuation of j_2, j_4 *(b)*, range of motion of j_6 *(c)*, range of motion of the wrist centre generated by actuation of j_1, j_2, j_3, and j_4 *(d)*

parameter	*value / description*
number of actuated joints	7
kinematics	roll-pitch-yaw-pitch-roll-pitch-roll
workspace	compare figure 5.15 *(a - d)*
payload	3 kg
weight	9.8 kg
implemented interaction approaches	autonomous, hands-on, and telerobotic applications
available control modes on joint level	position, torque, impedance
available control modes on Cartesian level	position, torque/ force, impedance
motor torque control cycles	20 kHz ($miro_1$ - $miro_{45}$), 100 kHz ($miro_{67}$)
integrated electronics	all, besides AC/DC conversion and PCIe communication board
integrated sensors	joint-sided torque sensors, motor- and joint-sided position sensors
cabling	internal cable conduit of the complete robot cable harness
instrument interface	switchable electro-magnetic coupling
position error in accuracy tests (60 poses)	0.5 mm (standard deviation: 0.26 mm)
position error in repeatability tests	0.2 mm
Cartesian position accuracy in closed-loop control with external tracking system (*ARTrack2, Advanced Realtime Tracking GmbH*)	< 0.1 mm
maximum stiffness of Cartesian impedance control	$K_{x(max)} = \begin{bmatrix} 4000\ N/m \\ 4000\ N/m \\ 4000\ N/m \\ 300\ Nm/rad \\ 300\ Nm/rad \\ 300\ Nm/rad \end{bmatrix}$
safety brakes	motor-sided, spring-applied
external control unit interfaces	Ethernet TCP/IP, e-stop
control cycle up to Cartesian control level	3 kHz
Cartesian control cycle latency	$< 333\ \mu$s

Table 5.1: *MIRO*: characteristics and performance data

Chapter 6

Conclusion and Outlook

This thesis presents the development of the versatile lightweight robot for surgical applications: *MIRO*. The intention of designing a surgical robot which is optimised with respect to versatility is motivated by the diversity of clinical applications, workflows, and surgeons' preferences. The final two sections of this thesis (6.1 and 6.2) summarise the work and give an outlook on future topics.

6.1 Conclusion

In contrast to the approach of building multiple specialised systems for different applications, this research focuses on a versatile robot covering multiple surgical applications, enabling different robotic (e.g. control) approaches for the same application, and covering a maximum number of different steps within an operation by utilising the robot.

Model concepts of versatile products in industry were analysed and discussed regarding how versatility is achieved. Furthermore, it was shown that the aspects versatility, usability, and performance are linked with each other and must be balanced carefully.

Based on a survey of the current state of surgical robotics and lightweight robotics, a set of central design aspects for robots has been identified. Additionally, the limitations of current systems were identified by analysing the applied taxonomies in the literature. As a result, the group of redundant lightweight robots consider the demand for versatility more than the surgical robots presented, but are not optimised for the environment of an operating room and for certain surgical procedures, like minimally invasive surgery.

Then, different design strategies for the *MIRO* were compared. The modular approach (e.g. modular robotics) thereby focuses on the composition and configuration of physical components according to the requirements of an application. In contrast, the versatile approach already integrates all physical components, which are then reconfigured for a certain application mainly by means of software. Regarding the requirement of covering multiple steps during an operation, the modular approach has been judged infeasible for the robot arm. Therefore, the *MIRO* is designed for configurability mainly by means of software. However, the complete surgical robotic system, which integrates additional components like instruments and user interfaces, is based on a modular approach. Then, central design aspects of robotic systems were derived from the current state of surgical robotics and partitioned into three subsets. Subset 1 comprises features and design aspects, which are proposed to benefit all surgical applications. Among these are: an adaptable number of robot arms in the robotic system, various mounting options, programmable constraints, various control modes, methods for collision avoidance, and compatibility with different kinds of surgical instruments. The second subset comprises performance requirements (payload, accuracy, workspace), which are derived from applications. The third subset includes optimisation goals (reduced weight and size), which again commonly enhance the application of a robotic system in the operating room. The author formulated the hypothesis that a robot which fulfils all aspects of the first subset and covers a significant range of the second subset, with optimised parameters of the third subset, is a robot with enhanced versatility.

The applied design methodology for the *MIRO* avoids the limitations of the desired versatility in early development phases. Based on the versatile aspects defined in subset 1 combined with a set of design paradigms, a generic design of the robot arm was developed. These five design paradigms comprise lightweight, compact and slender design, redundant and anthropomorphic kinematics, integration of different sensors, and the seamless integration of electronics and cabling into the robot arm. In the next step, technological components were identified for the implementation of the generic design. Besides general requirements (e.g. performance, efficiency), the main eligibility criterion for the selection of technologies has been their integration level (size, compactness). Not till then concrete performance requirements of a range of surgical applications were derived. These requirements were applied to scale the generic design, resulting in the prototypical implementation of the robot arm *MIRO*. During the mechanical design of the robots, the requirements for internal cabling and also most compact and slender design proved challenging, as the diameter of a cable harness and the size of connectors scale only marginally with the payload of the robot. Especially, the hollow shaft diameters of components like motors and reduction

gears turned out to be bottlenecks for conducting the cable harness. By integrating a large amount of electronic components into the robot arm, the diameter of the cable harness bridging a joint was reduced significantly. By introducing 2-DoF joint designs, the usable space for the integration of electronic components was defragmented. Furthermore, the wrist-joint design avoids the necessity of conducting cables through motors and reduction gears. Additionally, the wrist integrates a hollow-shaft design of the last DoF, which enables the optimised use of endoscopic instruments. The design of an interface at the TCP for signal and power supply of instruments has been proposed. Its implementation as well as the design of the sterile drape according to the introduced concepts is pending.

Figure 6.1 summarises graphically the derivation of selected design decisions (indicated by exclamation marks) for the *MIRO* robot, starting with the three major questions of how to provide versatility, usability, and safe use (indicated by question marks). As the central aspect of this thesis, versatility demands for various setup options, multiple control modes, different surgical techniques, different numbers of robots, and multiple steps of an operation. Mainly, this is achieved by lightweight design, 2-DoF joints, integrated joint torque sensors, a large motion range of j_6, hollow shaft design of j_7, joint redundancy, and configurability by means of software.

Three *MIRO* robot arms have been integrated and evaluated so far, besides the earlier generation *KineMedic*. The *MIRO* robot weighs just less than 10 kg and is based on a serial kinematics with seven joints, realising a maximum payload of 3 kg in the current scaling. Structured into a dedicated shoulder with three DoF, the upper arm, an elbow with two DoF, the forearm, and a wrist with two DoF, the *MIRO* kinematics intentionally resembles those of the human arm. This analogy is intended to increase the familiarity of non-technical users with the robot arm, especially regarding its motion capabilities. Integrated joint torque sensors enable various control approaches. They are applied to measure external interaction forces, enabling hands-on robot approaches or detecting collisions. Furthermore, these sensors are applied to calculate the position errors of the flexible joints caused by the lightweight approach. A position repeatability of approximately 0.2 mm, which is relevant for high accuracy surgical tasks, was thus achieved.

The *MIRO* and *KineMedic* robots have been integrated and evaluated in prototypical surgical applications at the *DLR*. In a navigated, robot-assisted biopsy application, the *KineMedic* robot has been integrated with a surgical navigation system and combines hands-on with autonomous procedural steps.

In the *ASTMA* project, the *MIRO* robot guides an ultrasound Doppler transducer in order to explore the shape and location of the left internal thoracic artery.

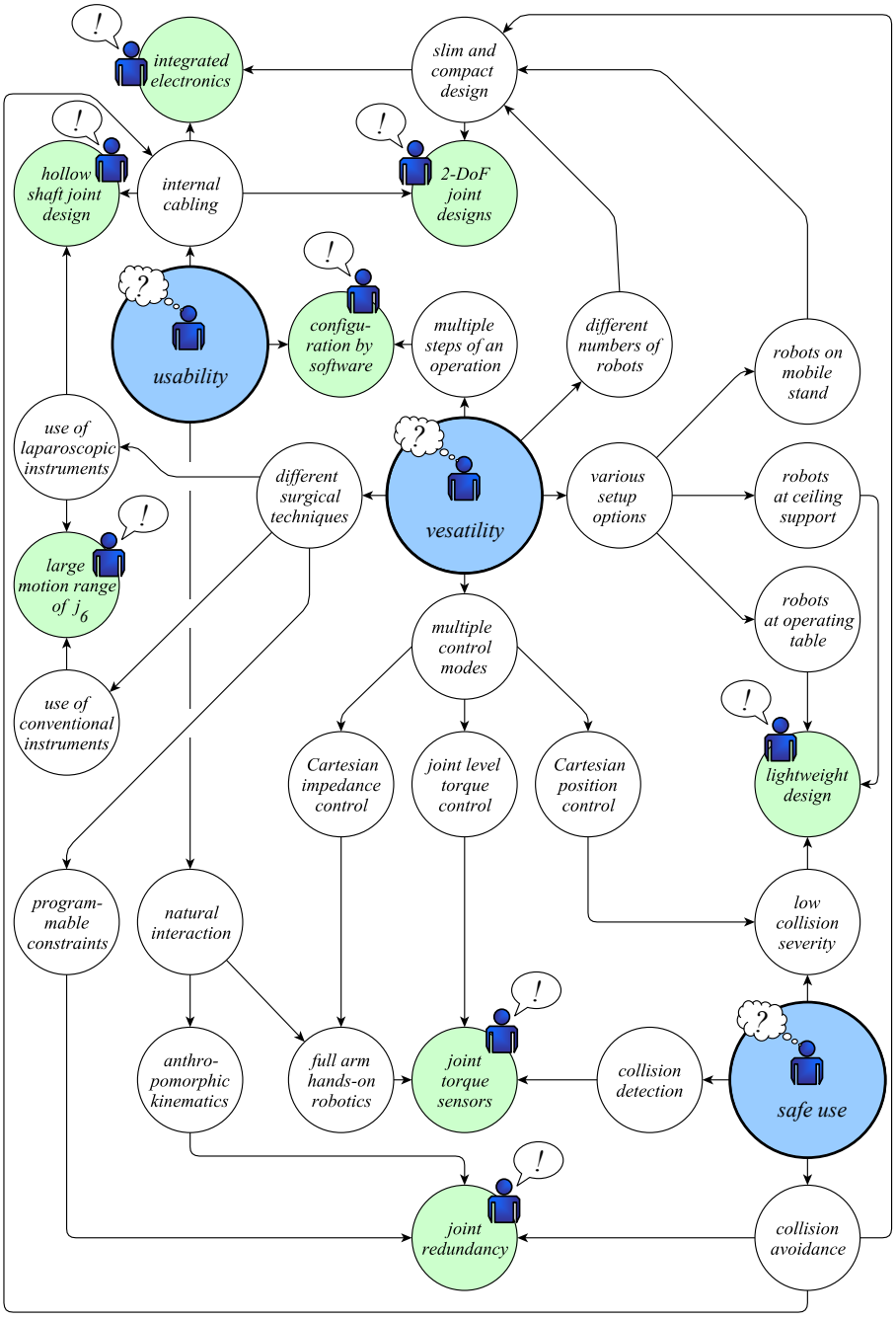

Figure 6.1: Abstracted decision map for selected design topics of the *MIRO* robot

There, the robot joint torque sensors are applied to enable sensitive force-controlled contact of the transducer with the body tissue. The torque sensors are also applied to move the transducer along the vessel using a hands-on robotics approach.

In evaluation tests for osteotomy tasks in orthopaedic surgery, the *MIRO* robot proved compatible with the vibrations of an oscillating saw. However, an evaluation regarding the achievable accuracy with the *MIRO* is pending. For laser-applied osteotomy, the accuracy of the *MIRO* was evaluated, resulting in a position accuracy of approximately 0.5 mm and a position repeatability of 0.2 mm. In a setup integrating an additional optical tracking system which captures the location of the robot's end effector, a remaining position control error of below 0.1 mm was identified.

In the *MiroSurge* system, three *MIRO* arms have been integrated as telemanipulators for telerobotic minimally invasive surgery. In this case, the low weight and the possibility of programmable constraints (fulcrum point) allow for a wide range of possible robot arm setups, comprising operating table, cantilever stand, mobile cart, and ceiling-mounted configurations. In this system, the *MIRO* proved its compatibility with the peculiarities of endoscopic instruments and the fulcrum point constraint. Although the *MIRO*s are controlled remotely during the operation, the hands-on robotic capabilities offer a convenient method for the setup of the robots. Compact and slender design, absence of interference geometries (e.g. external cabling), and the redundant kinematics (null-space motion of the elbow) allow for the integration of multiple *MIRO* arms on a small footprint.

In conclusion, the *MIRO* robot transfers the features and characteristics of redundant lightweight robots to the particular needs of surgery and conditions of an operating room. Compact dimensions, joint redundancy, and low weight have been identified to simplify the integration of various setups in the operating room, where space is limited. Furthermore, the integrated torque sensors and the lightweight design can detect collisions with other objects or personnel and can help to reduce their severity. In conclusion, this thesis has proven the feasibility of a robot with extended versatility, optimised for the use in operating rooms and applicable in a comprehensive, but not unlimited range, of surgical applications.

6.2 Outlook

The central aim of the *MIRO* project is to provide a versatile robotic platform for rapid implementation of existing and new surgical applications. Therefore, future topics focus on further improvement of the robot itself and on its evaluation in additional surgical procedures. The aspect of safety must be analysed for every application, for example regarding functional safety, applied loads, or emergency stopping distance.

These aspects must be regarded for the entire robotic system, but may lead to necessary modifications of the robot, like mechanical overload protection of torque sensors or safe communication protocols.

One open question is whether the robot is suited for guiding conventional instruments (e.g. oscillating saws, milling machines) for osteotomy tasks with adequate accuracy, or whether a scaled *MIRO* is more promising. Therefore, experiments with such instruments need to be carried out. In order to reduce the forces exerted on the robot caused by the cutting, an active control of the cutting speed (e.g. rpm of the milling machine) in conjunction with force-control of the robot appears to be an interesting approach [Cunha-Cruz et al., 2009]. In experiments for laser-applied osteotomy tasks, research on sensors providing the actual cutting depth is most relevant for an integrated robotic system. For minimally invasive telerobotic applications, a new generation of minimally invasive forceps is being developed at the *DLR*, which will be connected to the *MIRO*'s electronics and power supply. Therefore, the proposed signal and power interface will be integrated into the flange of the *MIRO*. Additionally, an alternative setup integrating multiple *MIRO* robots on a single compact mobile cart is planned. However, other setup options, like the ceiling-support mounted version, need to be analysed with clinicians regarding their benefits and limitations. Here, the availability of the robotic system in multiple operating rooms of a clinic in relation to the time effort for setup is especially challenging.

Besides a possible transfer into a commercial product, the *MIRO* robots will be provided to other research groups within the context of future national and international research projects. Therefore, a low-level developer interface for the robot control and an open instrument interface specification is proposed. Naturally, the most relevant goal for the *MIRO* is to bring it into the operating rooms.

Appendix A

Tools

According to the doctoral degree regulations of the *Gottfried Wilhelm Leibniz University Hannover*, the tools used for the composition of this thesis are listed in the following:

- LyX, MiKTeX, and MacTeX for writing the manuscript
- Microsoft PowerPoint, Ulead PhotoImpact, and Inkscape for sketching of figures
- MATLAB and wxmaxima for creating plots
- Pro/ENGINEER Wildfire for the mechanical design of the robot and for renderings in figures
- Adobe Acrobat for generating PDF

Appendix B

Surgical Robotic Systems

The basic results of the survey on state-of-the-art surgical robotics are summarised in this appendix. Systems are categorised according to the kinematic constraint during the main application to the following tables B.1, B.2, B.3, B.4, B.5, B.6, B.7, and B.8. The tables also classify the systems according to the taxonomies according to the medical domain, type of interaction, level of autonomy and level of remoteness described in section 3.1. Systems that are used in surgical procedures but which do not perform a surgical task (e.g. guiding imaging sensors) are put in parentheses. Robots that position the patient in relation to a stationary instrument (e.g. in radiation therapy) are not considered.

Name, Institution	*Medical Domain*	*Type of Interaction*	*Level of Autonomy*	*Level of Remoteness*
A73, University Erlangen	neurosurgery (osteotomy)	active	telerobotics and autonomous	physical: high time: low
ACROBOT®, The Acrobot Company Ltd.	orthopaedics	semi-active	shared control	physical: low time: high
CASPAR®, URS GmbH	orthopaedics	active	autonomous	physical: high time: high
DAANS, DIMEG	radiotherapy	active	telerobotics	physical: high time: low
MAKO®, Makosurgical Corp.	orthopaedics	active	shared control	physical: low time: low
MBARS, Carnegie Mellon University	orthopaedics	active	autonomous	physical: high time: high
MODICAS®, modiCAS Ltd.	orthopaedics	active	shared control	physical: low time: high
OTTO (1 & 2), Surgical Robotics Lab Berlin	neurosurgery (osteotomy)	active	autonomous/ shared control	physical: high/ low time: high
RIO®, MAKO Surgical Corporation™	orthopaedics	active	shared control	physical: low time: high
ROBACKA, University of Karlsruhe	orthopaedics	active	autonomous	physical: high time: high
ROBODOC®, Integrated Surgical Systems Ltd.	orthopaedics	active	autonomous	physical: high time: high
RONAF, University Bayreuth	neurosurgery (osteotomy)	active	autonomous	physical: high time: high
RSPR3, Technion	orthopaedics	active	autonomous	physical: high time: high
[Westphal et al., 2008], University of Braunschweig	orthopaedics	active	telerobotics	physical: high time: low

Table B.1: Surgical Robotic Systems constrained in zero DoF

Name, Institution	*Medical Domain*	*Type of Interaction*	*Level of Autonomy*	*Level of Remoteness*
(Hippocrate), LIRMM	echography	active	telerobotics	physical: low time: low
(MEDIROB), Medirob AB	echography	active	telerobotics	physical: high time: low
(OTELO), Sinters SA	echography	active	telerobotics	physical: high time: low
(TER), TIMC-IMAG	echography	active	telerobotics	physical: high time: low

Table B.2: Surgical Robotic Systems constrained in one DoF

Name, Institution	*Medical Domain*	*Type of Interaction*	*Level of Autonomy*	*Level of Remoteness*
(AESOP®), Computer Motion	minimally invasive surgery	passive	shared control	physical: high time: low
ACTIVE TROKAR, University of Tokyo	minimally invasive surgery	active	telerobotic	physical: high time: low
(AKTORMED™), AKTORmed GmbH	minimally invasive surgery	passive	telerobotic	physical: high time: low
ARTEMIS, Forschungszentrum Karlsruhe	minimally invasive surgery	active	telerobotic	physical: high time: low
(CLEM), TIMC-IMAG	minimally invasive surgery	active	telerobotic	physical: high time: low
BLACK FALCON, MIT	minimally invasive surgery	active	telerobotic	physical: high time: low
CoBRASurge, University of Nebraska-Lincoln	minimally invasive surgery	active	telerobotic	physical: high time: low
D2M2, Université Montpellier II	minimally invasive surgery	active	telerobotic	physical: high time: low
dA VINCI®, Intuitive Surgical Inc.	minimally invasive surgery	active	telerobotic	physical: high time: low
(ENDOASSIST®, FREEHAND®), Prosurgics Ltd.	minimally invasive surgery	active	telerobotics	physical: high time: low
ENDOBOT, Rensselaer Polytechnic Institute	minimally invasive surgery	active	shared control	physical: low time: low
ENDOPAR/ Aramis, Technical University Munich	minimally invasive surgery	active	telerobotic	physical: high time: low
(FIPS), Forschungszentrum Karlsruhe	minimally invasive surgery	active	telerobotics	physical: high time: low
HYPER FINGER, Nagoya University	minimally invasive surgery	active	telerobotic	physical: high time: low

Table B.3: Surgical Robotic Systems constrained in two DoF (Part 1)

Name, Institution	*Medical Domain*	*Type of Interaction*	*Level of Autonomy*	*Level of Remoteness*
LAPROTEK®, endoVia medical Inc.	minimally invasive surgery	active	telerobotic	physical: high time: low
(LER), TIMC-IMAG	minimally invasive surgery	active	telerobotics	physical: high time: low
MC2E, Université Pierre et Marie Curie	minimally invasive surgery	active	shared control	physical: low time: low
(PAROMIS), RWTH Aachen	minimally invasive surgery	active	shared control	physical: low time: low
ROBIN HEART, Technical University of Łódz	minimally invasive surgery	active	telerobotic	physical: high time: low
Zeus®,Computer Motion Inc.	minimally invasive surgery	active	telerobotic	physical: high time: low

Table B.4: Surgical Robotic Systems constrained in two DoF (Part 2)

Name, Institution	*Medical Domain*	*Type of Interaction*	*Level of Autonomy*	*Level of Remoteness*
BRIGIT, MedTech SA	orthopaedics	passive	shared control	physical: low time: low
DERMAROB / SCALPP, LIRMM	others (dermatom guidance)	active	shared control	physical: low time: low
[Götte, 2002], Technical University Munich	orthopaedics	passive	autonomous (positio-ning), passive (task)	physical: low time: high

Table B.5: Surgical Robotic Systems constrained in three DoF

Name, Institution	*Medical Domain*	*Type of Interaction*	*Level of Autonomy*	*Level of Remoteness*
ACUBOT / PAKY, Johns Hopkins University	orthopaedics	active	telerobotics	physical: high time: low
B-ROB II, Austrian Research Centers	punctures in neurosurgery	semi-active	high (positioning), low (task)	physical: low time: high
CT-BOT/ IRASIS, University of Strasbourg	punctures in neurosurgery	active	telerobotic	physical: high time: low
Evolution 1, URS GmbH	punctures in neurosurgery	active	high	physical: high time: high
INNOMOTION™, INNOMEDIC GmbH	punctures in neurosurgery	semi-active	high (positioning), low (task)	physical: low time: high
PADyC, TIMC-IMAG	punctures (other applications possible)	semi-active	low	physical: low time: high
MARS, Technion	orthopaedics	semi-active	autonomous (positioning)	physical: low time: low
MINERVA, Swiss Federal Institute of Technology	punctures in neurosurgery	active	telerobotics	physical high time low
NEUROARM, University of Calgary	punctures in neurosurgery	active	telerobotics	physical: high time: high
PATHFINDER®, Prosurgics Ltd.	punctures in neurosurgery	active	shared control	physical: low time: high
UMI, University of Tokyo	punctures in neurosurgery	active	high	physical: high time: high

Table B.6: Surgical Robotic Systems constrained in four DoF

Name, Institution	*Medical Domain*	*Type of Interaction*	*Level of Autonomy*	*Level of Remoteness*
FITBONE®, Wittenstein intens GmbH	orthopaedics	active	autonomous / telerobotics	physical: high time: high / low
ROMED, IPA Fraunhofer	orthopaedics	active	autonomous	physical: high time: high

Table B.7: Surgical Robotic Systems constrained in five DoF

Name, Institution	*Medical Domain*	*Type of Interaction*	*Level of Autonomy*	*Level of Remoteness*
CyberKnife®, Accuray® Inc.	radiosurgery	active	autonomous	physical: high time: high

Table B.8: Surgical Robotic Systems constrained in six DoF

Appendix C

Supplemental Information

The following sections comprise additional information in the form of legends, calculations, component data, and figures in order to supplement the referred sections of the thesis.

C.1 Legends

Table C.1 explains the acronyms used in figure 4.6, quantifies the number of objects with a minimum and maximum and states whether the object stands on the floor or is mounted to the ceiling.

Table C.2 is proposed as a supplement for figure 4.10 and lists the cables, which are conducted through joint 1 of the *DLR LWR III*. Auxiliary cables, like power supply for interfaces at the TCP are not considered. In contrast, table C.3 summarises the actuators, sensors and cables for a theoretical variant of the *DLR LWR III* with a minimum amount of integrated electronics. In this case, only the position sensor electronics are integrated into the robot. The cables categorised here represent a rough approximation. The AWG (American Wire Gauge) of the cables is assumed according to the appropriate current-cross section relation [Scherer, 2009] or by tests of the sensor components. This theoretical configuration neglects power drops on signal conductors and is therefore a best-case approximation regarding cable diameters. Due to proper EMC design shielded cables are proposed. Additionally, this list does not include auxiliary sensors (e.g. temperature sensors).

acronym	*description*	*qty*	*mounting*	*example, dimensions [mm]*
AN	anaesthetist	1	floor	-
AD	anaesthetics devices	1-2	floor, ceiling	*Dräger Cicero EM*, 850 x 700 x 1340
AH	anaesthetist helper	1	floor	-
AS	assistant surgeon	0-3	floor	-
BA	textile barrier	1	floor	-
CA	C-arm (X-ray)	0-1	floor	*Ziehm Viesta*, 1840 x 1340 x 800
CI	circulating nurse	1	floor	-
CM	C-arm monitor	0-1	floor, ceiling	*Ziehm Viesta 1*, 1690 x 580 x 500
CS	cell saver, suction devices	1	floor	*Haemonetics Cell Saver 3+*, 610 x 458 x 1011
CA	cardiac technician	0-1	floor	-
CU	ceiling supply units	0-5	ceiling	-
DI	displays, monitors	0-3	ceiling	-
EC	endoscopy cart	0-1	floor, ceiling	-
HLM	heart-lung machine	0-1	floor	*Sarns 7000*, 610 x 1151 x 643
IT	instrument table	1-5	floor	-
OL	operating light	2-3	ceiling	-
OT	operating table	1	floor	*ALPHAMAQUET 1150*, 2155 x 580 x 1215
P	patient	1	table	-
ST	scrub technician	1	floor	-
S	surgeon	1	floor	-
TB	trash bin	1-3	floor	-

Table C.1: Acronyms in figure 4.6

description	*ID*	*Signal*	*conductors*	*AWG*	*cable dimensions*
communication (fibre optics)	1	SERCOS	2x FOC	-	2x Ø 2.2 mm
sensor interface	2	SPI	20 (ribbon cable)	30	25.4 mm x 1.27 mm
electronics power supply	3	48VDC	3	23	Ø 4.5 mm
motor power supply	4	48VDC	2	15	2x Ø 2.9 mm
E-Stop backbone	5	10mA	2	28	2x Ø 0.62 mm

Table C.2: Cable dimensions of the *DLR LWR III* conducted through joint 1

component	*ID*	*signal type*	*conductors*	*voltage current*	*AWG*	*exemplary cable*	*cables*
motor type 1	6	PWM	3	48V 11A	16	*Telemeter 14/2106*	2x 5.6 mm
motor type 2	7	PWM	3	48V 7A	20	*Telemeter 14/2109*	3x 4.5 mm
motor type 3	8	PWM	3	48V 3.5A	22	*Telemeter 14/2110*	2x 3.8 mm
custom brake ($j_6 - j_7$)	9	PWM	2	48V 0.2A	28	*Telemeter 14/2103*	2x 2.7 mm
custom brake ($j_1 - j_5$)	10	PWM	2	48V 0.2A	28	*Telemeter 14/2103*	5x 2.7 mm
motor position sensor	11	BiSS-B [iC Haus, 2008]	8	signal and power	30	*Kabeltronik LifYDY 3408005*	7x 3.7 mm
joint-sided position sensor (potentiometer)	12	analogue	3	signal and power	34	*Telemeter 14/2079*	7x 1.9 mm
joint-sided torque sensor (2 full bridge circuits)	13	analogue	8	signal and power	30	*Kabeltronik LifYDY 3408005*	7x 3.7 mm

Table C.3: Cable dimensions of a theoretical *DLR LWR III* with external electronics. *Kabeltronik* and *Telemeter* cable types according to [Kabeltronik, 2009] and [Telemeter, 2009]

C.2 Operating Tables

The following table C.4 summarises the payloads of various operating tables.

manufacturer	*type*	*setup*	*maximum payload [kg]*	*reference*
Maquet	*Universal Table Top 1150.30*	ideal	360	[Maquet, 2009]
Maquet	*Operating Table Top 1150.25*	ideal	225	[Maquet, 2009]
Maquet	*Operating Table Top 1150.16*	arbitrary	225	[Maquet, 2009]
Maquet	*Operating Table Top 1150.15*	arbitrary	180	[Maquet, 2009]
Maquet	*Operating Table Top 1140.14*	arbitrary	135	[Maquet, 2009]
Schmitz u. Söhne	*OPX mobilis® 300*	arbitrary	135	[Schmitz, 2007]
Schmitz u. Söhne	*OPX mobilis® RC 40*	arbitrary	185	[Schmitz, 2007]
Berchtold	*Operon® B710*	ideal	350	[Berchtold, 2008a]
Berchtold	*Operon® D750*	arbitrary	225	[Berchtold, 2009]
Berchtold	*Operon® D7850*	ideal	450	[Berchtold, 2008b]
Trumpf	*TruSystem 7500*	ideal	360	[Trumpf, 2009]
Trumpf	*JUPITER System*	arbitrary	225	[Trumpf, 2008]

Table C.4: Payloads of operating tables

C.3 Supplemental Analysis of the Structural Parts

Three basic equations (C.1C.2C.3) determine the elastic displacement of a cantilever beam as depicted in figure C.1. Besides the material properties (Young's modulus (E), modulus of rigidity (G)), the main influence factors influencing the structural rigidity are therefore the geometry of the cross-section (cross-section area (A), the moment of area (I_x) and the torsion constant (I_T)).

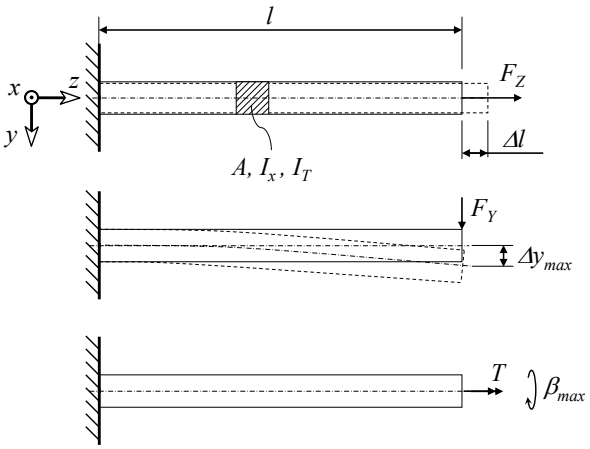

Figure C.1: Elastic displacement of a cantilever beam

$$\Delta l = \frac{F_Z \cdot l}{E \cdot A} \tag{C.1}$$

$$\Delta y_{max} = \frac{F_Y \cdot l^3}{3 \cdot E \cdot I_x} \tag{C.2}$$

$$\beta_{max} = \frac{T \cdot l}{G \cdot I_T} \tag{C.3}$$

Figure C.2 compares the cross-sections of the concepts *(b)*, *(c)* and *(e)* described in section 4.5.1 based on the following assumptions:

- Outside diameter of the link $D_{cover} = 67.00\,mm$
- Wall thickness of covers $t_{cover} = 1.5\,mm$
- PCB width $= 35.00\,mm$
- PCB thickness $= 1.5\,mm$
- Cross-section area of the link structure $= 600.00\,mm^2$

These values are derived from the actual design of the *MIRO* in order to compare the cross-section from a valid perspective. By defining a common cross-section area for all concepts, the calculation is normalised regarding the elongation due to F_Z (compare equation C.1) and the weight of the structures. The thickness of walls and diameters of the links result as depicted with the values in figure C.2.

The results for I_x and I_y are derived from calculations of CAD models in Pro/Engineer Wildfire. With U_m being the length of the middle line of the shell and A_m the cross-section area bordered by the middle line of the shell, the torsion constant is calculated according to BREDT'S second formula [Dubbel, 1997] with the equation:

$$I_T = \frac{1}{U_m} \cdot A_m^2 t \tag{C.4}$$

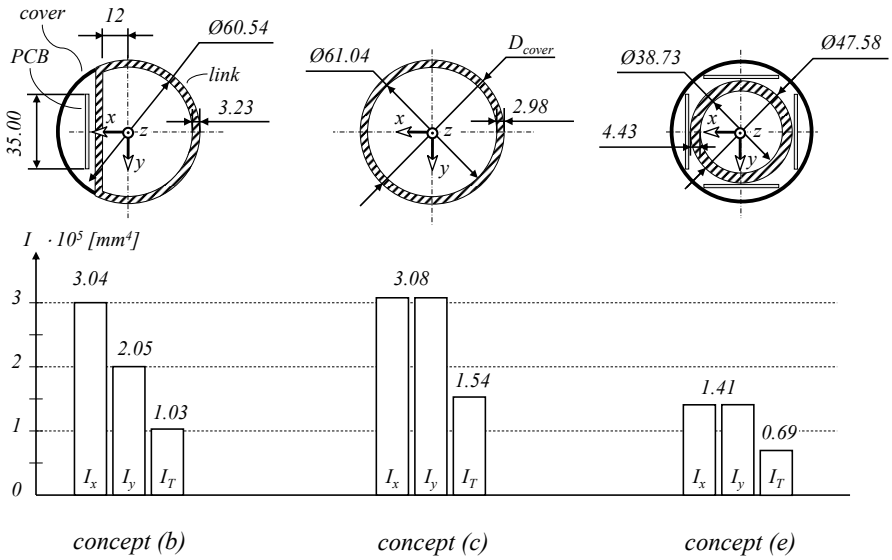

Figure C.2: Comparison of the cross-sections for the link concepts *(b)*, *(c)*, *(e)*

C.4 Diameter to Torque Correlations

Robotic rotary joints must be optimised with respect to their torque, stiffness and weight. Regarding the scaling paradigm, it is important to identify the geometric parameter with the highest impact on the performance of a component. The influence of the diameter on the maximum transmissible torque and stiffness of different components is compared with the impact of the length in this section.

First, an increased diameter benefits the transmissible torque of a component (e.g. motor, brake, structure) linearly because of the principle of leverage. Second, the circumference for the integration of force-transmitting elements (e.g. magnetic pairs in a motor, number of balls in a ball bearing) increases, which furthermore benefits the maximum torque linearly (the circumference of a circle is proportional to its diameter). Therefore, the maximum transmissible torque of components increases more or less in

a quadratic way with the diameter. In contrast, for most of the components (motors, bearings) the length of a component only increases its transmissible torque linearly.

Motors The torque of a rotary motor T is generated by tangential forces F_m, which act on the n_{wind} electric conductors (windings) in the magnetic field, where D_c denotes the diameter on which the conductors are integrated [Fischer, 1989]:

$$T = \frac{D_c}{2} \cdot \sum_{i=1}^{n_{wind}} F_{m,i} \tag{C.5}$$

Besides the value of the force, two parameters determine the torque of a motor: the diameter and the number of windings. The space for the windings is proportional to the circumference of the coil and therefore again proportional to the diameter. Therefore, the torque of a motor is proportional to the second power of the diameter. Tables C.5, C.6, and C.7 summarise basic dimensions (outside diameter D_{motor}, length l_{motor} of the stator lamination stack) and peak torques T_{peak} of different brushless, hollow shaft motor kits ($l_{motor} < 100\,mm$, DC and AC)[1]. The torque is then normalised with respect to the length ($\frac{T_{peak}}{l_{motor}}$), to allow for the influence of the diameter on the torque, which is depicted in figure C.3 (above). Two trendlines ($\sim D_{motor}^2$) show the quadratic influence of the diameter on the torque. Figure C.3 (below) depicts the more or less linear influence of the stator length on the maximum torque of two selected motor diameters.

[1] *Wittenstein Cybermotor MSSI* mini AC frameless [Wittenstein Cybermotor, 2009], *RoboDrive* brushless DC motor kits [RoboDrive, 2009], *Bayside* frameless motor kits [Bayside Motion, 2010], *MACCON Quantum* frameless motor kits [MACCON, 2009].

manufacturer	D_{motor} *[mm]*	T_{peak} *[Nm]*	l_{motor} *[mm]*	$\frac{T_{peak}}{l_{motor}}$ *[N]*	$\frac{T_{peak}}{D^2_{motor}}$ *[N/mm]*
Cybermotor	19	0.038	7.000	5.429	0.105
Cybermotor	19	0.097	17.000	5.706	0.269
Cybermotor	19	0.136	27.000	5.037	0.377
RoboDrive	25	0.100	5.000	20.000	0.160
Cybermotor	27	0.095	7.000	13.571	0.130
Cybermotor	27	0.194	17.000	11.412	0.266
Cybermotor	27	0.245	27.000	9.074	0.336
Bayside	32	0.095	6.350	14.961	0.093
Bayside	32	0.188	12.700	14.803	0.184
Bayside	32	0.281	19.050	14.751	0.274
Bayside	32	0.375	25.400	14.764	0.366
Bayside	32	0.544	38.100	14.278	0.531
Bayside	32	0.654	50.800	12.874	0.639
MACCON	35.8	0.650	12.700	51.181	0.507
MACCON	35.8	1.190	25.400	46.850	0.928
MACCON	35.8	1.870	38.100	49.081	1.459
MACCON	35.8	2.410	50.800	47.441	1.880
Cybermotor	38	0.235	7.500	31.333	0.163
Cybermotor	38	0.462	17.500	26.400	0.320
Cybermotor	38	0.724	27.500	26.327	0.501
RoboDrive	38	0.350	7.200	48.611	0.242
Bayside	44	0.397	6.350	62.520	0.205
Bayside	44	0.789	12.700	62.126	0.408
Bayside	44	1.116	19.050	58.583	0.576
Bayside	44	1.370	25.400	53.937	0.708

Table C.5: Data of brushless, hollow shaft motor kits (part 1)

manufacturer	D_{motor} *[mm]*	T_{peak} *[Nm]*	l_{motor} *[mm]*	$\frac{T_{peak}}{l_{motor}}$ *[N]*	$\frac{T_{peak}}{D^2_{motor}}$ *[N/mm]*
Bayside	44	1.817	38.100	47.690	0.939
Bayside	44	2.200	50.800	43.307	1.136
Cybermotor	49	0.702	15.000	46.800	0.292
Cybermotor	49	1.600	30.000	53.333	0.666
Cybermotor	49	2.300	45.000	51.111	0.958
RoboDrive	50	0.900	8.600	104.651	0.360
RoboDrive	50	1.400	14.600	95.890	0.560
MACCON	55.4	3.900	19.050	204.724	1.271
MACCON	55.4	7.900	38.100	207.349	2.574
MACCON	55.4	11.800	57.150	206.474	3.845
MACCON	55.4	15.600	76.200	204.724	5.083
Bayside	64	0.930	6.350	146.457	0.227
Bayside	64	1.870	12.700	147.244	0.457
Bayside	64	2.560	19.050	134.383	0.625
Bayside	64	3.230	25.400	127.165	0.789
Bayside	64	4.390	38.100	115.223	1.072
Bayside	64	6.470	50.800	127.362	1.580
RoboDrive	70	2.300	11.000	209.091	0.469
RoboDrive	70	4.000	19.000	210.526	0.816
MACCON	81.3	5.400	19.050	283.465	0.817
MACCON	81.3	10.800	38.100	283.465	1.634
MACCON	81.3	16.200	57.150	283.465	2.451
MACCON	81.3	20.900	76.200	274.278	3.162
RoboDrive	85	4.500	13.600	330.882	0.623
RoboDrive	85	7.300	23.600	309.322	1.010

Table C.6: Data of brushless, hollow shaft motor kits (part 2)

manufacturer	D_{motor} *[mm]*	T_{peak} *[Nm]*	l_{motor} *[mm]*	$\frac{T_{peak}}{l_{motor}}$ *[N]*	$\frac{T_{peak}}{D^2_{motor}}$ *[N/mm]*
Bayside	89	1.960	6.350	308.661	0.247
Bayside	89	3.920	12.700	308.661	0.495
Bayside	89	5.880	19.050	308.661	0.742
Bayside	89	7.840	25.400	308.661	0.990
Bayside	89	11.760	38.100	308.661	1.485
Bayside	89	12.870	50.800	253.346	1.625
Bayside	95	2.760	6.350	434.646	0.306
Bayside	95	5.140	12.700	404.724	0.570
Bayside	95	7.190	19.050	377.428	0.797
Bayside	95	9.000	25.400	354.331	0.997
Bayside	95	12.600	38.100	330.709	1.396
Bayside	95	14.820	50.800	291.732	1.642
RoboDrive	115	18.000	22.000	818.182	1.361
RoboDrive	115	40.000	51.400	778.210	3.025
MACCON	127	30.300	25.400	1192.913	1.879
MACCON	127	57.200	50.800	1125.984	3.546
MACCON	127	85.100	76.200	1116.798	5.276
Bayside	127	11.830	12.700	931.496	0.733
Bayside	127	21.040	25.400	828.346	1.304
Bayside	127	28.660	38.100	752.231	1.777
Bayside	127	35.240	50.800	693.701	2.185
Bayside	127	9.140	12.700	719.685	0.567
Bayside	127	16.460	25.400	648.031	1.021
Bayside	127	23.760	38.100	623.622	1.473
Bayside	127	28.320	50.800	557.480	1.756

Table C.7: Data of brushless, hollow shaft motor kits (part 3)

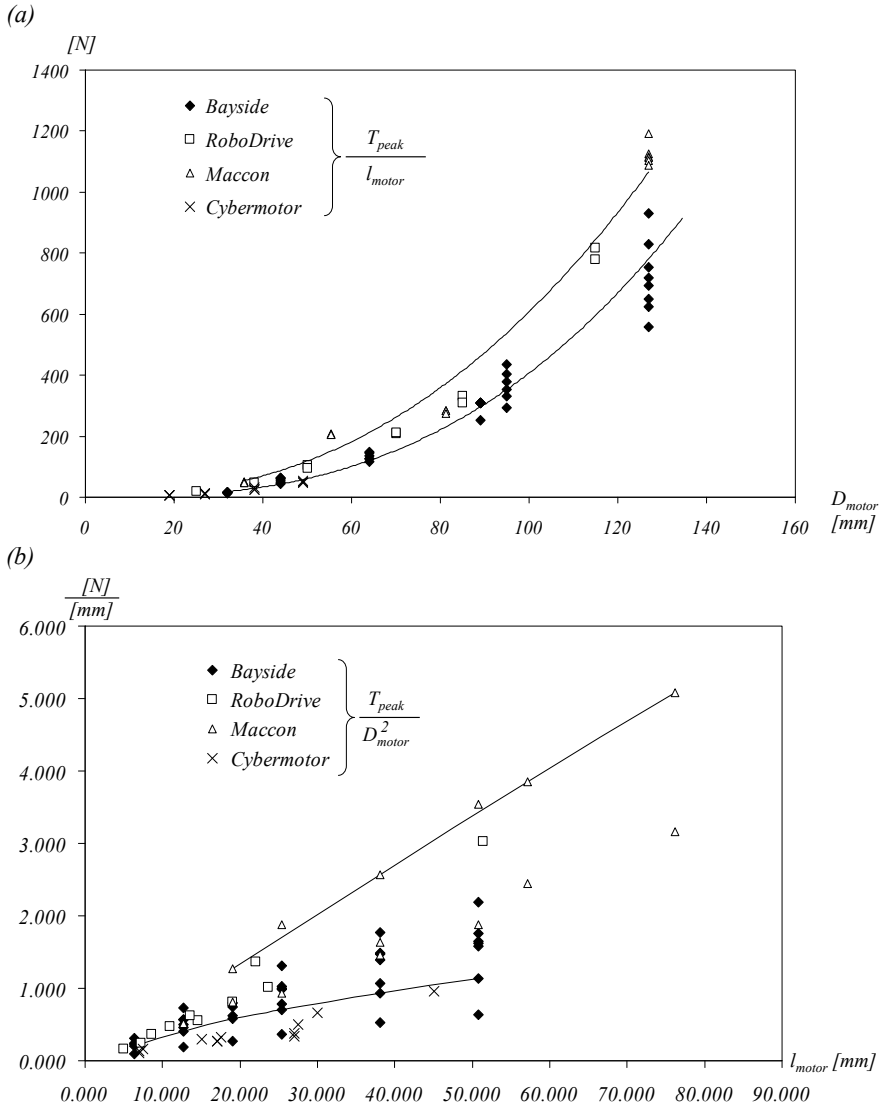

Figure C.3: Influence of motor diameter on the maximum peak torque supplemented with quadratic trendlines *(a)*, Influence of the stator lamination stack length on the maximum peak torque supplemented with two graphs for dedicated diameters (*Bayside* D_{motor}=44mm, *MACCON* D_{motor}=55.4mm) *(b)*

Bearings Bearings have a significant impact on the stiffness and maximal loads of a robotic joint. Here, the joint bearings which connect $link_i$ with $link_{i+1}$ are of special interest with respect to the stiffness of a joint. These bearings support all loads (radial, thrust, moment) acting on a joint other than the torque about the joint axis. The influence of the outside diameter D_{be} of a bearing on the maximum moment M orthogonal to the bearing axis is depicted in figure C.4 based on the data of the *KA* X-type series bearing (*Kaydon* Corporation) listed in table C.8. The included trendline depicts descriptively the quadratic impact of the diameter on the maximum torque. The influence of the bearing length on the maximum moment cannot be derived from the data of an X-type bearing, because the length is determined by the ball diameter. Increasing the length would therefore result in increasing the cross-section of the bearing and therefore the diameter. Besides X-type bearings, a classic "O" arrangement of two angular ball bearings can be applied as joint bearing (compare figure C.5). These bearings support only the radial and thrust loads in one direction. Therefore, an external force F_{ext} on the shaft creates a moment about an axis orthogonal to the shaft axis and results in radial loads F_R of the bearings.

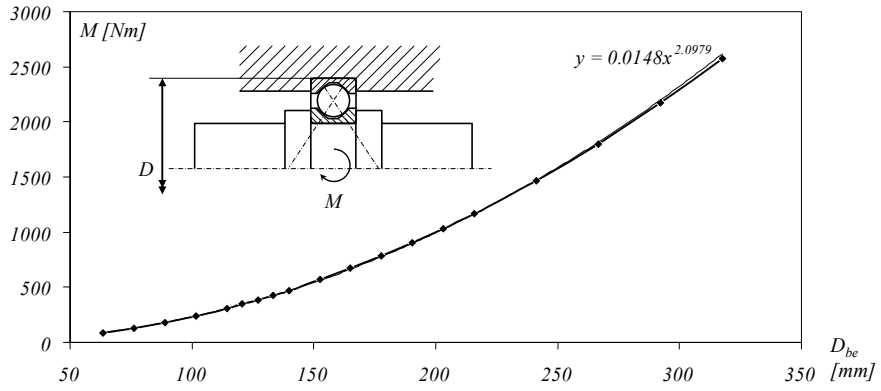

Figure C.4: Maximum static moment of *Kaydon* KA X-type bearings according to the outer diameter, supplemented with a quadratic trendline

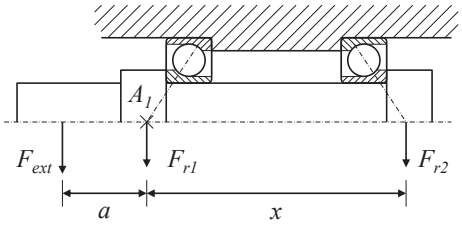

$$\Sigma M_{A_1} = 0$$
$$F_{ext} \cdot a - F_{r2} \cdot x = 0$$

Figure C.5: Bearing "O" arrangement with equilibrium of moments

D_{be} [mm]	width [mm]	M [N]
63.5	6.35	86.9946
76.2	6.35	129.927
88.9	6.35	180.768
101.6	6.35	240.6474
114.3	6.35	309.5652
120.65	6.35	346.8486
127	6.35	386.3916
133.35	6.35	428.1942
139.7	6.35	472.2564
152.4	6.35	567.1596

D_{be} [mm]	width [mm]	M [N]
165.1	6.35	669.9714
177.8	6.35	780.6918
190.5	6.35	901.5804
203.2	6.35	1030.3776
215.9	6.35	1167.0834
241.3	6.35	1467.6102
266.7	6.35	1800.9012
292.1	6.35	2170.3458
317.5	6.35	2572.5546

Table C.8: *Kaydon Realislim* bearings *KA* series X-type [Kaydon, 2007]

With the equilibrium of moments as depicted in figure C.5, the length of the bearing (i.e. distance x between the bearings) has a linear impact on the maximum moment.

Reduction gears The influence of the diameter on the maximum transmissible torque of a reduction gear is more complex than with the preceding examples and depends on the applied gear technology. For the design of the *MIRO*, gears based on the Harmonic Drive principle[2] are applied to generate the necessary torque of a joint. These gears apply a gearing between the flex and circular spline.

The influence of the length of this gearing (tooth face width b_{tooth}) on the transmissible load can be assumed linear according to the basic equations for tooth root stress (equation C.6) and pitting (equation C.7) [Matek et al., 1994]:

$$\sigma_b = \frac{F_t}{b_{tooth} \cdot modul} \cdot Y_{Fa} \quad \text{(C.6)}$$

$$\sigma_{H,max} = \sqrt{0.175 \cdot \frac{F_O \cdot E}{b_{tooth} \cdot \rho_{rad}}} \quad \text{(C.7)}$$

σ_b	tooth root stress
F_{tan}	tangential force on tooth
b_{tooth}	tooth face width
Y_{Fa}	shape correction factor
F_O	orthogonal force on surface
E	Young's modulus
ρ_{rad}	combined radii
$\sigma_{H,max}$	maximum Hertzian stress

[2]Basically, Harmonic Drive gears comprise a wave generator, which is connected to the motor, as well as the flexspline and the circular spline, which interface the static and the moving parts of the joint (e.g. circular spline connected to $link_i$, flex spline connected to $link_{i+1}$). Due to the rotation of the elliptical wave generator, the flex spline is deformed likewise and meshes with its radial teeth the circular spline. [Lauletta, 2006].

D_{rg} [mm]	average torque T_{AT} [Nm]	repeated peak torque T_{RPT} [Nm]	collision torque T_{CT} [Nm]	b_{tooth} [mm]	$\frac{T_{AT}}{b_{tooth}}$ [N]	$\frac{T_{RPT}}{b_{tooth}}$ [N]	$\frac{T_{CT}}{b_{tooth}}$ [N]
50	7.70	19	31.00	4.50	1711.11	4222.22	6888.89
60	27.00	37	55.00	5.00	5400.00	7400.00	11000.00
70	34.00	57	76.00	6.00	5666.67	9500.00	12666.67
85	75.00	110	135.00	7.00	10714.29	15714.29	19285.71
110	151.00	233	331.00	9.00	16777.78	25888.89	36777.78
135	260.00	398	578.00	11.00	23636.36	36181.82	52545.45
170	466.00	686	1320.00	13.50	34518.52	50814.81	97777.78

Table C.9: Performance data of *Harmonic Drive* CSD (1:100) reduction gears (component sets) [Harmonic Drive, 2008]

Table C.9 summarises basic dimensions (outside diameter d, tooth face width b_{tooth}) and the different torque limits of *Harmonic Drive CSD* (1:100) reduction gears [Harmonic Drive, 2008]. The torque is then normalised with respect to the length of the gearing ($\frac{T}{b_{tooth}}$) to allow for the influence of the diameter on the torque, which is depicted in figure C.6. It can be seen that the average torque T_{AT} and the repeated peak torque T_{RPT} increase more or less linearly with the diameter.

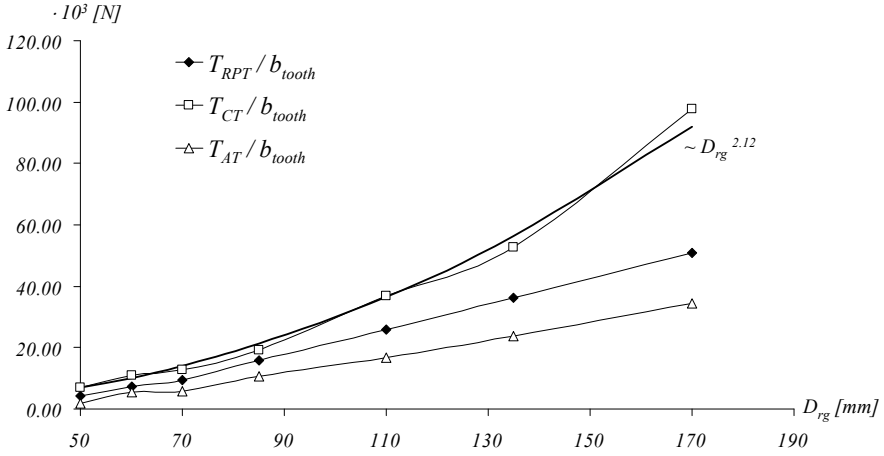

Figure C.6: Impact of the diameter on the different torque limits of *Harmonic Drive CSD* gear component sets

In contrast, the collision torque limit T_{CT} increases approximately with the second power of the diameter D_{rg}, as indicated by the trendline. It is assumed that the different torque limits are derived from different technical aspects of the gear (e.g.

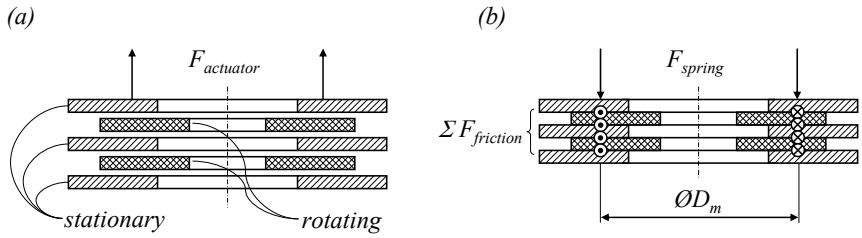

Figure C.7: Abstracted friction disc braking system: released brake *(a)*, locked brake *(b)*

gearing, fatigue of the flex spline, wave-generator bearing).

Brakes Robotic joints integrate brakes on the motor side in order to hold the robot during power-off periods and to perform emergency stops. For the *MIRO*, electromagnetic, safety-friction brakes are applied. These brakes use integrated mechanical springs causing friction between stationary and rotating parts and thereby stopping the rotating parts. In order to release the brake, one or multiple electromagnetic actuators neutralise the force of the springs. Figure C.7 depicts exemplary a disc braking system, integrating two rotating brake discs and three stationary counterparts. If the brake is locked, the holding torque of the brake T_{brake} is calculated with equation C.8.

Therefore, the holding torque increases linearly with the diameter, due to the principle of leverage. Additionally, a larger diameter allows for the integration of stronger or more springs/actuators. Therefore, the impact of the diameter on the holding torque of a brake is more than linear. The length of a brake can be reduced to the number of friction contacts n_c, which has a linear correlation with the holding torque as shown in equation C.8.

$$T_{brake} = \frac{D_m}{2} \sum F_{friction} = \frac{D_m}{2} \cdot \mu \cdot n_c \cdot F_{spring} \tag{C.8}$$

D_m	middle diameter of friction area
$F_{friction}$	friction forces
μ	friction coefficient
n_c	number of contacts
F_{spring}	spring force

C.5 BLDC Motors

The following tables C.10 to C.15 list basic performance data and dimensions of brushless DC motors, available as frameless kits. The motor constant K_M of the *Wittenstein Cybermotor MSSI* is calculated by the given motor torque constant K_T and the terminal resistance R_{TT} of the motors by the following equation:

$$K_M = \frac{K_T}{\sqrt{0,75 \cdot R_{TT}}} \tag{C.9}$$

Furthermore, for the *MSSI* types -032H- and -040H-, no data on the overall length without the commutation sensor is available. Therefore, an assumed thickness of the sensor of 1.4 mm is subtracted from the given total length, to obtain the stator length. The spatial volumes shown for all motors already subtract the usable volume of the hollow shafts.

type	τ_{Peak} *[Nm]*	K_M $[\frac{Nm}{\sqrt{W}}]$	w *[kg]*	*diameter [mm]*	*length [mm]*	*hollow shaft diameter [mm]*	*volume* $[mm^3]$
HT01000	0.24	0.010	0.040	26.70	20.60	5.84	10982
HT01001	0.53	0.018	0.060	26.70	30.70	5.84	16367
HT01002	0.83	0.026	0.090	26.70	40.90	5.84	21804
HT01500	0.58	0.017	0.070	37.80	21.90	9.52	23018
HT01501	1.17	0.031	0.130	37.80	32.00	9.52	33633
HT01502	1.79	0.042	0.190	37.80	42.20	9.52	44353
HT02000	1.33	0.034	0.120	49.20	21.90	20.06	34714
HT02001	3.16	0.066	0.220	49.20	32.10	20.06	50882
HT02002	4.95	0.090	0.320	49.20	42.20	20.06	66892
HT02300	2.32	0.056	0.170	60.40	20.90	28.95	46127
HT02301	4.76	0.106	0.330	60.40	31.10	28.95	68638
HT02302	7.31	0.147	0.480	60.40	41.30	28.95	91150
HT03800	4.70	0.120	0.470	94.70	23.90	42.67	134164
HT03801	11.80	0.250	0.850	94.70	34.00	42.67	190860
HT03802	16.90	0.340	1.230	94.70	44.10	42.67	247557

Table C.10: Specifications of *Allied Motion HT series* brushless DC frameless motors [Allied Motion, 2009]

type	τ_{Peak} *[Nm]*	K_M $[\frac{Nm}{\sqrt{W}}]$	w *[kg]*	*diameter [mm]*	*length [mm]*	*hollow shaft diameter [mm]*	*volume* $[mm^3]$
25	0.10	0.012	0.016	25.00	9.50	11.60	3659
38	0.35	0.039	0.052	38.00	13.70	18.00	12051
50	0.90	0.091	0.086	50.00	14.60	30.00	18347
50x14	1.40	0.125	0.135	50.00	20.60	30.00	25887
70	2.30	0.177	0.230	70.00	20.10	42.00	49507
70x18	4.00	0.255	0.340	70.00	28.20	42.00	69457
85	4.50	0.328	0.370	85.00	24.20	52.00	85929
85x23	7.30	0.426	0.550	85.00	34.20	52.00	121437

Table C.11: Specifications of *RoboDrive ILM* brushless DC frameless motors [RoboDrive, 2009]

type	τ_{Peak} *[Nm]*	K_M $[\frac{Nm}{\sqrt{W}}]$	w *[kg]*	*diameter [mm]*	*length [mm]*	*hollow shaft diameter [mm]*	*volume* $[mm^3]$
DIP20-06	0.10	0.012	0.065	50.80	15.24	7.06	30292
DIP20-09	0.30	0.023	0.140	50.80	22.86	7.06	45438
DIP20-12	0.42	0.030	0.187	50.80	30.48	7.06	60584
DIP20-15	0.56	0.036	0.246	50.80	38.10	7.06	75730
DIP20-19	0.66	0.042	0.311	50.80	48.26	7.06	95925

Table C.12: Specifications of *BEI KIMCO Magnetics DIP-20* brushless DC frameless motors [BEI Kimco, 2009]

type	τ_{Peak} *[Nm]*	K_M $[\frac{Nm}{\sqrt{W}}]$	w *[kg]*	*diameter [mm]*	*length [mm]*	*hollow shaft diameter [mm]*	*volume* $[mm^3]$
MSSI-022F-007D	0.04	0.0046	0.060	19.25	13.30	3.00	3777
MSSI-022F-017D	0.10	0.0086	0.082	19.25	23.30	3.00	6617
MSSI-022F-027D	0.14	0.0117	0.102	19.25	33.30	3.00	9456
MSSI-032H-007D	0.10	0.0077	0.130	27.50	15.80	5.50	9009
MSSI-032H-017D	0.19	0.0151	0.170	27.50	25.80	5.50	14711
MSSI-032H-027D	0.25	0.0224	0.215	27.50	35.80	5.50	20413
MSSI-040H-007D	0.24	0.0212	0.185	37.00	20.00	9.00	20232
MSSI-040H-017D	0.46	0.0417	0.265	37.00	30.00	9.00	30348
MSSI-040H-027D	0.72	0.0566	0.340	37.00	40.00	9.00	40464
MSSI-055H-015D	0.70	0.0625	0.620	49.00	35.00	15.00	59816
MSSI-055H-015D	1.60	0.1077	0.830	49.00	50.00	15.00	85452
MSSI-055H-015D	2.30	0.1450	1.040	49.00	65.00	15.00	111087

Table C.13: Specifications of *Wittenstein Cybermotor MSSI* brushless frameless motors [Wittenstein Cybermotor, 2009]

type	τ_{Peak} *[Nm]*	K_M $[\frac{Nm}{\sqrt{W}}]$	w *[kg]*	*diameter [mm]*	*length [mm]*	*hollow shaft diameter [mm]*	*volume* $[mm^3]$
QB01700	0.65	0.023	0.07	35.81	34.00	12	30398
QB01701	1.19	0.035	0.14	35.81	46.70	12	41753
QB01702	1.87	0.048	0.21	35.81	59.40	12	53107
QB01703	2.41	0.057	0.27	35.81	72.10	12	64462
QB02300	3.94	0.076	0.25	52.30	41.55	18	78689
QB02301	7.90	0.121	0.48	52.30	60.60	18	114766
QB02302	11.80	0.155	0.71	52.30	79.65	18	150843
QB02303	15.60	0.181	0.95	52.30	98.70	18	186921
QB03400	5.38	0.142	0.6	81.28	41.55	32	182174
QB03401	10.80	0.245	1.17	81.28	60.6	32	265697

Table C.14: Specifications of *MACCON Quantum* brushless frameless motors [MACCON, 2009]

type	τ_{Peak} *[Nm]*	K_M $[\frac{Nm}{\sqrt{W}}]$	w *[kg]*	*diameter [mm]*	*length [mm]*	*hollow shaft diameter [mm]*	*volume* $[mm^3]$
K032025	0.10	0.009	0.04	31.75	19.15	15.06	11750
K032050	0.19	0.016	0.07	31.75	25.50	15.06	15647
K032075	0.28	0.022	0.10	31.75	31.85	15.06	19543
K032100	0.38	0.027	0.12	31.75	38.20	15.06	23440
K032150	0.54	0.036	0.17	31.75	50.90	15.06	31232
K032200	0.65	0.044	0.26	31.75	63.60	15.06	39025
K044025	3.97	0.020	0.09	44.42	22.15	22.35	25636
K044050	7.89	0.035	0.13	44.42	28.50	22.35	32985
K044075	11.16	0.049	0.20	44.42	34.85	22.35	40335
K044100	13.70	0.060	0.22	44.42	41.20	22.35	47684
K044150	18.17	0.080	0.31	44.42	53.90	22.35	62383
K044200	22.00	0.097	0.40	44.42	66.60	22.35	77081
K064025	0.93	0.048	0.14	63.47	25.65	35.18	56222
K064050	1.87	0.087	0.29	63.47	32.00	35.18	70141
K064075	2.56	0.122	0.43	63.47	38.35	35.18	84059
K064100	3.23	0.150	0.57	63.47	44.70	35.18	97978
K064150	4.39	0.204	0.85	63.47	57.40	35.18	125815
K064200	6.47	0.244	1.13	63.47	70.10	35.18	153652
K089025	1.96	0.069	0.25	88.87	26.17	53.21	104138
K089050	3.92	0.164	0.50	88.87	32.52	53.21	129406
K089075	5.88	0.235	0.75	88.87	38.87	53.21	154675
K089100	7.84	0.283	1.00	88.87	45.22	53.21	179943

Table C.15: Specifications of *Bayside* frameless motor kits [Bayside Motion, 2010]

C.6 Graycode Principle

The *graycode* principle is based on a multiplicity of tracks with different binary encoding. For example, the digital signals of the six tracks are composed into an 6-bit binary word, which relates directly to the position. GRAY applies the *reflected binary coding* [Gray, 1953] instead of the standard binary coding, in order to prevent simultaneous switching on multiple tracks, which could lead to the wrong values if the edges of the code areas are not aligned precisely. Therefore, the pattern does not have coaligned boundaries of fields between all tracks. Figure C.8 shows an abstracted linear depiction of this code system with six tracks (bits). The sample position results in the 6-bit graycoded number "011011" and is decoded to the standard binary number with g_i representing the digit i of the graycode and b_i the digit i of the standard binary code by the following modulo 2 additions[3]:

$$\begin{aligned} b_6 &= g_6 \\ b_5 &= g_6 \oplus g_5 \\ b_4 &= g_6 \oplus g_5 \oplus g_4 \\ b_3 &= g_6 \oplus g_5 \oplus g_4 \oplus g_3 \\ b_2 &= g_6 \oplus g_5 \oplus g_4 \oplus g_3 \oplus g_2 \\ b_1 &= g_6 \oplus g_5 \oplus g_4 \oplus g_3 \oplus g_2 \oplus g_1 \end{aligned} \tag{C.10}$$

Therefore, the graycode number "011011" results in the binary standard number "010010", which equals decimal "18".

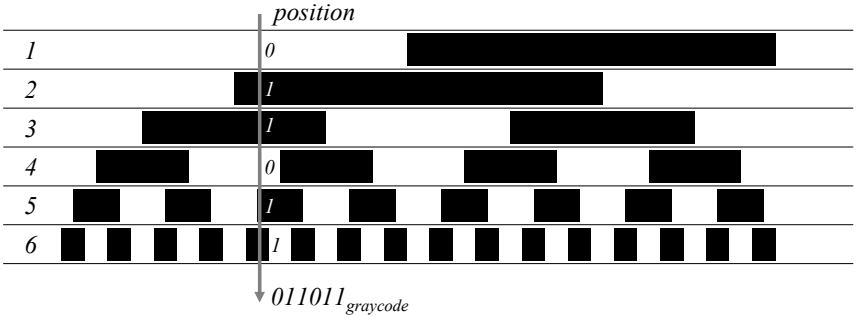

Figure C.8: 6 bit *graycode*

[3]Modulo 2 additions (XOR) additions generate the result "0" for even sums and "1" for odd sums.

Appendix D

Prototypes

D.1 The NaviPed Project

In the *NaviPed* project, funded by the *Bavarian Science Foundation,* the first (at that time nameless) robot was integrated as shown in figure D.1 *(a)*.

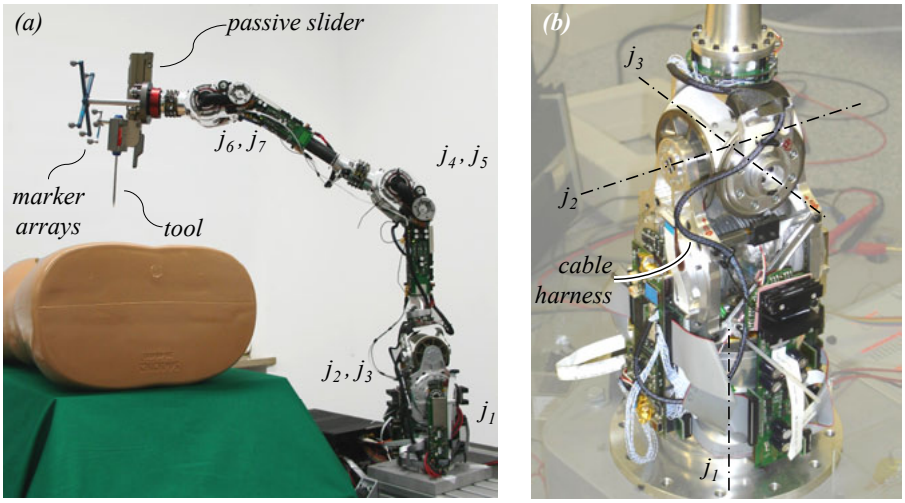

Figure D.1: Robot prototype developed within the *NaviPed* project equipped with a passive slider and marker arrays, photo copyright *DLR (a)*, tendon-based 2-DoF joint *(b)*

Designed for drilling holes for pedicle screws, the robot was equipped with a passive slider at its TCP in order to feed the drill machine manually by the surgeon. In order to establish the registration of the robot to the patient, the robotic system integrated

an intraoperative navigation system (*VectorVision® Spine* by *BrainLAB*, Germany), which also served as an external position sensor, tracking the TCP and vertebrae position. Therefore, the instrument was equipped with optical marker arrays.

The robot integrated seven actuated axes, integrated electronics and a prototypical external robot control. The first joint j_1 applied the concept, which was introduced in section 4.5.2. The pitch-yaw DoF of the shoulder was implemented by a tendon-based couple joint (compare concept *(1)* on page 113) as depicted in figure D.1 *(b)*. This joint showed remarkable performance in hands-on-robotics applications due to the absence of ripple as a consequence of the tendon-based coupling mechanism. However, the adjustment and stability of the tendons' pretension showed the deficits of this approach, due to the sticktion of the tendons on the pulleys. To adjust to a certain pretension of a tendon, the joint had to be moved permanently in order to provoke this pretension along the whole length of the tendons. Furthermore, the design of an internal cable conduit instead of the external cable loop (compare figure D.1 *(b)*), as well as the design of sealed housings, turned out to be difficult with this joint concept.

The elbow of this robot already integrated a 2-DoF couple joint based on concept *(2)* (compare section 4.5.3.2, page 122), utilising a 3-part bevel-gear assembly. This design was then duplicated for the wrist DoF, as depicted in figure D.1 *(a)*.

D.2 KineMedic

Based on the experiences with the *NaviPed* prototype described in the preceding section, the *KineMedic* robot arm was developed by order of *BrainLAB*, Germany (compare figure D.2 *(a)*). Besides a complete encapsulation of the arm with polymer housings, modified internal and external electronics, and a mechanical instrument interface, the central difference to the *NaviPed* prototype is the replacement of the tendon-based 2-DoF shoulder joint (j_2, j_3) by a design based on the bevel-gear concept (compare concept *(2)*, page 116). Due to the focus on navigated brain biopsy, this prototype still integrated the same 2-DoF joint design for the wrist and the elbow, not considering the optimised wrist design for laparoscopic instruments. The *KineMedic* development was awarded with the first prize of the *EUnited Robotics (EURON) Technology Transfer Award 2007*.

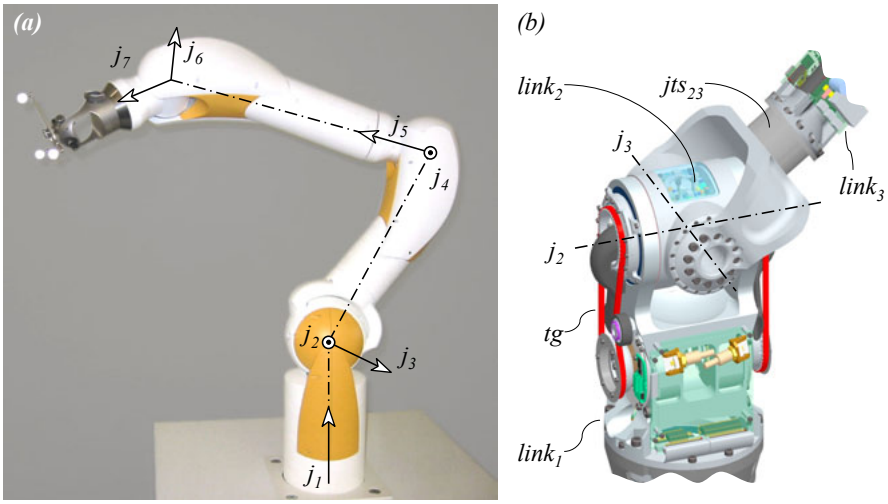

Figure D.2: The *KineMedic* robot equipped with a marker array for intraoperative navigation systems, picture courtesy of *BrainLAB AG (a)*, rendering of the 2-DoF couple joint for j_2, j_3 based on bevel gears *(b)*

List of Figures

List of Tables

Bibliography

[Albu-Schäffer et al., 2007a] Albu-Schäffer, A.; Haddadin, S.; Ott, C.; Stemmer, A.; Wimböck, T.; and Hirzinger, G. (2007a). "The DLR lightweight robot: design and control concepts for robots in human environments". *IND ROBOT*, 34(5), pp. 376–385, DOI: 10.1108/01439910710774386.

[Albu-Schäffer and Hirzinger, 2001] Albu-Schäffer, A. and Hirzinger, G. (2001). "Parameter identification and passivity based joint control for a 7DOF torque controlled light weight robot". In *Proceedings of the IEEE International Conference on Robotics and Automation, ICRA*, volume 3, pages 2852–2858, DOI: 10.1109/ROBOT.2001.933054.

[Albu-Schäffer et al., 2007b] Albu-Schäffer, A.; Ott, C.; Hagn, U.; and Ortmaier, T. (2007b). "Robot arm regulating method, for medical engineering, involves utilizing redundancy of hinges to optimize quality factor to adjust hinges at angle that is perpendicular to instrument axis, where force caused by regulating hinges is zero". *German Patent: DE 10 2005 054 575 B3*.

[Albu-Schäffer et al., 2007c] Albu-Schäffer, A.; Ott, C.; and Hirzinger, G. (2007c). "A unified passivity based control framework for position, torque and impedance control of flexible joint robots". *INT J ROBOT RES*, 26(1), pp. 23–39, DOI: 10.1177/0278364907073776.

[Allied Motion, 2009] Allied Motion (2009). "Specifications & Dimensions: HT Series Frameless Torque Motors". available online: http://www.alliedmotion.com/products/series.aspx?s=36, accessed in September 2009.

[Aluminium-Zentrale, 1988] Aluminium-Zentrale (1988). *Aluminium-Taschenbuch, 3rd edition*, chapter 2.5 Physikalische Eigenschaften, pages 98–118. Aluminium-Verlag, Düsseldorf, ISBN 3-87017-169-3.

[Ballantyne and Moll, 2003] Ballantyne, G. and Moll, F. (2003). "The da Vinci telerobotic surgical system: the virtual operative field and telepresence surgery". *SURG CLIN N AM*, 83(6), pp. 1293–1304, DOI: 10.1016/S0039–6109(03)00164–6.

[Balu, 2004] Balu, D. (2004). "Automotive Platform Sharing: An Overview". Frost & Sulivan, available online: http://www.frost.com/prod/servlet/market-insight-top.pag?docid=20843788, accessed in October 2008.

[Bayside Motion, 2010] Bayside Motion (2010). "Brochure: Frameless Motors and Gearmotors". available online: http://www.parkermotion.com/pdfs/bayside_cat/07%20Frameless%20Motors%20&%20Gearmotors.pdf, accessed in January 2010.

[BEI Kimco, 2009] BEI Kimco (2009). "BEI KIMCO Magnetics Brochure: Brushless DC Motors - Applications & Product Selection Guide". available online: http://www.beikimco.com/pdf/BLDC%20Product%20Guide.pdf, accessed in September 2009.

[Berchtold, 2008a] Berchtold (2008a). "Brochure: OPERON B710/B712 Surgical Table". available online: http://www.berchtold.biz/sites/default/files/download/Operon_B710_D.pdf, accessed in July 2009.

[Berchtold, 2008b] Berchtold (2008b). "Brochure: OPERON D 850 Surgical table". available online: http://www.berchtold.biz/sites/default/files/download/OPERON_D850_04.07_D.pdf, accessed in July 2009.

[Berchtold, 2009] Berchtold (2009). "Brochure: OPERON D750 OR-Tables". available online: http://www.berchtold.biz/sites/default/files/download/OPERON_D750_02.09_D.pdf, accessed in July 2009.

[Berkelman et al., 2003] Berkelman, P.; Cinquin, P.; Boidard, E.; Troccaz, J.; Letoublon, C.; and Ayoubi, J. (2003). "Design, Control, and Testing of a Novel Compact Laparascopic Endoscope Manipulator". *Journal of Systems and Control Engineering*, 217(14), pp. 329–341.

[Briot and Bonev, 2007] Briot, S. and Bonev, I. (2007). "Are Parallel Robots More Accurate Than Serial Robots?". *T CAN SOC MECH ENG*, 31(4), pp. 445–455.

[Brudniok, 2007] Brudniok, S. (2007). *Methodical development of highly integrated mechatronics systems by the example of a humanoid robot.* Phd thesis, University of Karlsruhe (TH), Germany.

[Bäuml and Hirzinger, 2006] Bäuml, B. and Hirzinger, G. (2006). "Agile Robot Development (aRD): A Pragmatic Approach to Robotic Software". In *Proceedings of*

the IEEE/RSJ International Conference on Intelligent Robots and Systems, IROS, pages 3741–3748, DOI: 10.1109/IROS.2006.281756.

[Burgner et al., 2009] Burgner, J.; Müller, M.; Raczkowsky, J.; and Wörn, H. (2009). "Robot assisted laser bone processing: Marking and cutting experiments". In *Proceedings of the International Conference on Advanced Robotics, ICAR*, pages 1–6.

[Butterfass, 2000] Butterfass, J. (2000). *Eine hochintegrierte multisensorielle Vier-Finger-Hand für Anwendungen in der Servicerobotik*. PhD thesis, Technische Universität Darmstadt, Germany.

[Butterfass et al., 2001] Butterfass, J.; Grebenstein, M.; Liu, H.; and Hirzinger, G. (2001). "DLR-Hand II: Next Generation of a Dextrous Robot Hand". In *Proceedings of the IEEE International Conference on Robotics and Automation, ICRA*, volume 1, pages 109–114, DOI: 10.1109/ROBOT.2001.932538.

[Butterfass et al., 1998] Butterfass, J.; Hirzinger, G.; Knoch, S.; and Liu, H. (1998). "DLR's multisensory articulated hand. I. Hard- and softwarearchitecture". In *Proceedings of the IEEE International Conference on Robotics and Automation, ICRA*, volume 3, pages 2081–2086, DOI: 10.1109/ROBOT.1998.680625.

[Cancer Research UK, 2002] Cancer Research UK (2002). "Glossary". available online: http://www.cancerhelp.org.uk/glossary.asp?search=s, accessed in October 2008.

[Čapek, 1920] Čapek, K. (1920). *R.U.R. Rossum's Universal Robots*. Penguin Classics, ISBN-10: 0141182083, 2004.

[Cenk Cavusoglu, 2006] Cenk Cavusoglu, M. (2006). *Wiley Encyclopedia of Biomedical Engineering*, chapter Medical Robotics in Surgery. John Wiley and Sons, Inc., ISBN-10: 047124967X.

[Chen, 2001] Chen, I. M. (2001). "Rapid Response Manufacturing Through Reconfigurable Robotic Workcells". *ROBOT CIM-INT MANUF*, 17(3), pp. 199–213, DOI: 10.1016/S0736–5845(00)00028–4.

[Cleary et al., 2001] Cleary, K.; Stoianovici, D.; Glossup, N.; Gary, K.; Onda, S.; Cody, R.; Lindisch, D.; Stanimir, A.; Mazilu, D.; Patriciu, A.; Watson, V.; and Levy, E. (2001). "CT-directed robotic biopsy testbed : Motivation and concept". In *Proceedings of the SPIE Medical Imaging Conference*, volume 4319, pages 231–236, DOI: 10.1117/12.428059.

[Craig, 1986] Craig, J. (1986). *Introduction to Robotics: Mechanics and Control*. Addison Wesley Longman Publishing, ISBN-10: 0201103265.

[Cunha-Cruz et al., 2009] Cunha-Cruz, V.; Follmann, A.; Popovic, A.; Bast, P.; Wu, T.; Heger, S.; Engelhardt, M.; Schmieder, K.; and Radermacher, K. (2009). "Robot- and computer-assisted craniotomy (CRANIO): from active systems to synergistic man-machine interaction". *Proceedings of the Institution of Mechanical Engineers, Part H: Journal of Engineering in Medicine*, page Doi: 10.1243/09544119JEIM596.

[Dario et al., 2004] Dario, P.; Dillman, R.; and Christensen, H. (2004). "EURON Research Roadmaps". Research roadmap, EURON European Robotics Research Network, page 50, available online: http://www.cas.kth.se/euron/euron-deliverables/ka1-3-Roadmap.pdf, accessed in October 2007.

[Davies, 2002] Davies, B. (2002). "Robotic surgery: is a "hands-on" approach the way forward?". In *Proceedings of Surgetica: Computer-aided Medical Interventions - Tools and Applications*, pages 57–62.

[Döbele, 2008] Döbele, S. (2008). *Die transpedikuläre Bohrung: eine biomechanische und theoretische Analyse der transpedikulären Bohrung zur Auslegung eines navigationsgestützten, semi-aktiven Roboters*. Phd thesis, Technische Universität München, Germany.

[Densmore and Davare, 2008] Densmore, D. and Davare, A. (2008). *A platform-based design methodology for the electronic system level*. Vdm Verlag Dr. Müller.

[Desai et al., 2007] Desai, J. P.; Tholey, G.; and Kennedy, C. (2007). "Haptic Feedback System for Robot-Assisted Surgery". In *Proceedings of the IEEE Conference of Performance Metrics for Intelligent Systems, PerMIS*, pages 202–209.

[Devol, 1970] Devol, G. (1970). "Work-Head Automatic Motion Controls". *US-Patent 3,543,910*.

[Dietrich et al., 2003] Dietrich, J.; Grebenstein, M.; Lange, T.; Schedl, M.; and Neumann, P. (2003). "Devices for robot drive units". *European Patent: EP 1 293 024 B1*.

[Diftler and Ambrose, 2001] Diftler, M. and Ambrose, R. (2001). "Robonaut: A Robotic Astronaut Assistant". In *Proceedings of the 6th International Symposium on Artificial Intelligence and Robotics & Automation in Space i-SAIRAS*, pages 179–197.

[DIN 6-1, 1986] DIN 6-1 (1986). "Standard: Technical drawings - Representation in normal projection - Views and special representations". DIN, The German Institute for Standardization, published by Beuth Publishing Germany.

[DIN ISO 9409-1, 2004] DIN ISO 9409-1 (2004). "Standard: Manipulating industrial robots - Mechanical interfaces - Part 1: Plates (ISO 9409-1:2004); German version EN ISO 9409-1:2004". DIN, The German Institute for Standardization, published by Beuth Publishing Germany.

[Dombre et al., 2004] Dombre, E.; Michelin, M.; Pierrot, F.; Poignet, P.; Bidaud, P.; Morel, G.; Ortmaier, T.; Sallé, D.; Zemiti, N.; Gravez, P.; Karouia, M.; and Bonnet, N. (2004). *Lecture Notes in Computer Science LNCS*, volume 3217, chapter MARGE Project: Design, Modeling, and Control of Assistive Devices for Minimally Invasive Surgery, pages 1–8. Springer Berlin / Heidelberg, ISBN 978-3-540-22977-3.

[Dräger, 2007] Dräger (2007). "Agila - Deckenversorgungseinheiten". available online: http://www.draeger.com/media/10/01/02/10010289/agila_br_9050659_de.pdf, accessed in January 2010.

[Dubbel, 1997] Dubbel (1997). *Dubbel - Taschenbuch für den Maschinenbau*, chapter C Strength of materials, pages C28–C29. Beitz, W. (ed), and Grote, K.H.(ed), Springer.

[Eckmann et al., 2003] Eckmann, C.; Olbrich, G.; Shekarriz, H.; and Bruch, H. (2003). "The empty OR-process analysis and a new concept for flexible and modular use in minimal invasive surgery". *Surgical Technology International Online*, 11, pp. 45–49.

[ECSS, 2003] ECSS (2003). "ECSS E-50-12A SpaceWire - Links, nodes, routers and networks". ECSS European Cooperation for Space Standardization, available online: http://www.ecss.nl/forums/ecss/dispatch.cgi/standards/docProfile/100302/d20060808084754/No/t100302.htm, accessed in September 2007.

[Faulhaber, 2009] Faulhaber (2009). "Datasheet: Linear Actuators - smoovy® Technology". available online: http://www.faulhaber.com/uploadpk/EN_03A_S3_DFF.pdf, accessed September 2009.

[Festo, 2008] Festo (2008). "Brochure: Fluidic Muscle DMSP/MAS". available online: http://www.festo.com/cat/de_de/data/doc_engb/PDF/EN/DMSP-MAS_EN.PDF, accessed in January 2010.

[Fischer et al., 2004] Fischer, H.; Kutter, S.; Vagner, J.; Felden, A.; Pfleiderer, S.; and Kaiser, W. (2004). "ROBITOM II: robot for biopsy and therapy of the mamma". In *Proceedings of IEEE International Conference on Systems, Man and Cybernetics*, volume 3, pages 2530–2534, DOI: 10.1109/ICSMC.2004.1400710.

[Fischer, 1989] Fischer, R. (1989). *Elektrische Maschinen*, chapter Allgemeine Grundlagen elektrischer Maschinen, page 14. Carl Hanser Publishing, ISBN 3-446-15600-3.

[Fite et al., 2006] Fite, K. B.; Withrow, T. J.; Wait, K. W.; and Goldfarb, M. (2006). "Liquid-Fueled Actuation for an Anthropomorphic Upper Extremity Prosthesis". In *Proceedings of the 28th IEEE Annual International Conference of the Engineering in Medicine and Biology Society, EMBS*, pages 5638–5642, DOI: 10.1109/IEMBS.2006.259638.

[Frumento et al., 2006] Frumento, S.; Michelini, R.; Konietschke, R.; Hagn, U.; Ortmaier, T.; and Hirzinger, G. (2006). "A Co-Robotic Positioning Device for Carrying Surgical End Effectors". In *Proceedings of ASME Conference on Engineering Systems Design and Analysis, ESDA*, pages 1–8.

[Gangloff, 2004] Gangloff, J. (2004). "Asservissements visuels en chirurgie robotisée". Techreport, University of Louis Pasteur, Strasbourg.

[Garshelis et al., 1997] Garshelis, I. J.; Aleksonis, J. A.; and Jones, C. A. (1997). "Development of a Magnetoelastic Torque Transducer for Automotive Transmission Applications". *SAE International, paper No. 970605*, SP-1220, pp. 35–44, available online: http://www.sae.org/technical/papers/970605, accessed in October 2008.

[Goel et al., 2003] Goel, V. K.; Dick, D. C.; Rengachary, S. S.; Garg, I.; and Ebraheim, N. A. (2003). "Tapered Pedicle Screw Pull Out Strengths: Effect Of Increasing Screw Height Outside The Pedicle". In *Proceedings of the Summer Bioengineering Conference of the ASME Bioengineering Division*, pages 0117–0118.

[Gray, 1953] Gray, F. (1953). "Pulse code communication". *US Patent: 2,632,058*.

[Grebenstein, 2005] Grebenstein, M. (2005). "Joint unit e.g. for robot, has engine arranged within framework and has stored driving pulleys with differential bevel gear provided having bevel gear pair coaxially within framework". *German Patent: DE 10 2004 059 235 B3*.

[Grip GmbH, 2009] Grip GmbH (2009). "Datasheet: MGW series - Manual gripper changing system". available online: http://www.grip-gmbh.com/downloads/datenblaetter/en/MGW.pdf, accessed September 2009.

[Görner et al., 2008] Görner, M.; Wimböck, T.; Baumann, A.; Fuchs, M.; Bahls, T.; Grebenstein, M.; Borst, C.; Butterfass, J.; and Hirzinger, G. (2008). "The DLR-Crawler: A Testbed for Actively Compliant Hexapod Walking Based on the Fingers of DLR-Hand II". In *Proceedings of the IEEE/RSJ International*

Conference on Intelligent Robots and Systems, IROS, pages 1525–1531, DOI: 10.1109/IROS.2008.4650655.

[Götte, 2002] Götte, H. (2002). *Entwicklung eines Assistenzrobotersystems für die Knieendoprothetik*. PhD thesis, Technische Universität München, Germany.

[Haddadin et al., 2008] Haddadin, S.; Albu-Schäffer, A.; and Hirzinger, G. (2008). "The Role of the Robot Mass and Velocity in Physical Human-Robot Interaction - Part I: Unconstrained Blunt Impacts". In *Proceedings of the IEEE International Conference on Robotics and Automation, ICRA*, pages 1331–1338, DOI: 10.1109/ROBOT.2008.4543388.

[Hagn, 2004] Hagn, U. (2004). "Non-laparoscopic or laparoscopic instrument connecting device for use during robot-supported minimal invasive surgery, has segment in form of flange provided at end surface of another segment over roller link". *German Patent: 10 2004 054 866 B3*.

[Hagn, 2005] Hagn, U. (2005). "Roboterarm sowie Roboter-Tragstruktur". *German Patent Application: DE 10 2005 052 443 A1*.

[Hagn, 2009] Hagn, U. (2009). "Steriles Abdecksystem zum sterilen Verkleiden eines medizintechnischen Roboterarms sowie Verfahren zum sterilen Verkleiden eines medizintechnischen Roboterarms". *German Patent Application: DE 102009019695.1*.

[Hagn et al., 2009] Hagn, U.; Konietschke, R.; Tobergte, A.; Nickl, N.; Jörg, S.; Kübler, B.; Passig, G.; Gröger, M.; Fröhlich, F.; Seibold, U.; Le-Tien, L.; Albu-Schäffer, A.; Nothhelfer, A.; Hacker, F.; Grebenstein, M.; and Hirzinger, G. (2009). "DLR MiroSurge: a versatile system for research in endoscopic telesurgery". *International Journal of Computer Assisted Radiology and Surgery*, DOI: 10.1007/s11548-009-0372-4.

[Hagn et al., 2008a] Hagn, U.; Nickl, M.; Jörg, S.; Passig, G.; Bahls, T.; Nothhelfer, A.; Hacker, F.; Le-Tien, L.; Albu-Schäffer, A.; Konietschke, R.; Grebenstein, M.; Warpup, R.; Haslinger, R.; Frommberger, M.; and Hirzinger, G. (2008a). "The DLR MIRO: A versatile lightweight robot for surgical applications". *IND ROBOT*, 35(4), pp. 324–336, DOI: 10.1108/01439910810876427.

[Hagn et al., 2008b] Hagn, U.; Ortmaier, T.; Konietschke, R.; Kübler, B.; Seibold, U.; Tobergte, A.; Nickl, M.; Jörg, S.; and Hirzinger, G. (2008b). "Telemanipulator for remote minimally invasive surgery". *IEEE ROBOT AUTOM MAG*, 15(4), pp. 28–38, DOI: 10.1109/MRA.2008.929925.

[Harashima et al., 1996] Harashima, F.; Tomizuka, M.; and Fukuda, T. (1996). "Mechatronics - "What Is It, Why, and How?" - an editorial". In *IEEE-ASME T MECH*, volume 1, pages 1–4.

[Harmonic Drive, 2008] Harmonic Drive (2008). "Catalogue 2008". Technical report, Harmonic Drive AG, Germany.

[Hayashibe et al., 2005] Hayashibe, M.; Suzuki, N.; Hashizume, M.; Kakeji, Y.; Konishi, K.; Suzuki, S.; and Hattori, A. (2005). "Preoperative Planning System for Surgical Robotics Setup with Kinematics and Haptics". *INT J MED ROBOT COMP*, 1(2), pp. 76–85.

[H.C. Starck Ceramics, 2009] H.C. Starck Ceramics (2009). "Brochure: Ceramic Parts According to Customer Demands". available online: http://www.hcstarck-ceramics.de/medien/dokumente/document_141_CeramicParts.pdf, accessed in September 2009.

[Hein et al., 2001] Hein, A.; Klein, M.; Lüth, T.; Queck, J.; Stien, M.; Schermeier, O.; and Bier, J. (2001). "Integration and Clinical Evaluation of an Interactive Controllable Robotic System for Anaplastology". In *Proceedings of the Conference on Medical Image Computing and Computer-Assisted Intervention, MICCAI, published in Lecture Notes in Computer Science*, volume 2208/2009, pages 591–598, DOI: 10.1007/3–540–45468–3. Springer.

[Hering et al., 1989] Hering, E.; Martin, R.; and Stohrer, M. (1989). *Physik für Ingenieure, 3rd edition*, chapter 4.4.4 Materie im Magnetfeld, page 305. VDI Publishing, ISBN 3-18-400916-5.

[Hexmoor and Kortenkamp, 2000] Hexmoor, H. and Kortenkamp, D. (2000). "Introduction to autonomy control software". *J EXP THEOR ARTIF INTELL*, 12(2), pp. 123–127, DOI: 10.1080/095281300409784.

[Higuchi et al., 2003] Higuchi, M.; Kawamura, T.; Kaikogi, T.; Murata, T.; and Kawaguchi, M. (2003). "Mitsubishi Clean Room Robot -Clean Material Handling Originated from Plant Equipment Inspection". Technical Review, volume 40 (5), Mitshubishi Heavy Industries, Ltd., available online: http://www.mhi.co.jp/technology/review/pdf/e405/e405298.pdf, accessed in May 2009.

[Hirzinger et al., 1993] Hirzinger, G.; Baader, A.; Koeppe, R.; and Schedl, M. (1993). "Towards a new generation of multisensory light-weight robots with learning capabilities". In *Proceedings of the IFAC World Congress*.

[Hirzinger et al., 2000] Hirzinger, G.; Butterfass, J.; Fischer, M.; Grebenstein, M.; Hähnle, M.; Liu, H.; Schaefer, I.; and Sporer, N. (2000). "A mechatronics approach to the design of light-weight arms and multifingered hands". In *Proceedings of the IEEE International Conference on Robotics and Automation, ICRA*, volume 1, pages 45–54, DOI: 10.1109/ROBOT.2000.844038.

[Hirzinger et al., 2002] Hirzinger, G.; Sporer, N.; Albu-Schäffer, A.; Hähnle, M.; Krenn, R.; Pascucci, A.; and Schedl, M. (2002). "DLR's Torque-controlled Light Weight Robot III - Are We Reaching The Technological Limits Now?". In *Proceedings of the IEEE International Conference on Robotics and Automation, ICRA*, volume 2, pages 1710– –1716, DOI: 10.1109/ROBOT.2002.1014788.

[Hoffelt, 2006] Hoffelt, S. (2006). "Gamma Knife vs. CyberKnife". *ONCOL ISSUES*, 21(5), pp. 18–21.

[Howe and Matsuoka, 1999] Howe, R. D. and Matsuoka, Y. (1999). "Robotics for Surgery". In *ANNU REV BIOMED ENG*, volume 1, pages 211–240, DOI: 10.1146/annurev.bioeng.1.1.211.

[iC Haus, 2008] iC Haus (2008). "BiSS C Protocol Description". available online: http://www.biss-ic.de/files/Bissinterface_c5es.pdf, accessed in October 2008.

[ISO 8373, 1996] ISO 8373 (1996). "Manipulating industrial robots - Vocabulary (ISO 8373:1994); German version EN ISO 8373:1996". DIN, the German Institute for Standardization, published by Beuth Publishing Germany.

[ISO 9283, 1998] ISO 9283 (1998). "Manipulating industrial robots – Performance criteria and related test methods". International Organization for Standardization.

[Jones and Ryffel, 1984] Jones, F. and Ryffel, H. H. (1984). *Gear Design Simplified*, chapter Spiral Bevel Gears - Gleason System, page 63. Industrial Press Inc, 3rd Edition, ISBN 0831111593.

[Jörg et al., 2006] Jörg, S.; Nickl, M.; and Hirzinger, G. (2006). "Flexible Signal-Oriented Hardware Abstraction for Rapid Prototyping of Robotic Systems". In *Proceedings of the IEEE/RSJ International Conference on Intelligent Robots and Systems, IROS*, pages 3755–3760, DOI: 10.1109/IROS.2006.281759.

[Jürgens, 2004] Jürgens, H. (2004). "Update of anthropometric measures for DIN 33 402 - Part 2". Technical report, BAUA, Federal Institute for Occupational Safety and Health, Germany, available online: http://www.baua.de/nn_28502/de/Publikationen/Forschungsberichte/2004/Fb1023,xv=vt.pdf? accessed in July 2009.

[Kabeltronik, 2009] Kabeltronik (2009). "datasheet: Mini-control cable, highly flexible, shielded LifYDY". available online: http://www.kabeltronik.de/electronical-wires-industrial-cables/control-cables-shielded/mini-control-cable-temperature-resistant-shielded-extremely-flexible-lifydy-t/?print=true, accessed in July 2009.

[Kawalla, 2007] Kawalla, G. (2007). *Ist die Robodoc® gestützte Prothesenschaftimplantation bei der Alloarthroplastik des Hüftgelenkes so schlecht wie ihr Ruf?* Phd thesis, Universität Leipzig, Germany.

[Kaydon, 2007] Kaydon (2007). *REALI-SLIM® Ball & Roller Bearings: Catalog 300*, chapter Open REALI-SLIM® Bearing Selections Type X Four-Point Contact, page 23. KAYDON Corporation.

[Kelling, 1923] Kelling, G. (1923). "Zur Colioskopie". *ARCH CLIN CHIR*, pages 126–226.

[Kennedy and Desai, 2003] Kennedy, C. W. and Desai, J. P. (2003). "Estimation and modeling of the harmonic drive transmission in the Mitsubishi PA-10 robot arm". In *Proceedings of the IEEE/RSJ International Conference on Intelligent Robots and Systems, IROS*, volume 4, pages 3331–3336.

[Khalid and Mekid, 2008] Khalid, A. and Mekid, S. (2008). *Innovative Production Machines and Systems*, chapter Computation and Analysis of Dexterous Workspace in PKMs, pages 13–18. MEC. Cardiff University, UK.

[Khatib et al., 2004] Khatib, O.; Brock, O.; Chang, K. C.; Ruspini, D.; Sentis, L.; and Viji, S. (2004). "Human-Centered Robotics and Interactive Haptic Simulation". *INT J ROBOT RES*, 23(2), pp. 167–178, DOI: 10.1177/0278364904041325.

[Konietschke, 2008] Konietschke, R. (2008). *Planning of Workplaces with Multiple Kinematically Redundant Robots*. PhD thesis, Technische Universität München, Germany.

[Konietschke et al., 2009] Konietschke, R.; Hagn, U.; Nickl, M.; Jörg, S.; Tobergte, A.; Passig, G.; Seibold, U.; Le.Tien, L.; Kübler, B.; Gröger, M.; Fröhlich, F.; Rink, C.; Albu-Schäffer, A.; Grebenstein, M.; Ortmaier, T.; and Hirzinger, G. (2009). "The DLR Miro Surge - A Robotic System for Surgery". Video contribution presented at the the IEEE International Conference on Robotics and Automation, ICRA.

[Konietschke et al., 2006a] Konietschke, R.; Hirzinger, G.; and Yan, Y. (2006a). "All Singularities of the 9-DoF DLR Medical Robot Setup for Minimally Invasive Applications". In Lenarcic, J. and Roth, B., editors, *Proceedings of the International Symposium on Advances in Robot Kinematics (ARK)*, Springer, pages 193–200, DOI: 10.1007/978–1–4020–4941–5_21.

[Konietschke et al., 2007] Konietschke, R.; Knöferle, A.; and Hirzinger, G. (2007). "The Autopointer: A New Augmented-Reality Device for Transfer of Planning Data into the Operating Room". In *Proceedings of the 21st International Congress and Exhibition of Computer Assisted Radiology and Surgery, CARS*, page 503.

[Konietschke et al., 2006b] Konietschke, R.; Ortmaier, T.; Ott, C.; Hagn, U.; Le-Tien, L.; and Hirzinger, G. (2006b). "Concepts of Human-Robot Cooperation for a new Medical Robot". In *Proceedings of the 2nd International Workshop on Human-Centered Robotic Systems, HCRS*.

[Konietschke et al., 2003a] Konietschke, R.; Ortmaier, T.; Weiß, H.; Engelke, R.; and Hirzinger, G. (2003a). "Optimal Design of a Medical Robot for Minimally Invasive Surgery". In *Proceedings of the 2nd Annual Meeting of the German Society for Computer and Robot Assisted Surgery, CURAC*, pages 1–8.

[Konietschke et al., 2003b] Konietschke, R.; Ortmaier, T.; Weiss, H.; Engelke, R.; and Hirzinger, G. (2003b). "Link length optimisation of a medical robot in minimally invasive surgery". In Lemke, H.; Inamura, K.; Vannier, M.; Farman, A.; Doi, D.; and Reiber, J., editors, *Proceedings of the 17th International Congress and Exhibition of Computer Assisted Radiology and Surgery, CARS*, page 1368.

[Kreuzer, 2008] Kreuzer, M. (2008). "Strain Measurement with Fiber Bragg Grating Sensors". Technical report, HBM Measurement, Germany, available online: http://www.hbm.com/fileadmin/mediapool/techarticles/2007/FBGS_StrainMeasurement_en.pdf, accessed in September 2009.

[Kuchling, 1989a] Kuchling, H. (1989a). *Taschenbuch der Physik, 13. Edition*, chapter 28.6.3. Spannungsteiler, page 404. Harri Deutsch Publishing, Germany, ISBN 3-8171-1020-0.

[Kuchling, 1989b] Kuchling, H. (1989b). *Taschenbuch der Physik, 13. Edition*, chapter T Tabellen: Haftreibungszahlen, page 584. Harri Deutsch Publishing, Germany, ISBN 3-8171-1020-0.

[KUKA, 2002] KUKA (2002). "KR 240-2 Technical Data". available online: http://www.kuka-robotics.com/NR/rdonlyres/

E08FA2E3-7B8B-4BEB-BB87-FE9FEA5AAFD9/0/kr_240_2.pdf, accessed in May 2009.

[KUKA, 2004a] KUKA (2004a). "KR 16 Technical Data". available online: http://www.kuka-robotics.com/NR/rdonlyres/5CF0125F-C80C-4258-83FF-B6C99D0388C9/0/kr_16.pdf, accessed in May 2009.

[KUKA, 2004b] KUKA (2004b). "KR C2 controller". available online: http://www.kuka-robotics.com/NR/rdonlyres/9C38A5C6-1F2B-4361-94FC-65181E4F1D9B/0/KR_C2_Engl.pdf, accessed in July 2009.

[KUKA, 2010] KUKA (2010). "KR 1000 titan, KR 1000 L750 with F variants: Specification". available online: http://www.kuka-robotics.com/res/sps/e6c77545-9030-49b1-93f5-4d17c92173aa_Spez_KR_1000_titan_en.pdf, accessed in August 2010.

[Lande and David, 1980] Lande, M. and David, R. (1980). "Articulation for Manipulator Arm.". *US-Patent 4,300,362*.

[Larkin et al., 2007] Larkin, D.; Cooper, T.; Duval, E.; Mcgrogan, A.; Mohr, C.; Rosa, D.; Schena, B.; Shafer, D.; and Williams, M. (2007). "Minimally Invasive Surgery System". *Patent Publication WO 2007/146987 A2*, (WO 2007/146987 A2).

[Lauletta, 2006] Lauletta, A. (2006). "The Basics of Harmonic Drive Gearing". *Gear Product News Magazine, April 2006 issue*, pages 32–36, available online: http://www.gearproductnews.com/issues/0406/harmonic_drive_gearing.pdf, accessed in September 2009.

[Le-Tien, 2010] Le-Tien, L. (2010). *Ansätze zur entkoppelten Regelung von mechanisch gekoppelten Doppelgelenken eines DLR-Medizinroboters*. PhD thesis, Technische Universität Dresden.

[Le-Tien et al., 2007] Le-Tien, L.; Albu-Schäffer, A.; and Hirzinger, G. (2007). "MIMO state feedback controller for a flexible joint robot with strong joint coupling". In *Proceedings of the IEEE International Conference on Robotics and Automation, ICRA*, pages 3824–3830, DOI: 10.1109/ROBOT.2007.364065.

[Lemke and Hirzinger, 2004] Lemke, P. and Hirzinger, G. (2004). *Elektrisch-mechanische Antriebssysteme: Innovationen-Trends-Mechatronik*, chapter Auslegungsoptimierung einer hochpoligen einzelpolbewickelten permanenterregten Synchronmaschine, pages 107–125. VDE VERLAG, ISBN-13: 978-3800728527.

[Lueth, 2006] Lueth, T. (2006). "Medical Device Development". Presentation at MaRS Center, University of Toronto on 31 January 2006, available online: http://www.ibbme.utoronto.ca/Assets/news+and+events/cctmd/luethpres.pdf, accessed in May 2009.

[Lum et al., 2004] Lum, M.; Rosen, J.; Sinanan, M.; and Hannaford, B. (2004). "Kinematic Optimization of a Spherical Mechanism for a Minimally Invasive Surgical Robot". In *Proceedings of the IEEE International Conference on Robotics and Automation, ICRA*, pages 829–834, DOI: 10.1109/ROBOT.2004.1307252.

[MACCON, 2009] MACCON (2009). "Brochure: MACCON Quantum Series - Size 17, 23, 34 and 56 Brushless Servo Motors". available online: http://www.maccon.de/fileadmin/FTPROOT/Quantum_kdb_e.pdf, accessed in January 2010.

[MacDorman, 2006] MacDorman, K. (2006). "Subjective Ratings of Robot Video Clips for Human Likeness, Familarity, and Eeriness: An Exploration of the Uncanny Valley". In *Proceedings of the 5th International Conference of the Cognitive Science, ICCS*, pages 48–51.

[Madhani et al., 1998] Madhani, A.; Niemeyer, G.; and Salisbury, J. (1998). "The Black Falcon: a teleoperated surgical instrument for minimally invasive surgery". In *Proceedings of the IEEE/RSJ International Conference on Intelligent Robots and Systems, IROS*, volume 2, pages 936–944, DOI: 10.1109/IROS.1998.727320.

[MAKO, 2009] MAKO (2009). "Brochure: Amazing Precision. Beautiful Results. The next evolution of MAKOplasty is here.". Technical Report 202538 r00, MAKO Surgical Corp., available online: http://www.makosurgical.com/pdfs/202538r00_MAKOplasty_Brochure.pdf, accessed in May 2009.

[Maquet, 2009] Maquet (2009). "Operating Table System - ALPHAMAQUET 1150". available online: http://www.maquet.com/content/SurgicalWorkplaces/Documents/Brochures/1150_MSW_BR_10000002_EN_4_ALL_V.pdf, accessed in July 2009.

[Matek et al., 1994] Matek, W.; Muhs, D.; Wittel, H.; and Becker, M. (1994). *Roloff/Matek Maschinenelemente*, chapter 15. Zahnräder und Zahnradgetriebe, pages 550–551. 13th edition, Vieweg Publishing, ISBN 3-528-74028-0.

[Maxon, 2009a] Maxon (2009a). "Datasheet: Planetary Gearhead GP 6 A". available online: http://shop.maxonmotor.com/maxon/assets_external/Katalog_neu/eshop/Downloads/Katalog_PDF/maxon_gear/Planetengetriebe/new/newpdf_09/GP-6-A-199687_09_EN_203.pdf, accessed in September 2009.

[Maxon, 2009b] Maxon (2009b). "Maxon Online Database: Planetary Gearheads". available online: https://shop.maxonmotor.com/ishop/gear.xml, accessed in September 2009.

[Mayer, 2008] Mayer, H. (2008). *Human-Machine Skill Transfer in Robot Assisted, Minimally Invasive Surgery.* Phd thesis, Technische Universität München, Germany.

[Mayer et al., 2007] Mayer, H.; Nagy, I.; Knoll, A.; Braun, E. U.; Bauernschmitt, R.; and Lange, R. (2007). "Haptic Feedback in a Telepresence System for Endoscopic Heart Surgery". *PRESENCE-TELEOP VIRT*, 16(5), pp. 459–470.

[Mayr, 2008] Mayr (2008). "Brochure: Overview Safety Brakes". available online: http://www.mayr.de/fileadmin/user_upload/Dokumentationen/englisch/1_General_Catalogue-Safety_Brakes.pdf, accessed September 2009.

[Melzer et al., 2008] Melzer, A.; Gutmann, B.; Remmele, T.; Wolf, R.; Lukoscheck, A.; Bock, M.; Bardenheuer, H.; and Fischer, H. (2008). "INNOMOTION for Percutaneous Image-Guided Interventions". *IEEE ENG MED BIOL MAG*, 27(3), pp. 66–73.

[Metallux, 2006] Metallux (2006). "Datasheet: Conductive Plastic Potentiometer Elements on FR4 or Polymer for rectilinear and angle position sensing". available online: http://www.metallux.de/fileadmin/specs/Potentiometerelemente-E/Metallux-PE_E.pdf, accessed in June 2007.

[Metris, 2009] Metris (2009). "Brochure: K-Series DMM". available online: http://us.metris.com/downloads/download.php?f=69.kseries_dmm_eng_1007.pdf&n=kseries_dmm_eng_1007.pdf&p=53, accessed in June 2009.

[Michelin, 2004] Michelin, M. (2004). "La robotique médicale". available online: http://www.lirmm.fr/doctiss04/art/S08.pdf, accessed in July 2009.

[Moctezuma and Schuster, 1995] Moctezuma, J. and Schuster, D. (1995). "A New Surgery Tool for Robotic Aided Treatment Delivery". In *Proceedings of the Second International Workshop: Mechatronics in Medicine and Surgery (MEDIMEC95)*, pages 35–46.

[Moctezuma de la Barrera, 1995] Moctezuma de la Barrera, J. (1995). *Ein durchgängiges System zur computer- und robotergestützten Chirurgie.* PhD thesis, Technische Universität München, Germany.

[Moore, 1998] Moore, G. (1998). "Cramming more components onto integrated circuits". *Proceedings of the IEEE*, 86(1), pp. 82–85, DOI: 10.1109/JPROC.1998.658762.

[Morales, 2009] Morales, R. (2009). "Robotic surgical system for performing minimally invasive medical procedures". *US Patent Application Publication: US 2009/0024142 A1.*

[Mori, 1970] Mori, M. (1970). "The Uncanny Valley". *ENERGY*, 7(4), pp. 33–35.

[Musser, 1959] Musser, C. W. (1959). "Strain wave gearing". *US-Patent: 2,906,143.*

[Nabtesco, 2009] Nabtesco (2009). "Brochure: Precision Reaches A New Level". available online: http://www.nabtesco-precision.de/downloads/NP_0406.pdf, accessed in September 2009.

[NCTEngineering, 2006] NCTEngineering (2006). "Brochure: Bending Sensor - Design & Dimension". available online: http://www.ncte.de/ncte/cms/upload/downloads/D&D_Bending_e.pdf, accessed in October 2009.

[Nickl et al., 2009] Nickl, M.; Jörg, S.; and Hirzinger, G. (2009). "The Virtual Path: The Domain Model for the Design of the MIRO Surgical Robotic System". In *Proceedings of the 9th International IFAC Symposium on Robot Control*, pages 97–103.

[Optolab Microsystems, 2006] Optolab Microsystems (2006). "Brochure: NEMO3 - Low Cost Absolute Encoder (Product Information)". available online: http://www.optolab.com/downloads/nemo3sf.pdf, accessed in December 2007.

[Ortmaier, 2003] Ortmaier, T. (2003). *Motion Compensation in Minimally Invasive Robotic Surgery.* PhD thesis, Technische Universität München, Germany.

[Ortmaier et al., 2005] Ortmaier, T.; Gröger, M.; Boehm, D.; Falk, V.; and Hirzinger, G. (2005). "Motion estimation in beating heart surgery". In *IEEE Transactions on Biomedical Engineering*, volume 52, pages 1729–1740, DOI: 10.1109/TBME.2005.855716.

[Ortmaier and Hirzinger, 2000] Ortmaier, T. and Hirzinger, G. (2000). "Cartesian Control Issues for Minimally Invasive Robot Surgery". In *Proceedings of the IEEE/RSJ International Conference on Intelligent Robots and Systems, IROS*, volume 1, pages 565–571, DOI: 10.1109/IROS.2000.894664.

[Ortmaier et al., 2006] Ortmaier, T.; Weiss, H.; Hagn, U.; Grebenstein, M.; Nickl, M.; Albu-Schäffer, A.; Ott, C.; Jörg, S.; Konietschke, R.; Le-Tien, L.; and Hirzinger, G. (2006). "A hands-on-robot for accurate placement of pedicle screws". In *Proceedings of the IEEE International Conference on Robotics and Automation, ICRA*, pages 4179–4186, DOI 10.1109/ROBOT.2006.1642345.

[Ott et al., 2006] Ott, C.; Eiberger, O.; Friedl, W.; Bäuml, B.; Hillenbrand, U.; Borst, C.; Albu-Schäffer, A.; Brunner, B.; Hirschmüller, H.; Kielhöfer, S.; Konietschke, R.; Suppa, M.; Wimböck, T.; Zacharias, F.; and Hirzinger, G. (2006). "A Humanoid Two-Arm System for Dexterous Manipulation". In *Proceedings of the IEEE International Conference on Humanoid Robots, IEEE-RAS*, pages 276–283, DOI: 10.1109/ICHR.2006.321397.

[Philips Electronics, 2009] Philips Electronics (2009). "FieldStrength, Publication for the Philips MRI Community: New MultiTransmit technology advances 3.0T imaging". available online: http://www.healthcare.philips.com/main/products/mri/systems/achievaTX, accessed in August 2010.

[Physik Instrumente, 2009] Physik Instrumente (2009). "Datasheet: M-850 Hexapod 6-Axis Positioning System". available online: http://www.physikinstrumente.com/en/pdf/M850_Datasheet.pdf, accessed in May 2009.

[Pierrot et al., 1999] Pierrot, F.; Dombre, E.; Dégoulangeb, E.; Urbain, L.; Caronb, P.; Boudetc, S.; Gariépyd., J.; and Mégniend, J. (1999). "Hippocrate: a safe robot arm for medical applications with force feedback". *MED IMAGE ANAL*, 3(3), pp. 285–300, DOI: 10.1016/S1361–8415(99)80025–5.

[Podsedkowski, 2005] Podsedkowski, l. (2005). "RobIn Heart 0, 1, and 3 - mechanical construction development". In *Bulletin of the Polish Academy of Sciences, Technical Sciences*, volume 53, pages 79–85.

[Pott, 2010] Pott, P. (2010). "MERODA Medical Robotics Database". available online: http://www.ma.uni-heidelberg.de/apps/ortho/meroda, accessed in August 2010.

[Pott et al., 2005] Pott, P.; Scharf, H.-P.; and Schwarz, M. L. R. (2005). "Today's State of the Art of Surgical Robotics". *Journal of Computer Aided Surgery*, 10(2), pp. 101–132.

[Provancher, 2003] Provancher, W. R. (2003). *On Tactile Sensing and Display*. Doctoral thesis, Stanford University, U.S.A., Stanford, CA, USA.

[Pschyrembel, 1993] Pschyrembel (1993). *Pschyrembel - Medizinisches Wörterbuch*. 257th edition, Walter de Gruyter, ISBN 3-933203-04-X.

[Reichenspurner et al., 1999] Reichenspurner, H.; Damiano, R.; Mack, M.; Boehm, D.; Gulbins, H.; Detter, C.; Meiser, B.; Ellgass, R.; and Reichart, B. (1999). "Use of the voice-controlled and computer-assisted surgical system zeus for endoscopic coronary artery bypass grafting". *J THORAC CARDIOV SUR*, 118, pp. 11–16.

[Rininsland, 1993] Rininsland, H. (1993). "Basics of Robotics and Manipulators in Endoscopic Surgery". *Endoscopic Surgery and Allied Technologies*, 1, pp. 154–159.

[RoboDrive, 2009] RoboDrive (2009). "Brochure: Leichtbau Torque-Servomotor".

[Rooks, 2006] Rooks, B. (2006). "The harmonious robot". *IND ROBOT*, 33(2), pp. 125–130, DOI: 10.1108/01439910610651446.

[Rosenberg, 1993] Rosenberg, L. B. (1993). "Virtual fixtures: Perceptual tools for telerobotic manipulation". In *Proceedings of the IEEE Annual International Symposium on Virtual Reality*, pages 76–82.

[Rosheim, 1989] Rosheim, M. (1989). *Robot Wrist Actuators*. Wiley-Interscience Publication, ISBN 0-471-61595-1.

[Roventa and Weber, 2006] Roventa, P. and Weber, J. (2006). "Automobilzulieferer-Mittelstand - quo vadis?". Corfina AG, available online: http://www.corfina.de/downloads/Automobilzulieferer-Mittelstand-quovadis.pdf, accessed in January 2010.

[Scherer, 2009] Scherer (2009). "General Capacities According To Cross Sections". available online: http://www.scherer-kabel.com/e_800/belastbarkeiten.php, accessed in July 2009.

[Schleifring, 2007] Schleifring (2007). "Schleifring datasheet: Series K". available online: http://www.schleifring.com/en_pdf/products/download/Series_K.pdf, accessed in July 2009.

[Schmitz, 2007] Schmitz (2007). "OPX Operating Tables for outpatient Departments and Operating Theatres". available online: http://www.schmitz-soehne.de/fileadmin/media/pdf/kataloge/en/schmitz_kat60_en.pdf, accessed in July 2009.

[Schnell et al., 1992] Schnell, W.; Gross, D.; and Hauger, W. (1992). *Technische Mechanik 2 - Elastostatik*, chapter Dünnwandige offene Profile, page 168. Springer, ISBN 3-540-55289-8.

[Schulz et al., 2001] Schulz, S.; Pylatiuk, C.; and Bretthauer, G. (2001). "A New Ultralight Antrhropomorphic Hand". In *Proceedings of the IEEE International Conference on Robotics and Automation, ICRA*, pages 2437–2441, DOI: 10.1109/ROBOT.2001.932988.

[Schunk, 2007a] Schunk (2007a). "Brochure: LWA 3 - Lightweight Arm". available online: http://www.schunk.com/schunk_files/attachments/LAW3__ModulareRobotik0907___DE_EN.pdf, accessed in June 2009.

[Schunk, 2007b] Schunk (2007b). "Brochure: Product Overview - Automation". available online: http://www.schunk.com/schunk_files/attachments/SCHUNK_Automation_ProductOverview_200710_EN.pdf, accessed in June 2009.

[Schweitzer, 1989] Schweitzer, G. (1989). "Mechatronik - Aufgaben und Lösungen". In *VDI Berichte*, volume 787, pages 1–15.

[Segura et al., 1997] Segura, J.; Preminger, G.; Assimos, D.; Dretler, S.; Kahn, R.; Lingeman, J.; and Macaluso, J. (1997). "Ureteral stones clinical guidelines panel summary report on the management of ureteral calculi". *The Journal of Urology*, 158(5), pp. 1915–1921, DOI: 10.1016/S0022–5347(01)64173–9.

[Seibold et al., 2008] Seibold, U.; Kübler, B.; and Hirzinger, G. (2008). *Medical Robotics*, chapter Prototypic force feedback instrument for minimally invasive robotic surgery, pages 377–400. I-Tech Education and Publishing, ISBN 978-3-902613-18-9.

[Sensitec, 2007] Sensitec (2007). "Datasheet: LK29A - MagnetoResistive Length Sensor for 1 mm pole length". available online: http://www.sensitec.com/en/download.php?a=14, accessed in September 2009.

[Shadow Robot Company, 2003] Shadow Robot Company (2003). "Design of a Dextrous Hand for advanced CLAWAR applications". In *Proceedings of 6th International Conference on Climbing and Walking Robots and the Support Technologies for Mobile Machines, CLAWAR*.

[Shiomi et al., 2000] Shiomi, H.; Inoue, T.; Nakamura, S.; and Inoue, T. (2000). "Quality Assurance for an Image-guided Frameless Radiosurgery System using Radiochromic Film". *RADIAT MED*, 18(2), pp. 107–113.

[Siewert, 1993] Siewert, J. R. (1993). *Laparo-Endoskopische Chirurgie*, chapter Geleitwort, page 9. Hans Marseille Verlag.

[Simaan et al., 1998] Simaan, N.; Glozman, D.; and Shoham, M. (1998). "Design Considerations of New Six Degrees-Of-Freedom Parallel Robots". In *Proceedings*

of the IEEE International Conference on Robotics and Automation, ICRA, pages 1327–1333, DOI: 10.1109/ROBOT.1998.677289.

[Slawin and Kella, 2005] Slawin, K. and Kella, N. (2005). *Atlas of the Prostate*, chapter Robotic Radical Prostatectomy, pages 3rd edition, 171–182. Current Medicine Group.

[Smith-Guerin et al., 2008] Smith-Guerin, N.; Nouaille, L.; Vievres, P.; and Poisson, G. (2008). "A medical robot kinematics design approach based on knowledge management". *IND ROBOT*, 35(4), pp. 316–323, DOI: 10.1108/01439910810876418.

[Sporer and Hähnle, 2003] Sporer, N. and Hähnle, M. (2003). "Torque sensor for an electric motor comprises a monolithic disk shaped receiving component with connection legs linking inner and outer flanges and having sensors attached to them, said component being inserted in the motor drive". *German Patent Publication: DE 103 04 359 A1*.

[Stemmer et al., 2007] Stemmer, A.; Albu-Schäffer, A.; and Hirzinger, G. (2007). "An Analytical Method for the Planning of Robust Assembly Tasks of Complex Shaped Planar Parts". In *Proceedings of the IEEE International Conference on Robotics and Automation, ICRA*, pages 317–323, DOI: 10.1109/ROBOT.2007.363806.

[Stewart, 1965] Stewart, D. (1965). "A Platform with Six Degrees of Freedom". In *Proceedings of the UK Institution of Mechanical Engineers*, volume 180, pages 371–386.

[Stolzenburg et al., 2007] Stolzenburg, J.-U.; Gettman, M.; and Liatsikos, E. (2007). *Endoscopic Extraperitoneal Radical Prostatectomy: Laparoscopic and Robot-Assisted Surgery*. Springer.

[Strong et al., 2008] Strong, E.; Rafii, A.; Holhweg-Majert, B.; Fuller, S.; and Metzger, M. (2008). "Comparison of 3 Optical Navigation Systems for Computer-Aided Maxillofacial Surgery". *ARCH OTOLARYNGOL HEAD NECK SURG*, 134(10), pp. 1080–1084.

[Sugiura et al., 2006] Sugiura, H.; Gienger, M.; Janssen, H.; and Goerick, C. (2006). "Real-Time Self Collision Avoidance for Humanoids by means of Nullspace Criteria and Task Intervals". In *Proceedings of the IEEE International Conference on Humanoid Robots, IEEE-RAS*, pages 575–580, DOI: 10.1109/ICHR.2006.321331.

[Sukovich et al., 2006] Sukovich, W.; Brink-Danan, S.; and Hardenbrook, M. (2006). "Miniature robotic guidance for pedicle screw placement in posterior spinal fusion:

early clinical experience with the SpineAssist". *INT J MED ROBOT COMP*, 2, pp. 114–122.

[Suppa et al., 2007] Suppa, M.; Kielhofer, S.; Langwald, J.; Hacker, F.; Strobl, K.; and Hirzinger, G. (2007). "The 3D-Modeller: A Multi-Purpose Vision Platform". In *Proceedings of the IEEE International Conference on Robotics and Automation, ICRA*, pages 781–787, DOI: 10.1109/ROBOT.2007.363081.

[Sutherland et al., 2008a] Sutherland, G.; Latour, I.; and Greer, A. (2008a). "Integrating an Image-Guided Robot with Intraoperative MRI". *IEEE ENG MED BIOL*, 27(3), pp. 59–65, DOI: 10.1109/EMB.2007.910272.

[Sutherland et al., 2008b] Sutherland, G.; Latour, I.; Greer, A.; Fielding, T.; Feil, G.; and Newhook, P. (2008b). "An image-guided magnetic resonance-compatible surgical robot". *NEUROSURGERY*, 62(2), pp. 286–293, DOI: 10.1227/01.neu.0000315996.73269.18.

[Taylor and Stoianovici, 2003] Taylor, R. and Stoianovici, D. (2003). "Medical Robotics in Computer-Integrated Surgery". In *IEEE Transactions on Robotics and Automation*, volume 19, pages 765–781, DOI: 10.1109/TRA.2003.817058.

[Telemeter, 2009] Telemeter (2009). "Brochure: PTFE-Kabel und Litzen nach MIL-Spezifikation". available online: http://www.telemeter.de/index.php/shop/content/download/2667/39427/file/thema_Kabel.pdf, accessed in July 2009.

[Thielmann et al., 2010] Thielmann, S.; Seibold, U.; Haslinger, R.; Passig, G.; Bahls, T.; Jörg, S.; Nickl, M.; Nothhelfer, A.; Hagn, U.; and Hirzinger, G. (2010). "MICA - A new generation of versatile instruments in robotic surgery". In *Proceedings of the IEEE/RSJ International Conference on Intelligent Robots and Systems, IROS*, accepted.

[Tie et al., 2007] Tie, H.; Allen, P.; and Fowler, D. (2007). "In-vivo pan/tilt endoscope with integrated light source". In *Proceedings of the IEEE/RSJ International Conference on Intelligent Robots and Systems, IROS*, pages 1284–1289, DOI: 10.1109/IROS.2007.4399259.

[Tobergte et al., 2010] Tobergte, A.; Fröhlich, F.; Pomarlan, M.; and Hirzinger, G. (2010). "Towards Accurate Motion Compensation in Surgical Robotics". In *Proceedings of the IEEE International Conference on Robotics and Automation, ICRA*, pages 4566–4572, DOI: 10.1109/ROBOT.2010.5509545.

[Tobergte et al., 2009] Tobergte, A.; Konietschke, R.; and Hirzinger, G. (2009). "Planning and Control of a Teleoperation System for Research in Minimally

Invasive Robotic Surgery". In *Proceedings of the IEEE International Conference on Robotics and Automation, ICRA*, pages 1589–1590, DOI: 10.1109/ROBOT.2009.5152512.

[Trejos et al., 2008] Trejos, A.; Jayender, J.; Perri, M.; Naish, M.; Patel, R.; and Malthaner, R. (2008). "Experimental evaluation of robot-assisted tactile sensing for minimally invasive surgery". In *Proceedings of the IEEE RAS & EMBS International Conference on Biomedical Robotics and Biomechatronics, BioRob*, pages 971–976, DOI: 10.1109/BIOROB.2008.4762808.

[Troccaz et al., 2002] Troccaz, J.; Berkelman, P.; Cinquin, P.; and Vilchis, A. (2002). "Surgical robot dependability: propositions and examples". In *Proceedings of the IARP/IEEE-RAS Joint Workshop on Technical Challenge for Dependable Robots in Human Environments*, pages 112–121.

[Trumpf, 2008] Trumpf (2008). "Brochure: JUPITER - Ahead of its time". available online: http://www.trumpf-med.com/index.php?eID=tx_nawsecuredl&u=0&file=fileadmin/DAM/trumpf-med.com/prospekte-29.01.2009/gb_1234230_jupiter.pdf&t=1264160214&hash=aec18b60df91d0889c9a0c7befe336b6, accessed in July 2009.

[Trumpf, 2009] Trumpf (2009). "Brochure: TruSystem 7500: The art of perfection". available online: http://www.trumpf-med.com/index.php?eID=tx_nawsecuredl&u=0&file=fileadmin/DAM/trumpf-med.com/prospekte-10.12.2008/TruSystem-7500-E.pdf&t=1264160016&hash=d4e8cbd91d04e0b9d22d5e9bd377c4df, accessed in July 2009.

[Tsai, 2000] Tsai, L.-W. (2000). *Mechanism design: enumeration of kinematic structures according to function*, chapter 1.3. Link and Joints, page 5. CRC Press, ISBN 0849309018.

[van Brussel, 1996] van Brussel, H. M. J. (1996). "Mechatronics - A Powerful Concurrent Engineering Framework". In *IEEE/ASME Transactions on Mechatronics*, volume 1, pages 127–136, DOI: 10.1109/3516.506149.

[VDI 2206, 2004] VDI 2206 (2004). "Design methodology for mechatronic systems". VDI The Association of German Engineers, published by Beuth.

[VDI 2221, 1993] VDI 2221 (1993). "Systematic approach to the development and design of technical systems and products". VDI The Association of German Engineers, published by Beuth.

[VDI 2861, 1988] VDI 2861 (1988). "Assembling and handling; characteristics of industrial robots; designation of coordinates". VDI The Association of German Engineers, published by Beuth.

[Volmer. et al., 1995] Volmer., J.; Brock, R.; Hammerschmidt, C.; Jacobi, P.; Müller, W.; Neßler, W.; Raths, W.; and Schönherr, J. (1995). *Getriebetechnik Grundlagen*. Verlag Technik, ISBN 3-341-01137-4, 2nd edition.

[Vujisic et al., 2007] Vujisic, M.; Osmokrovic, P.; and loncar, B. (2007). "Gamma irradiation effects in programmable read only memories". *J PHYS D APPL PHYS*, 40(18), pp. 5785–5789, DOI: 10.1088/0022–3727/40/18/041.

[Vázquez et al., 2008] Vázquez, A.; Mayoral, R.; Korb, W.; Voruganti, A.; Passig, G.; and Ortmaier, T. (2008). "S-PACS architecture for automated soft tissue manipulation with mechatronic assistance using endoscopic doppler guidance". In *Proceedings of the International Congress and Exhibition on Computed Assisted Radiology and Surgery, CARS*, volume 3, pages 147–148.

[Weinberg et al., 2000] Weinberg, A.; Pietsch, I.; Helm, M.; Hesselbach, J.; and Tscherne, H. (2000). "A new kinematic model of pro- and supination of the human forearm". *J BIOMECH*, 33, pp. 487–491.

[Weiss, 2008] Weiss, M. (2008). "Robot control, industrial robot and method for obtaining an absolutely precise model". *European Patent Application EP1 980 374 A2*.

[WEMO Automation, 2009] WEMO Automation (2009). "Brochure: WGS - Quick-Lock". available online: http://www.wemo.se/BinaryLoader.aspx?OwnerID=4e590610-fc85-49eb-9bf3-5de83035c950&OwnerType=2&ModuleID=a8429cd5-a9d9-4e2b-a1d8-4a7cf26cd7a3&PropertyCollectionName=Content&PropertyName=Files&ValueIndex=0, accessed in August 2009.

[Westphal et al., 2008] Westphal, R.; Winkelbach, S.; Gösling, T.; Oszwald, M.; Hüfner, T.; Krettek, C.; and Wahl, F. (2008). *Medical Robotics*, chapter Telemanipulated Long Bone Fracture Reduction, pages 507–526. I-Tech Education and Publishing, ISBN 978-3-902613-18-9.

[Wintermantel and Ha, 2009] Wintermantel, E. and Ha, S.-W. (2009). *Medizintechnik - Life Science Engineering, 5th edition*, chapter 5 Sterilisation, pages 113–125. Springer, ISBN-13: 978-3540939351.

[Wittenstein Cybermotor, 2009] Wittenstein Cybermotor (2009). "Brochure: MSSI Mini AC-Servomotoren". available online: http://www-alt.alphagetriebe.de/pdf/msside0108.pdf, accessed in July 2009.

[Wösch and Feiten, 2002] Wösch, T. and Feiten, W. (2002). "Reactive Motion Control for Human - Robot Tactile Interaction". In *Proceedings of the IEEE International Conference on Robotics and Automation, ICRA*, volume 4, pages 3807–3812, DOI: 10.1109/ROBOT.2002.1014313.

[Yan et al., 2006] Yan, L.; Chen, I.; Yang, G.; and Lin, W. (2006). "Torque modelling of spherical actuators with double-layer poles". In *SIMTech technical reports*, volume 7, pages 214–219.

[Yoshikawa, 1990] Yoshikawa, T. (1990). *Foundations of Robotics: Analysis and Control*. The MIT Press, ISBN: 0262514583.

[Zatsiorsky, 1997] Zatsiorsky, V. (1997). *Kinematics of Human Motion*, chapter 2.2.3. Kinematics Models and Mobility of the Human Body, page 109. Human Kinetics Publishing, ISBN: 0880116765.

[Zhang et al., 2009] Zhang, X.; Oleynikov, D.; and Nelson, C. (2009). "Portable tool positioning robot for telesurgery". *ST HEAL T*, 142, pp. 438–43.